AN EVALUATION OF ULTRA-WIDEBAND PROPAGATION CHANNELS

by

R. Jean-Marc Cramer

A Dissertation Presented to the

FACULTY OF THE GRADUATE SCHOOL

UNIVERSITY OF SOUTHERN CALIFORNIA

In Partial Fulfillment of the

Requirements for the Degree

DOCTOR OF PHILOSOPHY

(ELECTRICAL ENGINEERING)

December 2000

Contents

List of Tables

List of Figures

AN EVALUATION OF ULTRA-WIDEBAND PROPAGATION CHANNELS

by

R. Jean-Marc Cramer

Abstract

Ultra-wideband (UWB) communication systems have been proposed for use in a number of different applications where the large fractional bandwidth of the transmitted UWB signals may lead to advantages over more narrowband communication waveforms. In order to gain a more complete understanding of the potential of UWB communication systems, models describing the UWB propagation channel must be developed. From these models, radio algorithms can be verified, system performance can be predicted and design trades made.

The work presented here consists of two main parts. First techniques appropriate for processing the baseband signals considered in this work are developed. These algorithms permit evaluation of the received waveform, the angle-of-arrival and the time-of-arrival of UWB signals incident on an array of sensors. Given the fractional bandwidth of the signals of interest here, many traditional techniques for source location and sidelobe reduction are not applicable. An iterative solution is attempted, based on the CLEAN algorithm from radio astronomy. The original CLEAN algorithm is modified to improve operation in the presence of sensor-to-sensor signal fluctuations across the receiver antenna array. Post-processing algorithms are also developed to improve the signal estimates provided by this routine.

In the second part of this work, the processing routines are applied to measured data taken on an array of sensors at a number of different locations in an office building. The recovered signal information is used to evaluate the indoor UWB propagation channel,

including the path loss characteristics and a clustering phenomenon in the arrival of the multipath components. The parameters of these models are compared, where possible, to existing models for narrowband signal propagation in the indoor environment.

Chapter 1

Introduction

1.1 Motivation and Definitions

Ultra-wideband (UWB) communication systems have been proposed for use in a number of different applications where the impulsive nature of the transmitted UWB signals may have advantages over more narrowband communication waveforms. In order to gain a more complete understanding of the potential of UWB communication systems, models describing the UWB propagation channel must be developed. From these models, radio algorithms can be verified, system performance can be predicted and design trades made.

A bandwidth measure appropriate for UWB signals is the fractional bandwidth B_f, defined as,

$$B_f = 2\frac{f_H - f_L}{f_H + f_L} \tag{1.1}$$

where f_H and f_L are the upper and lower 3 dB points of the signal spectrum, respectively. The Defense Advanced Research Project Agency's (DARPA) Assessment of Ultra-Wideband Radar written in 1990 [9], established a definition for UWB signals as having a fractional bandwidth of greater than 25%. Signals which satisfy this constraint include the baseband

Gaussian pulse and the derivative Gaussian pulses employed as signal models in this work, as well as radio-frequency pulses of duration less than four cycles of the carrier waveform. In contrast, narrowband signals are defined to have a fractional bandwidth of less than 1%, and signals with fractional bandwidths between 1% and 25% are termed wideband [56].

The motivation for considering UWB signals for the transmission of information is given by the target applications, some of which require operation in dense multipath and perhaps shadowed environments. In these applications, UWB waveforms may have advantages over more narrowband signals in several respects. First, the fine multipath resolution inherent in the short time-duration pulses can result in reduced signal level fluctuations and hence lower required transmitter power. Second, the UWB signals considered here are baseband; there is no carrier signal involved. This means that the signal energy is concentrated in as low of a frequency range as possible. It is known that electromagnetic signals radiated at lower frequencies tend to have better material penetration properties than signals radiated at higher frequencies. Thus, in a shadowed environment, these UWB waveforms may stand a better chance of propagating sufficient signal energy to maintain a link than a system operating with the same bandwidth, but employing a carrier signal.

Propagation studies and have been reported over channels with smaller fractional bandwidths than those of interest here, for both the indoor and outdoor environments [15], [22], [30], [35], [37], [48], [49], [29]. Most of these studies account for basic parameters, such as the signal power distributions and Doppler spread, and some also include more detailed spatial and temporal information, such as joint angle-of-arrival and time-of-arrival statistics. Given that the transmitted signals for the UWB communication systems of interest here are baseband pulses of approximately one nanosecond in duration, it is possible that the results presented in these references do not completely describe the UWB propagation channel. Further, the fractional bandwidth and the dynamic nature of the received UWB

signals preclude many traditional techniques for obtaining spatial information from direct application to the UWB channel characterization problem. Although the radar community has reported work on the scattering characteristics of UWB waveforms [56], research on UWB signal propagation for the purpose of communication channel characterization has not been accomplished. The UWB channel parameters to be characterized in this work include the joint time-of-arrival and angle-of-arrival statistics of the multipath signal components, determined from measured propagation data taken on an array of sensors.

A body of literature has been developed to address the problems of source location and sidelobe reduction for the case of narrowband signals incident on an array of sensors [23], [32]. Wideband techniques have also been reported [4], [16], [21]. Fundamental differences exist between these classical array signal processing techniques, predicated on the incidence of constant envelope signals, and the problem of interest here, where the signals are impulsive in nature. In the narrowband case, as well as the wideband generalizations, an assumption is usually made that each signal-of-interest is present at all sensors at any given moment in time. If these techniques were to be applied to baseband UWB signals, a time window of large enough extent to encompass the incident signal at each sensor in the array would have to be employed. This is accomplished at the expense of time resolution, one of the motivating factors for the use of UWB signals.

Antenna arrays for the processing of UWB signals have been investigated, primarily by the radar community [21], [46], [41], [54], [56]. Array signal processing algorithms for these signals have also been reported [21]. The problems addressed in this work are distinct from those discussed in these references, due to the need to resolve and identify the multipath signal components present in the indoor environment, rather than more isolated radar returns.

The main UWB array signal processing algorithm proposed herein is related to the CLEAN algorithm, first introduced in [19], and well established in the radio astronomy and microwave communities [11], [43], [48], [52], [54], [57] as a non-linear, iterative deconvolution technique. The CLEAN algorithm has also been discussed in the context of relaxation techniques for the solution of elliptic differential equations [10]. Although the CLEAN algorithm has been reported for use on wideband signals [54], the bandwidth in the reported experiment was synthesized by sweeping a tone over a bandwidth of 200 MHz in 2 MHz steps, a smaller bandwidth than that of the UWB waveforms considered here. It has also been previously used in the deconvolution of measured data for communication channel characterization [48], [49], [60], in each case over a smaller bandwidth than that considered here. Application of the CLEAN algorithm to the processing of impulsive UWB waveforms in the time domain has not been previously reported in the available literature, nor has the processing algorithm been applied in a spatio-temporal context on impulsive signals.

Modifications to the CLEAN algorithm were made in order improve the performance on UWB signals. The original algorithm assumes perfect knowledge of the received signal, something not readily available in the UWB case. It was modified so that an estimate of the received signal could be made and utilized on each iteration. This modified algorithm was called Sensor-CLEAN in order to reflect the fact that the relaxation step was moved from beam-space to sensor-space. Post-processing algorithms were also developed in order to further improve the accuracy and reliability of the signal estimates provided by the Sensor-CLEAN algorithm.

In order to generate spatio-temporal models for the UWB propagation channel, two main tasks were considered in this research. First, the signal processing techniques related to the Sensor-CLEAN algorithm were developed. This permitted the signal arrival information to be extracted from measured propagation data. Second, the recovered signal information

was used to create models which describe the propagation of UWB signals in an indoor environment.

1.2 Review of the Multipath Propagation Experiment

A UWB signal propagation experiment was performed by Moe Z. Win in an office building by sounding the channel with an UWB waveform [66]. Signal measurements were made from a fixed impulse transmitter location to receiver locations at 14 different rooms and hallways of the office building, transmitting a pulse train of duty cycle 0.2% and of period of 500 nanoseconds. The building floor plan is shown in Figure 1-1. In each receiver location, measurements were made over a time window of 300 nanoseconds at 49 different points arranged spatially in a fixed-height, 7 sensor $\times$ 7 sensor square grid with 6 inch inter-sensor spacing, covering 3 feet by 3 feet, shown in Figure 1-2. In this figure, θ represents the azimuth look direction. The elevation look angle, ϕ, is measured from a perpendicular to the array. The same absolute delay reference for all recorded profiles was used.

Considering the measured data, samples of the signal received at location P in the building are shown in Figure 1-3, Figure 1-4, and Figure 1-5. This is a relatively high SNR case, and these measurements are from sensors located along a diagonal of the measurement array, at the upper left hand sensor, the middle sensor and the lower right-hand sensor. Further details of the experiment can be found in [66]. Note the arrival of a relatively clean pulse via a line-of-sight (LOS) path, not corrupted by multipath, near the beginning of each trace. The direction-of-arrival of this direct path response can be inferred from the time-of-arrival at the sensors, but beyond that, it is difficult to determine much about the angle-of-arrival of the multipath components by inspecting the traces. One of the main goals of this work is to resolve and characterize the time-of-arrival and the angle-of-arrival of these multipath components.

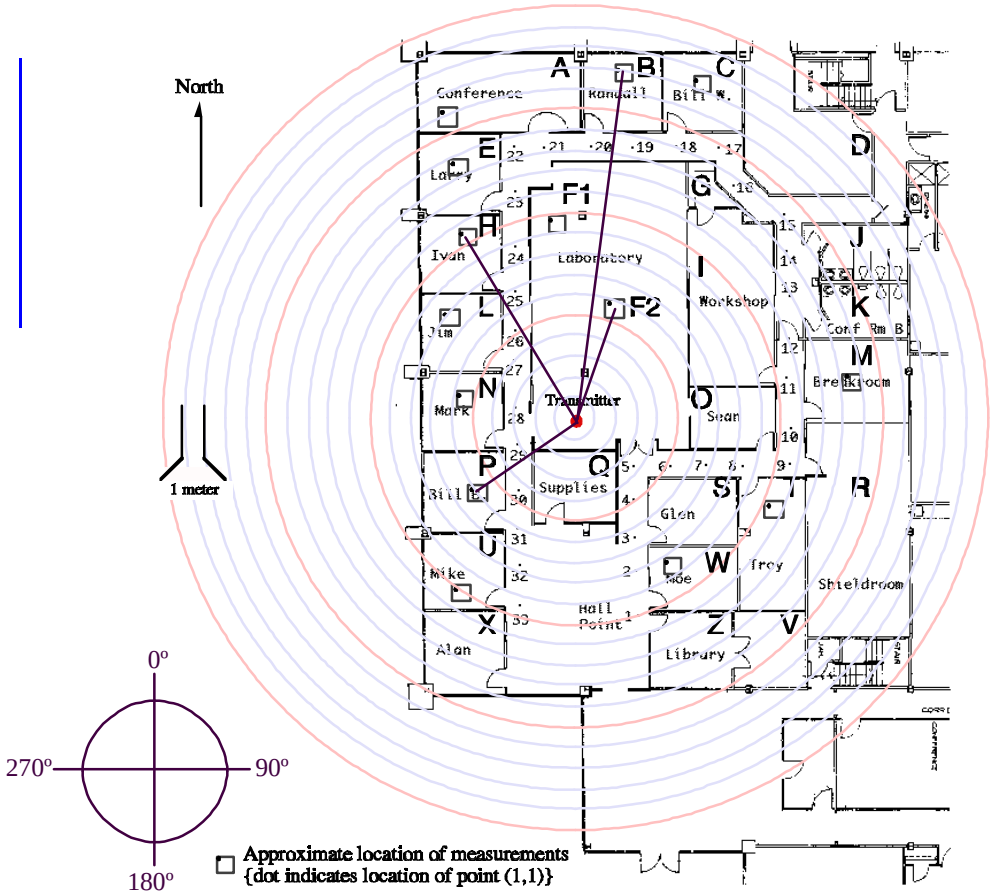

Figure 1-1: Floor plan of building in which experiment was conducted.

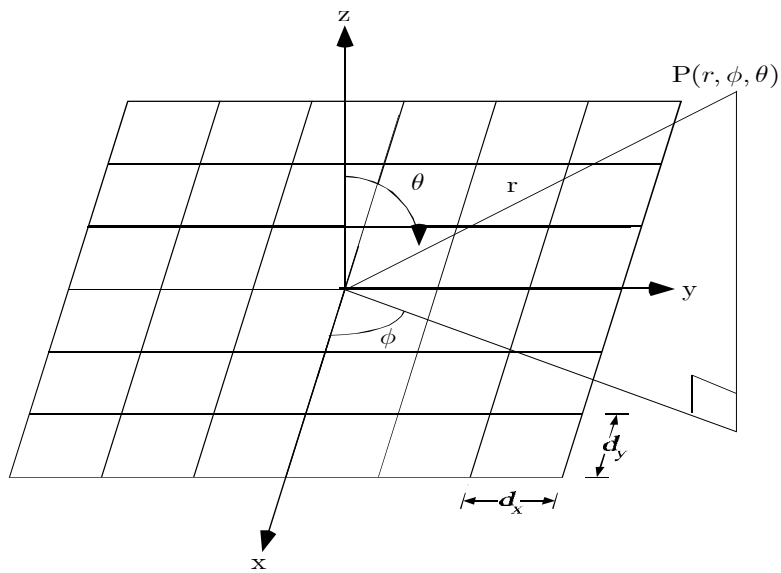

Figure 1-2: Geometry of the measurement array.

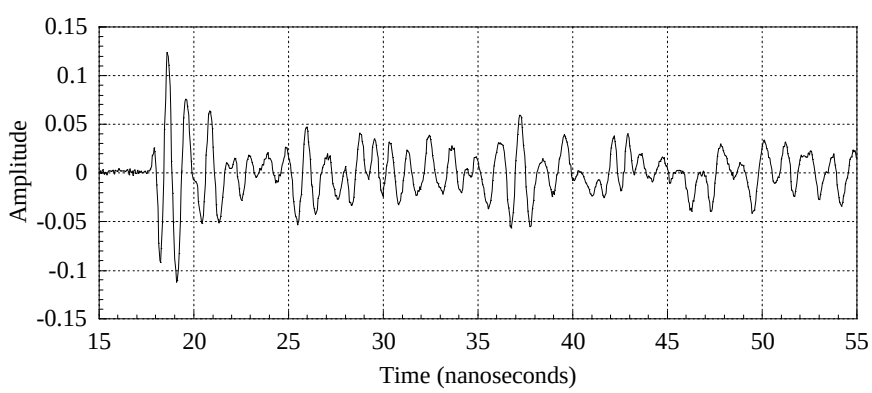

Figure 1-3: Measured signal at sensor (1,7) for a high SNR case.

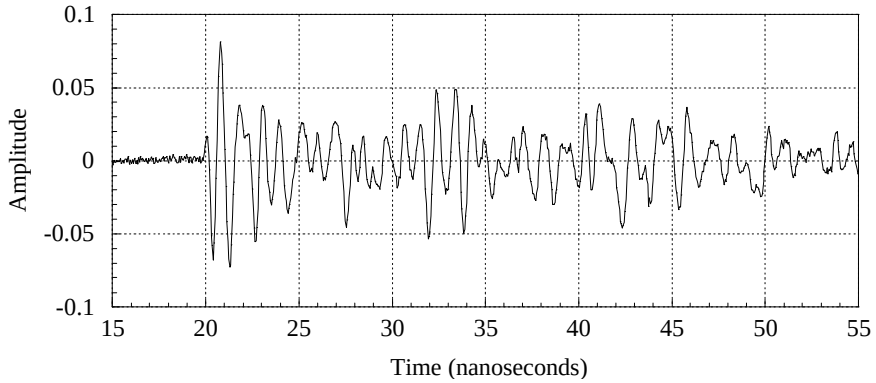

Figure 1-4: Measured signal at sensor (4,4) for a high SNR case.

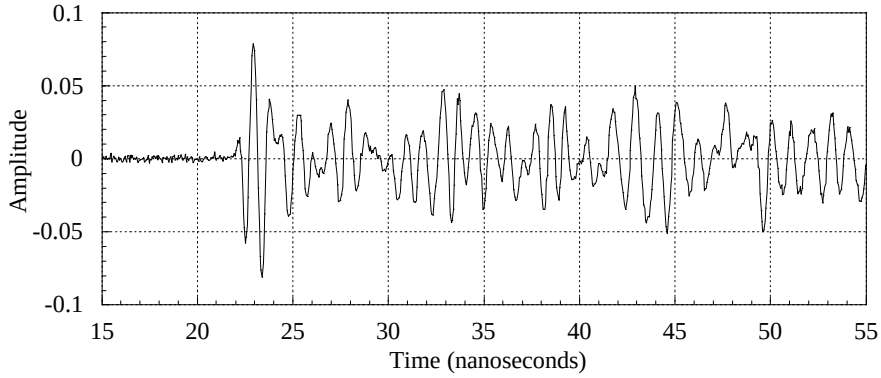

Figure 1-5: Measured signal at sensor (7,1) for a high SNR case.

1.3 Representations of the Ultra-Wideband Waveforms

One of the challenges in developing an analytic framework for the study of UWB communication systems is in establishing appropriate signal models. In previous analyses, the signal at the input of the transmit antenna has been modeled as a Gaussian waveform, according to

$$p_0(t) = A_0 \exp\left[-2\pi\left(\frac{t-t_d}{\tau_m}\right)^2\right], \tag{1.2}$$

where t_d represents the location of the pulse center in time and τ_m is a parameter which determines the temporal width of the pulse. Under this assumption, the ideal transmitted pulse shape, which arrives at the receive antenna can be modeled as

$$p_1(t) = A_1(t-t_d) \exp\left[-2\pi\left(\frac{t-t_d}{\tau_m}\right)^2\right]. \tag{1.3}$$

This equation is plotted in Figure 1-6 for a hypothesized impulse width parameter of τ_m=0.8 nanoseconds. This value for τ_m was determined as a best fit to the direct path signal in the measured data.

The response of the receive antenna to this pulse is modeled by the time-derivative of equation (1.3), given as

$$p_2(t) = A_2\left[1-4\pi\left(\frac{t-t_d}{\tau_m}\right)^2\right] \exp\left[-2\pi\left(\frac{t-t_d}{\tau_m}\right)^2\right] \tag{1.4}$$

and shown in Figure 1-7, where the parameters have the same interpretation as above. Note the tendency of the antennas to radiate a signal proportional to the derivative of the driving current. This is a general characteristic of antennas [56], but is not a concern in the narrowband case, as the properties of the derivative are well approximated by a phase

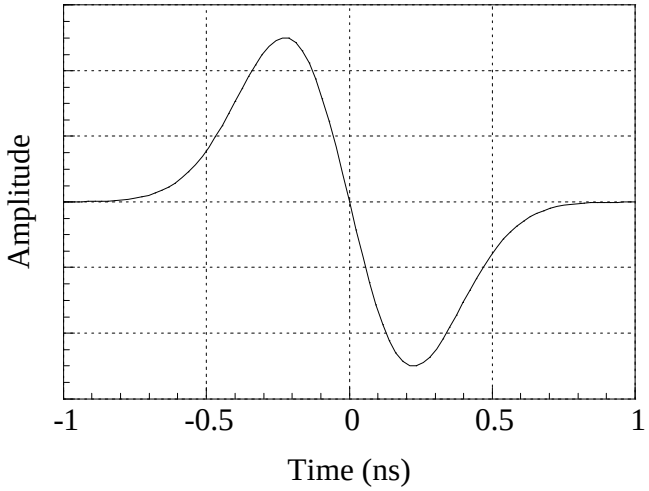

Figure 1-6: Transmitted pulse shape

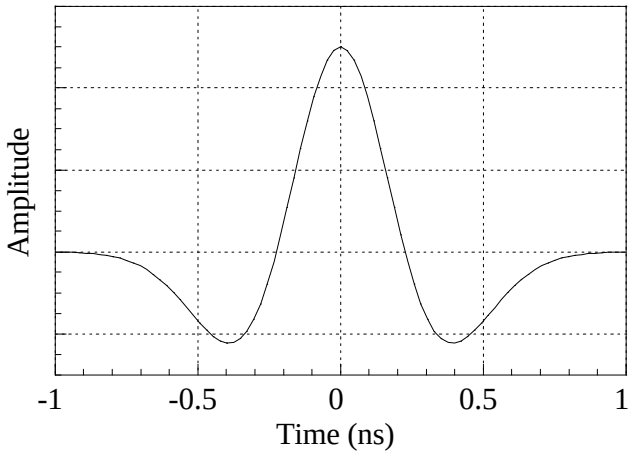

Figure 1-7: Pulse shape at input to demodulator

shift. The implications are that antenna design for UWB systems is a distinct problem from antenna design for more narrowband systems.

Taking the Fourier transform of these pulses, the magnitude of the frequency spectra are given by

$$P_1(f) = \frac{A_1 f \tau_m^3}{2\sqrt{2}} \exp\left(-\frac{\pi f^2 \tau_m^2}{2}\right), \tag{1.5}$$

$$P_2(f) = \frac{A_2 \pi f^2 \tau_m^3}{\sqrt{2}} \exp\left(-\frac{\pi f^2 \tau_m^2}{2}\right). \tag{1.6}$$

These equations are plotted in Figure 1-8 and Figure 1-9 using the same impulse width parameter of τ_m=0.8 ns. The bandwidth of these signals is noted. These transforms can be taken utilizing properties of Hermite functions, by representing the transmitted signal as a linear combination of Hermite functions [62],

$$p_n(t) = \sum_k a_k H_k. \tag{1.7}$$

The transform is then given as,

$$P_n(\omega) = \sqrt{2\pi} \sum_k (-1)^k a_k H_k(\omega). \tag{1.8}$$

This representation will be developed further in Appendix A.

The received signal model associated with this waveform is complicated by the fact that transmitted pulses undergo significant shaping in the radiation and propagation processes [56]. In addition, the channel adds multipath components and noise, as seen in Figure 1-3, 1-4 and 1-5. The cumulative effect can result in a received signal which is no longer

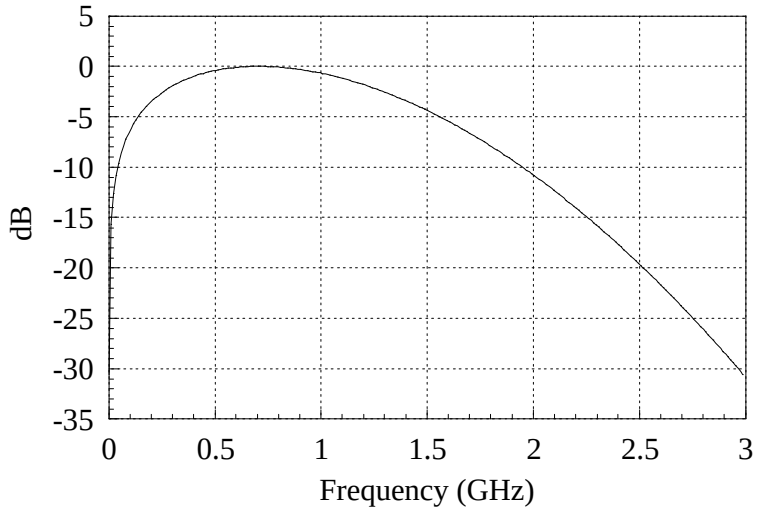

Figure 1-8: Magnitude spectrum of transmitted pulse

well modeled by these Gaussian pulses. As discussed in Appendix A, this phenomenon eliminated these sorts of models from having any significant application in this work.

1.4 Overview of the Dissertation

Following the introduction to UWB signals and the motivation for considering them, given in this chapter, Chapter 2 develops the concept of UWB beamforming. In Chapter 3, the properties of UWB arrays are presented, as distinct from those of more narrowband arrays. The unique problems associated with processing UWB signals are also included in the discussion. An iterative solution to the problem of UWB signal detection and identification is introduced in Chapter 4. This algorithm is developed and verified and the post-processing of the results is addressed in both Chapter 4 and Chapter 5. Finally, the processing algorithms are applied to the measured data to recover estimates of the incident signal parameters, including the azimuth angle-of-arrival, the elevation angle-of-arrival, the time-of-arrival and the received waveform. This recovered signal information is used in Chapter 6 and Chapter

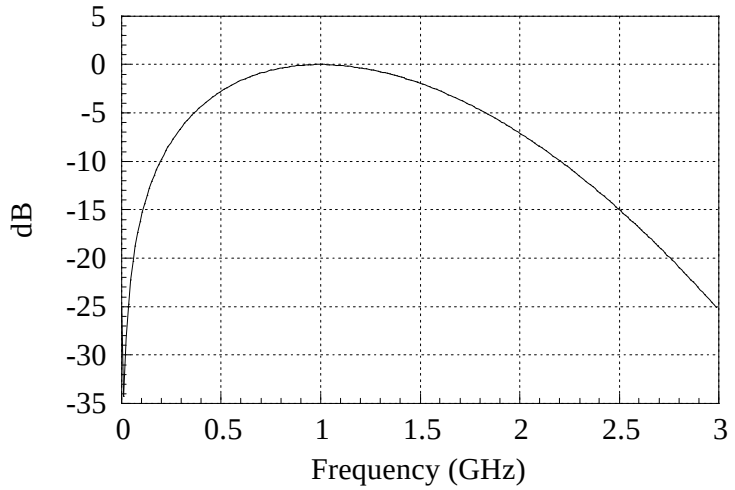

Figure 1-9: Magnitude spectrum at the output of the receive antenna

7 to derive the UWB channel models that form the main result of this work. Chapter 8 concludes.

During the course of this work, a number of techniques are introduced and developed for processing the received UWB signals. A diagram of the various techniques and algorithms introduced or utilized in this work is shown in Figure 1-10. As mentioned, Chapter 2 and Chapter 3 deal with UWB beamforming, in the context of a delay-and-sum beamformer. In Chapter 4, iterative techniques for processing the signals at the output of the delay-and-sum beamformer are introduced, first as the CLEAN algorithm. Modifications which permit the iteration to update the original sensor data, rather then the beamformer output, are made to the CLEAN algorithm, which is then re-named the Sensor-CLEAN algorithm. The output of the Sensor-CLEAN algorithm may contain artifacts due to noise or multiple detections of the same signal. A technique called the Wave-Map algorithm is therefore also developed in Chapter 4 to post-process the output of the Sensor-CLEAN algorithm with a goal of combining multiple detections which likely belong to the same incident signal. In Chapter

5, a technique called the Arrival Combiner is introduced, which combines the outputs of multiple Wave-Maps, run at different resolutions, to further reduce the probability of false signal detections. The output of the Arrival Combiner consists of a list of the time and angle-of-arrival of the detected signals, as well as the recovered waveforms. This is the information that is used to characterize the UWB channel.

Delay-and-sum beamforming is a well known operation, as is the CLEAN algorithm. The Sensor-CLEAN algorithm, the Wave-Map algorithm and the Arrival Combiner, however, are all introduced and developed in this work, to deal with problems inherent in the processing of UWB signals.

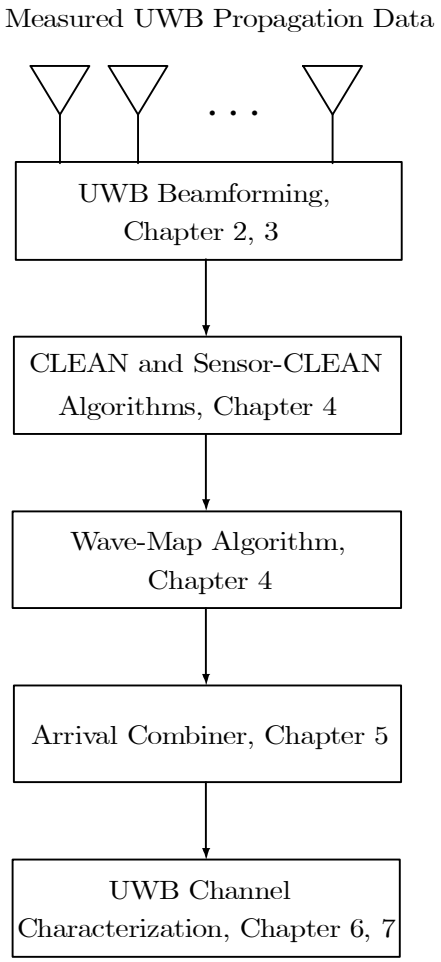

Figure 1-10: Hierarchy of the algorithms developed in this work for processing the UWB signals.

Chapter 2

Ultra-Wideband Array Signal Processing

2.1 Narrowband vs. Ultra-Wideband Array Signal Processing

Fundamental differences exist between the classical array signal processing techniques, predicated on the incidence of narrow-band signals, and the problem of interest here, where the signals have significant fractional bandwidth. In the narrowband case, the signal is generally assumed to be present at all sensors during the observation interval, and to maintain a constant envelope during this time. These assumptions lead to the concept of the array factor as a time-invariant measure of the beamformer response to an incident signal from a particular direction. The beamformer then imparts only a scaling in amplitude as a function of the look direction, but does not affect the time variation of the incident signals. A body of literature has been developed to handle problems such as source location and sidelobe reduction for the narrowband case [16], [20], [23], [32].

Given the impulsive nature of the UWB signals considered in this work, the assumption of a constant envelope does not hold. In fact, the signal is not even guaranteed to be present at all sensors at the same instant in time. Further, UWB signals are not well approximated by a tone, and therefore a time-shift is not well approximated by a phase-shift. These

differences eliminate many of the established narrowband techniques for processing signals at the output of an array of sensors from direct application to this problem.

For the case of wideband signals, a general approach to determining directional information involves either breaking the problem down into a collection of narrowband problems via filtering, channelization or the use of a delay-and-sum beamformer [4], [16]. In the channelized solutions, an aperture taper might then be applied to each channel in order to achieve sidelobe suppression. A solution such as this is generally accomplished at the expense of time-resolution and is therefore not well-suited to the problem at hand.

Other direct techniques for angle-of-arrival (AOA) determination from array data, such as constrained optimizations, require relatively strong assumptions on the form of the incident signals. The performance of these techniques tends to degrade rapidly in the presence of variations from the assumed signaling functions. Again, the time varying nature of the received UWB signals, seen earlier in Figure 1-3, Figure 1-4, and Figure 1-5, precludes the use of these sorts of techniques, since it is difficult to predict the precise shape of the received signals, and therefore the contribution of individual signals to the constraint equations.

As mentioned above, the incident UWB signals are not well modeled as identical to within a phase-shift at all sensors, and the assumption that the signal maintains a constant envelope during interaction with the sensors in the array does not hold in the UWB case. As a consequence, the Fourier analogy between the aperture and the antenna pattern, as exists in the narrowband case, does not hold for UWB beamforming. This then eliminates the concept of aperture tapers for sidelobe reduction. Instead, considering Figure 2-1, in the case of a delay-and-sum beamformer, the maximum achievable peak-to-sidelobe level ratio over all angles-of-arrivals for a linear array of M elements with sensors weights $\{a_m\}_{m=0}^{M-1}$ upon incidence of UWB signals is

$$
\begin{aligned}
PSL &= \frac{\sum_{m=0}^{M-1} a_m}{\max\{a_m\}_{m=0}^{M-1}} \\
&\square \quad M,
\end{aligned}
\tag{2.1}
$$

where this expression assumes that the incident pulses do not interfere in the sidelobe region. This relation can be seen as follows. First assume a constraint exists on the sensor weights such that $\sum_{m=0}^{M-1} a_m = 1$. Then suppose that a set of sensor weights exists which provides a peak-to-sidelobe ratio of better than M. Then either $\max\{a_m\}_{m=0}^{M-1} < 1/M$, in which case the constraint cannot be met, or $\sum_{m=0}^{M-1} a_m > 1$, which again violates the constraint. Thus uniform weighting of the aperture provides the best achievable peak-to-maximum sidelobe level for UWB beamforming. This expression also holds in the case of higher dimensional arrays and plane wave incidence, with the generalization that M corresponds to the ratio of the total number of elements in the array to the number which lie on any line segment drawn through the array. Note that if signal level fluctuations exist from sensor to sensor, the inequality (2.1) will be strict.

Implicit in the limit on the achievable peak-to-sidelobe level in equation (2.1) is a limit on the dynamic range available at the output of the UWB beamformer. It is possible then, that UWB beamforming alone is not capable of resolving the incident signals with sufficient dynamic range to adequately characterize the UWB communication channel. In other words, under the assumption that signals arriving with an amplitude of less than that of the largest sidelobe cannot be reliably identified, a technique for increasing the dynamic range of the UWB beamformer output is needed. Note that for the work presented here, the angular resolution of the array is accepted and no discussion is undertaken on increasing it beyond the physical limit established by the array.

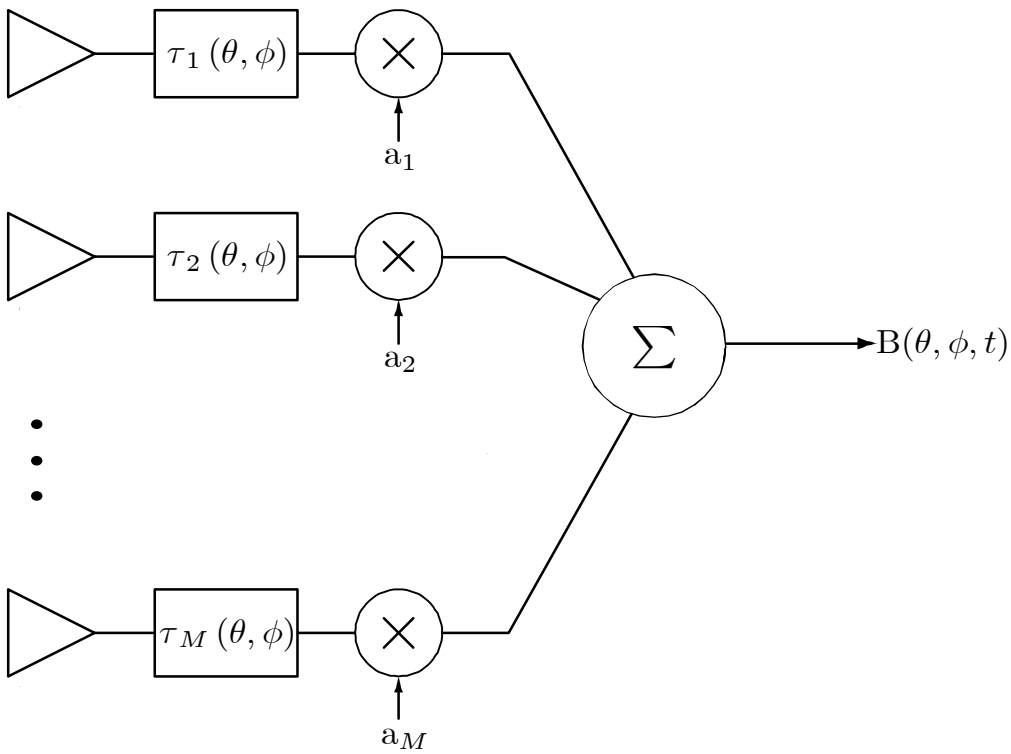

Figure 2-1: A delay-and-sum beamformer, with the steering delay for sensor n specified by $\tau_n(\theta, \phi)$ and the weight by a_n.

A goal of this research is therefore to develop an appropriate processing technique for resolving the incident UWB signals over a large enough dynamic range to adequately characterize the UWB propagation channel. Given the fractional bandwidth of the baseband UWB signals considered here, it is of interest to investigate time-domain solutions to the problem, as well as methods that do not exhibit a strong dependence on the shape of the received signal. This chapter develops the properties of the UWB beamformers which comprise the first stage in the processing of the incident signals.

2.2 UWB Delay-and-Sum Beamforming

Given the fractional bandwidth of the UWB signals and the corresponding lack of a time-invariant Fourier analogy between the aperture and the array pattern, a uniformly-shaded, delay-and-sum beamformer is applied to the data. In order to implement this beamformer, the delay equations which describe the propagation of the signal across the array are needed. Consider the delay-and-sum beamformer in Figure 2-1, with a regularly-spaced, linear array of sensors and $a_n = a_m$, for all m, n. Then, as in Figure 2-2, with a plane wave incident at an azimuth angle of θ degrees with respect to broadside, the relative propagation distance between any two sensors is $\mathrm{d}\sin\theta$. In order to resolve both the azimuth angle-of-incidence and the elevation angle, in one hemisphere, another dimension must be added to the array. This leads to the planar structure shown in Figure 2-3. In this case, the incremental delay in the x-direction is given by $(d_x/c)\cos\theta\sin\phi$ and in the y-direction by $(d_y/c)\sin\theta\sin\phi$ where d_x is the sensor spacing in the x-direction, d_y is the sensor spacing in the y-direction and ϕ is the elevation angle-of-arrival.

In theory, the delay-and-sum beamformer of Figure 2-1 can be analyzed in either the time or frequency domain. In the frequency domain, its response can be described at a single frequency by the narrowband array factor, and temporally the array can be described by

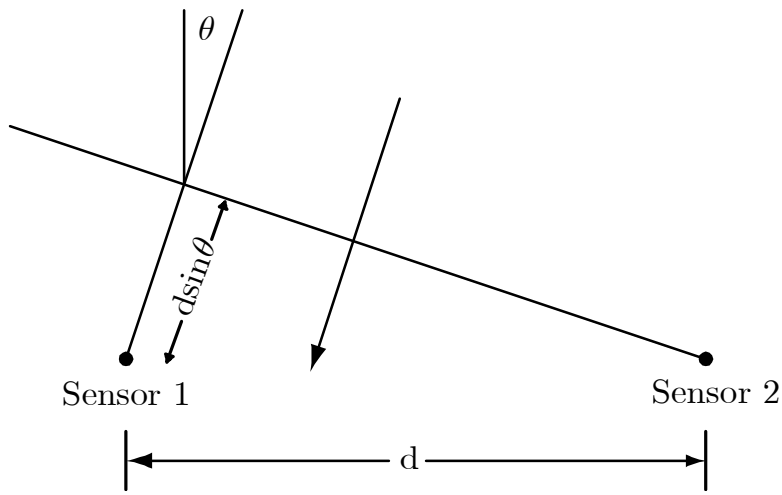

Figure 2-2: Differential propagation distance between sensors for plane wave incidence.

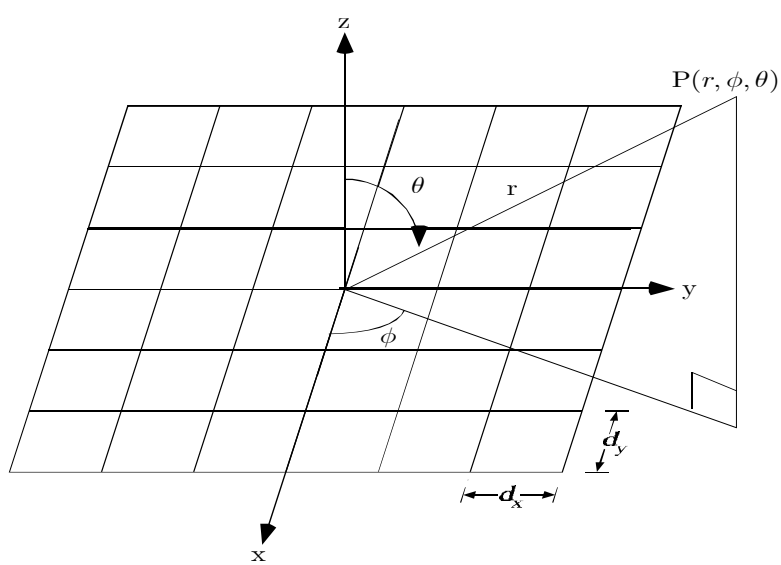

Figure 2-3: Planar array geometry and definitions

the impulse response. For the general case of a planar array, the array factor at a single frequency is given as [3]

$$AF(k,\phi,\theta) = \frac{\sin\left(\frac{M}{2}\psi_{\mathrm{x}}\right)}{\sin\left(\frac{1}{2}\psi_{\mathrm{x}}\right)} \times \frac{\sin\left(\frac{N}{2}\psi_{\mathrm{y}}\right)}{\sin\left(\frac{1}{2}\psi_{\mathrm{y}}\right)}, \tag{2.2}$$

where

$$\psi_x = kd_{\mathrm{x}}\left(\cos\theta_{\mathrm{o}}\sin\phi_{\mathrm{o}} - \cos\theta\sin\phi\right) \tag{2.3}$$

and

$$\psi_y = kd_{\mathrm{y}}\left(\sin\theta_{\mathrm{o}}\sin\phi_{\mathrm{o}} - \sin\theta\sin\phi\right) \tag{2.4}$$

for $k = \frac{2\pi}{\lambda}$ radians/meter. Here θ_{o} represents the azimuth angle of incidence, while θ represents the beamformer azimuth look direction. The elevation angle of incidence is given by ϕ_{o} and the beamformer elevation look direction is denoted by ϕ. In addition, N is the number of sensors per row of the array, M is the number of sensors per column of the array, d_x is the sensor spacing in the x-direction and d_y is the sensor spacing in the y-direction.

As mentioned, given the fractional bandwidth of the signals involved here, it is preferable to work in the time-domain. For a time-domain description of the array, consider the impulse response. Assuming isotropic sensors, the impulse response for a planar array, with uniform spacing in the x and the y-directions, is derived from the delay-and-sum operations as

$$h(t) = \sum_{n=0}^{N-1}\sum_{m=0}^{M-1}\delta\left(t - n\alpha - m\beta\right), \tag{2.5}$$

where

$$\alpha = \frac{d_{\mathrm{x}}}{c}\left(\cos\theta_{\mathrm{o}}\sin\phi_{\mathrm{o}} - \cos\theta\sin\phi\right), \tag{2.6}$$

$$\beta = \frac{d_y}{c}\left(\sin\theta_o \sin\phi_o - \sin\theta \sin\phi\right) \tag{2.7}$$

and the angles have the same interpretation as above.

In the event that the incident radiation is due to a near field source, the wavefront will display curvature, which implies that the previous results for time-of-arrival of a far-field source are not applicable. The radial distance to the source is measured from the center of the array, and the distance to the sensor of interest is measured relative to the array center. In this case, the differential distance between propagation to the center of the array and propagation to the sensor located at (nd_x, md_y) meters away is given by

$$\Delta r_{mn} = r - \sqrt{r^2 - 2r\sin\theta\left(nd_x\cos\varphi + md_y\sin\varphi\right) + \left(md_x\right)^2 + \left(nd_y\right)^2} \tag{2.8}$$

The associated propagation delay to sensor (n, m) is then given by $\Delta r_{mn}/c$. It will be assumed in this work that all signals are incident with planar wavefronts. No attempt will be made to optimize the processing for non-planar wavefronts.

For the forty-nine element planar array utilized in the measured UWB data described in Chapter 1, the array factor at a single spatial frequency takes the form

$$\begin{aligned} A\left(k_o, \theta, \theta_o\right) &= \frac{\sin\left(\frac{7}{2}k_o d_x\left(\sin\theta\sin\phi - \sin\theta_o\sin\phi_o\right)\right)}{\sin\left(\frac{1}{2}k_o d_x\left(\sin\theta\sin\phi - \sin\theta_o\sin\phi_o\right)\right)} \\ &\quad \times \frac{\sin\left(\frac{7}{2}k_o d_y\left(\cos\theta\sin\phi - \cos\theta_o\sin\phi_o\right)\right)}{\sin\left(\frac{1}{2}k_o d_y\left(\cos\theta\sin\phi - \cos\theta_o\sin\phi_o\right)\right)} \end{aligned} \tag{2.9}$$

$$= A_x\left(k_o, \theta, \theta_o, \phi, \phi_o\right) A_y\left(k_o, \theta, \theta_o, \phi, \phi_o\right) \tag{2.10}$$

where $k_o = \frac{2\pi}{\lambda_o}$, as before, θ is the beamformer azimuth look direction, θ_o is the azimuth angle-of-incidence, ϕ is the beamformer elevation look direction and ϕ_o is the elevation

angle-of-incidence. This illustrates the principle of pattern multiplication, which holds for the array factor at a single frequency.

This array can also be interpreted in the time domain by the convolutional model, using the appropriate set of delta functions to represent the relative delays at which the signals from the various sensors are summed to form the beampattern, according to,

$$h\left(t,\varphi,\varphi_o\right)=\sum_{n=0}^{3}\sum_{m=0}^{3}\delta\left(t\pm 2nx\pm 2my\right), \tag{2.11}$$

where

$$x=\frac{1}{2}\frac{d_y}{c}\left(\cos\theta\sin\phi-\cos\theta_{\mathrm{o}}\sin\phi_{\mathrm{o}}\right) \tag{2.12}$$

and

$$y=\frac{1}{2}\frac{d_x}{c}\left(\sin\theta\sin\phi-\sin\theta_{\mathrm{o}}\sin\phi_{\mathrm{o}}\right). \tag{2.13}$$

This time domain approach is a more useful characterization for UWB beamforming. Note that both the frequency domain and the domain representations make the assumption that all sensors contribute, in other words no sensor is shadowed from the signal.

Since the Fourier transform relation between the aperture and the pattern does not hold for the incidence of UWB signals upon the array, consider a general equation for the uniformly-shaded, delay-and-sum beamformer output as the form most applicable to UWB waveform processing,

$$B\left(\theta,\phi,t\right)=\sum_{n}s\left(t+t_n\left(\theta_{\mathrm{o}},\phi_{\mathrm{o}}\right)-\tau_n\left(\theta,\phi\right)\right), \tag{2.14}$$

where the delay at sensor n, $\tau_n(\theta,\phi)$, is explicitly a function of the beamformer azimuth and elevation look direction.

Evaluating this equation for the case of a uniformly-shaded linear array of M elements and a signal incident at time $t = 0$ gives

$$B(\theta, t) = \frac{1}{2\pi} \int_{-\infty}^{\infty} S(\omega) \frac{\sin\left(M \frac{\omega}{2} \frac{d}{c} \gamma\right)}{\sin\left(\frac{\omega}{2} \frac{d}{c} \gamma\right)} e^{j\omega t} d\omega, \tag{2.15}$$

where

$$\gamma = \sin\theta_{\mathrm{o}} - \sin\theta, \tag{2.16}$$

and for an $M \times M$ planar array, the equation becomes

$$B(\theta, \phi, t) = \frac{1}{2\pi} \int_{-\infty}^{\infty} S(\omega) \frac{\sin\left(M \frac{\omega}{2} \frac{d}{c} \gamma_x\right)}{\sin\left(\frac{\omega}{2} \frac{d}{c} \gamma_x\right)} \frac{\sin\left(M \frac{\omega}{2} \frac{d}{c} \gamma_y\right)}{\sin\left(\frac{\omega}{2} \frac{d}{c} \gamma_y\right)} e^{j\omega t} d\omega, \tag{2.17}$$

where

$$\gamma_{\mathrm{x}} = \sin\theta_{\mathrm{o}} \sin\phi_{\mathrm{o}} - \sin\theta \sin\phi \tag{2.18}$$

and

$$\gamma_{\mathrm{y}} = \cos\theta_{\mathrm{o}} \sin\phi_{\mathrm{o}} - \cos\theta \sin\phi \tag{2.19}$$

Again, the principle of pattern multiplication for UWB arrays is seen to hold in the integrand, at a single frequency. This implies that the array response at any angle is the superposition of the array response to each frequency component, at the current look direction.

Equation (2.15) also defines the existence of the beamformer pattern sidelobes as a function of frequency. In order to reduce the sidelobes in the beamformer pattern, the kernel

$$\frac{\sin\left(N \frac{\omega}{2} \frac{d}{c} \gamma\right)}{\sin\left(\frac{\omega}{2} \frac{d}{c} \gamma\right)} \tag{2.20}$$

where

$$\gamma = \sin\theta_{\mathrm{o}} - \sin\theta \tag{2.21}$$

must be constrained to be as close to a constant value over the frequencies in the support of $S(\omega)$ as possible, so that the spectrum of $S(\omega)$ is not altered by the beamformer. This implies that for a fixed intersensor distance d, a larger value of N will allow for a larger peak-to-sidelobe level. This is in accordance with the time-domain analysis, from which the peak-to-sidelobe level is limited to the number of elements in any linear configuration.

Having established some of the fundamental differences between UWB and narrowband arrays, it is now appropriate to study the properties of UWB arrays in greater detail. This is the subject of the next chapter.

Chapter 3

Properties of Ultra-Wideband Arrays

3.1 Characterization of the Time-Domain Beamformer Response

Following as in equation (2.14), let the output of a uniformly-shaded delay-and-sum beamformer for a linear array of sensors, steered to an azimuth look direction of θ radians, on incidence of a plane wave with time variation $s(t)$ from an azimuth angle of θ_{o} radians, be represented by [56]

$$B(\theta, t) = \sum_n b_n(\theta_{\mathrm{o}})\, s\left(t - n\frac{d}{c}(\sin\theta_{\mathrm{o}} - \sin\theta)\right). \tag{3.1}$$

where $b_n(\cdot)$ is the antenna pattern associated with an individual element. As before, d represents the inter-element spacing and c is the speed of light. This equation assumes that the same signal is received by all elements of the array. If each sensor in the array has the same antenna pattern, it can be removed from the summation. The expression

$$\sum_n s(t - n\frac{d}{c}(\sin\theta_{\mathrm{o}} - \sin\theta)) \tag{3.2}$$

is then the equivalent array factor for the time-domain case and the signal $s(t)$. Just as the expression for the array factor in the narrowband case was dependent on the assumed

sinusoidal signal characteristics, the time-domain expression here also explicitly depends on the received waveform. Neglecting a constant, the array factor of equation (3.2) represents the pattern associated with a uniformly-shaded linear array of isotropic sensors on incidence of a plane wave with time variation $s(t)$ from an azimuth angle of θ_o degrees.

Consider an example from [46] to illustrate this time-domain beamforming process. A uniformly-shaded linear array of three sensors is shown in Figure 3-1, with a sensor spacing of $2\lambda_o$. Here, λ_o is defined as the wavelength of a received monocycle, also shown in Figure 3-1. Assume this monocycle is incident upon the array at broadside, so that the signal is received by each sensor at the same instant in time. As shown in 3-2 (a), at broadside the beamformer output is a replica of the incident signal, scaled in amplitude by the number of sensors; the sensor outputs add "coherently". If the beamformer is instead steered so that the delays cause the monocycles to add at $\frac{1}{2}\lambda_o$ out of "phase", corresponding to a look direction of 14.48^o, the waveform in Figure 3-2 (b) is output from the beamformer. At a look direction of 30°, the output waveform consists of three consecutive monocycles, shown in Figure 3-2 (c). As the look direction progresses to angles greater than 30°, the monocycle continues to appear in the output, but the spacing between successive signals increases. Thus, at angles less than 30°, the energy in the output waveform varies, but above 30° the energy in the output waveform is constant, but the temporal distribution of the energy varies. In this case, 30° defines the critical angle for the beamformer, θ_c. In general, θ_c is defined for a linear array of sensors as the angle at which $cT = d \sin\theta$, where T is the time duration of the impulse.

This variation in the output pattern as a function of time is in contrast to the narrowband case, where the array pattern is constant as a function of time, and for an N element linear array is given by,

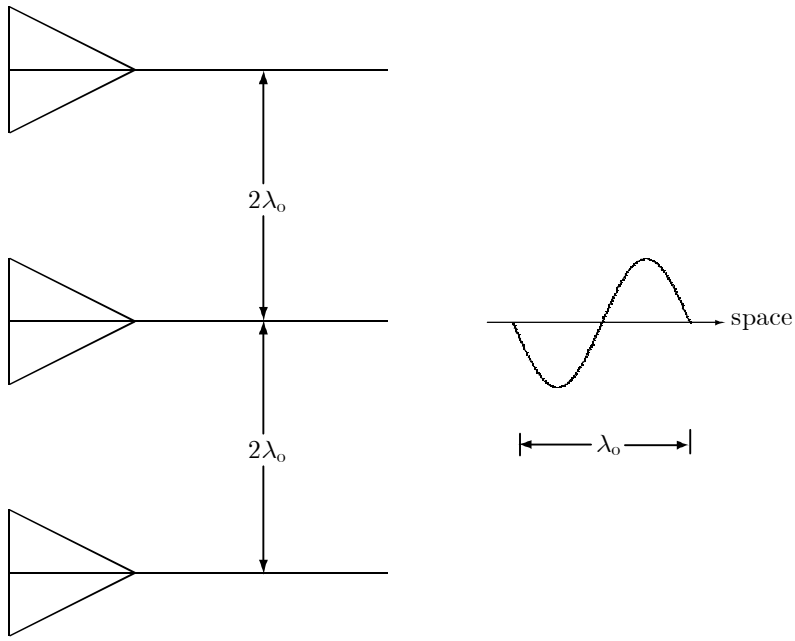

Figure 3-1: Three element UWB receive array and the received monocycle.

$$B(\theta) = \frac{\sin\left(\frac{N\pi d}{\lambda}\sin\theta\right)}{\sin\left(\frac{\pi d}{\lambda}\sin\theta\right)}. \tag{3.3}$$

Given that the UWB beamformer output is a function of the incident waveform and that the transmitted UWB signals can undergo significant shaping in the radiation and propagation processes, it is not possible to predict the beamformer output patterns that will result when operating on measured data. For the sake of example, the second derivative Gaussian pulse, denoted by $p_2(t)$, will be used here to demonstrate some typical patterns.

Consider first the output of a three element linear array with inter-sensor spacing of $d = 1.0$ meter, on broadside incidence of a plane wave with time variation $p_2(t)$. Figure 3-3 (a) shows the beamformer response to the incident waveform when steered to the angle-of-incidence at broadside. The signal is not distorted by the array and is scaled in amplitude by the number of sensors. Figure 3-3 (b) shows the beamformer output at a look direction

(a) UWB beamformer output at a look direction of 0°

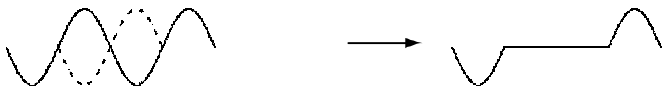

(b) UWB beamformer output at a look direction of 14.48°

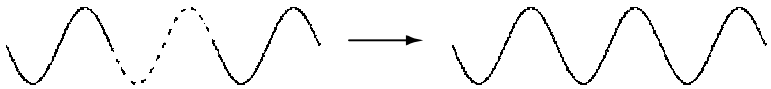

(c) UWB beamformer output at a look direction of 30°

(d) UWB beamformer output at a look direction of 45°

Figure 3-2: Time domain UWB beamformer example for the three element UWB array

of 17°. The waveform has been distorted, and now has peak amplitude equal to that of a single incident impulse. Figure 3-3 (c) shows the beamformer output at 34°, approximately the critical look angle, θ_c, for this array and waveform. The waveforms from each sensor are now distinct and emerge from the beamformer sequentially in time. As the look direction increases beyond θ_c, the distance in time between successive pulses is seen to increase, to a maximum value at a look direction of 90° shown in Figure 3-3 (d). The maximum amplitude of the off-peak waveform establishes the sidelobe level for the beamformer, and therefore

determines the maximum available dynamic range of the beamformer. In this case the maximum sidelobe level is given by the output of a single sensor.

More generally, the maximum sidelobe level of an UWB array will be determined by the number of impulse signals which can add coherently at an off-peak look direction. It is therefore instructive to give another plot of the beamformer output, where the time dependence has been removed and the maximum amplitude at each look direction for across all time instants is recorded. This is called the maximum projection [41], and is given for this three element array in Figure 3-4. This plot confirms the sidelobe level discussed above. Figure 3-4 also gives some insight into the angular resolution performance of the array, generally taken as proportional to the width of the main lobe.

To emphasize the time dependence of the array pattern, Figure 3-5 gives a plot of the beamformer output versus time and azimuth angle for this array geometry and waveform. Note the location in time and angle of the main response and of the sidelobes.

In order to demonstrate the increasing complexity of the array patterns as the number of elements is increased, Figure 3-6 shows the properties of a seven element linear array, with the same inter-sensor spacing of 1 meter, and 3-7 gives the maximum projection. Of particular note in these plots is the increase in the time extent of the beampattern, and the increase in the peak-to-sidelobe amplitude ratio (PSL) of the beamformer output. The increase in time extent is due to the increase in the propagation distance across the array, and the increase in the PSL is due to the coherent addition of seven sensors to form the on-peak waveform in conjunction with the lack of a mechanism for waveforms to combine coherently at an off-peak look angle.

Proper selection of inter-element spacing is necessary to design UWB arrays for particular scenarios. In fact, just as narrowband arrays might be designed to operate at a particular frequency, perhaps $d = \lambda_o/2$, a UWB array might be designed for a particular

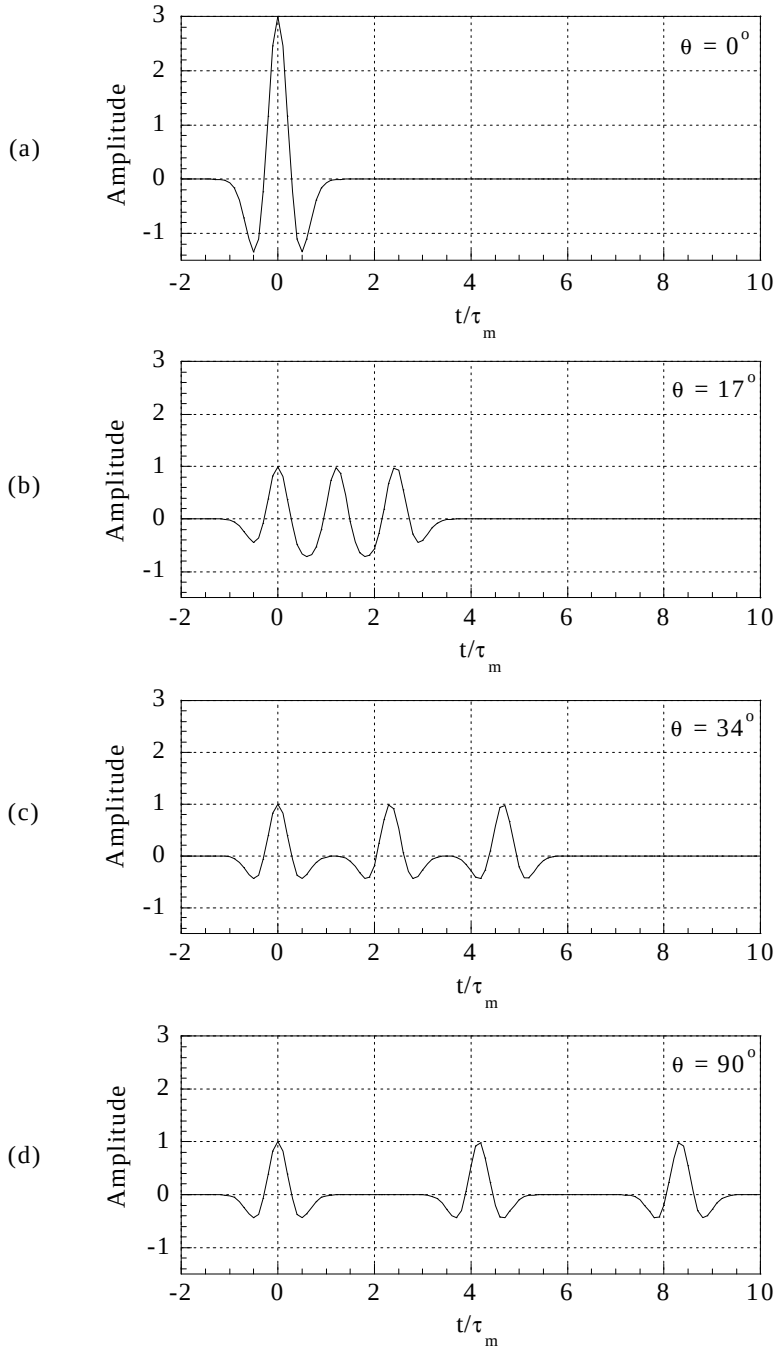

Figure 3-3: Three element beamformer output at the indicated look directions with $d = 1$ meter and $p_2(t)$ incident.

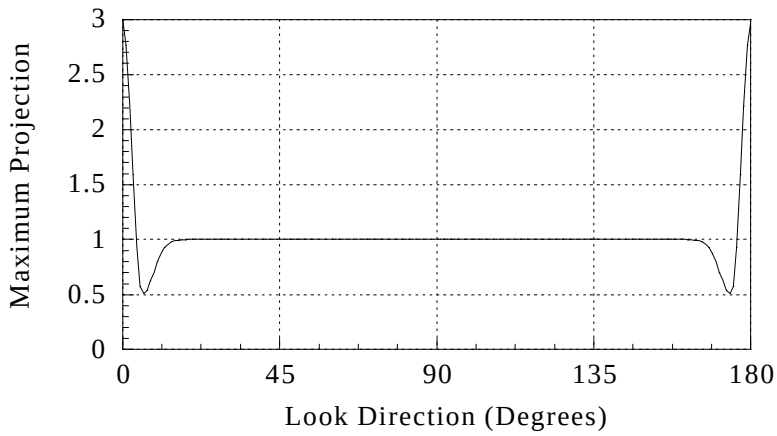

Figure 3-4: Maximum projection of the three element UWB array with $p_2(t)$ incident.

pulse width. Consider the narrowband case, where the sensor spacing must be selected so that $d < \lambda/2$, else grating lobes form. The trade-off is in overall aperture length L, determined by the number of elements in the linear array multiplied by the inter-element spacing, which determines the angular resolution limit of the array. The same trade exists in UWB arrays, as can be seen in the maximum projection plots for the different values of d, and will be developed formally below. As a prelude to this discussion, Figure 3-8 gives the maximum projection for a seven-element array with inter-element spacing of $d = 0.50$ meters, and Figure 3-9 does the same for $d = 0.152$ meters, the actual spacing used in the planar measurement array. In terms of angular resolution, the difference in the width of the main lobe of the maximum projection in the two plots is noted. Further, for a hypothesized pulse width parameter of $\tau_m = 0.8$ ns, at $d = 0.50$ meters, the critical angle is almost achieved by the array, due to the fact that the pulse length in space is just longer than d. For $d = 0.152$ meters, the critical angle is not achieved.

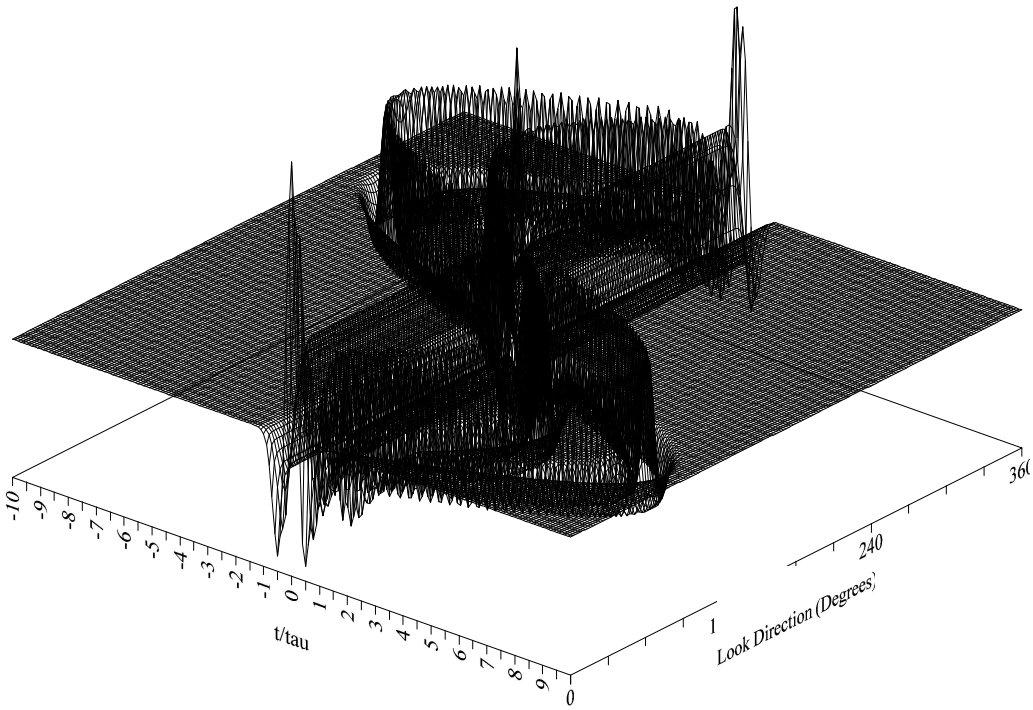

Figure 3-5: Time and angle dependence of the three element array pattern with inter-sensor spacing of 1 meter, upon incidence of $p_2(t)$.

Increasing the complexity of the array, the patterns associated with the seven by seven element planar array on with which the data was actually measured, shown in Figure 3-10, are given in Figure 3-11 for incidence of a signal with time variation $p_2(t)$ from an azimuth angle of $0^o$and an elevation angle in the plane of the array. The peak output is now generated by the addition of forty-nine sensors, and the maximum sidelobe is due to the off-peak addition of seven sensors. In order to demonstrate the spatial and temporal extent of these patterns, the response over time and azimuth angle is shown first in Figure 3-12 for an azimuth angle-of-incidence of 45° and an elevation look direction equal to the

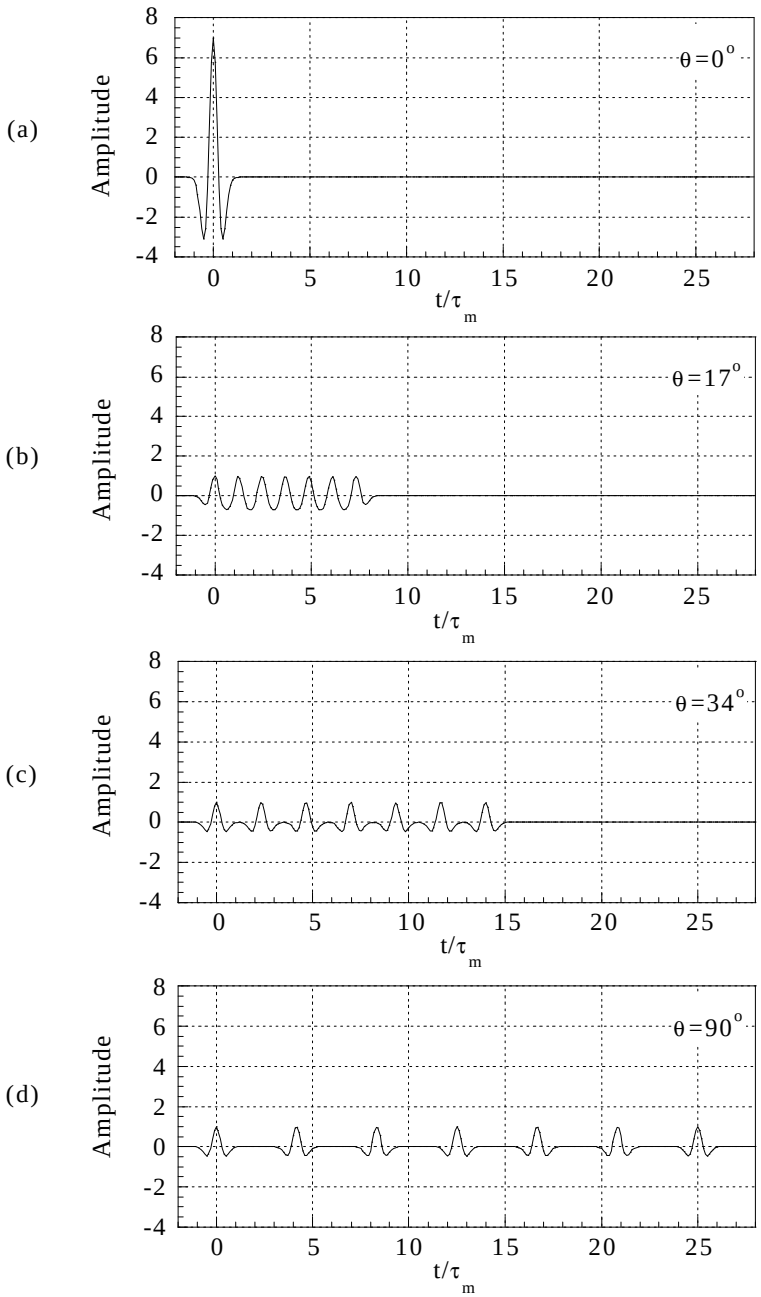

Figure 3-6: Seven element beamformer output at the indicated look directions with $d = 1$ meter and $p_2(t)$ incident.

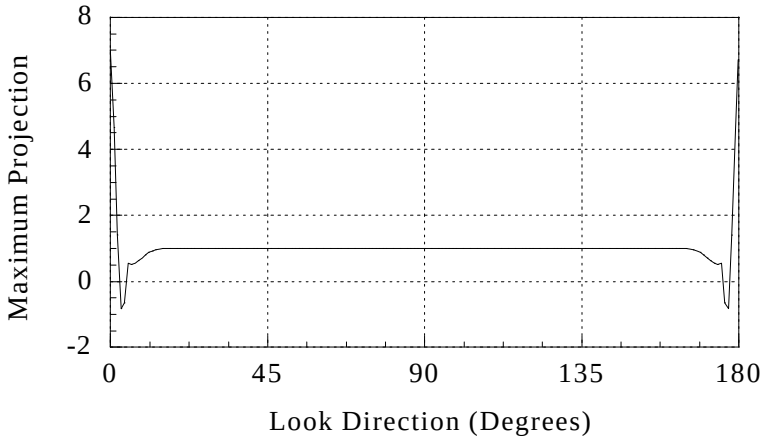

Figure 3-7: Maximum projection for the seven-element linear array with $d = 1$ m

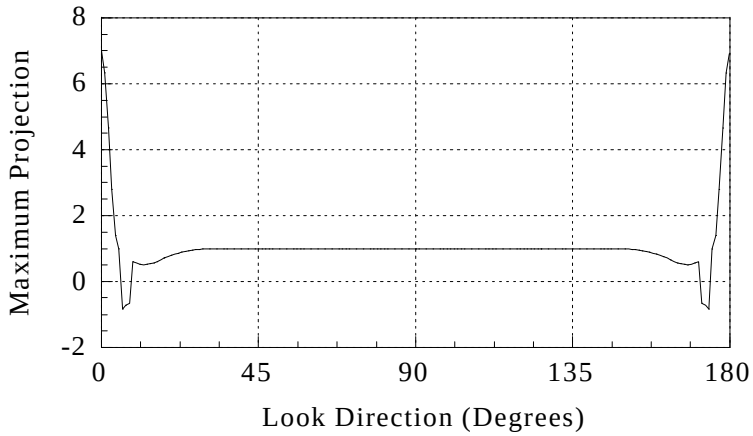

Figure 3-8: Maximum projection for a seven element array with $d = 0.50$ meters and $p_2(t)$ incident from 0°.

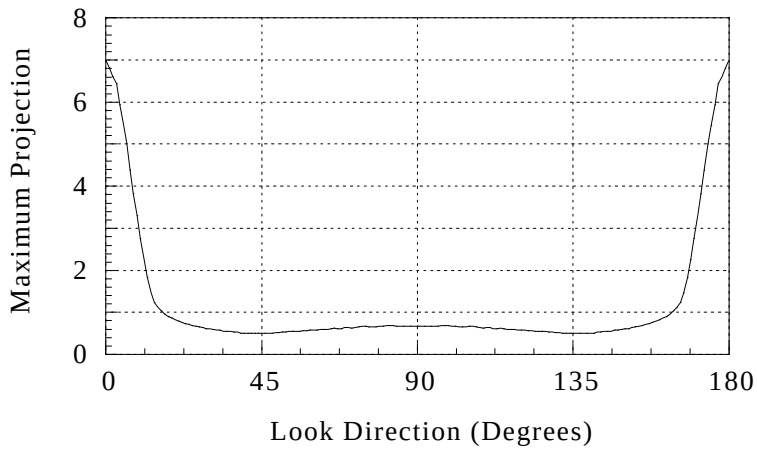

Figure 3-9: Maximum projection for a seven element array with $d = 0.152$ m and $p_2(t)$ incident from 0°.

elevation angle-of-incidence of 90°. In Figure 3-13 the azimuth angle of incidence is 220° and the elevation angle is still 90°. The location in time and angle of the peak response and of the sidelobes can be seen in the plots.

Removing the time dependence from these plots, two examples of the maximum projection for this array are shown in Figure 3-16 and Figure 3-17. Note that even as the number of sidelobes increases, the PSL remains roughly the same as in the seven element linear array, since now up to seven elements can combine at an off-peak look direction.

Next, consider Figure 3-14 and Figure 3-15, where an impulse is incident at an azimuth angle of 180°. The theoretical response of the beamformer versus azimuth and elevation look directions, at the peak response time, is shown for two different elevation angles-of-incidence. In the first case, the impulse arrives in the plane of the array, and a response with a single peak is noted. In the second case, with the impulse incident from an elevation angle of 45°, an ambiguity in the response is seen. This is due to the use of a two-dimensional array, which can only resolve elevation angles to within 90°. In other words, the two-dimensional array cannot distinguish whether a signal is incident from above or below the array.

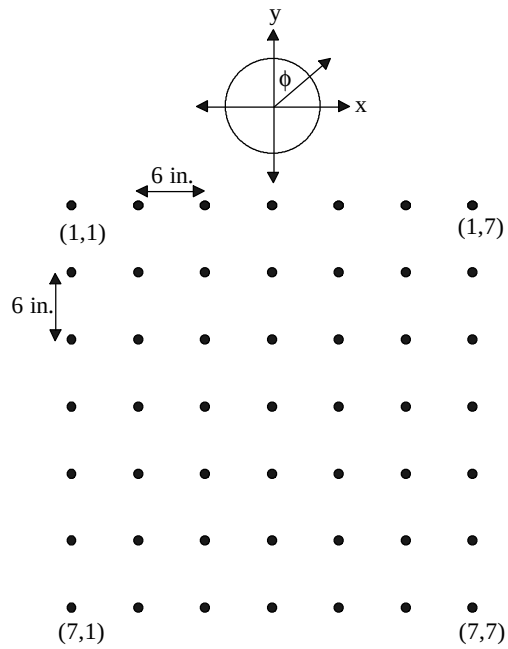

Figure 3-10: Geometry of the array on which measured data was taken.

Given the sidelobes inherent in the output of a UWB beamformer, and the lack of a systematic means for controlling them, a technique is needed to increase the dynamic range available at the output of the beamformer, if it is to be used to provide signal information for the characterization of the UWB propagation channel.

3.2 Angular Resolution of UWB Arrays.

The angular resolution performance of an UWB array is defined by the minimum required separation in both azimuth and elevation angles-of-arrival between two signals which are coincident in time, such that the UWB array is able to resolve the signals as distinct. In the narrowband case, with the incident signals taken as sinusoids, the angular resolution of a uniformly shaded linear array is typically defined by the Rayleigh resolution limit, given for a large array ($L >> \lambda_o$) as $\lambda_o/Nd = \lambda_o/L$, where λ_o is the wavelength of the incident

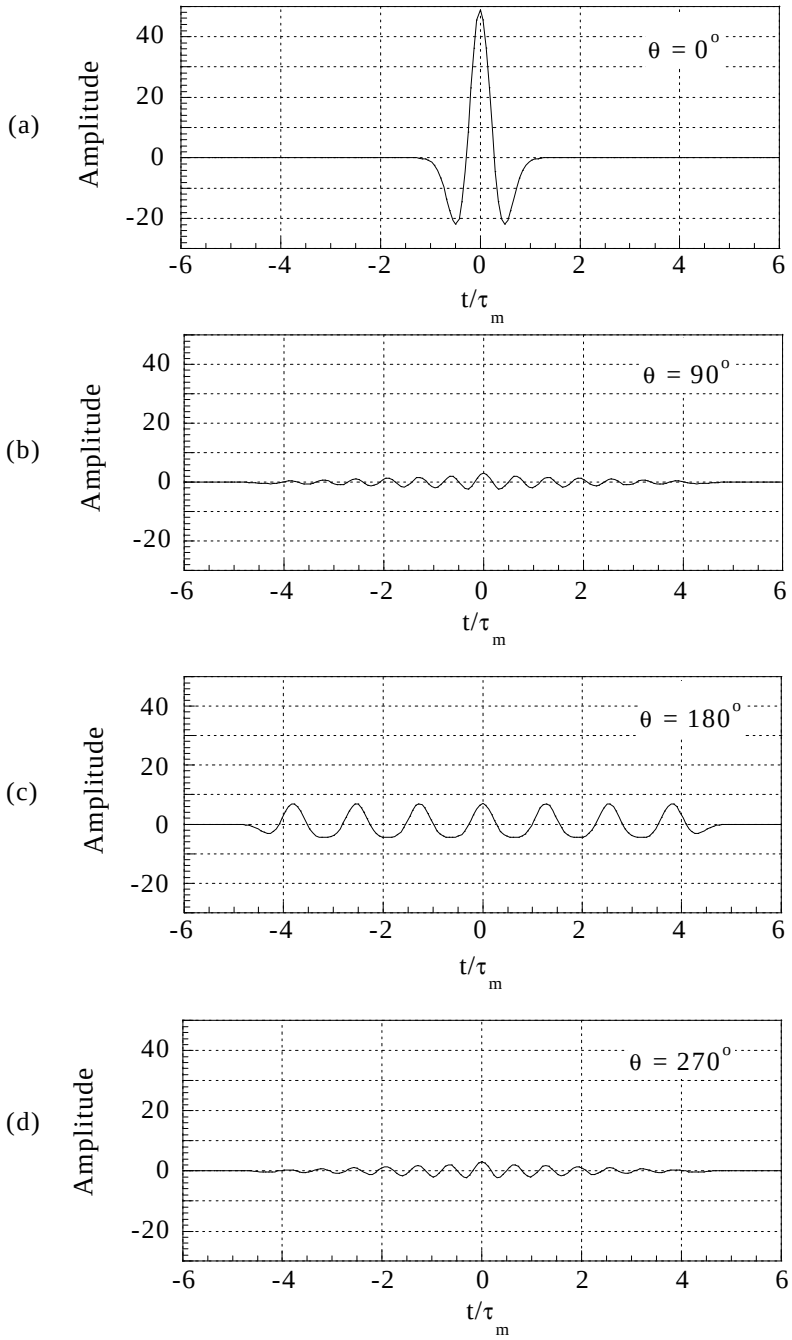

Figure 3-11: Forty-nine element planar array beamformer output on incidence of $p_2(t)$ from 0°, at the indicated look directions.

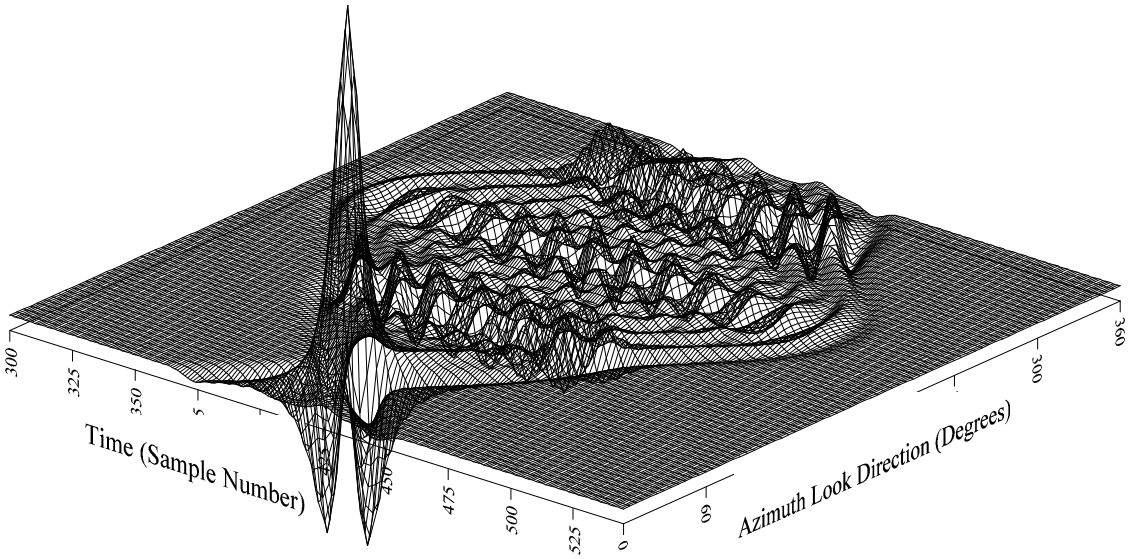

Figure 3-12: 7×7 element planar beamformer response to $p_2(t)$ arriving from an azimuth angle of 45° and an elevation angle of 90°.

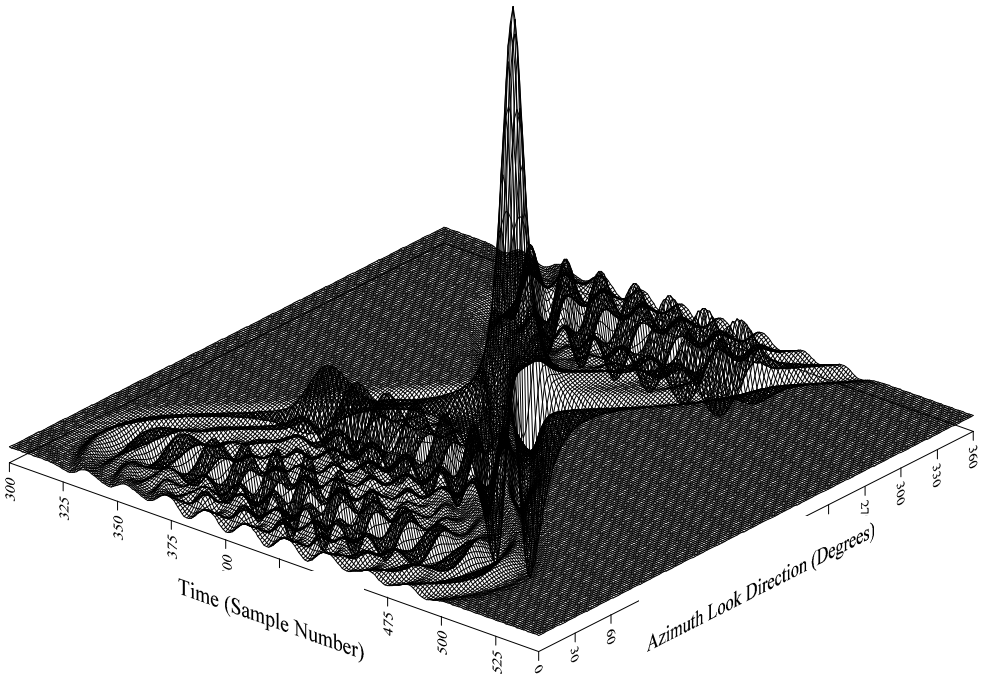

Figure 3-13: Planar beamformer response to $p_2(t)$, incident from an azimuth angle of 220° and an elevation angle of 90°.

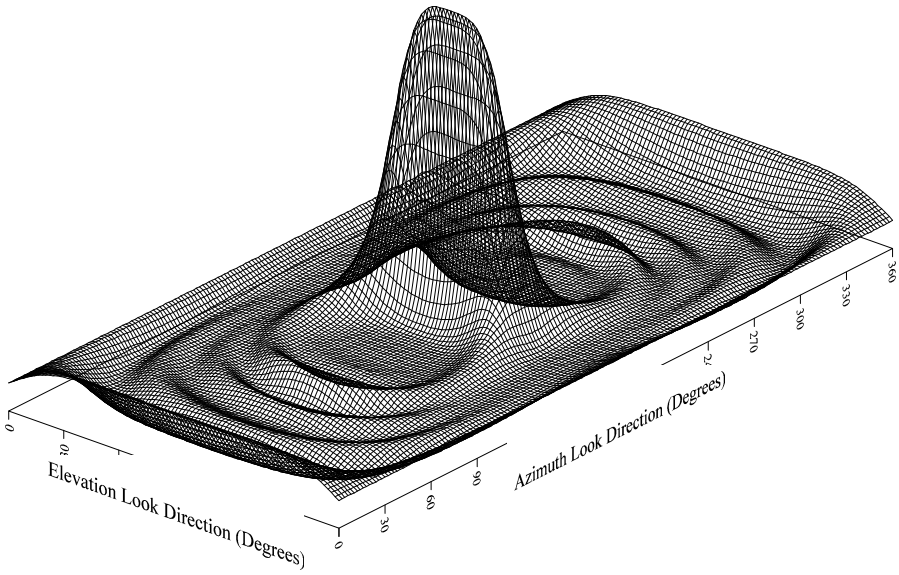

Figure 3-14: Planar beamformer output vs. azimuth and elevation angles at the peak response time, on incidence of $p_2(t)$ from an azimuth angle of 180° and an elevation angle of 90°.

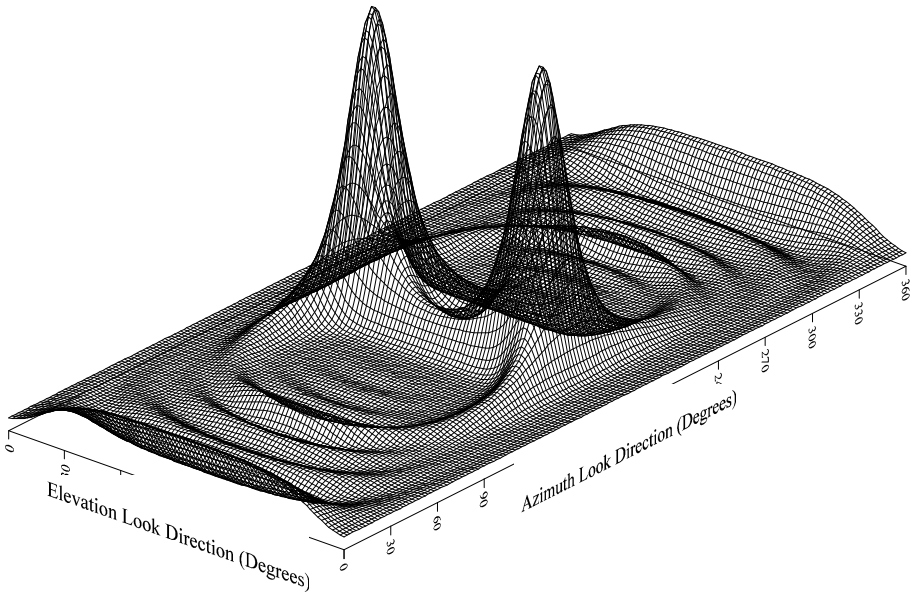

Figure 3-15: Planar beamformer output vs. azimuth and elevation angles at the peak response time, on incidence of $p_2(t)$ from an azimuth angle of 180° and an elevation angle of 45°.

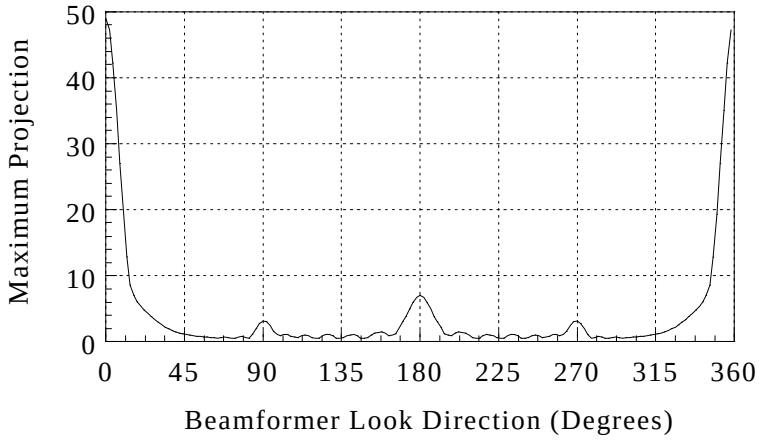

Figure 3-16: Maximum projection for the forty-nine element planar array for incidence of $p_2(t)$ from 0°.

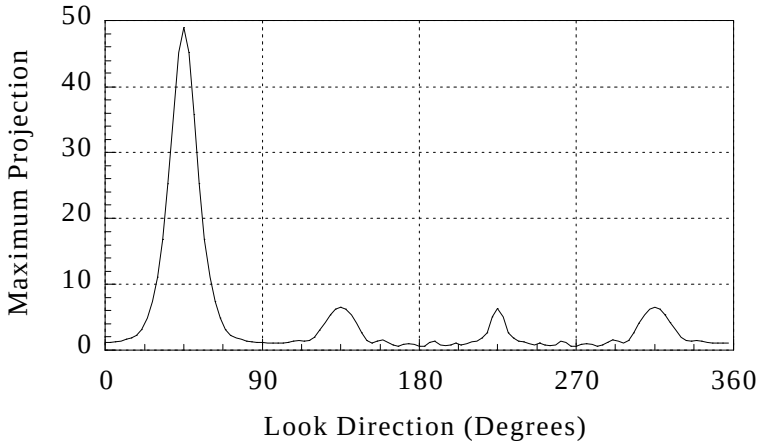

Figure 3-17: Maximum projection for the forty-nine element planar array for incidence of $p_2(t)$ from 45°.

sinusoid, N is the number of elements in the array, d is the inter-element spacing and L is the length of the array. Hence for a fixed array length, the angular resolution performance of the array is a function of the signal frequency. For the case of an UWB array, the equivalent expression for angular resolution can be given [56] as $ct_p/Nd = ct_p/L$, where c is the speed of light and t_p is the temporal extent of the pulse. This expression holds under the condition that the array is large relative to the spatial extent of the pulse, ct_p. A derivation of this expression is given in [56] assuming that the array is a continuous aperture and a Gaussian pulse is incident. Heuristic justification for this expression is given in Figure 3-18, adapted from [56].

Thus a distinction between narrowband arrays and UWB arrays is in the dependence of the angular resolution on the signal frequency versus the signal duration, respectively. Stated another way, narrowband arrays are often designed to operate at a single frequency, while UWB arrays are designed for a given pulse width.

Note that the in the case of a planar array, the resolution angle will be a function of the angle-of-incidence. For example, using an N element $\times$ N element square array, the array length at broadside is $L = Nd$ meters, while at an incidence angle of 45° it is $L = Nd\sqrt{2}$ meters.

A plot of the theoretical angular resolution versus the signal bandwidth, where bandwidth is approximated by $1/t_p$, is given in Figure 3-19 for a number of different array lengths. The measured data used in this work was taken on an array with Nd at just under 1 meter.

3.3 Beamformer Response to Measured Data

The beamformer patterns presented in this chapter give some intuition into the performance of UWB arrays. These results correspond to a particular incident signal, however, and as

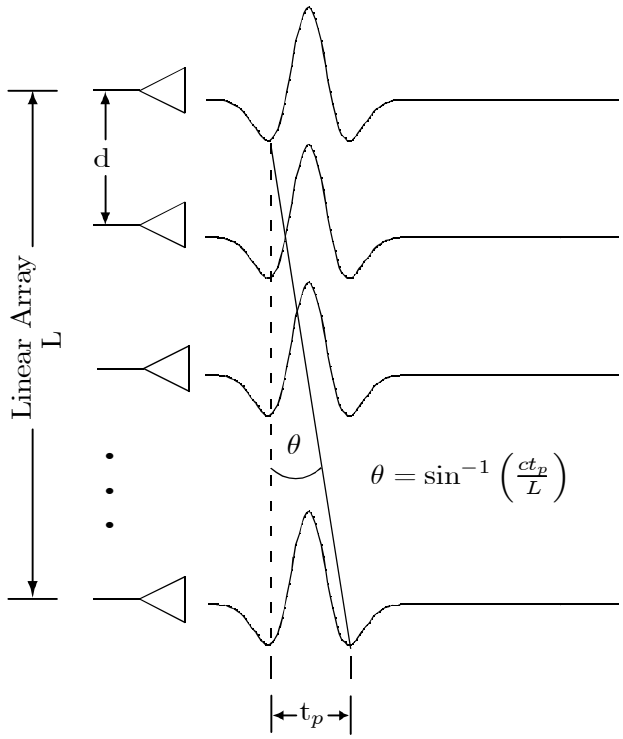

Figure 3-18: Angular resolution capability of a UWB array.

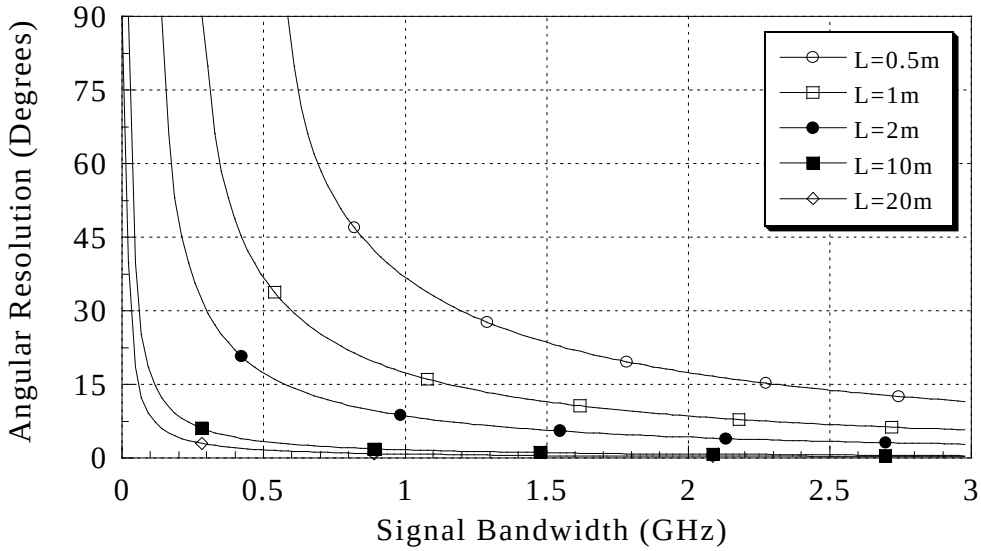

Figure 3-19: Angular resolution versus signal bandwidth.

seen in equation (3.2), the pattern is a function of this incident signal and will vary as the incident signal varies. Thus, if the incident waveform is not well known, it is difficult to predict the beampattern that will be generated by the waveform.

In summary, and to further motivate the problem of sidelobe reduction and signal identification addressed in the next chapter, a plot of the beamformer response to the measured data at location P is shown below in Figure 3-20 over a window in time around the arrival of the direct path signal. In this plot, the direct path signal is easily identified, as are significant additional contributions, due either to sidelobes or multipath. Processing algorithms for UWB sidelobe reduction and signal identification are the subject of the next chapter.

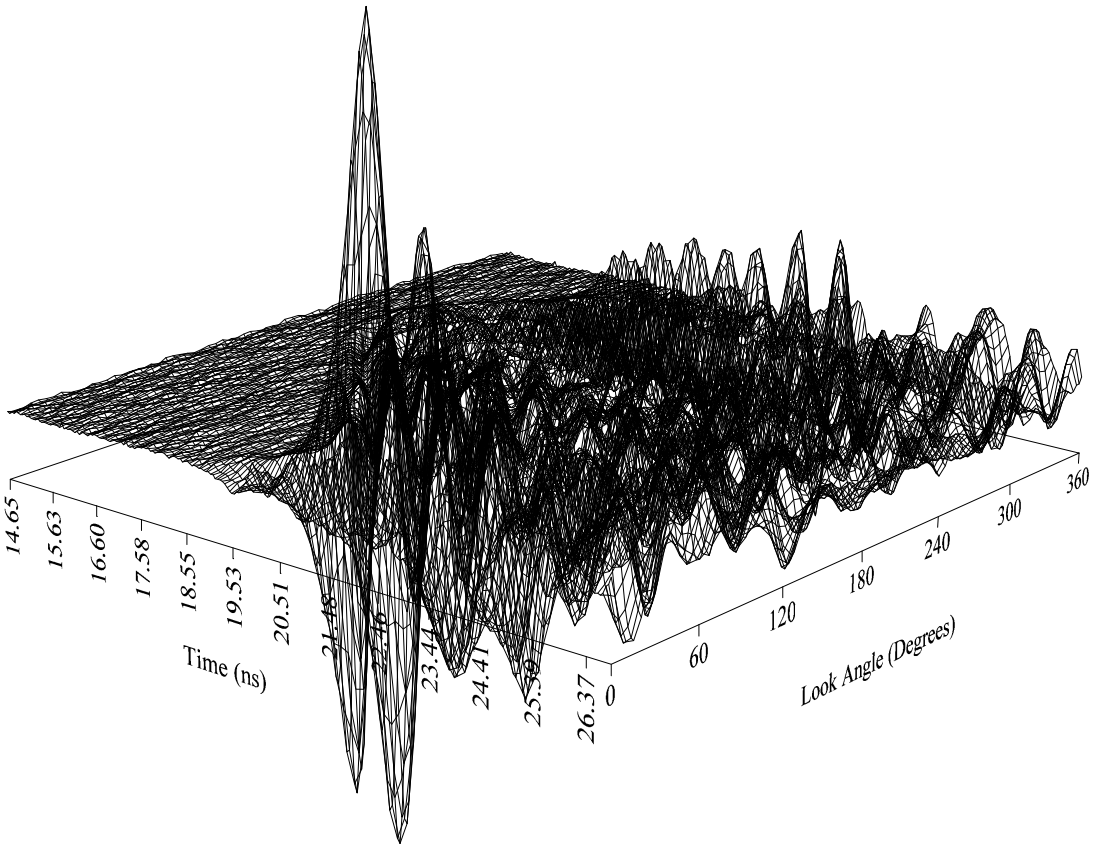

Figure 3-20: Beamformer response to the measured data taken at location P. Elevation look direction is 90°.

Chapter 4

Iterative Techniques for UWB Array Signal Processing

4.1 Description of the algorithm

Implicit in the limit on the achievable peak-to-sidelobe level in equation (2.1) is a limit on the dynamic range available at the output of the UWB beamformer. It is possible then, that UWB beamforming alone is not capable of resolving the incident signals with sufficient dynamic range to adequately characterize an UWB communication channel. In other words, under the assumption that a signal cannot be reliably identified if it arrives with an amplitude in the beamformer output of less than that of the largest sidelobe, a technique for increasing the dynamic range of the UWB beamformer is needed. As discussed in Chapter 2, the time-variation and the impulsive nature of the received UWB waveforms preclude the use of a direct technique for sidelobe reduction and identification of the incident signals. In the absence of an applicable direct technique, an indirect or iterative solution is attempted.

The technique proposed here for processing the incident UWB signals is based upon the CLEAN algorithm, introduced in [19] for the enhancement of radio astronomical maps of

the sky. More generally, the algorithm is related to the Gauss-Seidel relaxation technique [10], a method of successive displacements, and the Gauss-Southwell iteration. The CLEAN algorithm has also found utility in more general antenna sidelobe reduction problems, particularly in the microwave and radar imaging communities [48], [49], [57].

The problem of sidelobe level reduction for UWB arrays can be considered in the context of image restoration. For these problems, techniques have been developed for extracting information from multi-dimensional collections of data. Often, direct inversion to extract source information in these scenarios is not feasible, and a regularized or iterative solution is attempted. One form of iterative solution is given in [27] by the Van-Cittert (or Landweber) equation as

$$\mathbf{t}_{n+1} = \mathbf{t}_n + \gamma\left(\mathbf{g} - \mathbf{D}\mathbf{t}_n\right) \tag{4.1}$$

where $\mathbf{g}$ is a vector representing the image to be restored, formed by concatenating the rows of the image, $\mathbf{t}_n$ represents the restoration result at each iteration and $0<\gamma$ □ 1 is a loop gain term. In this context, $\mathbf{D}$ represents some blurring or distortion function, generally with a circulant structure. The idea is to solve $\mathbf{g} = \mathbf{D}\mathbf{t}$ approximately for $\mathbf{t}$ by driving the residual term $(\mathbf{g} - \mathbf{D}\mathbf{t}_n)$ to zero, and the iteration is terminated when a norm on this expression is less than some prescribed amount. This iteration converges if all eigenvalues, λ, of $\mathbf{D}$ satisfy $|1 - \gamma\lambda| < 1$ [27].

An iterative restoration algorithm such as equation 4.1 is generally implemented for two reasons. First, in the case of an ill–posed problem, the iteration can be terminated prior to significant noise magnification. Second, the use of this method eliminates the need to directly invert the matrix $\mathbf{D}$ in order to solve the problem. In this context, the term ill-posed implies that the solution does not depend continuously on the data [5]. The process

of achieving a balance between the fidelity and the stability of the solution is referred to as regularization, and is controlled by one or more regularization parameters [27]. These techniques often achieve this balance by incorporating a-priori information regarding the solution into the problem.

Implementation of the CLEAN algorithm involves a modification to the Van-Cittert algorithm (4.1), which allows for the selection of a single location in time and angle on each iteration where a signal arrival is likely to have occurred. This is appropriate in light of the fact that the problem at hand is essentially data detection rather than image restoration. The CLEAN algorithm is given as [19]

$$\mathbf{t}_{n+1} = \mathbf{t}_n + \gamma \overrightarrow{\max}\left(\mathbf{g} - \mathbf{D}\mathbf{t}_n\right) \tag{4.2}$$

where $\mathbf{t}_n$ is a LN element vector, formed by concatenating L beamformer look directions at N time instants, and is termed the *brightness distribution*, in analogy with the locations of sources in a radio astronomical map of the sky. The vector $\mathbf{g}$ also consists of LN elements, and represents the *dirty map,* or the beamformer response to the measured data. $\mathbf{D}$:$\mathbb{R}^{LN} \rightarrow \mathbb{R}^{LN}$ is an operator which maps the brightness distribution into the dirty map for each angle-of-incidence and look direction, over all time instants. The constant γ again represents the loop gain and is restricted to $0 < \gamma$ □ 1. The operator $\overrightarrow{\max}(\cdot)$: $\mathbb{R}^{LN} \rightarrow \mathbb{R}^{LN}$, returns the largest absolute element of the argument vector, at the location in the vector where it occurred, and zeroes elsewhere. The idea is to iteratively drive the residual term to zero by finding the brightness distribution which best approximates the actual location of signals impinging on the array, while allowing for errors in the estimation process to be iteratively corrected [10]. Here $\mathbf{D}$ is generally assumed to have a circulant structure,

in order to represent the convolution of the brightness distribution with the point-spread function.

It is important to note that this algorithm is not linear, but rather is modeled as piecewise linear, at best [10]. If the observation space over time and look-angle is divided into N regions such that in the ith region the residuals $|R_i|$ are due only to the signal $s_i(t)$, then the ith linear iterative relaxation process can be proposed to reduce this residual. The difficulty is in the fact that piecewise linear iterations are not easily analyzed, and the asymptotic behavior cannot be proven [10]. Convergence of the CLEAN algorithm has been demonstrated [42], under the conditions that $0<\gamma$ □ 1 and the blurring matrix $\mathbf{D}$ is symmetric and positive definite or semi-definite.

Use of the $\overrightarrow{\max}(\cdot)$ operator in (4.2) can also be justified by instead applying the Van-Cittert algorithm (4.1) to the beamformer response to an incident signal. Then, starting with $\mathbf{t}_0 = \mathbf{0}$, the first iteration gives $\mathbf{t}_1 = \gamma\mathbf{g}$, a scaled replica of the dirty map. For the signal detection problem at hand, $\mathbf{t}_1$ contains all of the signals of interest as well as the undesired artifacts. The dynamic range of this iteration is therefore limited immediately by γ.

In the UWB case, the matrix $\mathbf{D}$ describes the beampattern or the beamformer response over time and angle to a signal waveform, which is a function of the incident pulse shape as shown in Chapter 3. Given the dynamics of the received signal, as seen in Figure 1-3, the CLEAN technique in equation (4.2), must be used in conjunction with a decomposition, such as that given in equation (A.7) of the Appendix, in order to model the indoor UWB channel. In other words, no single pulse shape appears to provide an accurate model for all of the incident signals. This then implies that multiple blurring matrices $\mathbf{D}$ will be required, one corresponding to each waveform in the basis of the decomposition. As discussed in the Appendix, however, use of a signal model such as the Hermite collection

of pulses does not necessarily provide a robust solution. The problems with this basis for the decomposition of UWB signals include the lack of shift-orthogonality and the loss of orthogonality between different modes in the representation in the event of pulse dispersion or distortion. Thus, UWB sidelobe reduction and signal identification techniques based on these decompositions were not developed beyond this point. Further, there is no physical reason to expect the blurring matrix $\mathbf{D}$ to exhibit symmetry, given some transmitted pulse shape. This eliminates the previous analyses on the convergence of the CLEAN algorithm [43], [42] from applicability to this problem.

In practice, $\mathbf{D}$ was allowed to vary as a function of the iteration number. On each iteration, the incident signal and the resulting beampattern were estimated from the peak of the beamformer output, assuming that precisely the same signal was incident upon each of the sensors in the array. A more accurate statement of the CLEAN algorithm as it was implemented here is therefore given by

$$\mathbf{t}_{n+1} = \mathbf{t}_n + \gamma \overrightarrow{\max} \left(\mathbf{g} - \mathbf{D}_n \mathbf{t}_n \right). \tag{4.3}$$

The problem remains that the CLEAN algorithm attempts to estimate the beampattern associated with each incident signal based only on beamspace information. In the absence of any sensor-to-sensor fluctuations in the received signals, this is not a problem; there is no additional information in the sensor data beyond what is in the beamformer output. If sensor-to-sensor fluctuations exist, however, the performance of the CLEAN algorithm degrades, as it is no longer able to accurately estimate the beampatterns from beamspace information only. This is demonstrated in Figure 4-1. In Figure 4-1 (a), the maximum projection of the residual beamformer output upon incidence of a single second-derivative Gaussian pulse from an azimuth angle of 45° is shown over a number of iterations, when

no sensor-to-sensor fluctuations are present and $\gamma = 0.10$. It is seen that the sidelobes fall off at the same rate as the mainlobe. In this scenario, the sidelobes will fall below the detection threshold prior to the mainlobe and will not be detected as distinct arrivals. In Figure 4-1 (b), sensor-sensor fluctuations are present, and the sidelobes no longer fall off at the same rate as the mainlobe. In this case, there is a chance that one or more of the pattern sidelobes associated with the mainlobe will be detected as signals.

A modification to the CLEAN algorithm of equation (4.2) renders it more directly applicable to the problem at hand. Upon identification of the peak residual between the beamformer response to the measured data and the response to the recovered signals, the location in the data from *each sensor*, corresponding to the peak, is identified and the amplitude reduced by a factor of γ. The beampattern is then reformed from this adjusted data and the next peak located. This algorithm will be referred to as Sensor-CLEAN, since the relaxation step now takes place in the space of the sensor data, and can be described by the following equations

$$\mathbf{t}_{n+1} = \mathbf{t}_n + \gamma \overrightarrow{\max} \left[\mathbf{B} \left(\mathbf{d} - \mathbf{w}_n \right) \right] \tag{4.4}$$

$$\mathbf{w}_{n+1} = \mathbf{w}_n + \gamma \mathbf{T}_r \left[\mathbf{B} \left(\mathbf{d} - \mathbf{w}_n \right) \right], \tag{4.5}$$

where $\mathbf{B} : \mathbb{R}^{MN} \rightarrow \mathbb{R}^{LN}$ represents the delay-and-sum beamformer as a linear operator, over M sensors, L look directions and N time instants. The MN element vector $\mathbf{d}$ contains the measured data, $\mathbf{w}_n$ represents the recovered sensor data at iteration n, and $\mathbf{T}_r : \mathbb{R}^{LN} \rightarrow \mathbb{R}^{MN}$ achieves the inverse mapping of the beamformer peak onto the sensor data, assuming a signal length of $2T_p + 1$ samples. The modified algorithm is shown in Figure 4-2. The corresponding plots of the Sensor-CLEAN algorithm operating on a single incident signal, with the same parameters as in Figure 4-1, is shown in Figure 4-3. It is seen in the

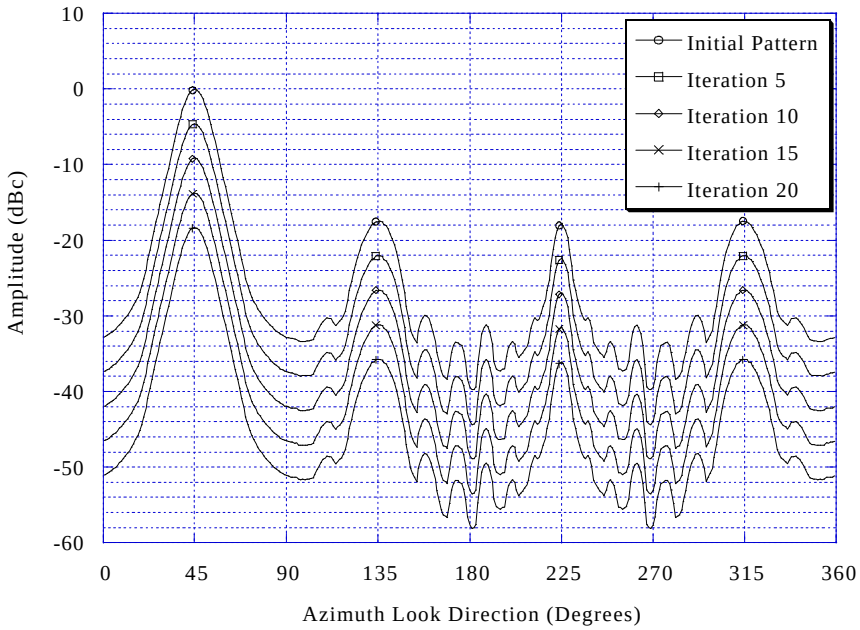

(a)

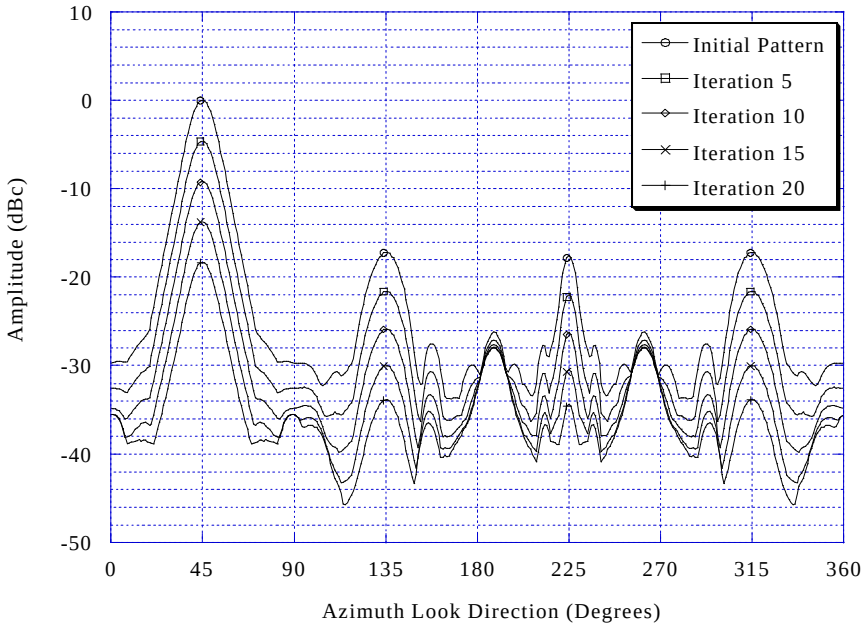

(b)

Figure 4-1: Example of CLEAN algorithm operation on a single incident signal (a) without and (b) with sensor-to-sensor signal fluctuations. The signal is incident from an azimuth of 45° and $\gamma = 0.10$.

figure that in this ideal case, when using Sensor-CLEAN in the presence of sensor-to-sensor signal fluctuations, the sidelobes of the pattern fall off at the same rate as the mainlobe.

The main difference between the CLEAN and Sensor-CLEAN is in the nature of the relaxation step, or the operation in which signals are identified and the amplitude is reduced by some fraction. In the CLEAN algorithm, this relaxation step occurs in the space of the beamformer output, where in Sensor-CLEAN, the relaxation step is applied directly on the sensor data. This permits the operation to proceed with minimal assumptions on the shape of the received signal waveform, since it is not necessary to estimate the resulting beampattern precisely. The only a-priori information that is assumed is the impulsive nature of the incident signals; that the signal will have support in time of less than some maximum number of samples. Again, it is the sensor-to-sensor signal fluctuations present in the received UWB data which makes the beampatterns difficult to predict and hence difficult to regenerate based only on beam-space information. No information is lost in the fact that the relaxation step in now done in the space of the sensor data, instead of in beam-space, since the data processing inequality guarantees that the sensor data contains at least as much information as the beamformer output formed from this sensor data.

The Sensor-CLEAN algorithm requires three parameters to be set prior to initiating the iteration. Given that this is an indirect technique and not an exact solution to the problem, the results provided by the algorithm will be a function of these parameters. The loop gain term, denoted γ, is the fraction of the signal amplitude removed from the measured data during the relaxation step. The parameter T_p represents the maximum window in time (in samples) that the algorithm will process as a single arrival. This is where the strongest assumptions on the nature of the incident signals are made; that they are impulsive and will have support in time of less than $2T_p + 1$ samples. Finally, a detection threshold must be established, providing a condition for termination of the iteration.

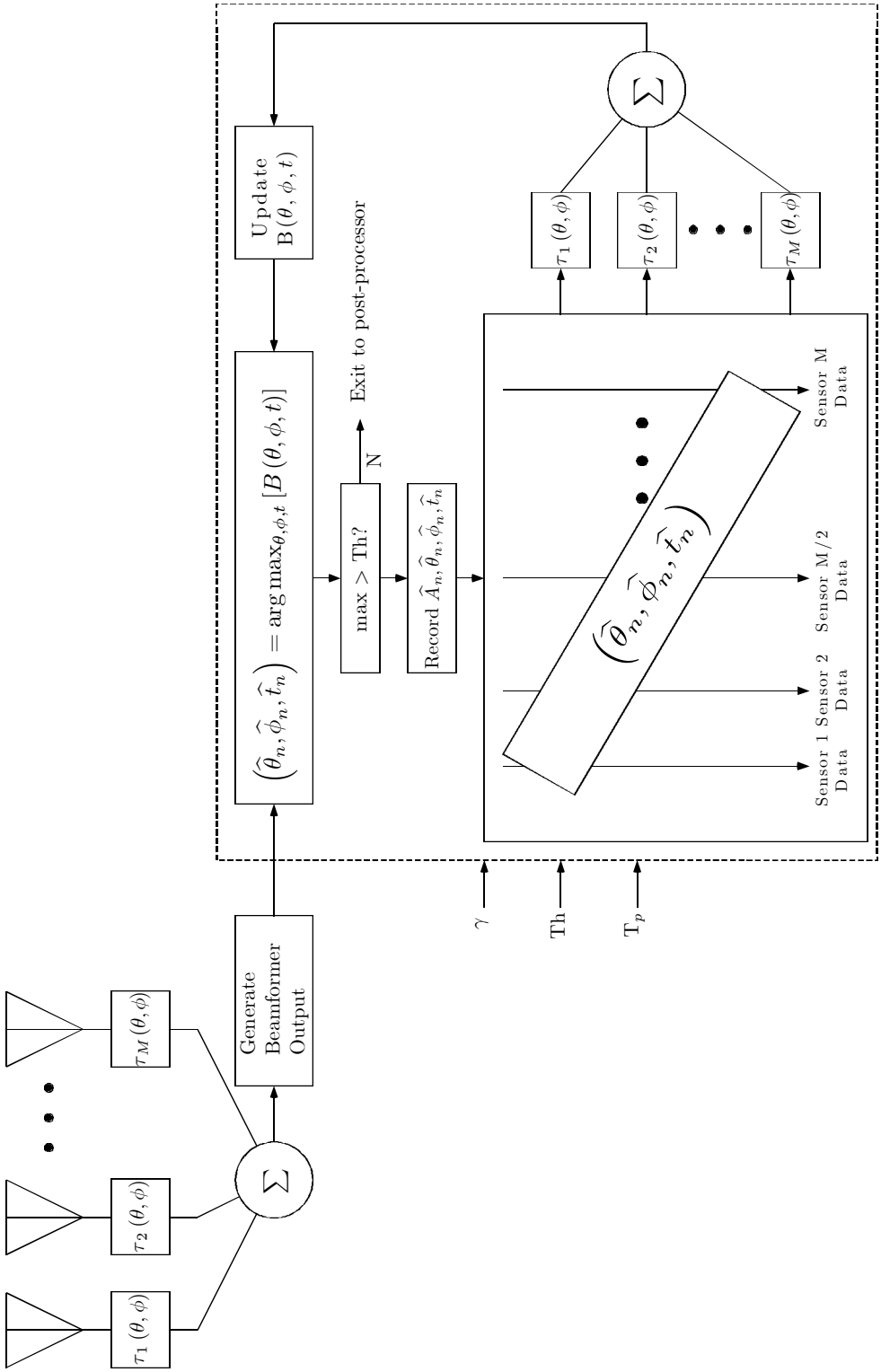

Figure 4-2: The Sensor-CLEAN algorithm

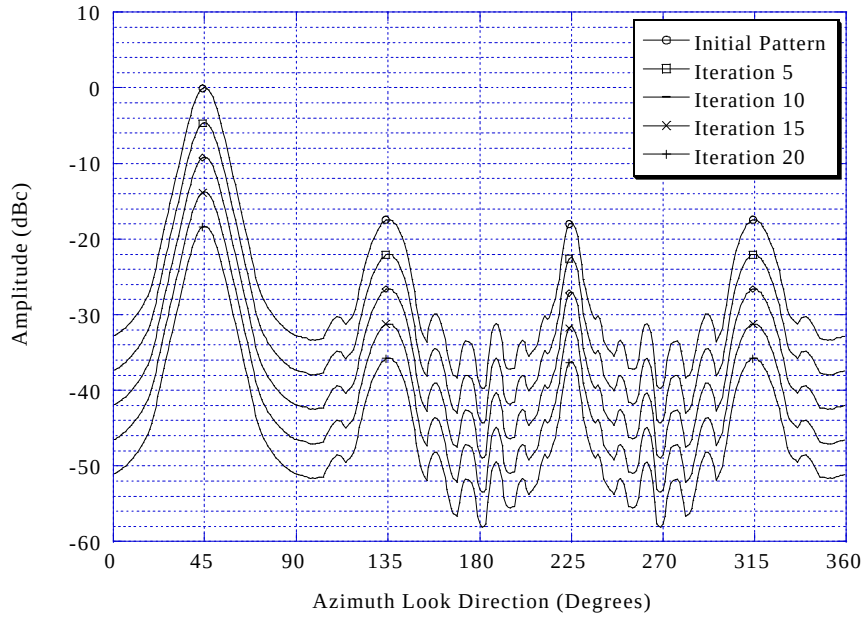

(a)

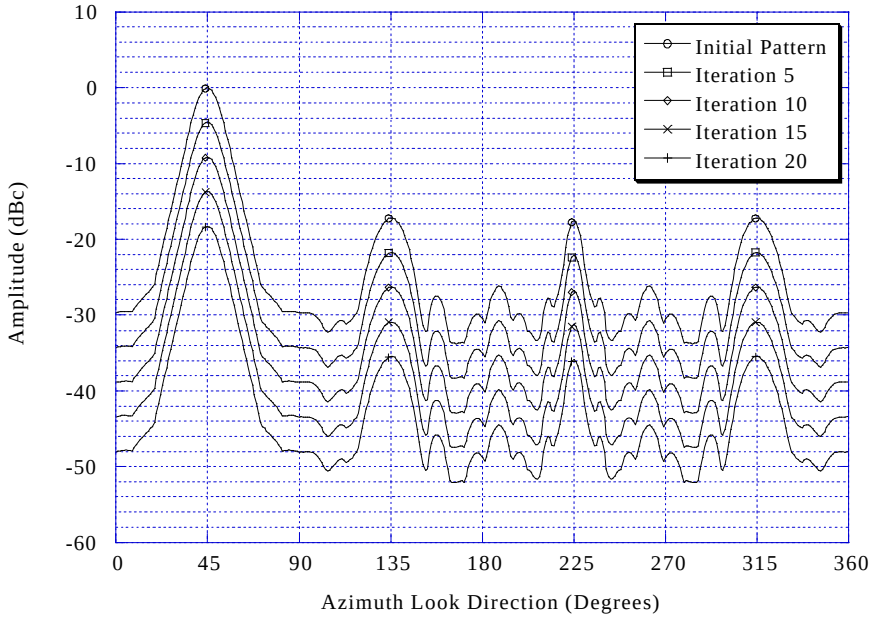

(b)

Figure 4-3: Example of the Sensor-CLEAN algorithm operation on a single incident signal (a) without and (b) with sensor-to-sensor signal fluctuations. The signal is incident from an azimuth of 45° and $\gamma = 0.10$.

Given the use of this algorithm, the following model for the response of the channel to a transmitted UWB signal can be discussed:

$$r(t) = \sum_{k=1}^{N} A_k s_k (t - \tau_k, \theta_k, \phi_k) + n(t), \tag{4.6}$$

where τ_k is the time-of-arrival of the kth out of N signal components, at an azimuth angle of θ_k degrees and an elevation angle, measured from a perpendicular to the array, of ϕ_k degrees. The received impulse waveform, $s_k(t)$ depends on the index k, due to variations in the received signal shape. This dictates that, for each detected signal, the algorithm should estimate $s_k(t)$ from the received data, in addition to the time-of-arrival and angle-of-arrival.

The operation of the Sensor-CLEAN algorithm is shown in Figure 4-2 and is described in the following steps:

1. Collect the received signal data on an array of sensors, and generate the delay-and-sum beamformer output over a window in time and in azimuth and elevation arrival angle, according to

$$\mathbf{s} = \mathbf{B}\mathbf{d}, \tag{4.7}$$

   where $\mathbf{S}$ is the beamformer response to the sensor data, $\mathbf{B}$ represents the delay-and-sum beamformer and $\mathbf{d}$ is a vector of the measured data at each sensor, as before.

2. Search this beamformer output for the peak absolute component, recording the azimuth angle θ_0, elevation angle ϕ_0 and time-of-arrival t_0 of the peak, or

$$\{\theta_0, \phi_0, t_0\} = \arg\max \mathbf{s}. \tag{4.8}$$

3. Determine the location in the data from each sensor corresponding to the peak residual. Either use an a-priori hypothesis on the support in time of the incident signal, or

determine the support of the incident signal by adjusting the window in each sensor over which the relaxation is conducted, and note the support which results in the minimum residual energy. The mapping of the beamformer peak location onto the sensor data is achieved by the operator $\mathbf{T}_r$ and the residual sensor components are then given by $\mathbf{T}_r\left[\mathbf{B}\left(\mathbf{d}-\mathbf{w}_n\right)\right]$ where $\mathbf{w}_n$ represents the recovered sensor data on the nth iteration and $\mathbf{w}_0$ is an all zeros vector.

4. Reduce the residual on each sensor corresponding to the peak by a fraction γ, by adding the signal component to the recovered sensor data $\mathbf{w}_n$, according to equation (4.5).

5. Regenerate the residual beamformer output over the affected range in time and angle, according to $\mathbf{B}\left(\mathbf{d}-\mathbf{w}_n\right)$.

6. Search again for the largest residual value in the beamformer output map, given on the nth iteration by

$$\{\theta_n, \phi_n, t_0\} = \arg\max\left[\mathbf{B}\left(\mathbf{d}-\mathbf{w}_n\right)\right], \tag{4.9}$$

   where $\mathbf{w}_n$ represents the recovered sensor data, as above. If the resulting peak is above the detection threshold, then update the recovered signal information according to according to equation (4.4) and continue with step 3, else terminate the iteration.

7. When all residuals have been liquidated, or no signal components remain with amplitude greater than the detection threshold, accumulate the signal information collected during the iteration, and generate the associated main beams. Add this to the residual noise floor left over from the iteration,

$$\mathbf{s}_c = \mathbf{B}'\mathbf{w}_J + \mathbf{B}\left(\mathbf{d}-\mathbf{w}_J\right), \tag{4.10}$$

where the iteration was terminated on the Jth iteration, $\mathbf{s}_c$ represents the "clean" map and $\mathbf{B}'$ is an operator which generates the mainbeams of the detected signals only.

8. Post-process the Sensor-CLEAN output, $\mathbf{s}_c$, to determine the signal arrival information from this "clean" map, in the absence of the sidelobes. This operation will be discussed in greater detail shortly.

A few remarks on the algorithm are in order. First, convergence of the Sensor-CLEAN algorithm is guaranteed through a monotonic reduction in the residual energy on each iteration. The residual energy, as well as the peak residual, is smaller on each iteration than on the last, which insures that the algorithm will converge to some solution. This is demonstrated in Section 4.2, which discusses the optimality of the Sensor-CLEAN algorithm. As with most indirect algorithms, however, the solution generated by the Sensor-CLEAN algorithm is a function not only of the data, but of the input parameters as well. Thus the solution is not unique, and the parameters must be selected based on some criterion which generally trades estimate fidelity against computation time. For example, the quality of the estimates and the required computation time are inversely proportional to the loop gain γ and the relaxation window size, for a fixed detection threshold. This implies that some knowledge or judgement, possibly in the absence of an applicable theory for selection of values, must be applied in the determination of these parameters. Note that all randomness is contained in the data and not the algorithm; for fixed parameter values and data, the Sensor-CLEAN algorithm will return consistent results.

4.1.1 Post-processing of Sensor-CLEAN information - The Wave-Map Algorithm

The output of the Sensor-CLEAN algorithm consists of a list $\{a_n, \theta_n, \phi_n, t_n, \mathbf{w}_n\}_{n=1}^{N}$ of the amplitude a_n, the azimuth look direction θ_n, the elevation look direction ϕ_n, the time-of-arrival, t_n and the waveforms $\mathbf{w}_n$ recovered on each iteration. The algorithm also records the residual noise floor which remains after all components above the detection threshold have been removed. Because all signal detections corresponding to a single incident signal may not occur at precisely the same location in time and angle, resulting in multiple detections of the same signal at distinct locations, this list of arrivals must be further processed in order to more accurately estimate the signal parameters. A post-processing algorithm is therefore applied to the data, which takes into account the known spatio-temporal resolution limits of the UWB beamformer, and attempts to combine multiple detections which likely correspond to a single signal. These results form an initial estimate of the signal parameters. Since each hypothesized signal can now be considered in the absence of other signals which may have biased the initial estimates, an attempt is made next to re-estimate parameters of each detected signal, comparing each signal with the original beamformer output.

The first of two post-processing algorithms introduced in this work is referred to as the Wave-Map algorithm, and is shown in Figure 4-4. In this routine, the mainbeams corresponding to each of the detections reported by the Sensor-CLEAN algorithm are formed, and added onto the residual output map, denoted in the figure by $\mathbf{R}(t_n, \theta_n, \phi_n)$. This composite map is then searched and the maximum value is recorded. If this maximum is greater than the detection threshold, then all elements in the list, $\{a_n, \theta_n, \phi_n, t_n, \mathbf{w}_n\}_{n=1}^{N}$, that are within a distance T_w seconds in time and Θ_w degrees in azimuth angle of the maximum are assumed to have contributed to the peak and are marked as detected and removed from further consideration. The parameters T_w and Θ_w are chosen to reflect the spatio-temporal

resolution limit of the UWB array and beamformer. The mainbeams associated with all remaining undetected elements of the arrival list are then formed and added to the residual map. This process repeats until the detection threshold is no longer satisfied.

When the formation of the mainbeams from the undetected arrivals results in no components in the output map with value greater than the detection threshold, the algorithm terminates and a re-estimation routine is applied. This routine compares the recovered signal amplitude, time-of-arrival and angle-of-arrival against the original measured data, and adjusts the recovered signal data to more accurately reflect the measured data, when necessary. The parameters required to accomplish this are the one-sided time window, T_{re}, azimuth angular window, Θ_{re}, and the elevation angular window, Φ_{re}, over which to search. The re-estimation procedure then generates the beamformer output from the measured data in a window around the detected arrival. This window is then searched for the maximum value, which is then reported as the final location in time and angle of the incident signal.

4.2 Optimality of the Sensor-CLEAN Algorithm

If the assumptions are made that the beampatterns associated with different pulses do not interfere, as defined below in equation (4.14), and that all of the incident pulses have equal energy, then the Sensor-CLEAN algorithm is optimal in that for fixed parameters, it generates the solution with minimum residual energy. This can be seen as follows. First, define the residual energy on iteration j as equal to

$$R_j = \sum_{n=0}^{N-1} \sum_{m=0}^{L-1} \left| B_j\left(n, m\right) \right|^2, \tag{4.11}$$

where $B_j\left(n, m\right) = \mathbf{B}\left(\mathbf{d} - \mathbf{w}_j\right)$ represents the residual beamformer output map at iteration j over N time samples and L look directions, as in equation (4.4) and equation (4.4). The

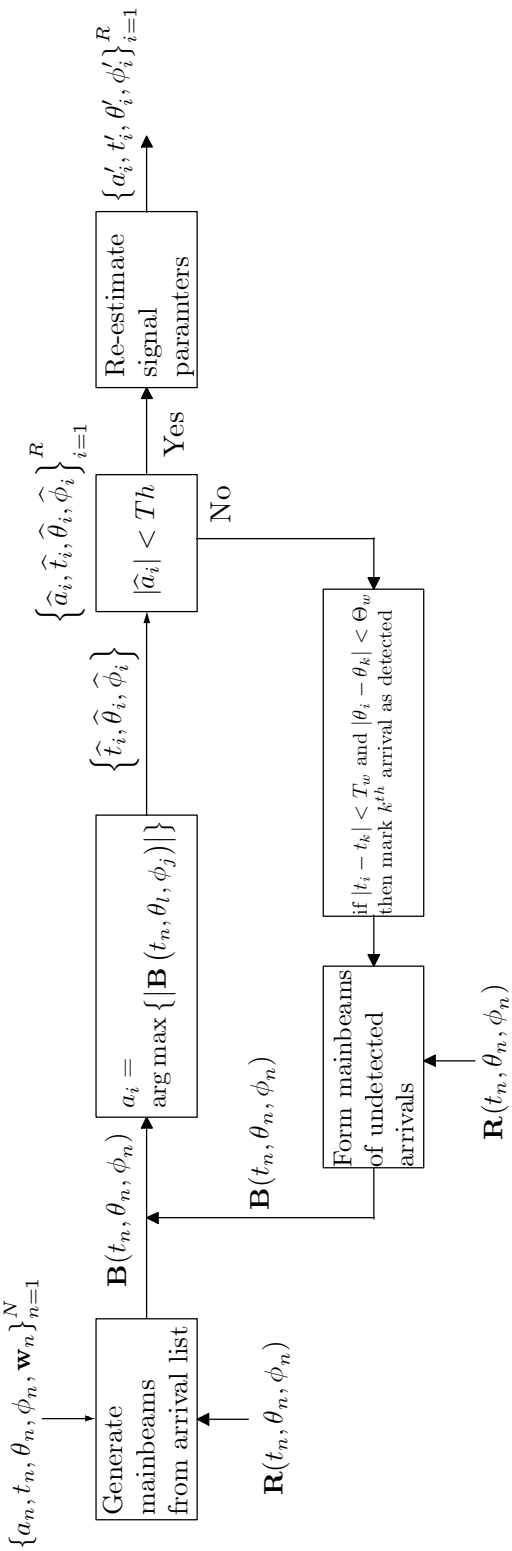

Figure 4-4: Post-processing algorithm, called the Wave-Map Algorithm.

initial output map can be modeled by considering the superposition of the incident pulses and their beampatterns,

$$B_0(n,m) = \sum_{k=0}^{K-1} A_{0,k} b_k(n-a_k, m-b_k), \tag{4.12}$$

where $b_k(\cdot)$ represents the beampattern associated with the kth incident pulse, at time a_k and angle b_k. Then, on iteration j,

$$|B_j(n,m)|^2 = \left| \sum_{k=0}^{K-1} A_{j,k} b_k(n-a_k, m-b_k) \right|^2. \tag{4.13}$$

If the assumption is made that the spatio-temporal beampatterns are orthogonal, or they do not interfere with each other, so that

$$\sum_{n=0}^{N-1} \sum_{m=0}^{L-1} b_i(n-a_i, m-b_i)\, b_j(n-a_j, m-b_j) = 0, \quad \forall i \neq j, \tag{4.14}$$

then

$$\begin{aligned} |B_j(n,m)|^2 &= |A_{j,0} b_0(n-a_0, m-b_0)|^2 + |A_{j,1} b_1(n-a_1, m-b_1)|^2 + \\ &\cdots + |A_{j,K} b_K(n-a_K, m-b_K)|^2 \\ &= |A_{j,0}|^2 |b_0(n-a_0, m-b_0)|^2 + |A_{j,1}|^2 |b_1(n-a_1, m-b_1)|^2 + \\ &\cdots + |A_{j,K}|^2 |b_K(n-a_K, m-b_K)|^2. \end{aligned} \tag{4.15}$$

The residual energy on the jth iteration can then calculated according to

$$
\begin{aligned}
R_j &= \sum_{n=0}^{N-1}\sum_{m=0}^{L-1}\left[\sum_{k=0}^{K-1}\left|A_{j,k}\right|^2\left|b_k\left(n-a_k,m-b_k\right)\right|^2\right] \\
&= \sum_{k=0}^{K-1}\left|A_{j,k}\right|^2\sum_{n=0}^{N-1}\sum_{m=0}^{L-1}\left|b_k\left(n-a_k,m-b_k\right)\right|^2 \\
&= \sum_{k=0}^{K-1}\left|A_{j,k}\right|^2 E_k, \qquad (4.16)
\end{aligned}
$$

where

$$
E_k = \sum_{n=0}^{N-1}\sum_{m=0}^{L-1}\left|b_k\left(n-a_k,m-b_k\right)\right|^2 \qquad (4.17)
$$

represents the energy contained in the spatio-temporal beampattern of the kth incident signal, integrating over time and angle. If the assumption is made that the suite of beampatterns associated with the received pulse shapes $b_k(\cdot)$, $k \in 0,\ldots,K-1$, all have equal energy, $E_k = E_j$, $\forall k,j$, then the residual energy on the jth iteration can be represented as

$$
R_j = \sum_{k=0}^{K-1}\left|A_{kj}\right|^2 E. \qquad (4.18)
$$

Order the amplitude terms of the K signals so that $|A_{0j}| \geq |A_{1j}| \geq \cdots \geq |A_{K-1,j}|$, for each iteration j. Let R_{ij} represent the residual energy when the ith term is relaxed on the jth iteration, or

$$
R_{ij} = \sum_{\substack{k=0\\k\neq i}}^{K-1}\left|A_{kj}\right|^2 E + (1-\gamma)^2\left|A_{ij}\right|^2 E. \qquad (4.19)
$$

The Sensor-CLEAN algorithm dictates that the largest component on each iteration is relaxed. By the ordering assumed above, this is given by A_{0j}. Given relaxation of this term, the residual energy is given by

$$\begin{aligned} R_{0j} &= \sum_{k=1}^{K-1} |A_{kj}|^2 E + (1-\gamma)^2 |A_{0j}|^2 E \\ &= R_{mj} - \left(|A_{0j}|^2 - |A_{mj}|^2\right) E + (1-\gamma)^2 \left(|A_{0j}|^2 - |A_{mj}|^2\right) E \\ &= R_{mj} + \left[(1-\gamma)^2 - 1\right] \left(|A_{0j}|^2 - |A_{mj}|^2\right) E, \end{aligned} \tag{4.20}$$

and $\left[(1-\gamma)^2 - 1\right] \left(|A_{0j}|^2 - |A_{mj}|^2\right) \square\ 0$, since $|A_{0j}|^2 \geq |A_{mj}|^2$ and $0 < \gamma \square\ 1$, which gives $R_{0j} \square\ R_{mj}$. Thus on each iteration, relaxing the largest component is the operation which minimizes the residual energy, and therefore, under the assumptions stated above, the algorithm is optimal in the sense that the solution generated has the minimum residual energy, for the parameters selected.

Again, the difficulty here is that in order to maintain generality in the channel characterizations, it is assumed that the actual received UWB signals are not known a-priori, and are not necessarily identical from multipath component to component. Further, in the measured data the beampatterns are not in general orthogonal, but can overlap to a significant extent. Thus although the analysis above gives some insight into the operation of the algorithm, it is not strictly applicable.

4.3 Use of A-Priori Information

As has been discussed throughout this thesis, a fundamental question concerns the minimum a-priori information required to solve the UWB signal location problem. In a discussion in Appendix A it is noted that signal models, such as the one based on the Hermite family of pulses, cannot accurately represent the received UWB waveforms; they imposes too

much structure and cannot handle the dynamics in the received signal appropriately. It is the absence of an applicable signal model which motivates the use of the Sensor-CLEAN algorithm over the CLEAN algorithm, because knowledge of the expected beampattern or the point spread function is required in order to accurately conduct the relaxation steps in beam-space. The Sensor-CLEAN algorithm, however, requires fewer assumptions on the nature of the incident waveforms. The only a-priori information regarding the input signal required at the input of the algorithm is that it is an impulsive signal, that it is going to have relatively narrow support in time. The maximum window in time that the algorithm will consider as a single arrival in time is then input to the Sensor-CLEAN algorithm as a parameter. Thus the Sensor-CLEAN algorithm essentially implements joint data and channel estimation; data in the sense that it estimates the spatial location of the signals, and the channel in that the waveform under consideration is estimated from the received data rather than from a static or a-priori model for the signal.

4.4 Verification of the Algorithm

To verify the performance of the Sensor-CLEAN algorithm and to establish reasonable parameter values, it was tested in a number of hypothetical scenarios involving known UWB signals and the 7×7 element planar array on which the actual propagation measurements were made. In the first set of tests, twenty-five UWB signals were distributed throughout a region measuring 70 ns in time by 360° in azimuth AOA and 70° in elevation AOA, from 90°, corresponding to arrival in the plane of the array, to 20°. A typical received signal profile is shown below in Figure 4-5.

The parameters which were manipulated in this test include the loop gain, γ, and the size of the time window, given by $2T_p + 1$ time samples, over which the detected signals were relaxed or reduced by γ on each iteration. In order to maintain compatibility with the

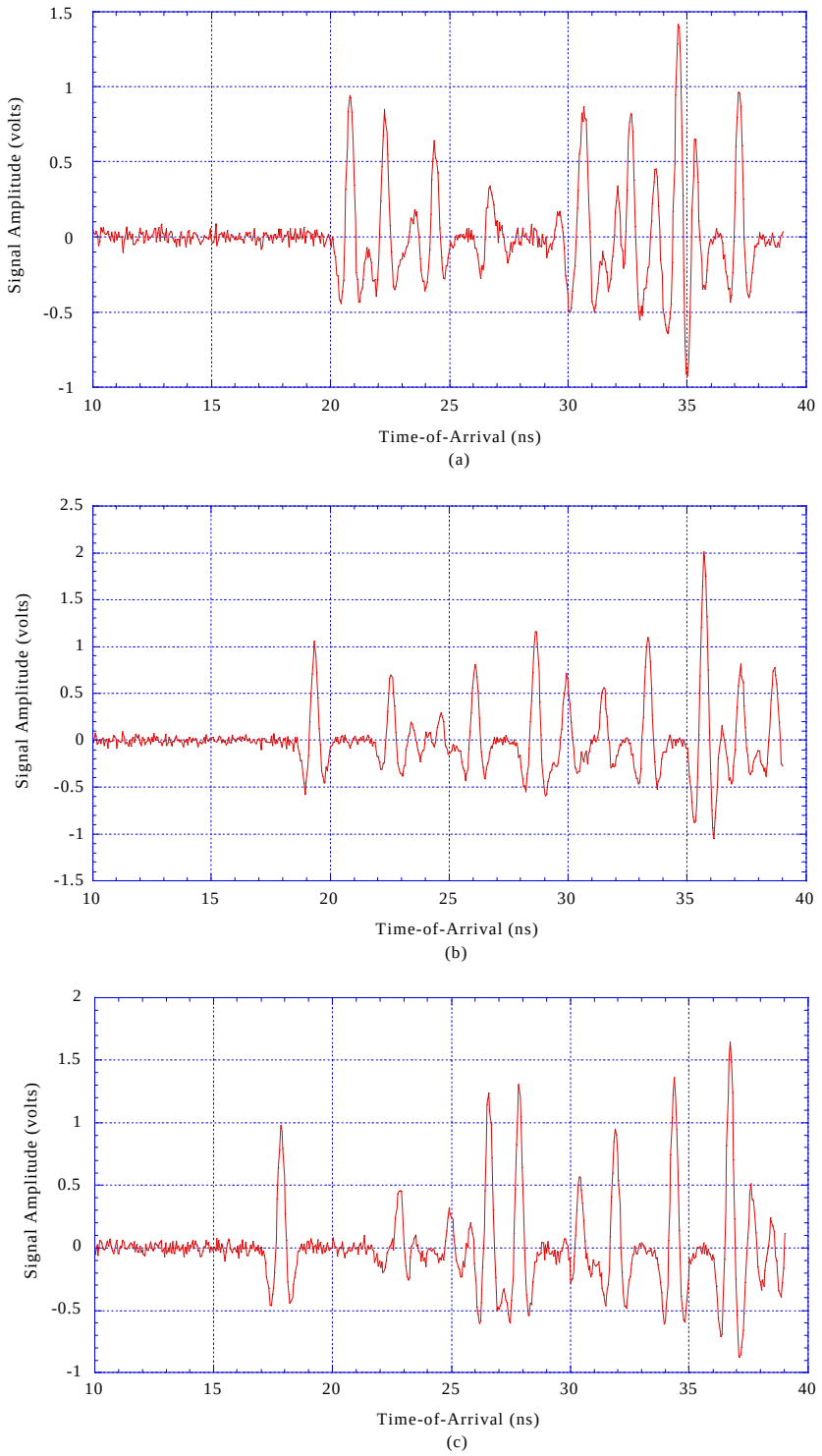

Figure 4-5: Initial section of generated signal at sensor (a) (1,1) (b) (4,4) and (c) (7,7).

measured data, the sampling rate in these results was maintained at $f_s = 20$Gsamples/sec. Three different methods were used to select this relaxation window. First, a fixed window was used, independent of the data. As shown in the table, several different fixed window sizes were employed. Next, the window size was established by the first zero-crossing above and below the peak residual in the beamformer output. Finally, T_p was set by choosing the window size which resulted in the smallest residual energy between the beamformer output corresponding to the current signal arrival and window size, and the actual beamformer output. Following the Sensor-CLEAN operation, the post-processor recombined the detected signals and formed the associated mainbeams, according to the Wave-Map algorithm. The results from the processing of the first set of test signals by these three relaxation techniques in the absence of noise are shown below in Table 4.1, prior to the re-estimation process. The results following the re-estimation are shown in Table 4.2. In each table the parameters of the test are specified, including γ, T_p and the post-processing resolution limit, T_w. The results of the test are given in the percent of the total energy in the signals that is recovered and the RMS azimuth and time estimation errors. For these cases, T_w was fixed at 16 samples, as this was a good match to the generated UWB pulses.

Next, noise was added to the received sensor data. For the first test, the noise standard deviation was set at 0.035 volts, where the peak signal amplitude was set at 1.0 volts. The results of this test are shown prior to the re-estimation process in Table 4.3, and following the re-estimation of the signal parameters in Table 4.4. Figure 4-6 and Figure 4-7 give a graphical representation of the signal recovery results for a number of cases. Further results on the verification of the algorithm will be presented with the remainder of the post-processing algorithm in the next section.

Considering the results in these tables several items are noted. First, the selection of the relaxation window by the criterion of minimizing the residual energy exhibits the worst

γ	T_p	T_w (samples)	% Energy Recovered	RMS AOA Error (deg.)	RMS TOA Error (ns)
0.07	6 samples	16	76.1	0.256	0.022
0.10	6 samples	16	76.1	0.256	0.022
0.10	8 samples	16	70.0	0.243	0.047
0.10	12 samples	16	71.9	0.357	0.000
0.10	Zero cross	16	69.5	14.203	1.991
0.10	Min. energy	16	68.2	0.385	0.014
0.15	6 samples	16	76.1	0.256	0.022
0.15	Zero cross	16	69.5	14.203	1.991
0.15	Min. energy	16	68.7	0.475	0.014
0.20	4 samples	16	77.8	0.079	0.022
0.20	6 samples	16	76.1	0.256	0.022
0.20	Zero cross	16	69.6	14.203	1.991
0.20	Min. energy	16	68.2	0.356	0.014

Table 4.1: Verification of Sensor-CLEAN algorithm, results prior to re-estimation for 25 signals and no noise.

γ	T_p (one-sided)	T_w (samples)	% Energy Recovered	RMS AOA Error (deg.)	RMS TOA Error (ns)
0.07	6 samples	16	96.7	0.402	0.000
0.10	6 samples	16	96.7	0.402	0.000
0.10	8 samples	16	96.7	0.402	0.000
0.10	12 samples	16	96.7	0.402	0.000
0.10	Zero cross	16	96.5	14.203	1.991
0.10	Min. energy	16	96.7	0.402	0.000
0.15	6 samples	16	96.7	0.402	0.000
0.15	Zero cross	16	96.4	14.203	1.991
0.15	Min. energy	16	96.7	0.402	0.000
0.20	4 samples	16	96.7	0.402	0.000
0.20	6 samples	16	96.7	0.402	0.000
0.20	Zero cross	16	96.5	14.203	1.991
0.20	Min. energy	16	96.7	0.402	0.000

Table 4.2: Verification of Sensor-CLEAN algorithm, following re-estimation for 25 signals and no noise

γ	T_p (one-sided)	T_w (samples)	% Energy Recovered	RMS AOA Error (deg.)	RMS TOA Error (ns)
0.10	8 samples	16	69.8	0.465	0.049
0.10	12 samples	16	71.7	0.381	0.000

Table 4.3: Results for 25 signals in AWGN with a peak SNR of 30dB, prior to parameter re-estimation.

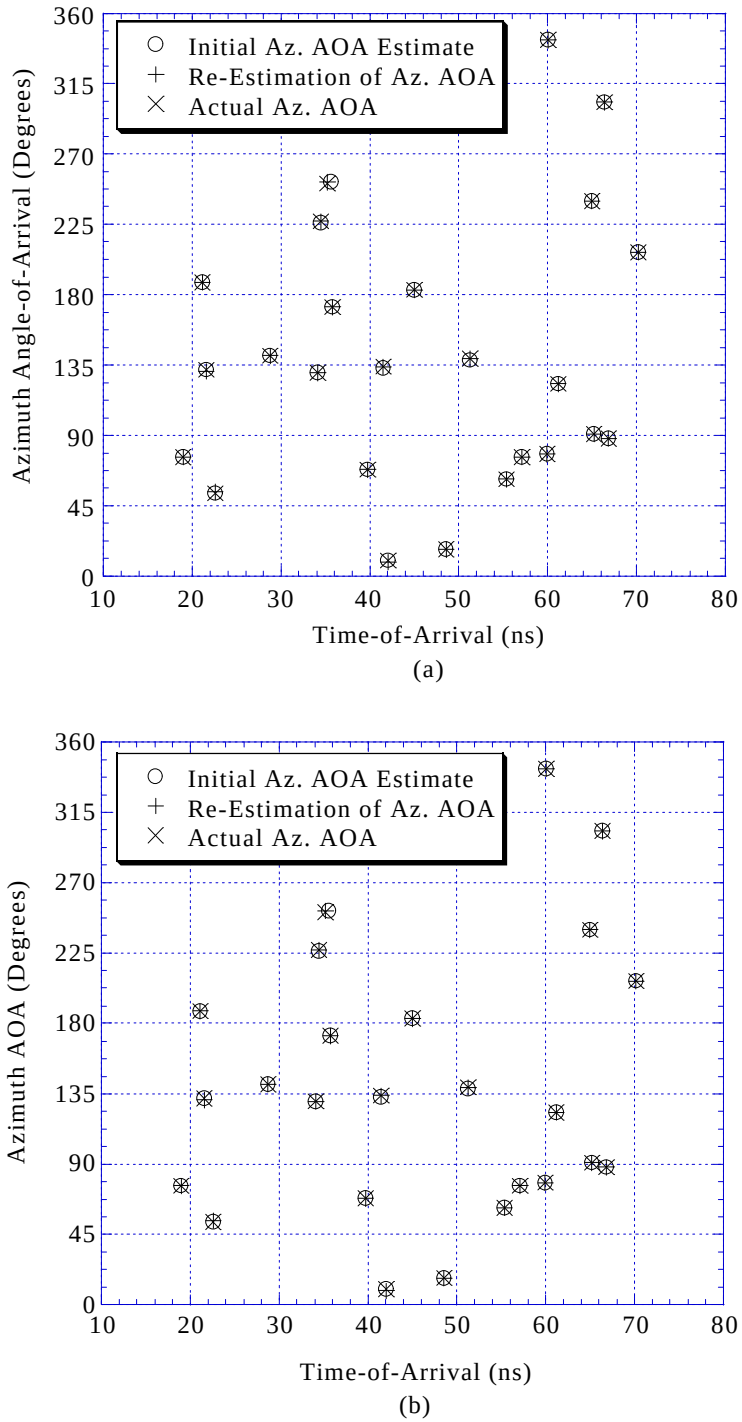

Figure 4-6: Actual, recovered and re-estimated signal locations for 25 signals, relaxation window of 6 samples and no noise, with (a) $\gamma = 0.07$ and (b) $\gamma = 0.10$.

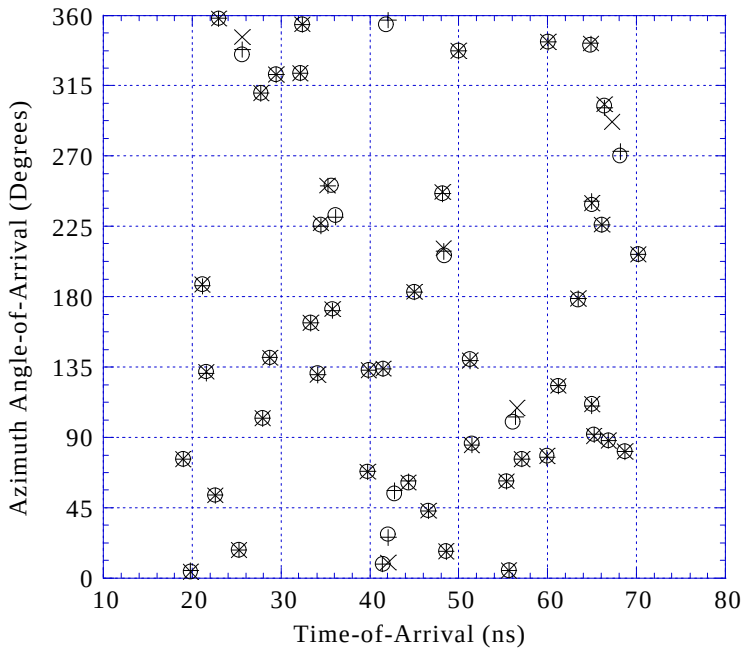

(a)

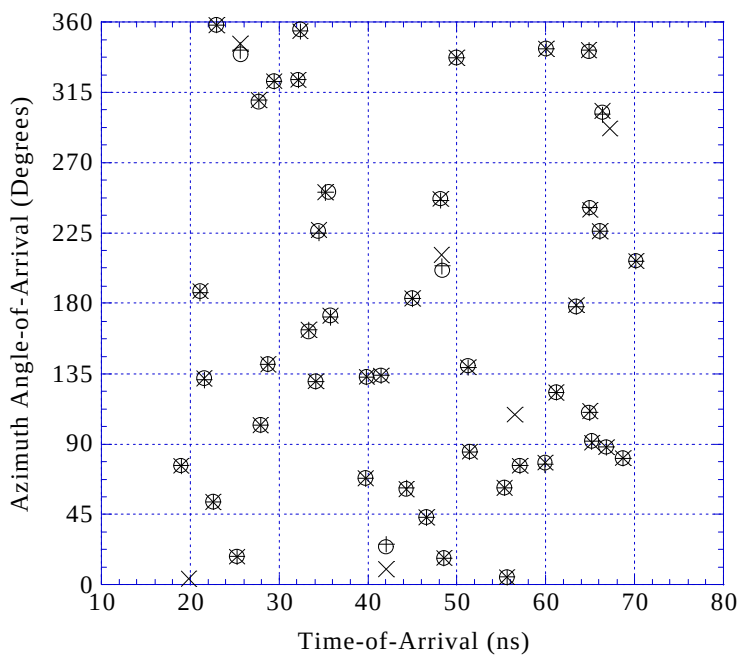

(b)

Figure 4-7: Actual, recovered and re-estimated signal locations for 50 signals, no noise and $\gamma = 0.10$ (a) relaxation window = 6 samples and (b) relaxation window = 12 samples

γ	T_p (one-sided)	T_w (samples)	% Energy Recovered	RMS AOA Error (deg.)	RMS TOA Error (ns)
0.10	8 samples	16	96.7	0.400	0.003
0.10	12 samples	16	96.7	0.404	0.000

Table 4.4: Results for 25 signals in AWGN with a peak SNR of 30dB, following parameter re-estimation.

performance in terms of the percentage of energy recovered, prior to re-estimation. This is because the criterion often leads to the selection of as large of a window as the algorithm will permit, which reduces the resolution and causes signals to be missed. Performing slightly better than the minimum residual energy technique is the method of zero-crossings, where the relaxation window is defined by the first zero-crossing above and below the location of the peak. If signals are closely spaced in time, then the location of a zero-crossing can be biased by a signal which arrives immediately before or after the signal of interest, leading to an inaccurate selection of the window size. The re-estimation process can then fail to adjust the location of the signal properly if this bias is too large. The technique which exhibited the best performance, prior to re-estimation, was simply to select a fixed window over which to conduct the relaxations. As expected, a smaller window resulted in more accurate estimates, with a penalty in terms of the computation time. Three window sizes were examined in the tables, $T_p = 6$ samples, $T_p = 8$ samples and $T_p = 12$ samples, with the size of the smallest window dictated by a reasonable computation time. Recall that the length of the associated time window is $2T_p + 1$ samples, centered on the peak.

This relationship between the accuracy of the results and the window size, for a fixed relaxation window is due to the fact that the smaller the relaxation window, the lower the probability that energy not belonging to the signal under consideration will also be removed. Thus the greater the probability that multiple signals closely spaced in time and angle-of-arrival will detected as distinct. In terms of the ability of the algorithm to detect signals over a large dynamic range, this property can also then increase the sensitivity of the

algorithm to small incident signals, since they are less likely to be removed during relaxation of the response to a nearby larger signal.

An example of the Sensor-CLEAN algorithm in operation is detailed in Figure 4-8 for γ=0.10 and $T_p = 8$ samples, and in Figure 4-9 for the same γ and $T_p = 12$ samples. Here, the algorithm is operating on the beamformer output of the measured data from location P. The section of the beamformer output on which the algorithm operates on the first nine iterations is shown, with the angular information suppressed. Considering Figure 4-8, the algorithm operates on the peak of the direct path signal for the first two iterations, with the relaxation window centered at time sample 427, before moving to operate on a different part of the same signal, centered at sample 437, on the third iteration. The information recovered from these two operation locations corresponds to the same signal, and must be recombined to correctly report the arrival information. If the size of the relaxation window is increased to ± 12 samples, shown in Figure 4-9, then it is seen that this problem does not occur, at least for the direct path signal. The algorithm operates on the direct path signal, with the relaxation window centered at sample 427, until the seventh iteration, when it initiates the processing of the next signal. It operates on this signal for an iteration, then moves back again to the direct path signal on the ninth iteration. This process of operating on the largest residual signal continues until no residuals with amplitude greater than the detection threshold are present.

4.5 Practical Application of Sensor-CLEAN to Measured Data

Although computationally expensive, the approach that was taken for the processing of the measured data based on these results was to use the three fixed window sizes in parallel runs of the Sensor-CLEAN and post-processing algorithms. The smallest window size, $T_p = 6$

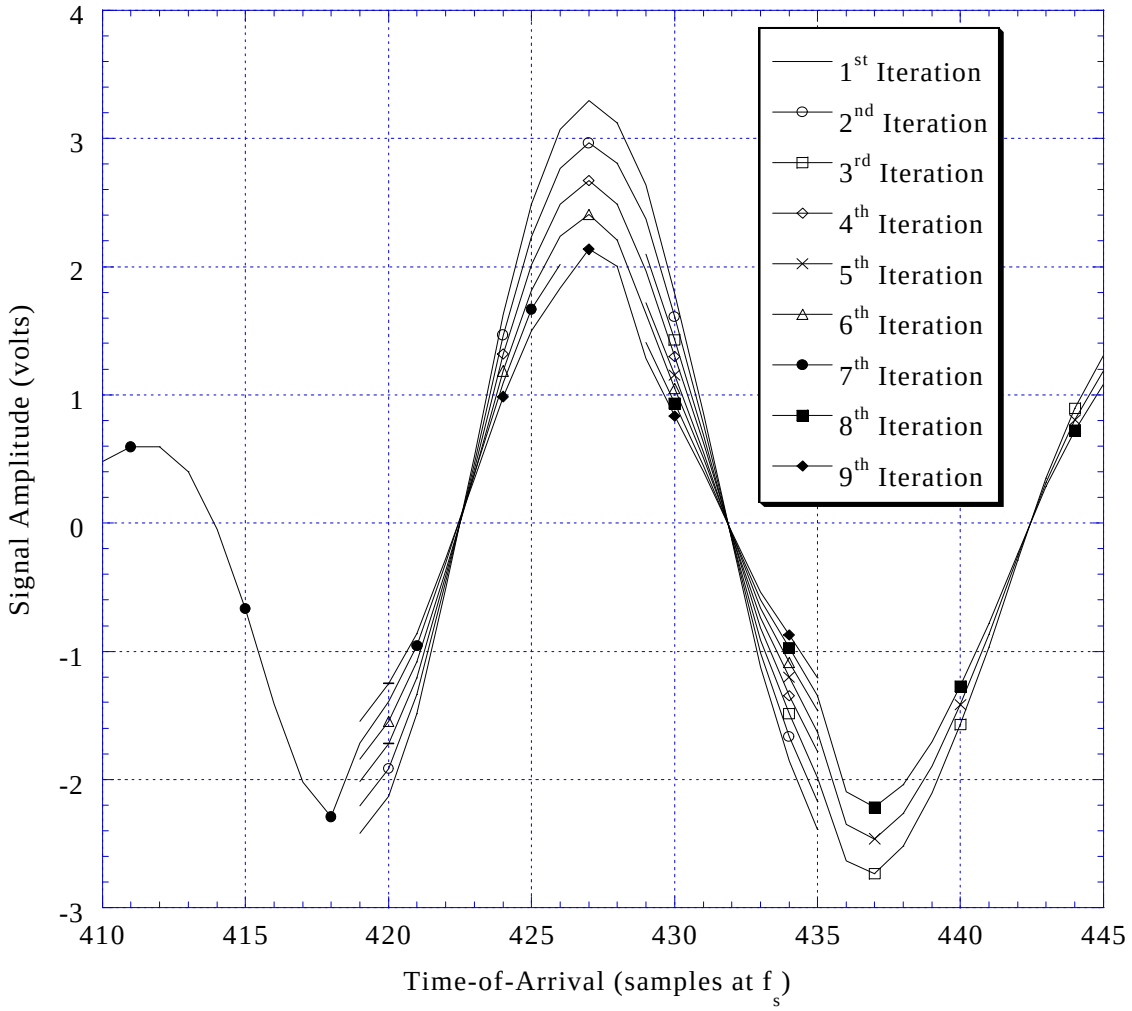

Figure 4-8: Sensor-CLEAN algorithm operating on the measured data from location P with $\gamma = 0.10$ and a relaxation window of ± 8 samples.

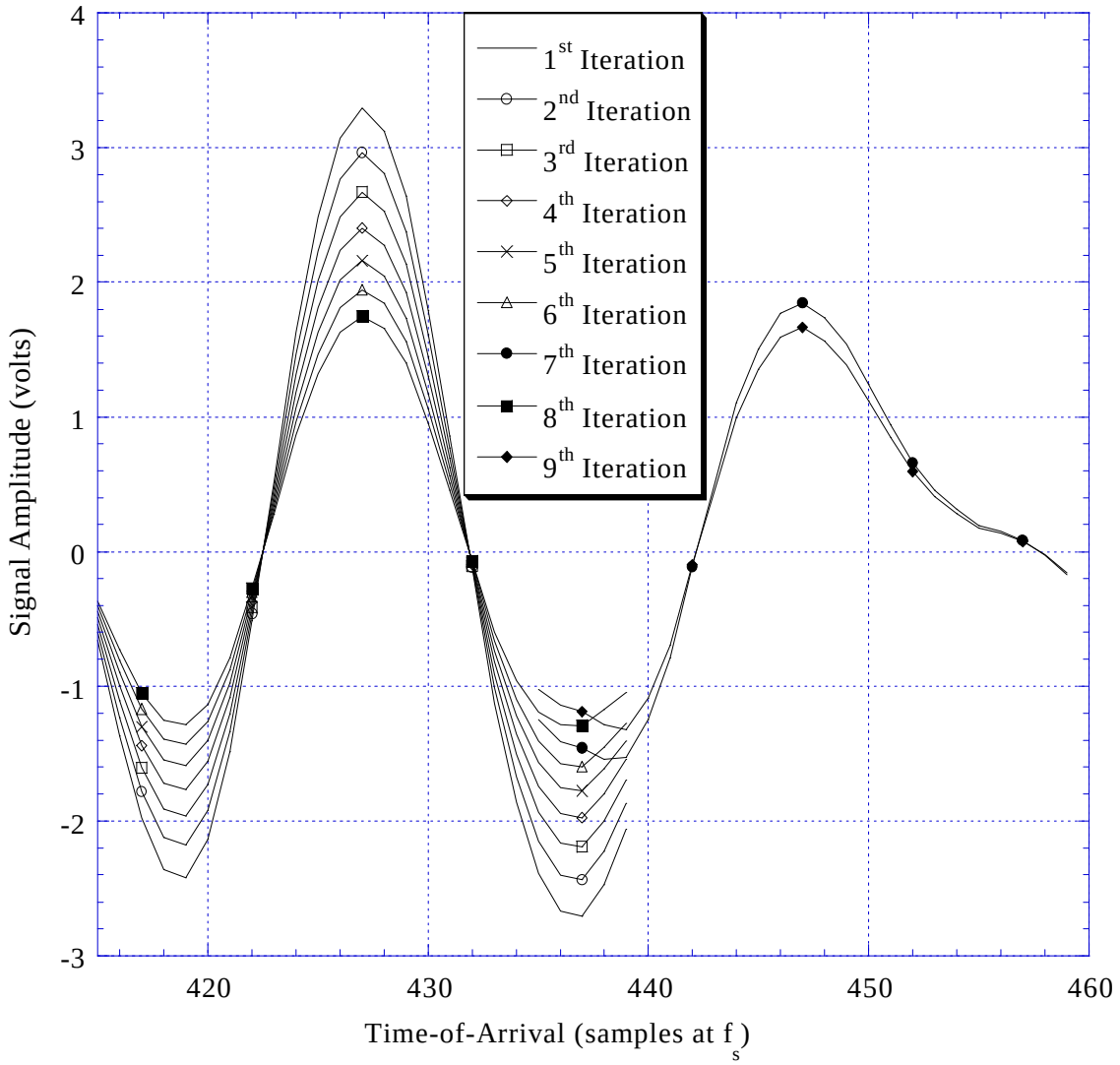

Figure 4-9: Sensor-CLEAN algorithm operating on the measured data from location P with $\gamma = 0.10$ and a relaxation window of ± 12 samples.

samples around the peak, provides the most accurate estimate, but at the largest computational cost, as more iterations will be required to reduce the residuals to the threshold level. Because it is the most sensitive of the windows, it is also subject to the generation of artifacts, or multiple detections of the same signal. The largest window, ± 12 samples around the peak, provides a more coarse result, and may miss closely spaced signals. It is less likely that this window will generate artifacts, however, because it is wide enough to span the duration of most incident signals. The window which is set at ± 8 samples around the peak provides middle ground between the other two windows. The idea is then to combine the outputs of these parallel runs to achieve a more accurate result than any single run could provide. The algorithm which accomplished is called the Arrival Combiner, and is introduced in the next chapter.

For this technique of fixed windows, little difference was noted between the performance of the algorithm with $\gamma = 0.10$ and with $\gamma = 0.07$, so in the interest of computation time, the larger value was used for the processing of all measured data.

Chapter 5

Further Post-Processing and Algorithm Verification

5.1 Arrival Combining Algorithm and Occurrence Thresholds

Since the precise shape and duration of the received signals is not available a-priori, and due to the potential for dynamics in these signals, it may be that a single set of parameters in the processing algorithms does not describe all of the received signals equally well. The Sensor-CLEAN algorithm and the Wave-Map post-processing algorithm were therefore run multiple times with different window sizes and beamwidths, to better match the processing to the expected variations in the received signals. The algorithm developed in this work to combine the results of the different processing paths is called the Arrival Combiner, and is shown below in Figure 5-1.

Under an assumption that the smallest windows won't miss too many signals, the main goal here is to discriminate between actual signals and false detections due to a signal artifact or noise. An artifact is generally due to multiple detections of the same signal that are not subsequently recombined in the Wave-Map algorithm. The criterion that is applied here is to demand that a potential signal appear in some number of the parallel processing paths,

corresponding to different Sensor-CLEAN and Wave-Map parameters, prior to declaring it a valid signal. The threshold number of occurrences is determined for each location in the building at which measurements were made. This processing reduces the number of false alarms or random detections due to noise, as well as the number of signal artifacts which are detected as independent arrivals, since it is likely that the artifacts at the Wave-Map output from different time windows and beamwidths will appear at different locations in time and angle. Thus it is more likely that only actual signals are identified at the output of the Arrival Combiner. In addition to the signal arrival location in time and in angle, the amplitude and waveform shape are also recovered by the Arrival Combiner.

For the remainder of the data processing and the results reported herein, the beamformer output is reported at 1° increments, and the following nineteen elevations angles were used: 90°, 88°, 86°, 84°, 82°, 80°, 78°, 76°, 74°, 72°, 70°, 65°, 60°, 55°, 50°, 45°, 40°, 30°, 20°. The three Sensor-CLEAN relaxation windows of $T_p = \pm 6$ samples, $T_p = \pm 8$ samples and $T_p = \pm 12$ samples were used, with $\gamma = 0.10$ and a detection threshold of 0.104 volts. Three resolution windows were also used in the Wave-Map algorithm. The angular resolution of each window was fixed at Θ_w=16°, and time resolution windows of $T_w = \pm 16$ samples, $T_w = \pm 20$ samples and $T_w = \pm 24$ samples were used. Due to computational constraints, it was necessary to limit the Wave-Map processing to three resolution windows, and these parameters seemed to provide the best estimates of the signal information. Further, three re-estimation windows were used as a final step in the Wave-Map algorithm. Thus, prior to re-estimation, nine sets of signal location information were generated, and following re-estimation there were 27 sets of data. These multiple re-estimation windows are used primarily to increase the accuracy of the estimates, but also to further mitigate the detection of signal artifacts. If a detection that does not correspond to a true signal occurs, the detection location might not be stable as a function of the re-estimation window size. This

is again the property exploited by the Arrival Combiner routine to reduce the probability that artifacts or noise is identified as signals.

The occurrence threshold, or the number of times which a potential signal must appear in the output of the Arrival Combiner in order to be recognized as a valid signal is selected as follows. First, the original measurement data from each sensor is retrieved and the total received energy is determined. The original measured response at each sensor is used to generate the received energy since it represents the actual data from which the signal information was derived, prior to any manipulations or modifications. This establishes an upper limit on the signal energy which can be recovered from the Wave-Map outputs, and the occurrence threshold must be set high enough that multiple detections of a signal, at slightly different locations, do not occur. The calculation of the received energy also includes the noise, which can be estimated for each measurement location based on the noise floor present in the received data prior to the arrival of the first UWB signal. The recovered signal waveforms from the Wave-Map outputs and the corresponding locations in time and angle are used to reconstruct the measured sensor data, under the assumptions that the incident signal wavefront is planar and the same signal is received at each sensor, or that no shadowing of the measurement array occurs. The occurrence threshold is then selected so that this recovered signal energy is as close to the original received signal energy as possible, without exceeding it, while allowing for the contribution of the noise.

Estimating the noise variance in each of the measurement locations from the sample variance of the data prior to the arrival of the first signal, the results are summarized below in Table 5.1. It is seen from the table that the noise power can vary significantly in different measurement locations. In particular, the noise is largest in the northwest corner of the building, at locations A and E. Rooms A and E also correspond to two of the measurement

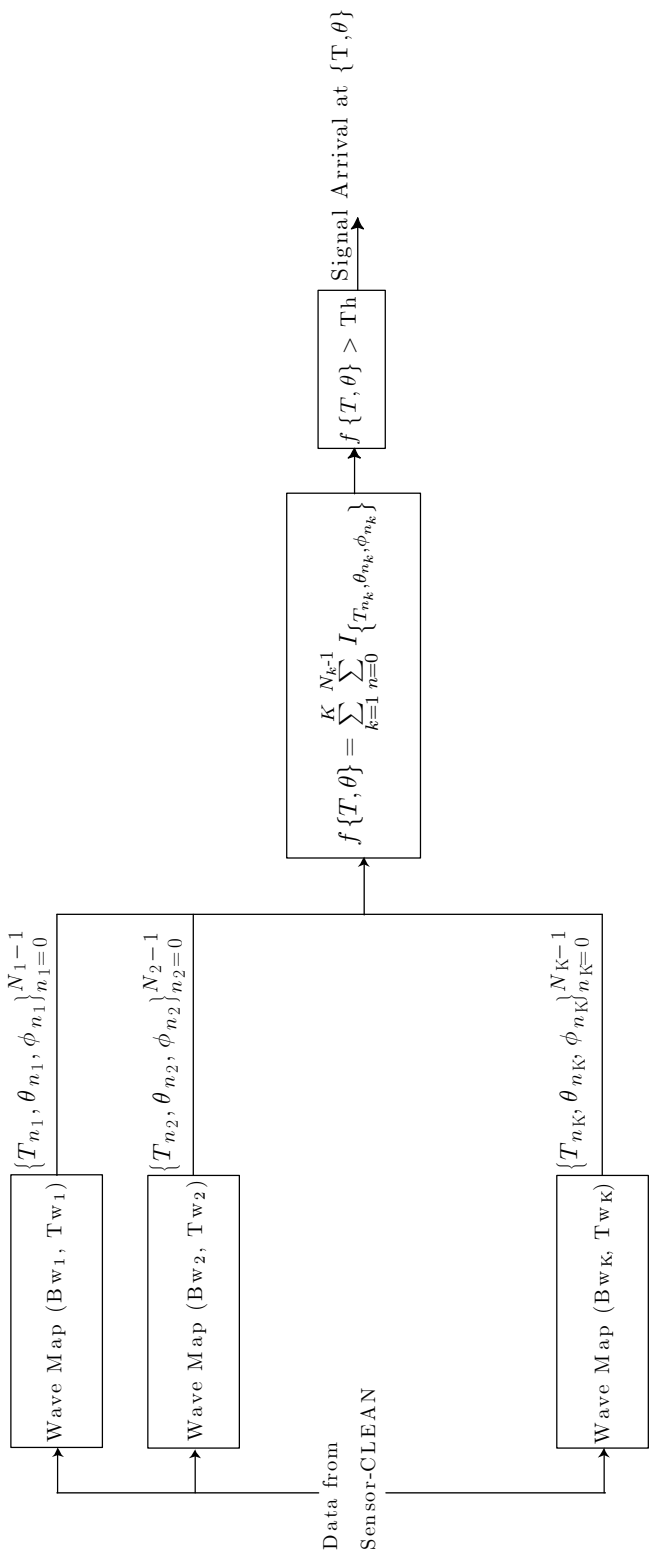

Figure 5-1: Algorithm for combining the outputs of Wave Maps run at different resolutions.

Measurement Location	Noise Variance (Volts^2)
P	2.9×10^{-6}
B	8.2×10^{-6}
F2	3.2×10^{-6}
H	2.8×10^{-6}
C	6.2×10^{-6}
F1	3.3×10^{-6}
L	2.7×10^{-6}
N	6.4×10^{-6}
A	1.2×10^{-5}
E	1.1×10^{-5}
M	4.0×10^{-7}
R	-
T	3.9×10^{-7}
U	4.7×10^{-6}
W	1.1×10^{-6}

Table 5.1: Estimated noise variance at each measurement location

locations that are most distant from the transmitter. This is reflected in the quality of the received UWB signals estimates, as discussed in the next chapter.

The noise power as a function of the location is shown in Figure 5-2, where a bubble with area proportional to the noise variance is shown at the point where the measurement was made, relative to the transmitter location at the origin.

The occurrence threshold was set so that the recovered signal energy plus the noise energy reported above was as close to the received signal energy, as defined above, without exceeding it. Because of the variation in signal and noise energy from location to location, a unique threshold is defined for each set of measurements. The occurrence thresholds and the resulting recovered signal energy for some example measurement locations are shown in Figure 5-3 - Figure 5-7. Note that thresholds can be defined for both results prior to and following re-estimation of the signal parameters. The remainder of this work will proceed using re-estimated signal information, as it provides better estimates of the actual received signal energy.

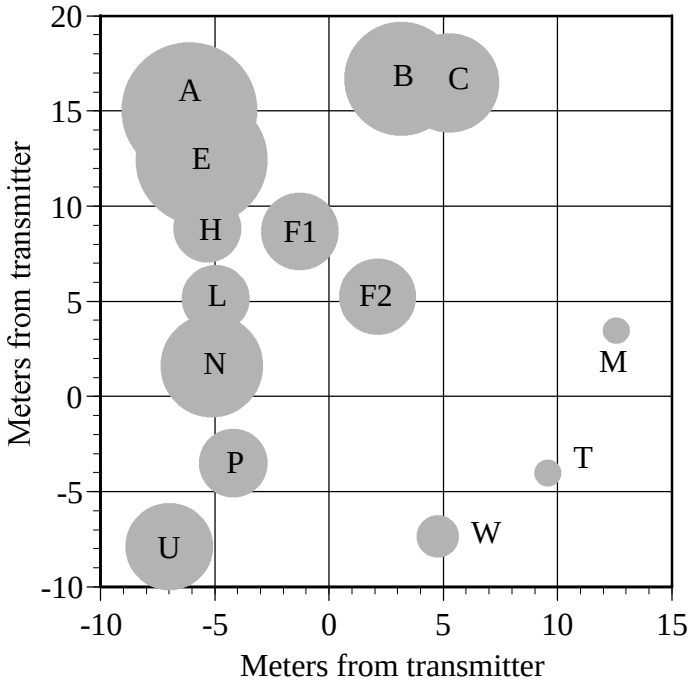

Figure 5-2: Estimated noise variance at measurement locations. Variance is proportional to area of the bubble.

For the re-estimated data, it is noted from the figures that the recovered signal energy is almost a piecewise linear function of the threshold, with steps in the recovered signal energy occurring at multiples of three in the threshold. This is because of the three resolution windows and hence three sets of re-estimated data which are generated by each run of the Wave-Map software.

Considering the figures, the low SNR cases result in the recovery of a smaller percentage of the received energy. This is due partly to the fact that the amplitude of the signal components are not as far above the noise as in some of the higher SNR cases. Sensor-CLEAN operates here to a common threshold across the measurements from all locations. Fewer iterations of the algorithm are required to reach the noise floor, and thus less of the signal energy is identified and recovered from the composite signal. It is also due in part to

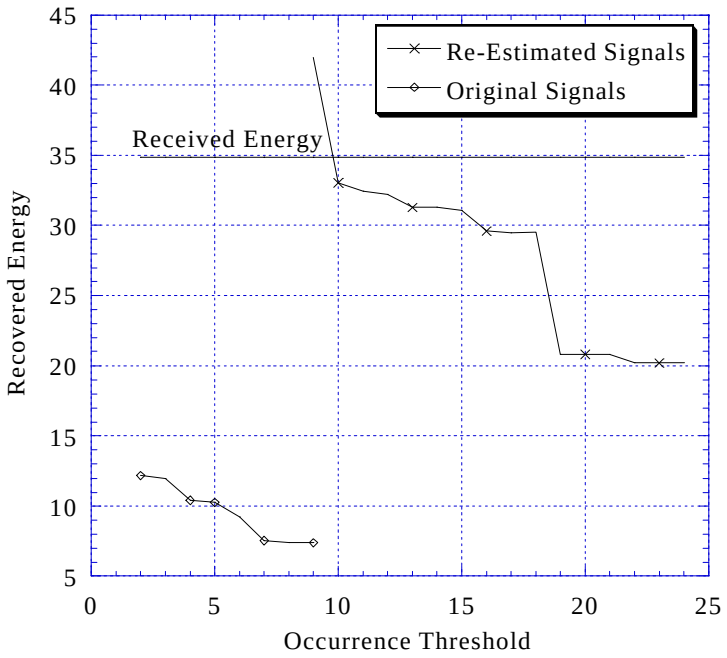

Figure 5-3: Recovered signal energy vs. occurrence threshold for location P.

the fact that the received energy represents the signal plus noise, and the recovered signal energy in a low SNR case represents a smaller fraction of this quantity.

Based on the calculated received signal energy and recovered signal energy, the thresholds chosen for the data processing are shown in Table 5.2. The signals recovered at the output of the Arrival Combiner, run with the thresholds in the table, will be used to generate UWB channel models in the next chapter.

5.2 Final Verification of the Algorithm Performance

Upon implementation of the Arrival Combiner, a final verification of the end-to-end performance of the UWB signal detection and estimation algorithms developed herein was executed. For this test, one hundred signals were generated over 125 ns in time, with a

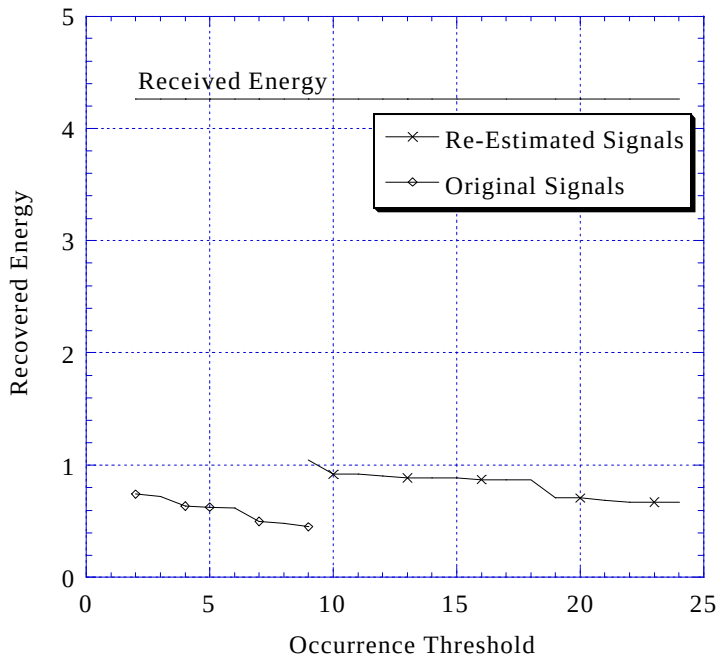

Figure 5-4: Recovered signal energy vs. occurrence threshold for location B.

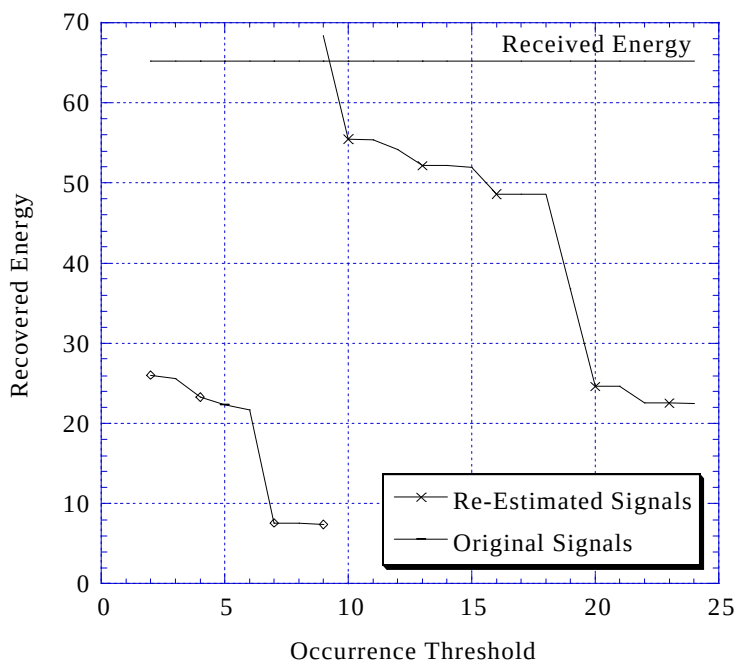

Figure 5-5: Recovered signal energy vs. occurrence threshold for location F2.

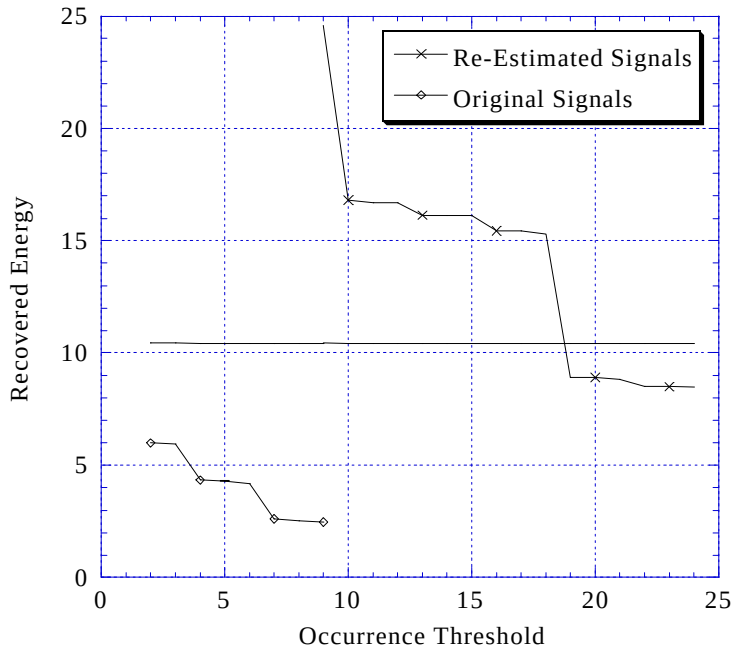

Figure 5-6: Recovered signal energy vs. occurrence threshold for location U.

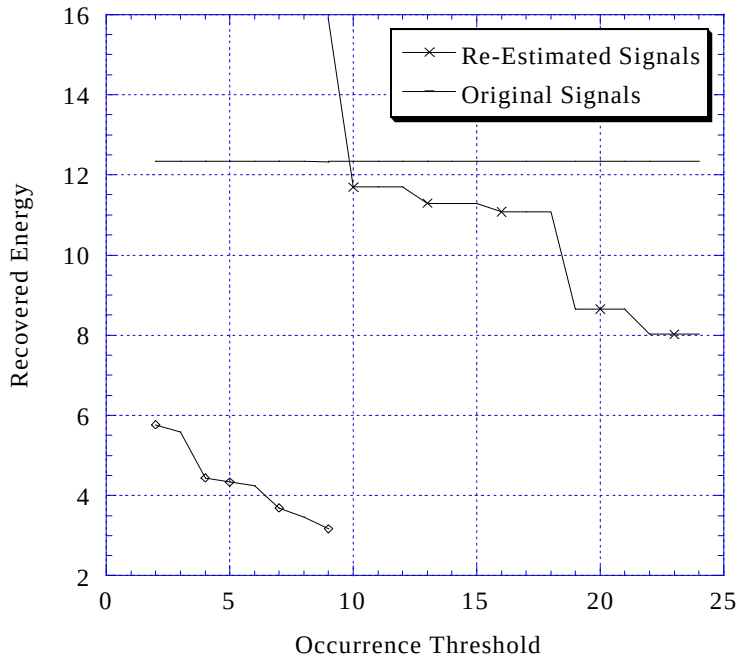

Figure 5-7: Recovered signal energy vs. occurrence threshold for location W.

Location	Threshold	Received Energy	Recovered Energy	# of Signals
P	16	34.85	29.62	430
B	16	4.26	0.88	181
F2	16	65.13	48.59	445
H	16	12.57	10.53	265
C	16	3.02	0.51	140
F1	16	57.63	44.18	309
L	15	33.19	23.59	310
N	15	30.52	14.29	364
A	16	3.88	0.48	228
E	15	4.75	1.37	223
M	16	5.45	2.20	142
T	16	7.96	5.28	283
U	19	10.42	8.91	272
W	16	12.33	11.09	351

Table 5.2: Occurence thresholds selected for data processing.

noise standard deviation of 0.05 volts. The amplitude of the impulses was distributed uniformly from a maximum value of 1 volt to a minimum of 0.1 volt. The generated waveforms were Gaussian, as in equation (1.2), first-derivative Gaussian, as in equation (1.3), and second-derivative Gaussian as in equation (1.4), all with a width parameter of τ_m=0.8 ns. Define the signal-to-noise ratio as

$$SNR = 10 \log \frac{\sum_{n=0}^{N-1} s^2(n)}{\sigma^2} \quad dB \tag{5.1}$$

where $s(n)$ represents the impulse waveform and NT_s is the support in time of the impulse, for a sampling interval of T_s seconds. This gives a peak SNR of approximately 26 dB for a second-derivative Gaussian pulse. The location of the impulses was restricted so that no two impulses fell within 0.8 ns and 16° of each other. The elevation angles are biased, so that the bulk of the signals are incident from between 70° and 90°. After processing by the front-end Sensor-CLEAN algorithm, the Wave-Map program and the Arrival Combiner, the

recovered signals are shown for re-estimated data in Figure 5-8 as scatter plots with the actual signal locations, for occurrence thresholds of 12 and 15.

Further studies were accomplished to demonstrate the stability of the processing algorithm, in the sense that the results depend somewhat continuously on the algorithm parameters. The main result is that the recovered signals do not change significantly when the occurrence thresholds are increased. A decrease in the occurrence thresholds can cause the recovered signal energy to exceed the received energy.

As was stated in the Chapter 1, this research project consists of two main parts. The first is to develop appropriate techniques for processing UWB signals incident on an array sensors, in order to determine such parameters as the time-of-arrival, the angle-of-arrival and an estimate of the waveform for each detected signal. The processing chain consisting of the Sensor-CLEAN algorithm, the Wave-Map algorithm and the Arrival Combiner accomplishes this goal. What remains is the application of these techniques to the measured data described earlier, resulting in a model for the propagation of UWB signals in an indoor environment. This is the subject of the next two chapters.

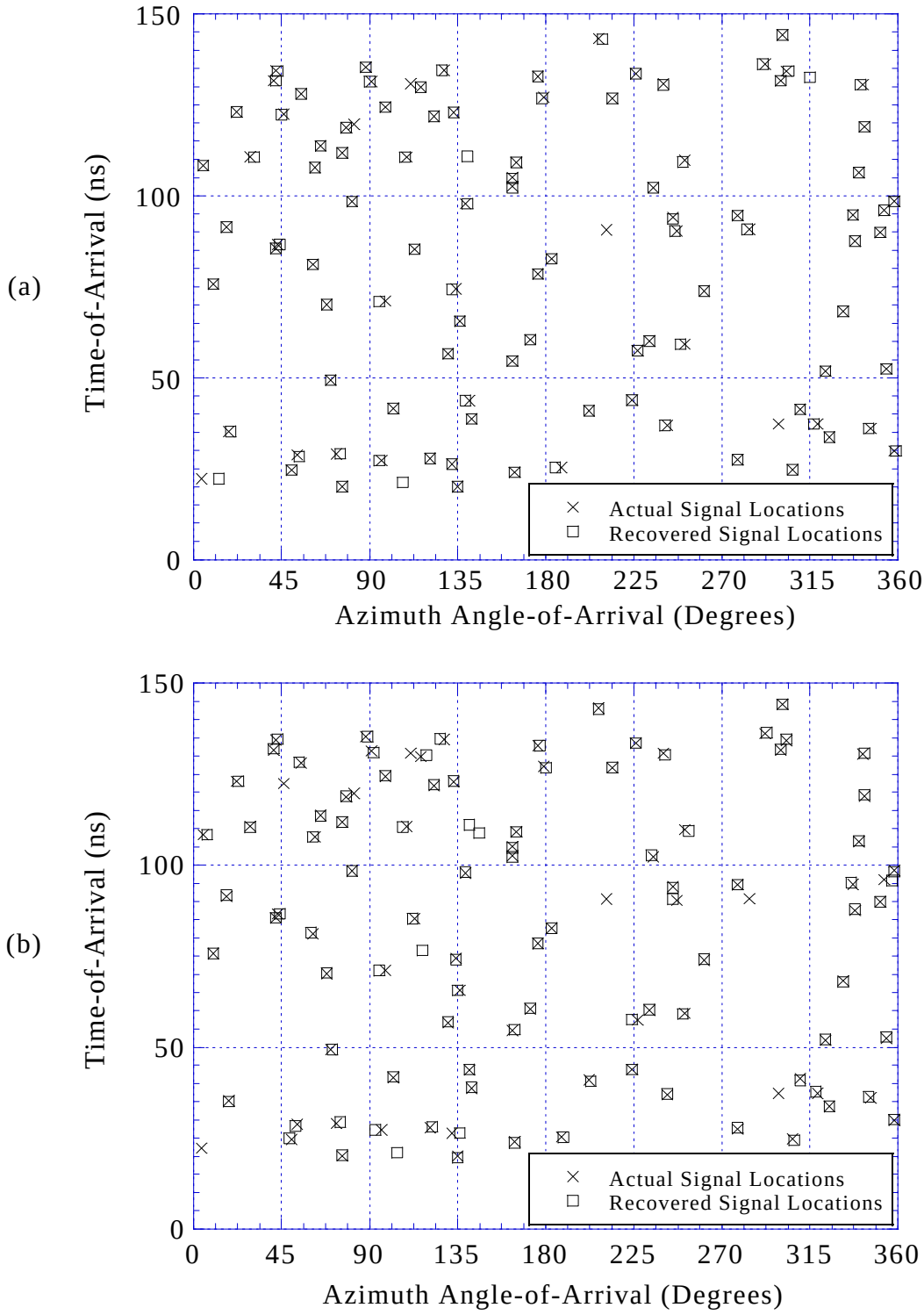

Figure 5-8: Output of the processing algorithm on input of 100 signals, for an occurrence threshold of (a) 12 and (b) 15.

Chapter 6

Channel Models for Ultra-Wideband Signal Propagation

6.1 Introduction, Verification and Preliminary Results

In previous chapters, algorithms were developed for processing UWB signals received on an array of sensors. In this chapter these techniques are applied to measured propagation data. The goal of this effort is to develop models by which quantitative comparisons of the UWB channel with more narrowband indoor propagation results [15], [29], [35], [49] can be made and the performance of UWB communication systems can be predicted. Given the large fractional bandwidth of the signals employed here, it is of interest to determine whether the above narrowband models are sufficient to describe the propagation of UWB signals or whether fundamental differences exist. Based on these results, channel models for UWB signal propagation in an indoor environment are proposed. A secondary goal is to use the output of the processing algorithms to study the effects of propagation on the transmitted UWB signals.

As a preliminary verification of the performance of the processing algorithms, consider the floor plan of the building in which the experiment was conducted, shown in Figure

6-1, with the location of the detected direct path or line-of-sight signal for each set of measurements indicated by an $\times$. Also shown is the reported location of the measurements [64], [66], indicated by the squares. This demonstrates some measure of consistency between the results and the realities of the measurement scenario. It should be noted that the reported measurement locations indicated on the floor plan are approximate, and therefore the comparison is not expected to be precise. The recovered measurement locations were determined by the time-of-arrival and azimuth angle-of-arrival of the first incident signal in time recovered by the algorithms. The corresponding direct path length was calculated according to

$$d_{LOS} = (n_1 - n_d) / f_s \times c + 1 \text{ meters} \tag{6.1}$$

where n_1 is the sample at which the first signal arrives, $n_d = 122$ is the known propagation delay in samples at a 1 meter separation between the transmitter and the receiver and c is the speed of light. With the exception of the result at location A in the building, the calculated measurement locations seem to correlate reasonably well with the floor plan. At location A, the received direct path signal has the lowest amplitude out of all of the measurement locations, and, from Figure 5-2, the noise variance is greatest in this room. These effects combine to introduce a bias into the calculated angle of arrival, although the recovered path length is reasonable. The recovered direct path distance, azimuth angle-of-arrival (AOA), and elevation angle-of-arrival are summarized in Table 6.1.

The recovered signal location and amplitude information is summarized graphically for a number of the measurement locations in the form of three-dimensional scatter plots in Figure 6-2 through Figure 6-10. In these diagrams, the location of the recovered signal in time and azimuth angle is given in the plane, and the height of the line is proportional to the amplitude of the recovered signal. Dependence on the elevation angle has been integrated

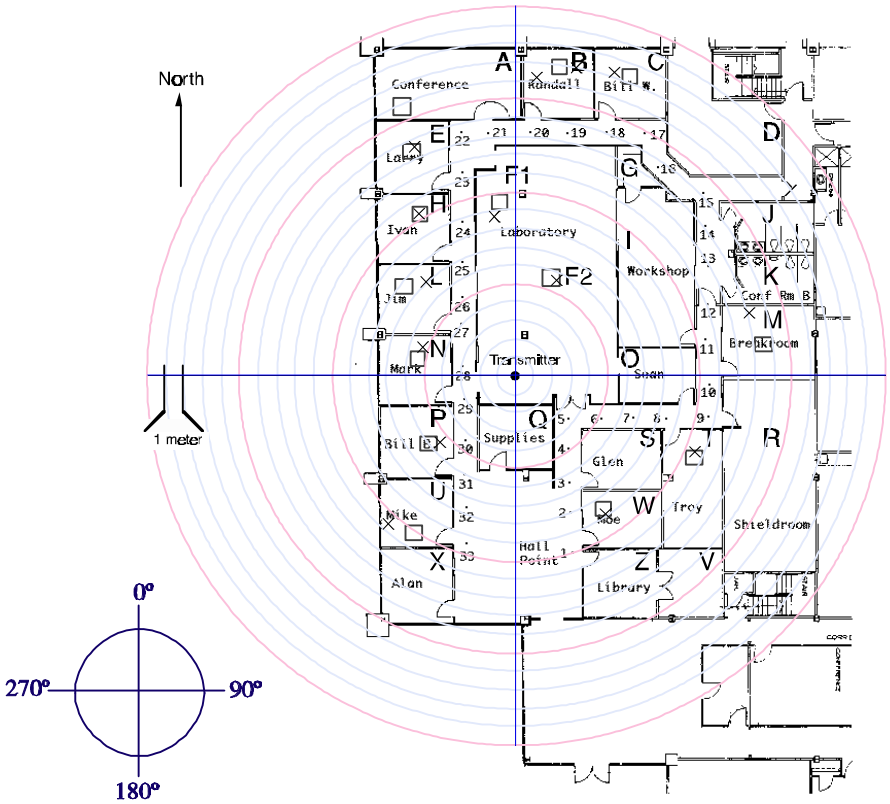

Figure 6-1: Calculated locations of the measurement sites.

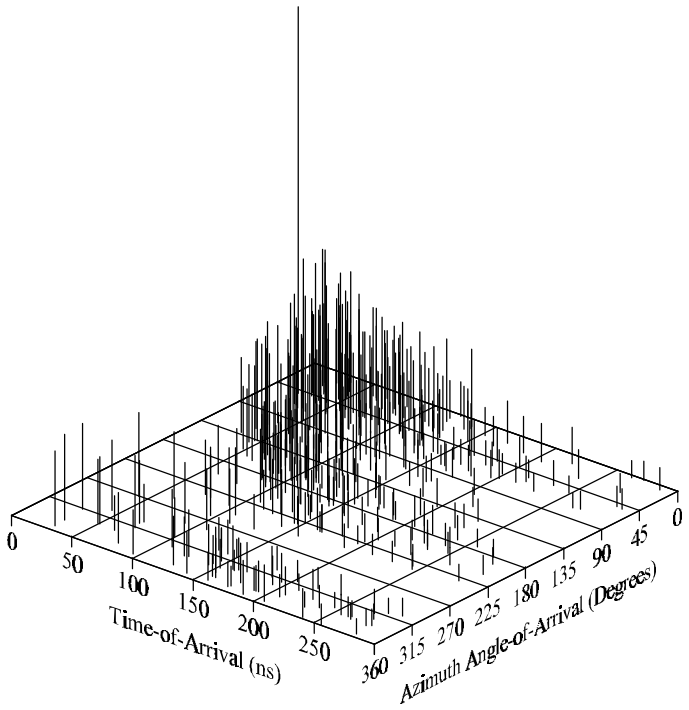

Figure 6-2: Recovered signal location and amplitude information at location P.

out. Several items are of note in these plots. First, in most of the figures, the existence of clusters of arrivals can be seen, some locations exhibiting a stronger effect than others. These are in general determined by the large scale building structure; features such as the walls, doors and hallways. Propagation models based on the statistics of these clusters of arrivals will be discussed below. Second, in most of the cases a dominant path arrives fairly early in the response, but not always as the direct path signal or first arrival in time.

The plots above represent the recovered signal location and amplitude. Signal waveform information was also recovered, and in particular, the direct path waveform recovered at each of the measurement locations was recorded. This gives some insight into the effect of this indoor propagation channel on the transmitted UWB waveforms. For comparison purposes, consider first the signal recorded at a 1 meter separation between the transmitter

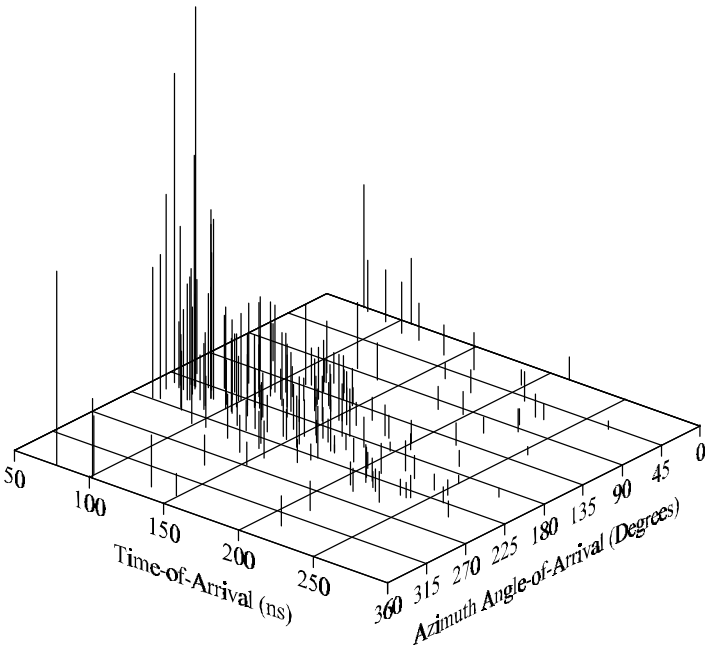

Figure 6-3: Recovered signal location and amplitude information at location B.

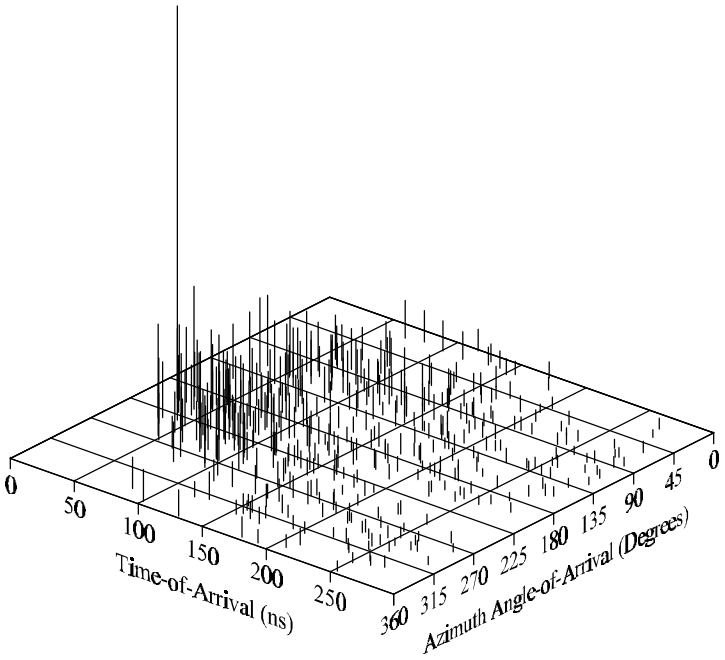

Figure 6-4: Recovered signal location and amplitude information at location F2.

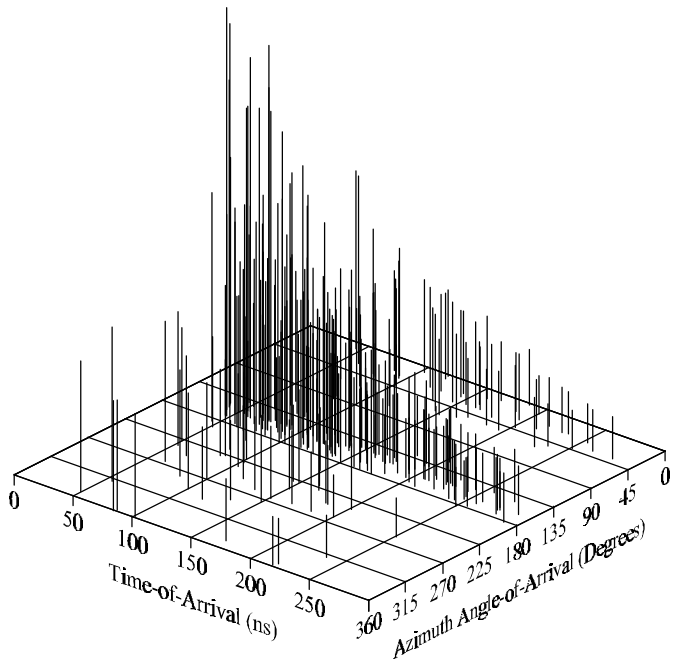

Figure 6-5: Recovered signal location and amplitude information at location H.

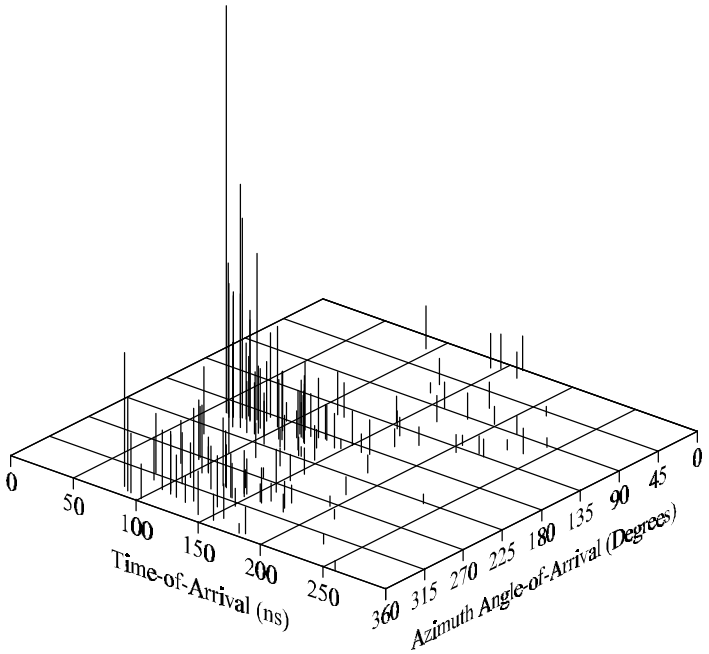

Figure 6-6: Recovered signal location and amplitude information at location C.

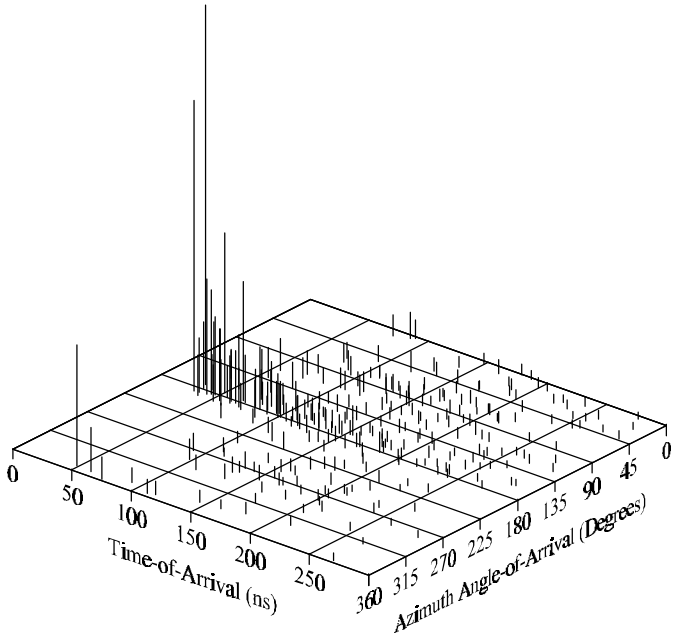

Figure 6-7: Recovered signal location and amplitude information at location F1.

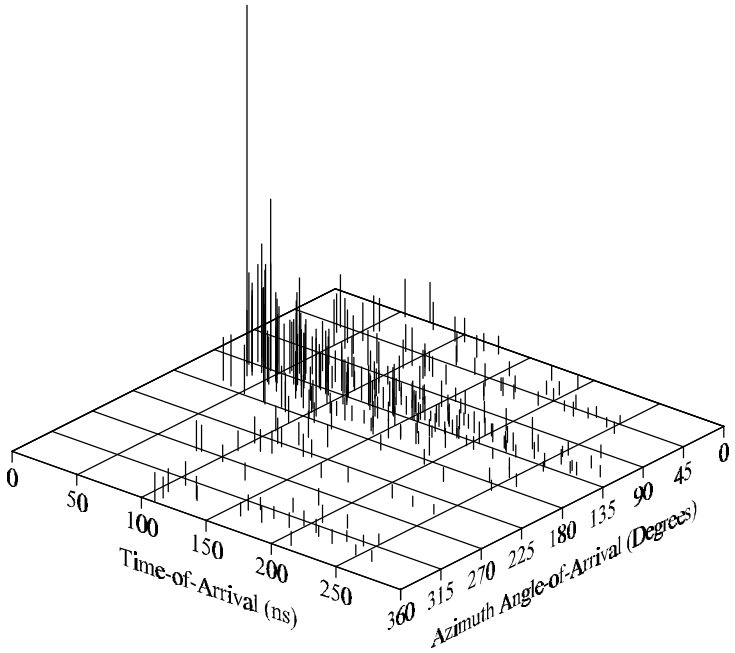

Figure 6-8: Recovered signal location and amplitude information at location L.

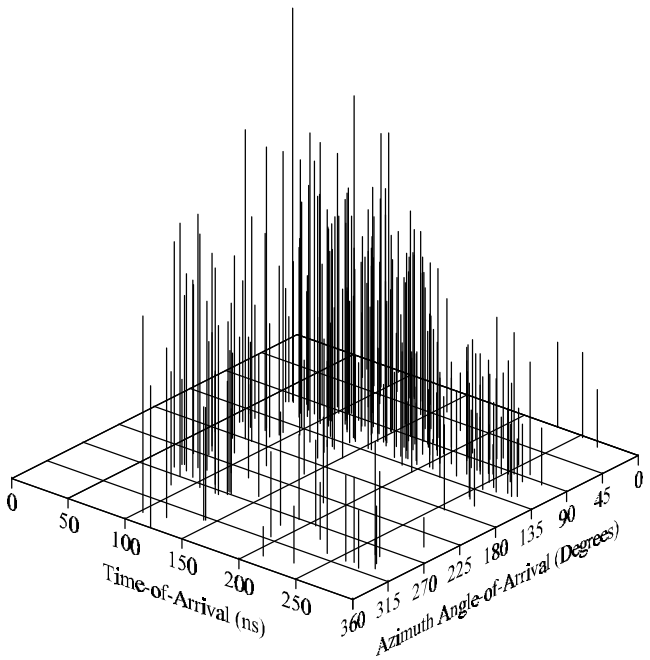

Figure 6-9: Recovered signal location and amplitude information at location A.

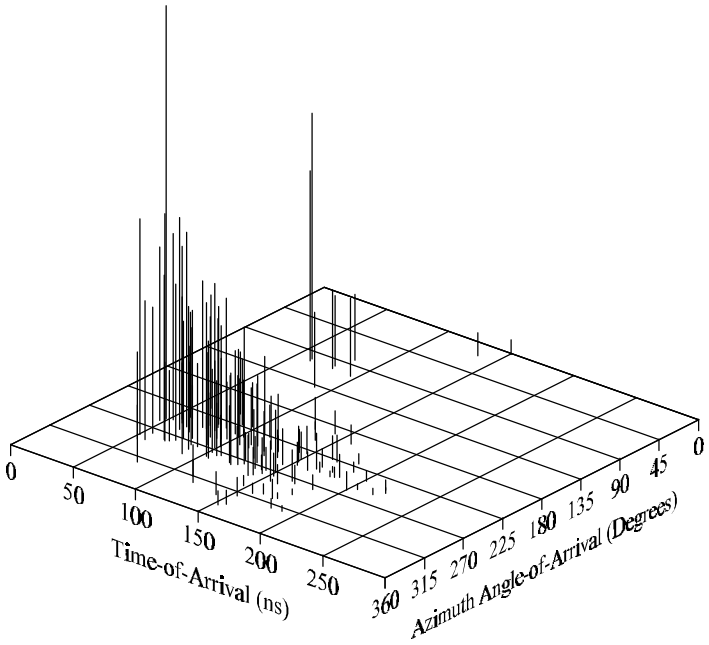

Figure 6-10: Recovered signal location and amplitude information at location M.

and the receiver, shown in Figure 6-11. This waveform is the average of three measurement taken 1 meter from the transmitter, at azimuth angles of 0°, 45° and 90°, with the reference angle as specified above in Figure 6-1.

Given the transmission of this signal and a detection threshold of 0.104 volts out of the beamformer, the direct path waveform recovered at each of the measurement locations in the building is shown below in 6-12 - Figure 6-27. This detection threshold was selected to give 30dB of dynamic range at Location P.

In regards to the recovered waveforms in Figure 6-12 - Figure 6-27, several points are of note. In the Arrival Combiner several different (time) resolution windows are applied to data at the output of the Sensor-CLEAN algorithm, to allow for received signals of different time widths to be processed. For a given signal detection, the combining algorithm selects the window which generates the largest amplitude signal to provide the waveform information. If two windows provide waveforms with equal amplitudes, then the algorithm selects the smallest time window, in order to maximize the time resolution and minimize the duplication of signal energy. This can result in several effects that are apparent the plots of the direct path signals. First, each of the waveform plots is actually two curves, corresponding to the waveform recovered in two different time windows. When a larger time window gives a more complete picture of the direct path signal, it is indicated by the signal with the dashed line in the plots. Again, if the goal of the algorithm was to estimate the direct path signal, then in these cases the larger time window would be used, but since the primary goal is a characterization of the multipath components, the smaller time window is used by the Arrival Combiner. In some cases, neither window recovers the leading edge of the waveform. This occurs when the signal is recovered in several distinct components, each of a particular time width. If the leading edge of a signal consist of a component that does not exceed the detection threshold, and is not included in the recovery of a component

which does exceed the threshold, then it will not be recovered. This effect is noted in Figure 6-13, Figure 6-15, Figure 6-17 and Figure 6-24, some of the lower amplitude direct path signals.

The third effect seen in the recovered direct path waveforms can occur when the direct path signal is not the largest signal, and a larger signal follows the direct path signal closely in time and in azimuth angle. The larger signal is detected first by the algorithm, and the energy in the tail of the waveform that might otherwise be assigned to the direct path signal is assigned to the larger, later signal. This is seen in Figure 6-15, and Figure 6-26.

At Location A and Location E, the amplitude of the direct path signal is comparable to that of the noise, and so the recovered signal shown in Figure 6-21 and Figure 6-22 is severely corrupted by the noise.

Defining the signal-to-noise ratio (SNR) as in the previous chapter by [12],

$$SNR_E = 10 \log \frac{\sum_{n=0}^{N-1} s^2(n)}{\sigma^2} \quad dB \tag{6.2}$$

where σ^2 represents the variance of the additive noise, given in Table 5.1, and $s(n)$ is the incident waveform, with support of N time samples, the SNR at each of the measurement locations is shown in Table 6.1. Note that this definition of the SNR corresponds to the ratio of the signal energy to the variance of the noise. An alternate definition might be the ratio of the power in the LOS signal to the noise variance, with the difference in the division of the numerator in equation 6.2 by the duration, or samples in the waveform. This measure is denoted SNR_P in Table 6.1. Although these two measures will given very different absolute results, the relative results, from measurement location to measurement location are fairly consistent; the SNR_E values presented in the table span a range of 49.17 dB and the SNR_P span a range of 45.27 dB. An explicit dependence of the results in this

Location	LOS Path (m.)	AOA (^{o})	Amp. (volts)	SNR_E (dB)	SNR_P (dB)
P	5.47	49	3.29	42.14	27.21
B	16.92	191	0.53	20.69	5.13
F2	5.61	203	7.44	48.35	33.20
H	10.20	149	0.72	27.12	13.93
C	17.23	198	0.59	24.11	9.32
F1	8.68	172	8.46	48.86	33.70
L	7.04	136	5.03	46.13	31.41
N	5.29	107	2.47	35.99	20.47
A	16.13	184	0.12	-0.31	-11.57
E	13.54	156	0.13	2.018	-9.14
M	13.07	255	0.50	33.05	18.57
T	10.48	293	0.35	29.98	14.89
U	10.57	41	0.65	24.47	9.21
W	8.87	327	0.73	33.87	18.40

Table 6.1: Recovered direct path information

chapter on the SNR is not derived, so further discussion on the applicability of SNR_E or SNR_P to the characterization of the UWB propagation channel will not be undertaken.

6.2 Ultra-Wideband Channel Models

This section derives channel models for indoor UWB signal propagation which can be compared to similar measures for more narrowband channels. The models derived in this section are static, in the sense that the distribution of the received signal energy as a function of time is independent of the statistics of the received signal energy versus the angle-of-arrival. In a later section, this assumption will be removed and the joint time-of-arrival and angle-of-arrival statistics of the propagation channel will be examined.

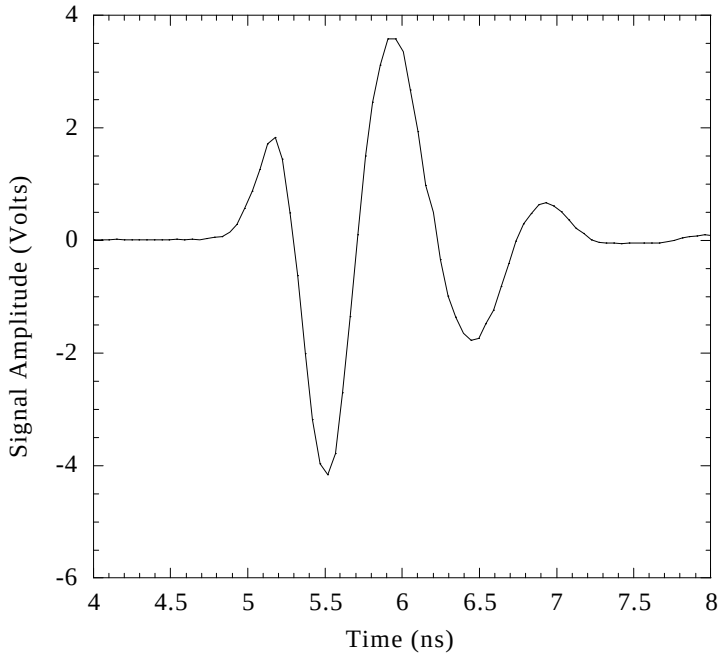

Figure 6-11: Received signal at a 1 meter separation between transmitter and receiver.

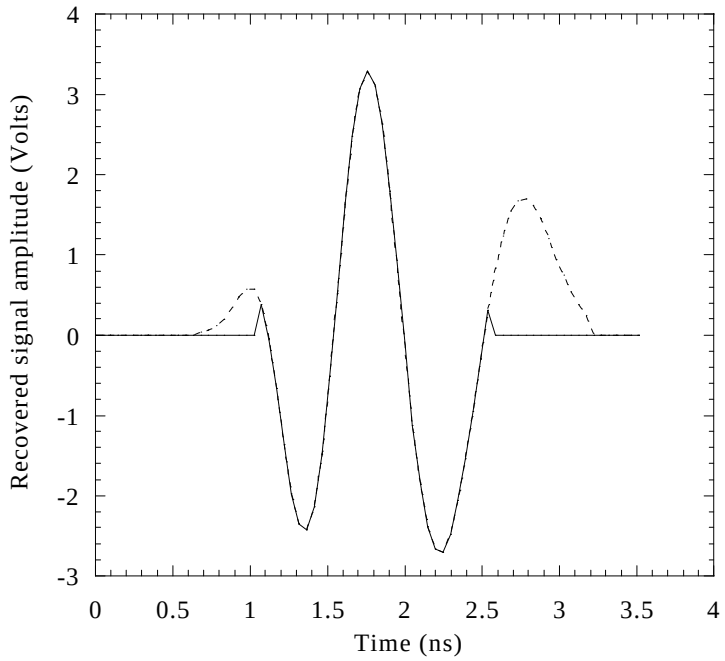

Figure 6-12: Recovered direct path waveform at location P.

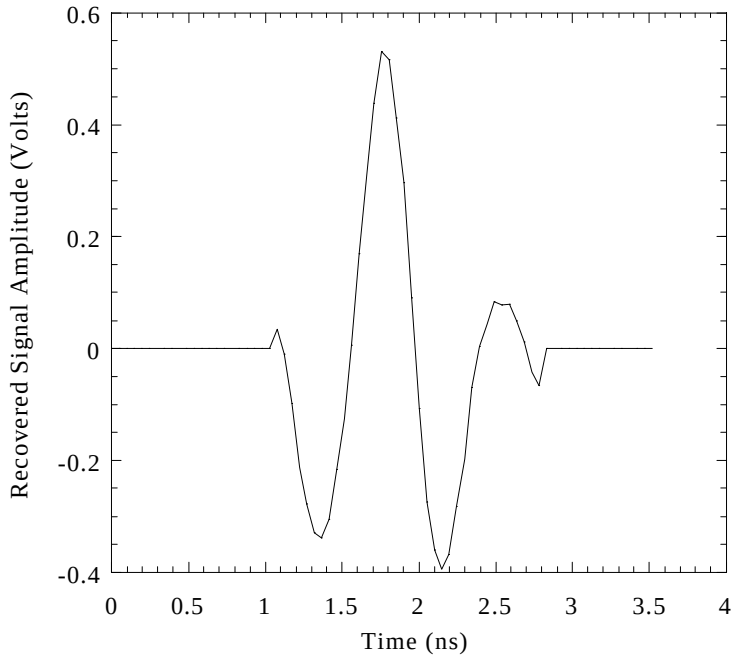

Figure 6-13: Recovered direct path waveform at location B.

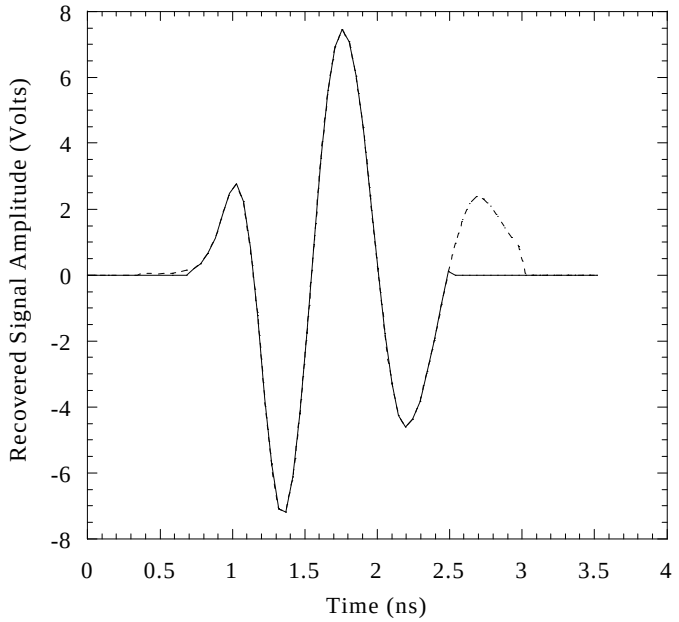

Figure 6-14: Recovered direct path waveform at location F2.

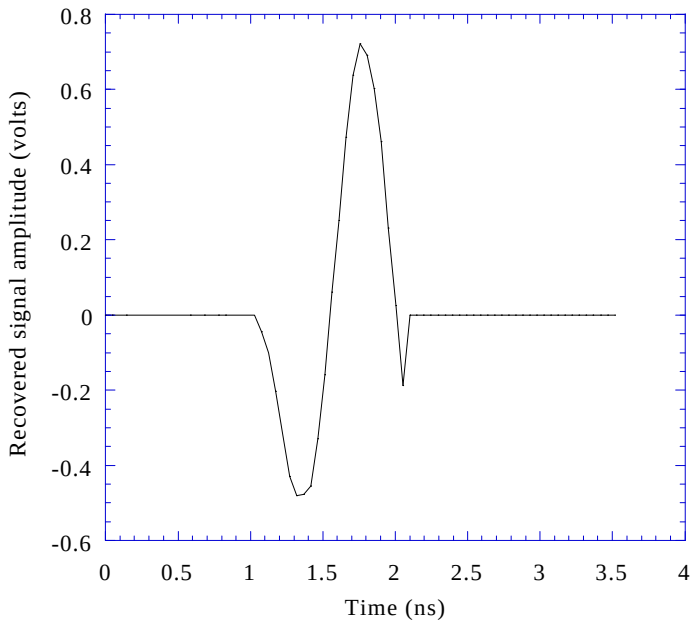

Figure 6-15: Recovered direct path waveform at location H

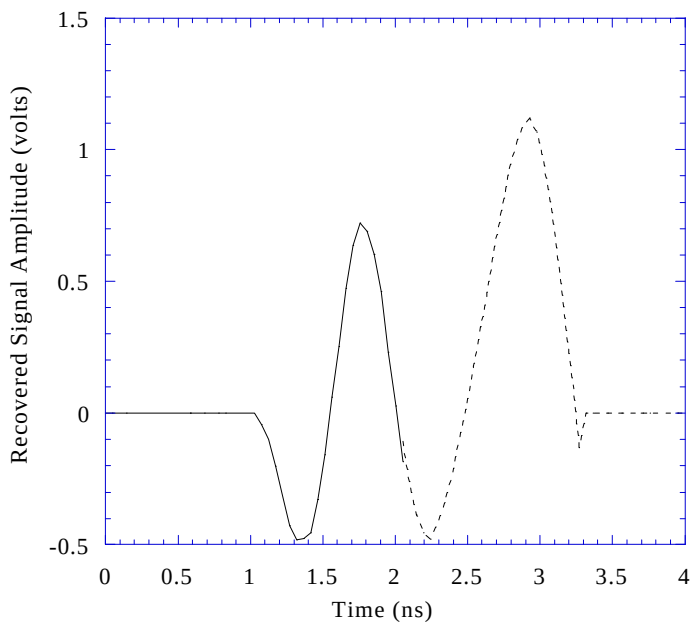

Figure 6-16: Direct path waveform at location H followed by a larger signal that is detected first.

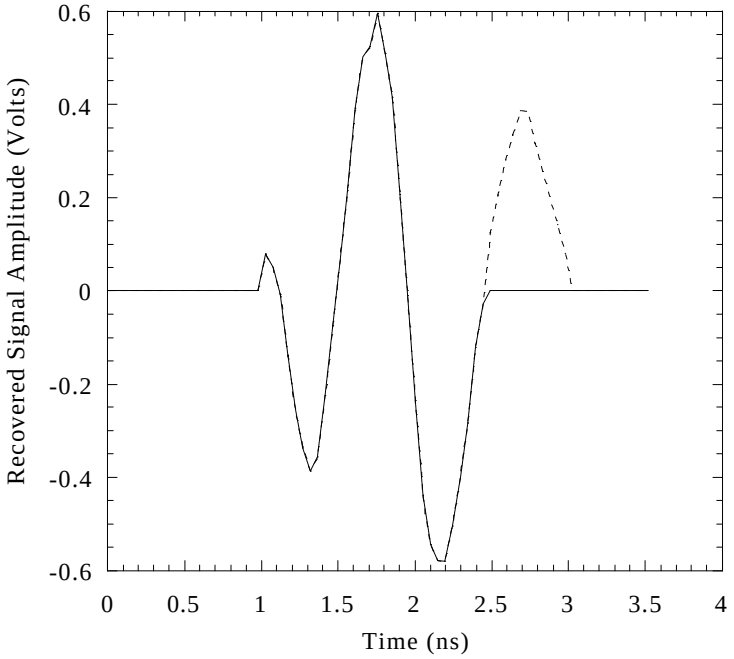

Figure 6-17: Recovered direct path waveform at location C

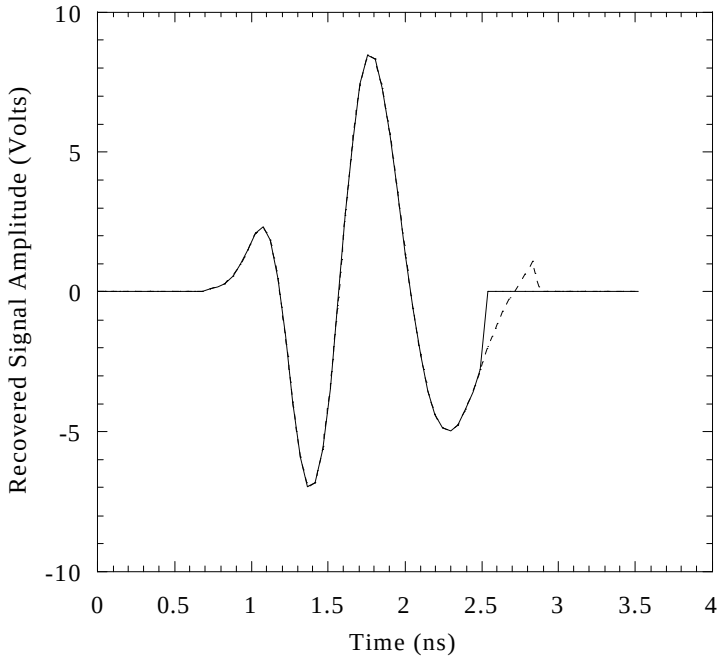

Figure 6-18: Recovered direct path waveform at location F1

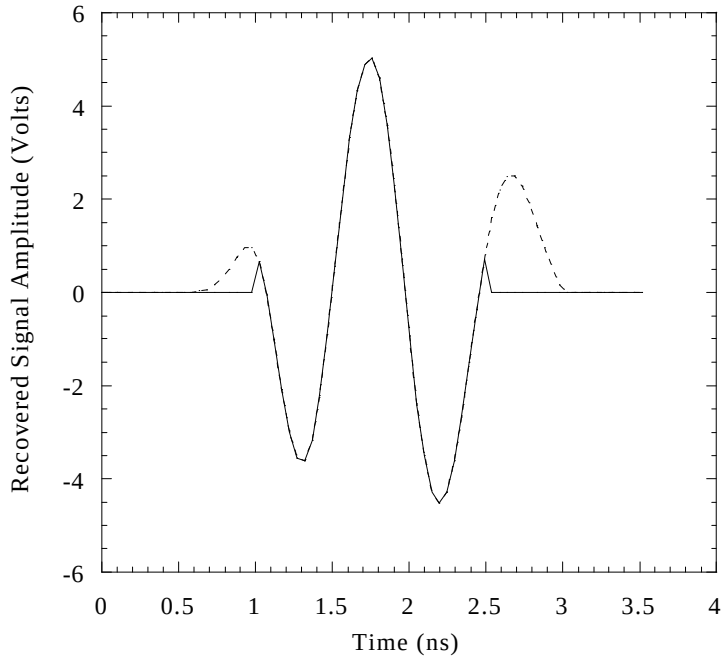

Figure 6-19: Recovered direct path waveform at location L.

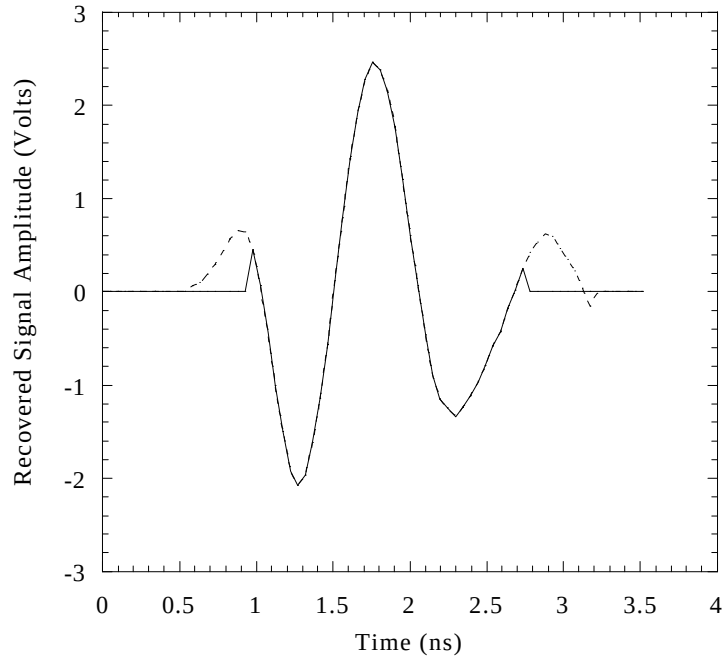

Figure 6-20: Recovered direct path waveform at location N.

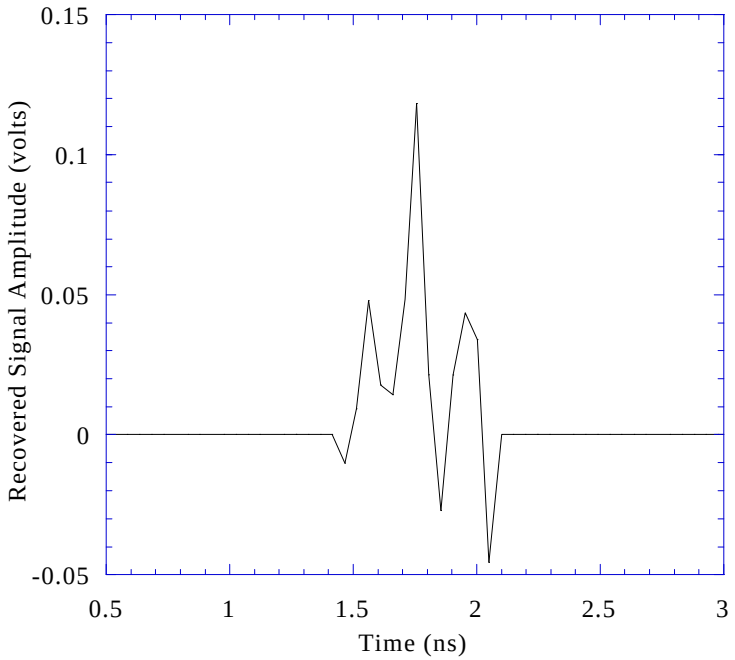

Figure 6-21: Recovered direct path waveform at location A.

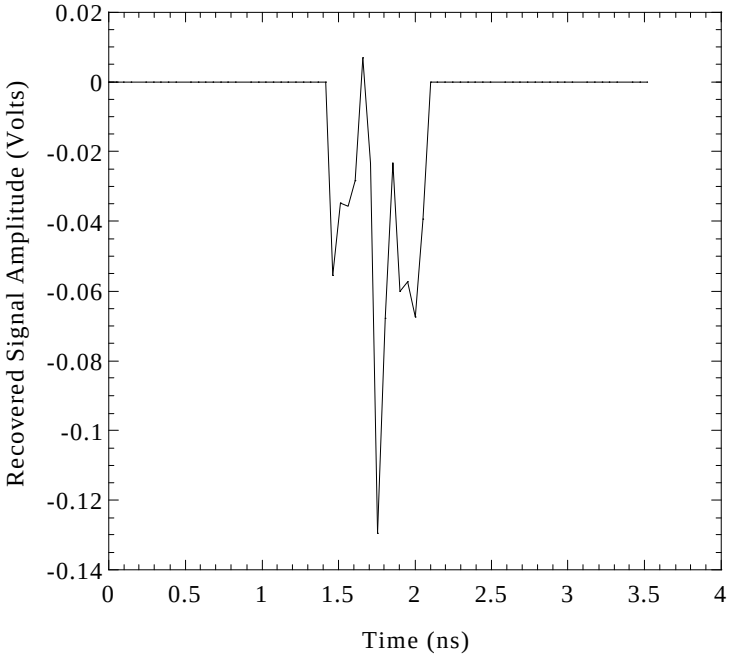

Figure 6-22: Recovered direct path waveform at location E.

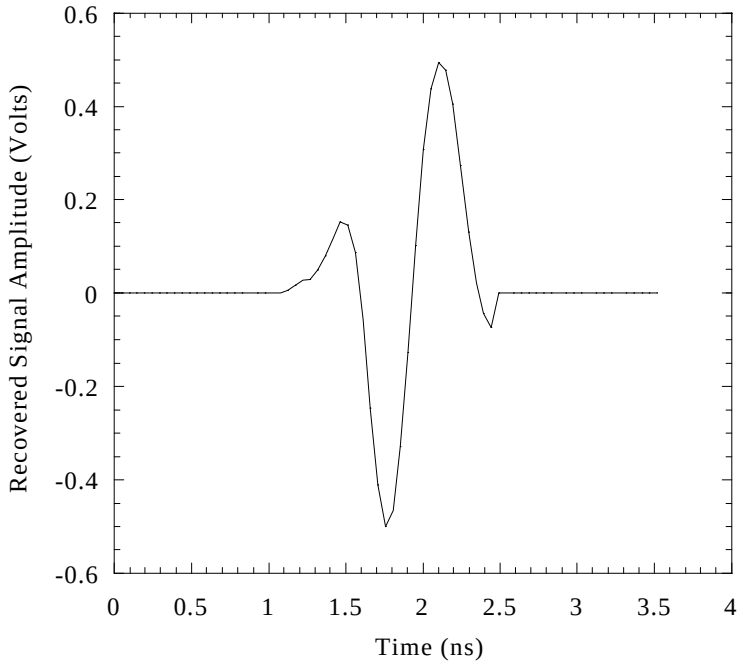

Figure 6-23: Recovered direct path waveform at location M.

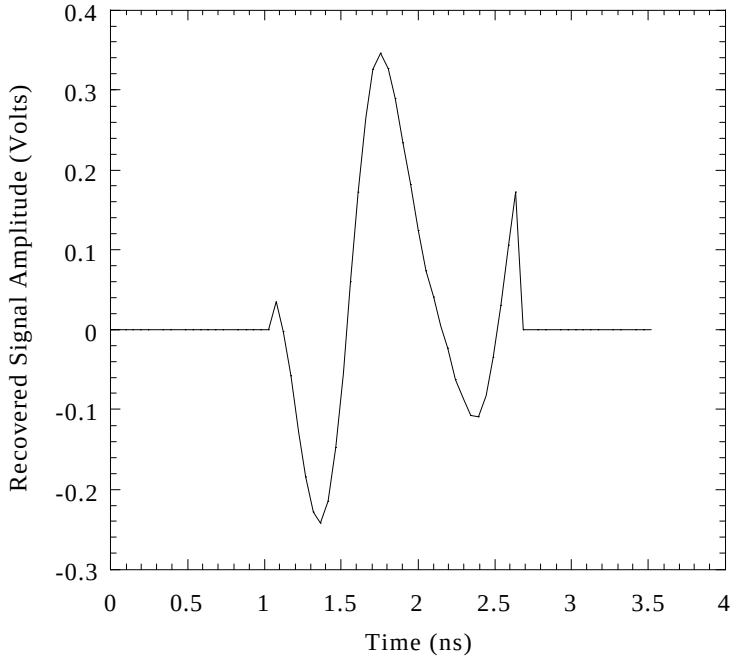

Figure 6-24: Recovered direct path waveform at location T.

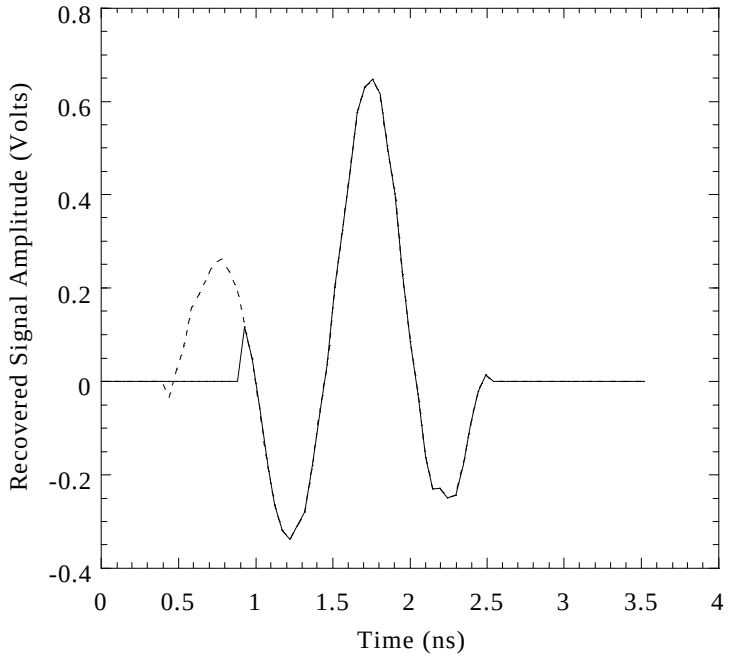

Figure 6-25: Recovered direct path waveform at location U.

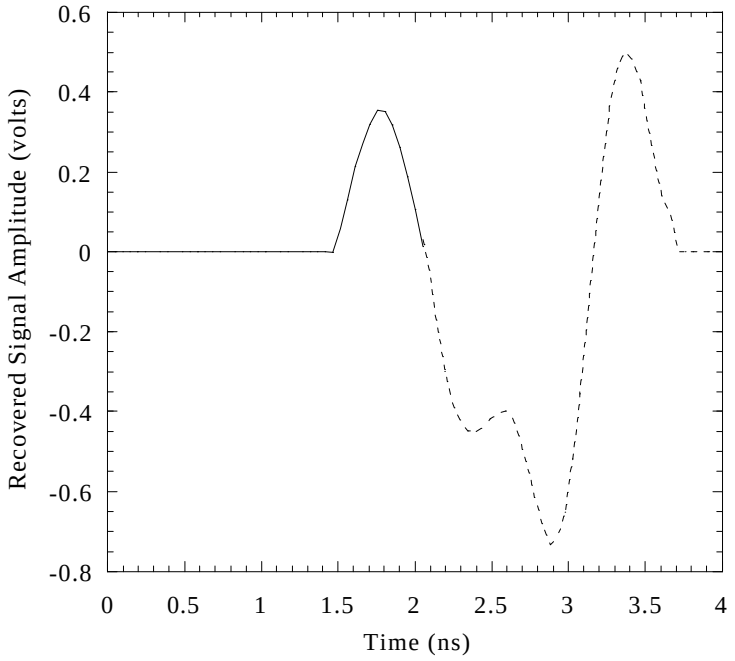

Figure 6-26: Recovered direct path waveform at location W.

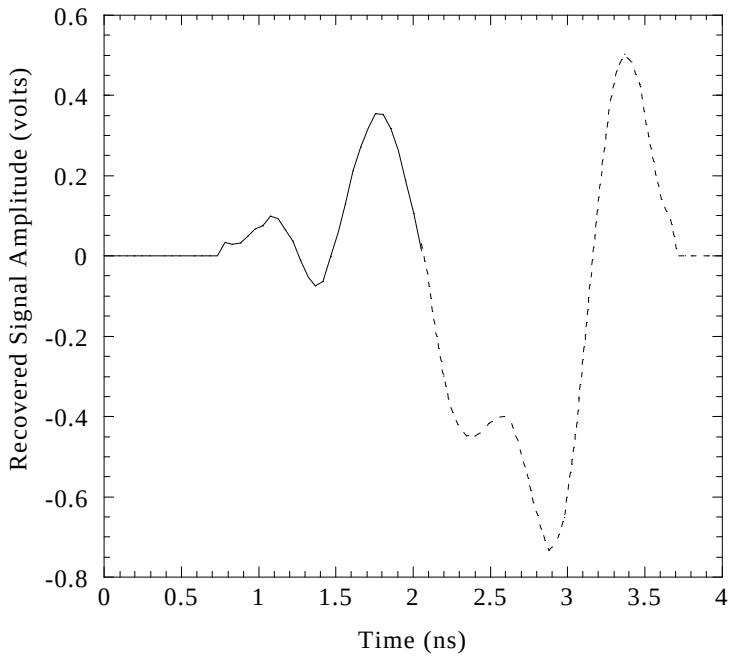

Figure 6-27: Recovered direct path waveform at location W.

6.2.1 Path-Loss Models for the UWB Propagation Channel

A common measure of the average large-scale path loss for a given separation distance d between the transmitter and the receiver is given by the path loss [67] as

$$\overline{PL}\,(d) \propto \left(\frac{d}{d_o}\right)^n \tag{6.3}$$

or, expressed in decibels,

$$\overline{PL}\,(d) = \overline{PL}\,(d_o) + 10n\log\left(\frac{d}{d_o}\right) \quad \text{(dB)}, \tag{6.4}$$

where n is the path loss exponent which determines the rate at which the received signal amplitude falls off as a function of distance, and d_o is a reference distance at which a signal

level measurement is made. As a check on the measurements themselves, consider first the path loss between the reference measurement, taken at a distance of 1 meter from the transmitter, and the measurements at location F1 in the building, which represents the only unobstructed, line-of-sight path in the data set. If the recovered energy and amplitude of the direct path signal is determined for each of the 49 sets of data at F1, and the resulting median recovered signal energy and amplitude are compared to median energy and amplitude in the set of three measurements made at the reference location, the plot in Figure 6-28 results. The path loss exponents found when considering the actual energy in the received waveform and when considering only the amplitude of the received waveform, under the assumption that all waveforms have the same fundamental pulse shape, are very close. When considering the energy in the received signal, a path loss exponent of 1.76 is found, and when the signal energy is taken to be proportional to the amplitude, a path loss exponent of 1.75 is found. These compare with typical path loss exponents for the indoor line-of-sight channel of between 1.6 and 1.8 [29], [67].

Consider next the path loss characteristics of the direct path signals when an unobstructed line-of-sight path is not available. Five different cases were considered here, in order to determine the sensitivity of the measurements to the inclusion of different information. First, exclude the measurements at locations F1 and F2 in the building from the model, since these locations are in the same room as the transmitter, which may cause the path loss to obey a different propagation law than if obstructions were present. This leads to the model shown in Figure 6-29, where four different path loss exponents are calculated. An exponent is calculated for the median signal level of the energy and amplitude resulting from consideration of the direct path at each sensor. Exponents are also calculated from the direct path signal energy and amplitude recovered by the processing algorithms. The

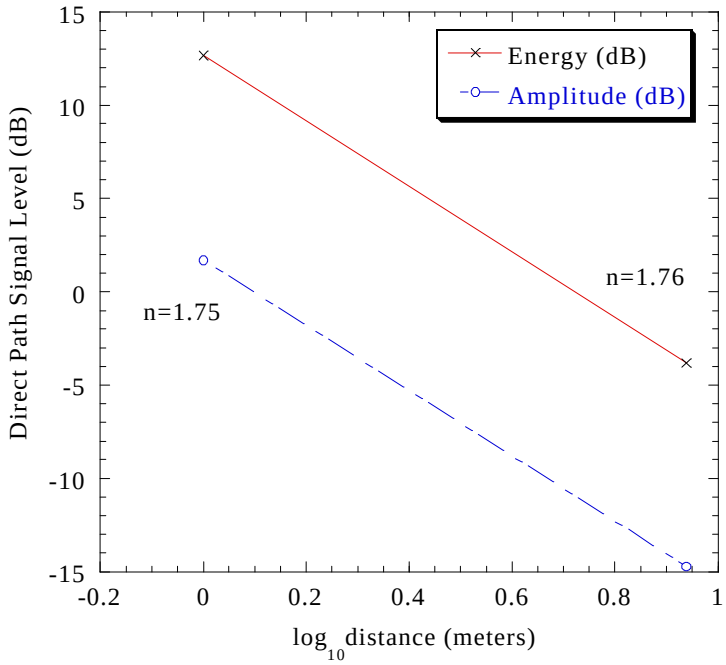

Figure 6-28: UWB path loss characteristics for an unobstructed line-of-sight channel

path loss exponents reported here are within the range of 4 to 6 reported in [29] and [67] for the indoor obstructed channel.

Also of note in Figure 6-29 is that the measurements at locations A and E seem to vary the most across the four different cases shown. These cases are also the ones where the estimate of the direct path signal is the least reliable. In light of this, the measurements at locations A and E are excluded, as well as the measurements at locations F1 and F2, which gives the results in Figure 6-30. Here the path-loss exponents are very close from case to case and are in the range from 3.50 to 3.85. This is slightly better than results reported for more narrowband indoor scenarios.

Path-loss models can be generated for other scenarios as well, depending on which cases are to be considered, and other variations are shown in Figure 6-31, Figure 6-32 and 6-33. The bottom line is that as long as the measurements at locations A and E are not considered

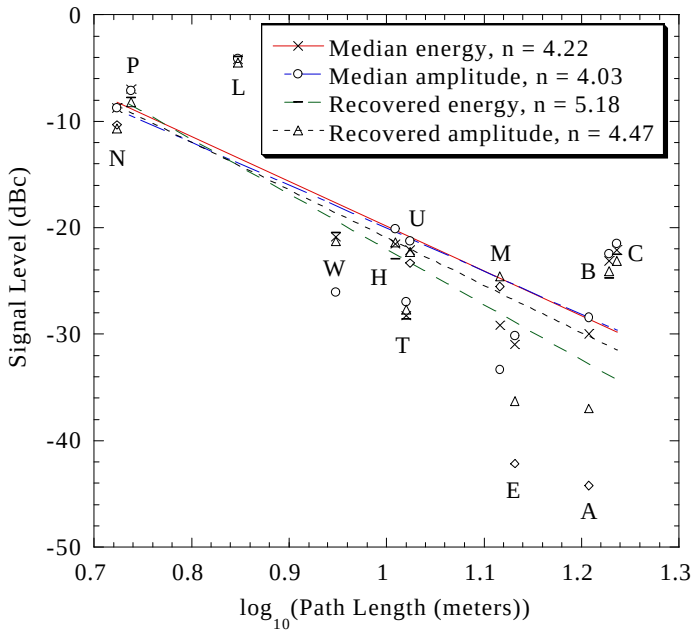

Figure 6-29: Path loss characteristic for the direct path signal, with measurements at locations F1 and F2 excluded.

in the model, the results are fairly consistent from case to case within a particular scenario, which improves confidence in the results of the Sensor-CLEAN and the post-processing algorithms. Further, all of the results are in approximate accordance with previous reports in the literature.

These results could also contribute to more detailed characterizations. It is possible that by considering the unobstructed results, the obstructed results and the floor plan, a figure representing the contribution of obstructions such as walls to the path loss could be determined.

6.2.2 Clustering Models for the Indoor Multipath Propagation Channel

Previous models for the indoor multipath propagation channel [15], [29], [37], [48], [49], [50] have reported a clustering of multipath components, in both time and angle. In the

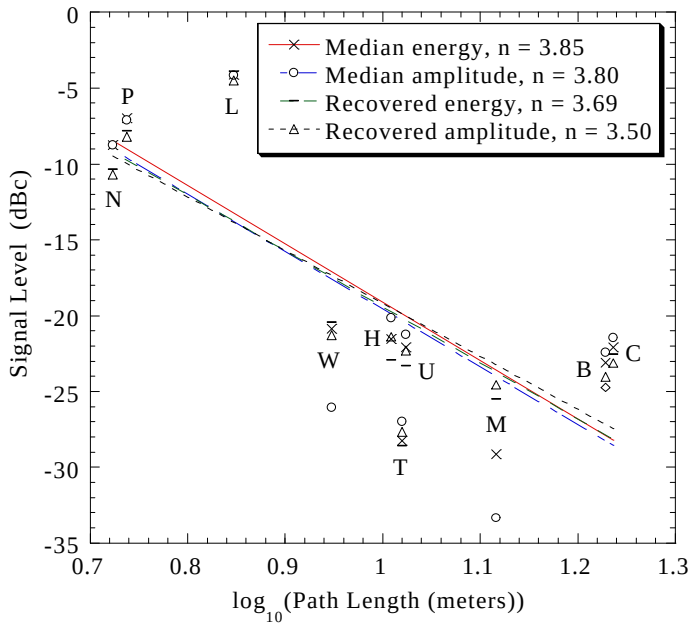

Figure 6-30: Path loss characteristic for the direct path signal, with measurements at locations F1, F2, A and E excluded.

model presented in [49], the received signal amplitude, β_{kl}, is a Rayleigh distributed random variable with a mean-square value that obeys a double exponential decay law, according to

$$\overline{\beta_{kl}^2} = \overline{\beta^2\,(0,0)} e^{-T_1/\Gamma} e^{-\tau_{kl}/\gamma} \tag{6.5}$$

where $\overline{\beta^2\,(0,0)}$ describes the average power of the first arrival of the first cluster, T_l represents the arrival time of the lth cluster, and τ_{kl} is the arrival time of the kth arrival within the lth cluster, relative to T_l. The parameters Γ and γ determine the inter-cluster signal level rate of decay and the intra-cluster rate of decay, respectively. The parameter Γ is generally determined by the architecture of the building, while γ is determined by objects close to the receive antenna, such as furniture. The results presented in [49] make the assumption

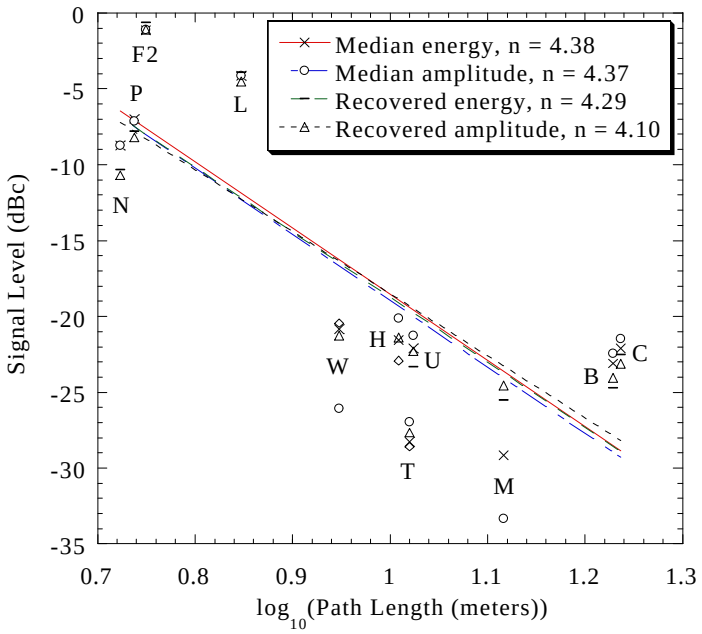

Figure 6-31: Path loss characteristic for the direct path signal, with measurements at locations F1, A and E excluded.

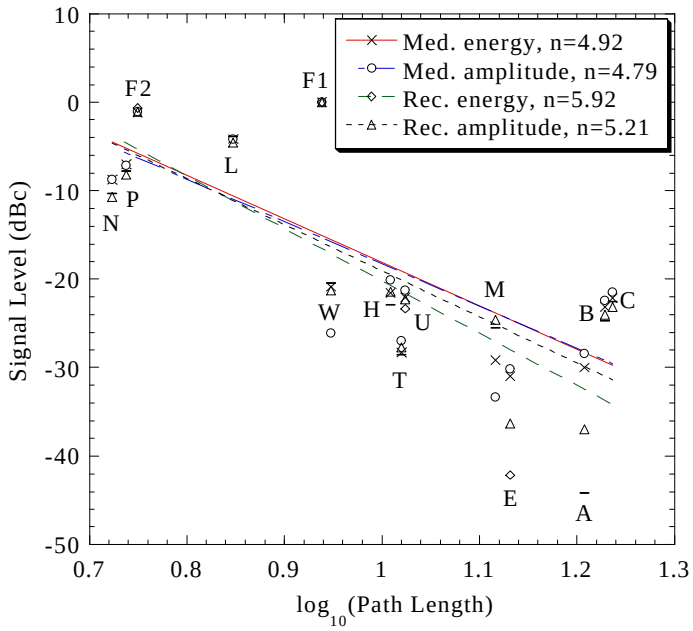

Figure 6-32: Path loss characteristic for the direct path signal, with all measurements included.

that the channel impulse response as a function of time and azimuth angle is a separable function, or

$$h(t,\theta) = h(t)\,h(\theta) \tag{6.6}$$

from which independent descriptions of the multipath time-of-arrival and angle-of-arrival are developed. This is justified by observing that the angular deviation of the signal arrivals within a cluster from the cluster mean does not increase as a function of time.

Following this model, and based upon the apparent existence of clusters in the UWB channel, seen in Figure 6-2 - Figure 6-10, UWB channel models which account for the clustering of multipath components can be developed. In order to identify the existence and location of clusters of signal components, a sliding window in time and angle was applied to the recovered signal information over time and azimuth angle, and arrivals inside

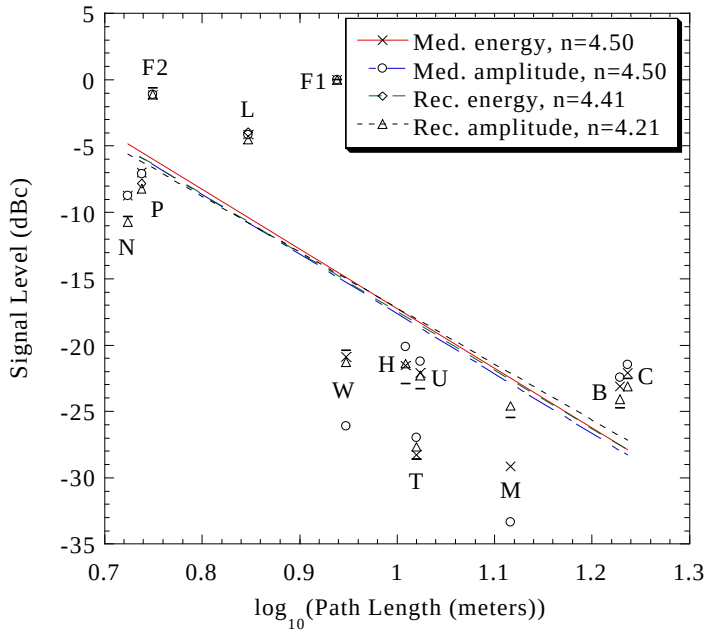

Figure 6-33: Path loss characteristic for the direct path signal, with measurements at locations A and E excluded.

the window were accumulated. As an example, the output of the sliding window is shown for the data measured at location P in Figure 6-34, for location B in Figure 6-35 and for location M in Figure 6-36. In each of these plots, the darker the area, the greater the density of detected signals at the corresponding region in time and azimuth angle. Cluster locations were determined by identifying the regions in these plots where the most signals were detected. As was noted in [48], it is very difficult to develop a robust algorithm for the automatic identification of cluster regions. Therefore, as in [48], the cluster regions were determined manually. Cluster regions were selected by considering both the sliding window plots shown in the figures, and scatter plots of the time and azimuth angle-of-arrival. The resulting cluster regions corresponding to Figure 6-34, Figure 6-35 and Figure 6-36 are shown in Figure 6-37, Figure 6-38 and Figure 6-39, respectively. In all, 65 clusters were identified in the recovered signals for the fourteen measurement locations.

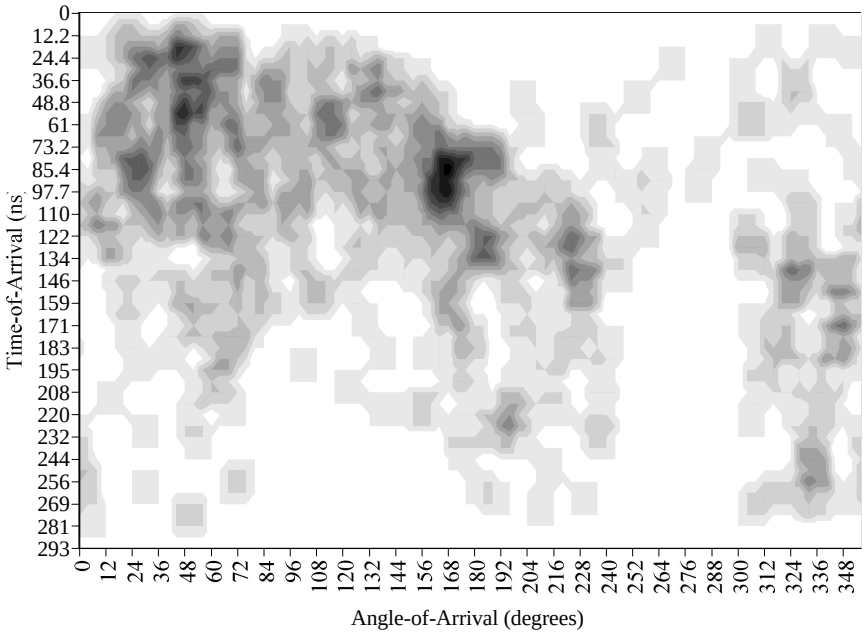

Figure 6-34: Map of recovered signal information at location P, obtained by accumulating arrivals over a window in time and azimuth angle.

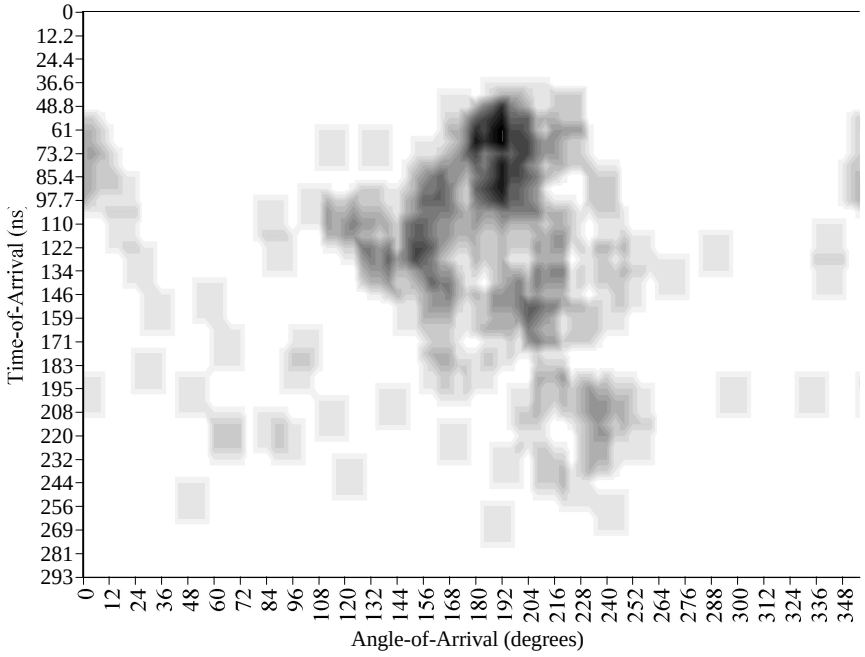

Figure 6-35: Cluster map at location B

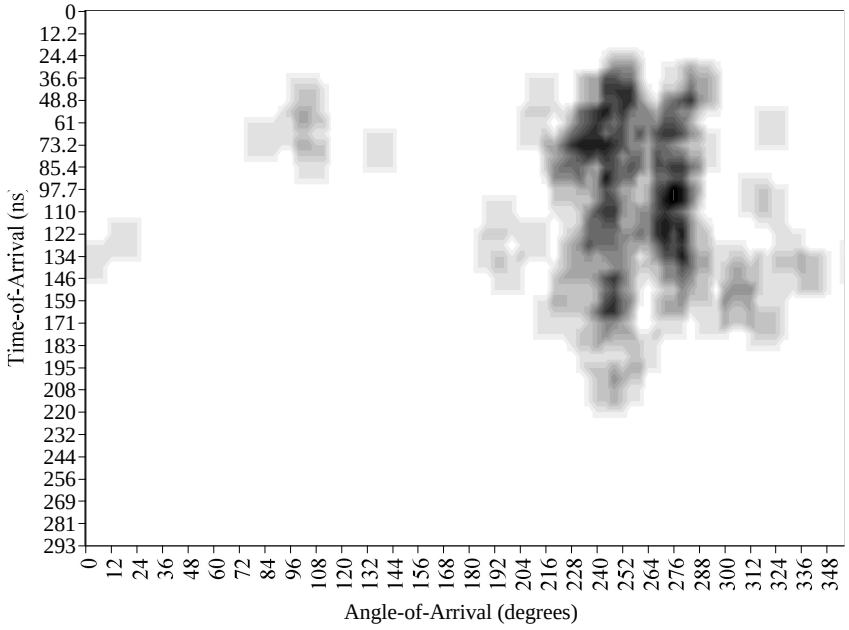

Figure 6-36: Cluster map at location M

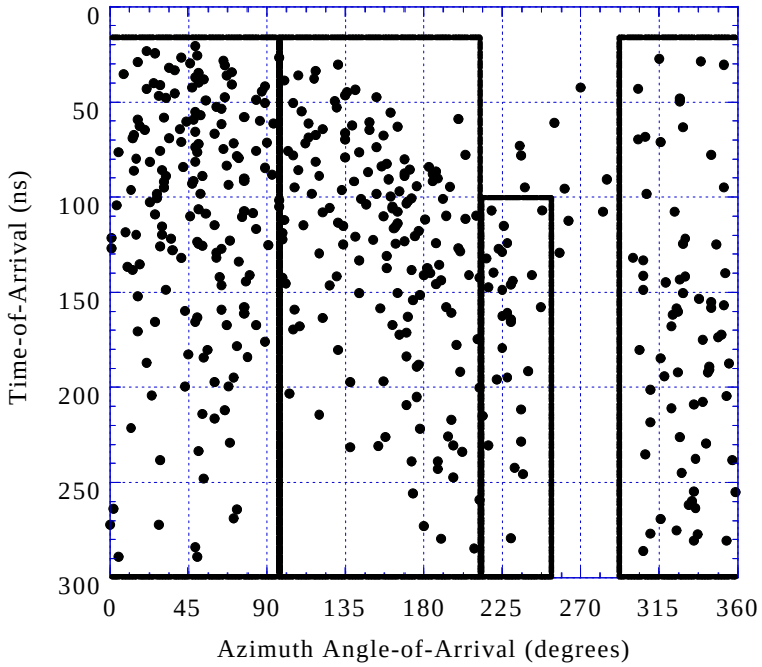

Figure 6-37: Cluster regions selected for recovered signals at location P.

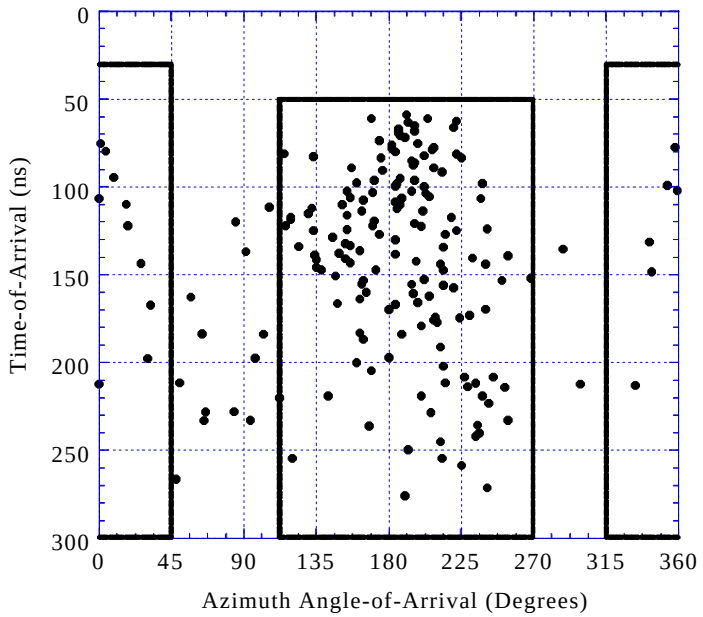

Figure 6-38: Cluster regions selected for recovered signals at location B.

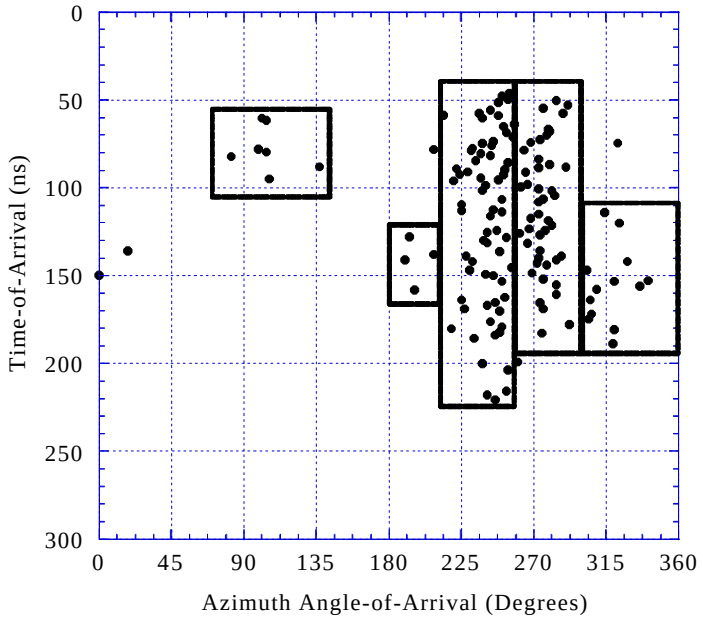

Figure 6-39: Cluster regions selected for recovered signals at location M.

Following the identification and sorting of the cluster information, the reference arrival, or the earliest arrival in each cluster was identified, and a decay exponent was determined, following the algorithm in [49]. In this algorithm, the time of the first arrival is set to zero, and all other arrivals are reported relative to this time. The recovered energy in the collection of signals is also reported relative to the energy in the first arrival in the first cluster, which is normalized to 1, and is referred to as the normalized relative energy, as in [49].

With the measurements at locations A and E excluded again, due to the low SNR, the resulting UWB cluster energy versus relative delay models for the indoor channel are shown below in Figure 6-40 and Figure 6-41. The first plot reports the decay of the energy in the recovered waveforms, and the second reports the energy as a function of the recovered amplitude only, under the assumption that all incident waveforms are identical. Several values for the decay exponent Γ are shown for each plot, in order to demonstrate the consistency of the results. Γ_{med} is the median and Γ_{mean} represents the mean of the values obtained by considering the best-fit line for each measurement location individually. Γ_{LS} is the exponent of the best fit line obtained by considering the clusters from all measurement locations simultaneously. In both cases, the results are fairly close, and Γ_{LS} is reported as the rate of decay of the inter-cluster energy versus delay. These results compare to values of 33.6 ns and 78.0 ns reported in [49] for two different buildings, and 60 ns reported in [37]. Thus the UWB signals recovered in this case exhibit a rate of decay that is comparable to some of the results reported previously, although it has been noted that this parameter is a strong function of the building architecture, as are many parameters of the propagation channel.

These results allow for comparison against other experiments reported in the literature and for the derivation of a common parameter, the decay exponent, Γ. A non-linear (on

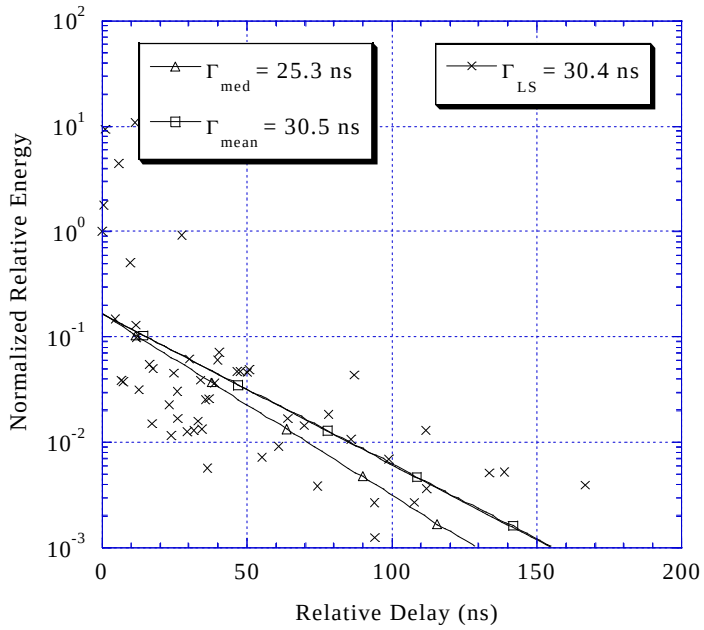

Figure 6-40: Inter-cluster loss vs. relative delay when considering the recovered energy (energy in the first arrival within a cluster).

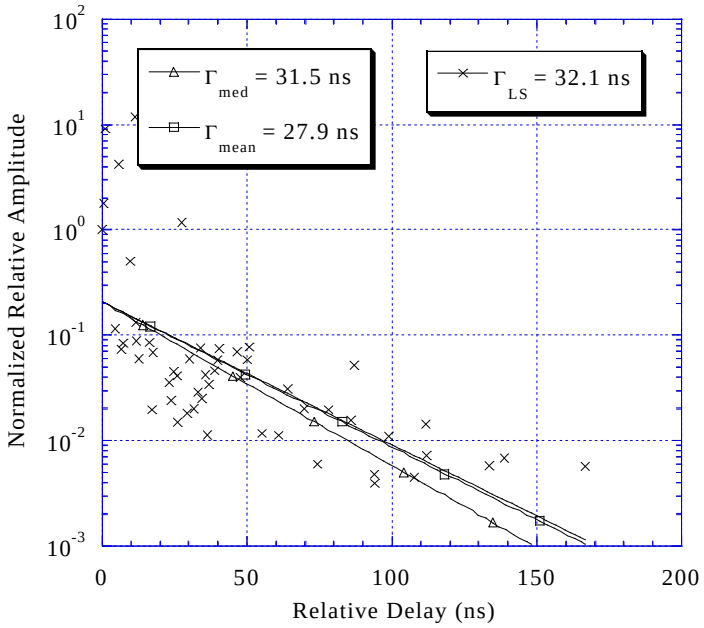

Figure 6-41: Inter-cluster loss vs. relative delay when considering the amplitude of the recovered waveform (amplitude of first arrival within a cluster).

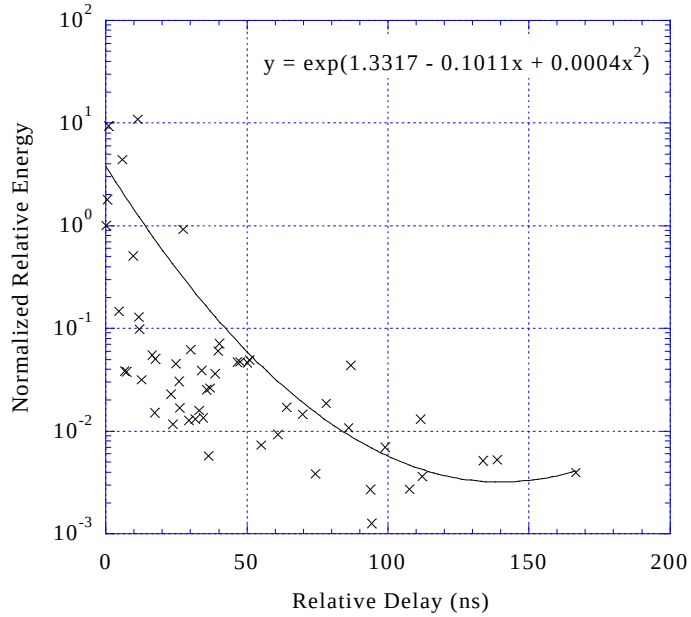

Figure 6-42: Nonlinear (on a log scale) fit to inter-cluster loss vs. relative delay when considering the recovered energy.

a log scale) fit to the data can also be attempted here, in order to obtain a model which weights the strong arrivals early in time more heavily, although there is no readily available basis for comparison in the literature. This is shown for the recovered signal energy in Figure 6-42, with the parameters of the curve fit given in the plot. Although the corresponding plot using the recovered signal amplitudes is not given, it is hypothesized that it would yield similar results, based on the similar values for decay exponents above.

Consider next the intra-cluster rate of decay, or the rate at which the recovered energy in the signal arrivals within a cluster falls off as a function of the delay. Following the terminology of [37] and [49], this is also called the ray decay rate. These plots are shown below in Figure 6-43 and Figure 6-44. The absolute deviation between the mean and median of the results from each measurement location and the least-squares fit to all of the recovered signal information is larger here, excluding the results at locations A and E. The results

generated by considering the energy in the recovered waveform and the results from the amplitude only are very close. In [49], very different results are found for the inter-cluster decay exponent γ, depending on which building the measurements were conducted in. In one building, a value of 28.6 ns is reported for γ, while in another building γ is found to be 82.2 ns. The earlier reference, [37] reported a γ of 20 ns. It is noted in [49] that the first measurement was made in a building constructed primarily out of cinder blocks, while the second was made in a building constructed from a steel-frame and gypsum boards. This difference in construction is reflected in the different rates of decay. The values for γ derived here for the UWB propagation channel are in the same neighborhood as those reported for the steel-frame building in [49].

Further, considering the relationship between Γ and γ, in both sets of measurements reported in [49] the values for Γ and γ are fairly close. In one case Γ is larger than γ, while in the other the opposite is true. What is not indicated in the reference is the physical relationship between the transmitter and the receiver. The results obtained here can be explained for the transmitter and receiver relationships at which the measurements were made. This relation is shown for all cases in Figure 6-1, and it can be seen that with the exception of the measurements at locations F1 and F2, at least one wall separates the transmitter and the receiver. Each cluster then represents a path that exists between the transmitter and the receiver along which signals propagate. This cluster path is generally a function of the architecture of the building itself, while the arrivals within a cluster are due to secondary reflections off of furniture or other objects. The implications are that the primary source of degradation is in the propagation from the transmit antenna to the receive antenna through the features of the building. This captured in the decay exponent Γ. Secondary reflections off of other objects in the neighborhood of the receive antenna do not always involve the penetration of additional obstructions, and therefore tend to

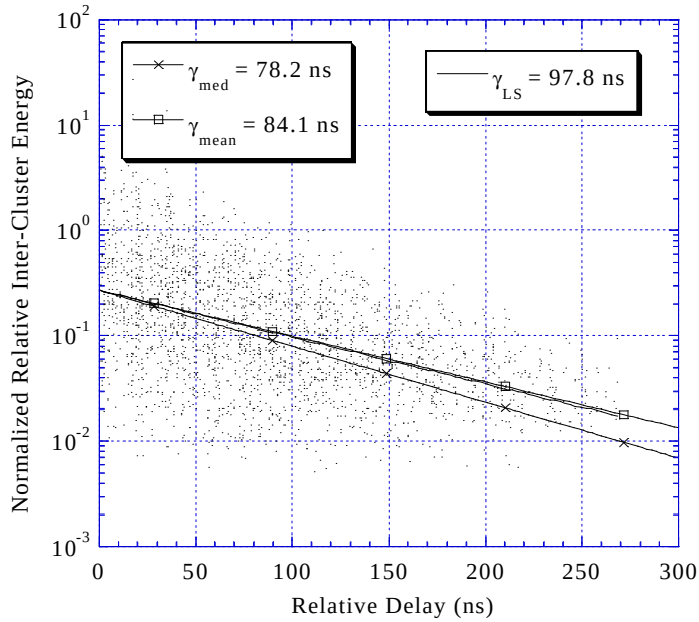

Figure 6-43: Intra-cluster loss versus delay energy.

contribute less to the decay of the signals. This is likely due to the building architecture and perhaps to the propagation characteristics of the UWB waveforms. This property of the UWB waveforms probably merits further study in different buildings.

As discussed in [49] and [37], a Rayleigh distribution has been shown to provide a good fit to the deviation of the arrival energy from the mean curve, where the Rayleigh probability density function is given by

$$f_x(x) = \frac{x}{\alpha^2} e^{-\frac{x^2}{2\alpha^2}}$$

A histogram of the deviation values is shown in Figure 6-45 and 6-46, with a Rayleigh density with $\alpha = 0.46$ overlaid on top of the recovered distribution. This distribution represents the best-fit to the recovered UWB data when considering the Rayleigh, lognormal, Nakagami-m and Rician distributions.

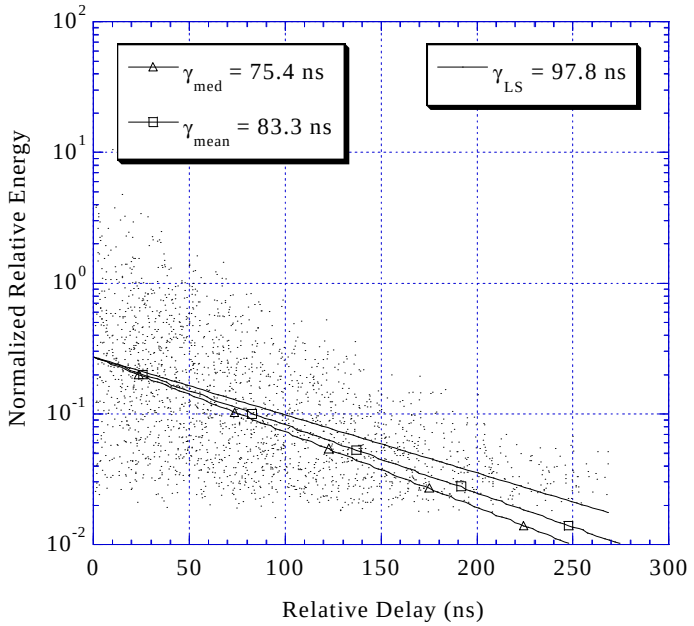

Figure 6-44: Intra-cluster loss versus delay amplitude

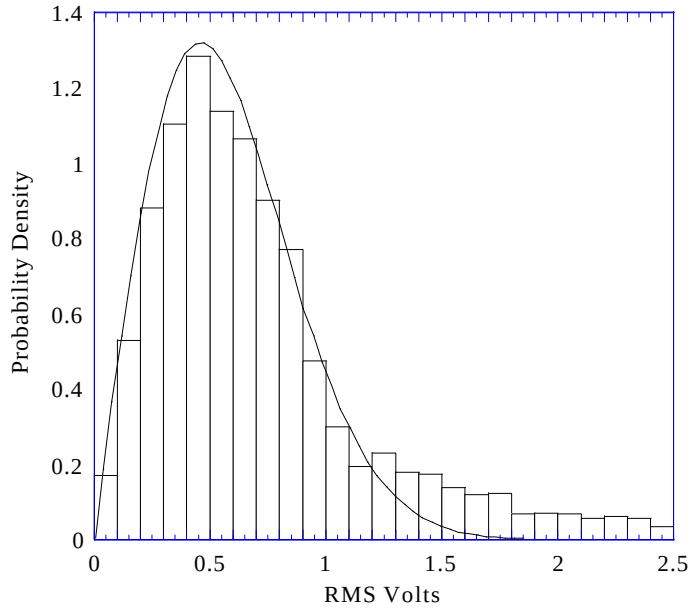

Figure 6-45: Distribution of the arrival energy deviation from the mean, with a Rayleigh density overlayed.

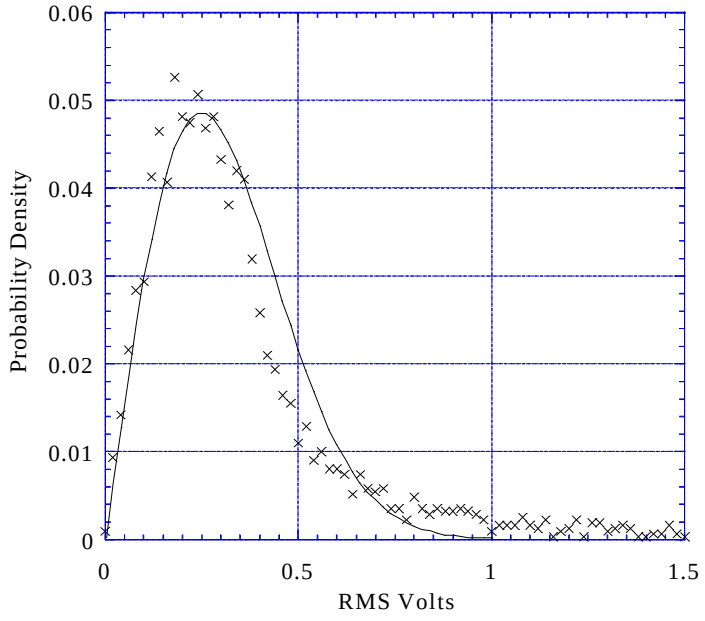

Figure 6-46: Histogram of the arrival energy deviation from the mean, with a Rayleigh density overlayed.

Consider next the angle-of-arrival properties of the cluster model. Assuming again the separable impulse response of equation (6.6), the model proposed in [49] to describe the angular impulse response is

$$h(\theta) = \sum_{l=0}^{\infty} \sum_{k=0}^{\infty} \beta_{kl} \delta(\theta - \Theta_l - \omega_{kl}) \tag{6.7}$$

where β_{kl} is the amplitude of the kth arrival in the lth cluster, Θ_l is the mean azimuth angle-of-arrival of the lth cluster and ω_{kl} is the azimuth angle-of -arrival of the kth arrival in the lth cluster, relative to Θ_l. It is proposed in [49] that Θ_l is distributed uniformly in angle, and ω_{kl} is distributed according to a zero-mean Laplacian distribution,

$$p(\theta) = \frac{1}{\sqrt{2}\sigma} e^{-|\sqrt{2}\theta/\sigma|} \tag{6.8}$$

The recovered ray or intra-cluster arrivals were tested against Gaussian and Laplacian hypotheses, and the best fit distribution and resulting standard deviation were reported. It was determined that the recovered UWB signals were best fit to a Laplacian density, with a standard deviation, σ, of 38°. The recovered signal information and the best-fit distribution are shown in Figure 6-47 at 1° of resolution, and in Figure 6-48 at five degrees of resolution. Note that these are histograms, and only take into account the fact that a signal has arrived, but not the energy in the arrival. The angular distributions associated with the waveform energy and amplitude are therefore identical. These distributions compare with standard deviations on the Laplacian density of 25.5^o and 21.5^o reported in [49] as the best fit to the recovered angular information for two different buildings. It is likely that this parameter is a function of the building architecture, which again would suggest that further propagation studies are needed to determine whether the results presented here are typical. It is also possible that the difference in the results is due in part to the fractional bandwidth of the

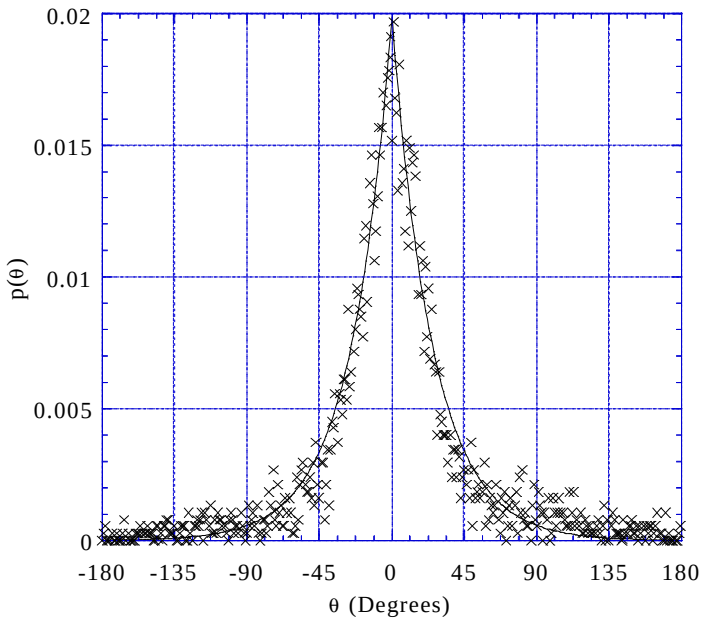

Figure 6-47: Ray arrival angles at 1° of resolution and a best fit Laplacian density with σ=38°

UWB waveforms used in this study. The penetration properties of these signals, including the larger γ, might lead to the detection of responses that would remain undetected at if transmitted at a single frequency or over a smaller frequency range.

It was found in [49] that the relative cluster azimuth arrival angles were approximated by a uniform distribution over all angles. The recovered cluster angles in this work are shown in Figure 6-49, relative to the reference cluster angle-of-arrival, where the reference cluster is taken to be the first cluster to arrive in time, for each measurement location. This distribution is also approximately uniform, although it is noted that no clusters were reported to exist at angles above approximately 135°. It is conjectured that if more measurements were taken, angles would occur in this region, and this function would tend to more closely approximate a uniform distribution.

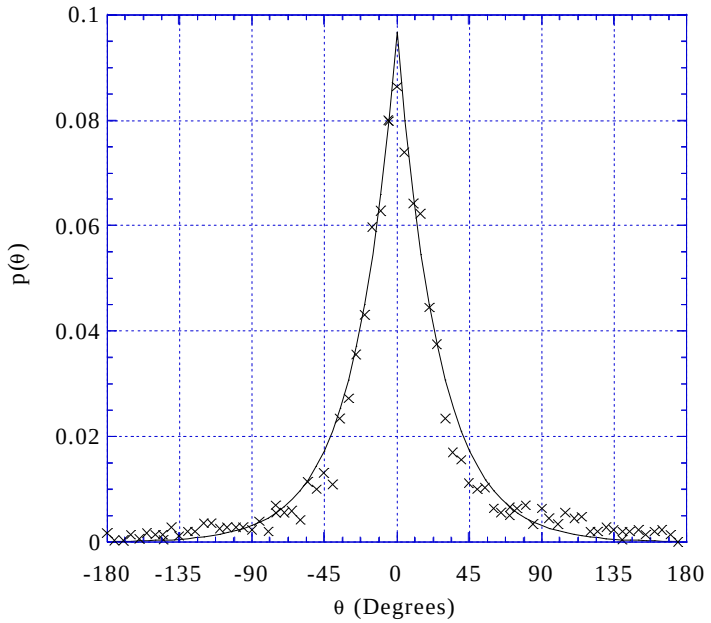

Figure 6-48: Ray arrival angles at 5° of resolution and a best fit Laplacian density with σ=37°

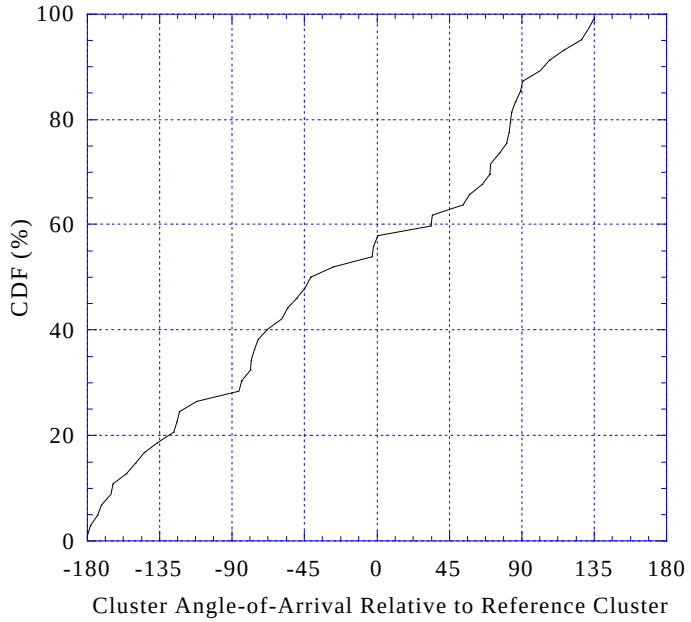

Figure 6-49: Distribution of the cluster azimuth angle-of-arrival, relative to the reference cluster.

Finally, in order to complete this model of the UWB propagation channel, based on the multipath clustering phenomenon, the rate of the cluster and the ray arrivals must be determined. Again following the model presented in [49], the inter-arrival times are hypothesized to follow an exponential rate law, given as

$$p\left(T_l \left| T_{l-1}\right.\right) = \Lambda e^{-\Lambda(T_l - T_{l-1})} \tag{6.9}$$

$$p\left(\tau_{kl} \left| \tau_{k-1,l}\right.\right) = \lambda e^{-\lambda(T_l - T_{l-1})} \tag{6.10}$$

where Λ is the cluster arrival rate and λ is the ray arrival rate. Following this model, the best fit exponential distributions, parameterized on Λ and λ were determined for the recovered UWB cluster and ray arrival times, respectively. The resulting plots are shown in Figure 6-50 and Figure 6-51. The ray arrival rate determined for the UWB signals was faster than that reported in either [49] or [37]. A ray arrival rate of $1/\lambda$=2.3 ns defined the best-fit exponential distribution for the ray arrival times over all measurement locations, while ray arrival rates of $1/\lambda$=5.1 ns and $1/\lambda$=6.6 ns were reported in [49] for the two different buildings. A ray arrival rate of $1/\lambda$=5.0 ns was given in [37]. Several reasons are possible for the faster arrival rate. First, it is again probably due at least in part to the building architecture. Second, the fractional bandwidth of the UWB signals and the post-processing algorithms permit multipath time resolution on the order of 1 ns. The measurement equipment used in [49] allowed a time resolution on the incident signals of about 3 ns. Also shown in Figure 6-50 is a curve which represents the best-fit exponential to ray arrival times of greater than 8 ns, although this represents less than 10% of the values.

A cluster arrival rate of $1/\Lambda$=45.5 ns was found to define the best-fit exponential distribution in the UWB signal propagation model. This value is larger than the cluster arrival rates of 16.8 ns and 17.3 ns reported in [49], but less than the 300 ns given in [37]. Again,

Parameter	UWB Propagation	Spencer et al.	Spencer et al.	Saleh-Valenzuela
Γ	27.9 ns	33.6 ns	78.0 ns	60 ns
γ	84.1 ns	28.6 ns	82.2 ns	20 ns
$1/\Lambda$	45.5 ns	16.8 ns	17.3 ns	300 ns
$1/\lambda$	2.3 ns	5.1 ns	6.6 ns	5 ns
σ	37°	25.5^o	21.5^o	-

Table 6.2: Summary of propagation model parameters

several explanations are possible to describe the differences. It could be due to the difference in the fractional bandwidths of the signals involved, the sensitivity of the measurement equipment or the building architecture. As discussed above, it could also be due to the orientation of the transmitter and receiver in the building. This information is not given in [48] or [49], but for the 14 measurement locations used in this work, only two were taken in the same room, and in the rest, the transmitter and receiver were separated by at least one wall. As shown in Table 6.1, eight out of the ten sets of measurements involved a separation between the transmitter and receiver of greater than 10 meters. At this separation, it is possible that relatively few distinct paths between the transmitter and receiver, each corresponding to a cluster, exist, as compared with the measurements in [48], [49]. Without further knowledge of the measurement scenario in [48] and [49], it is impossible to draw more concrete explanations.

The model parameters derived herein for the UWB signal propagation model and a comparison with the earlier work in [48], [49], [37] are summarized in Table 6.2.

6.3 Additional Models for the Ultra-Wideband Propagation Channel

A characterization of the UWB propagation channel can also be developed without considering cluster information. In this case, it is of interest to calculate the spatio-temporal

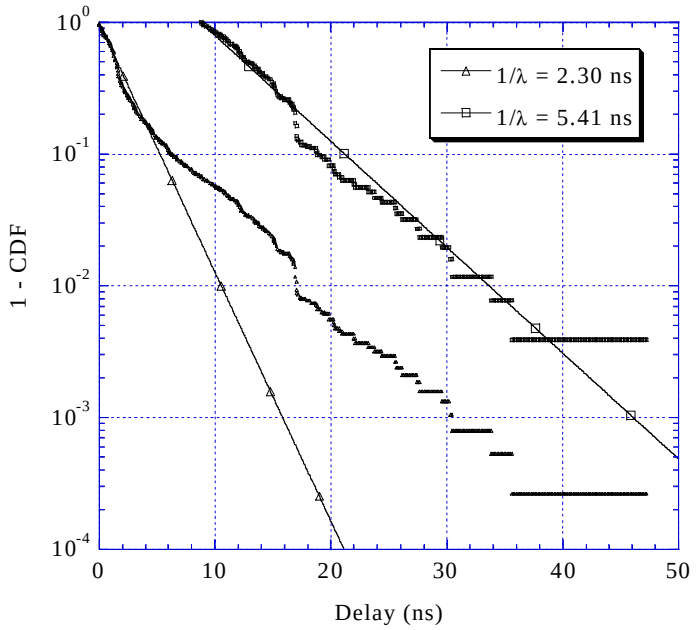

Figure 6-50: Ray arrival rate for the indoor UWB channel considered here.

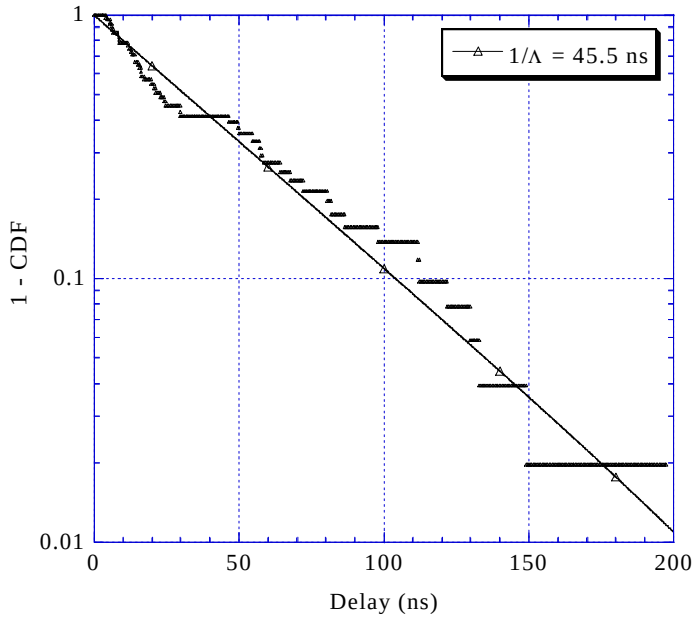

Figure 6-51: Cluster arrival rate for the indoor UWB channel considered here.

distribution of the received UWB signals and to examine any correlation between the time-of-arrival and angle-of-arrival of the received UWB signals. First, channel models will be discussed which consider the spatial and temporal variations in the channel independently, then joint spatio-temporal distributions will be presented.

6.3.1 Independent spatial and temporal channel descriptions - best-fit distributions

Communication channels are often characterized by assuming that the spatial and temporal variations in the channel are independent [35], [49]. Under this assumption, consider the best-fit distributions to the recovered angles-of-arrival and the recovered energy of all signals, shown in Figures 6-52, 6-53 and 6-54. Two versions of the angle-of-arrival distribution are shown, with markedly different results. For the angle-of-arrival distributions, each plot represents the best-fit distribution which results when the data is fit to a Laplacian distribution and to a Gaussian distribution. In both cases here, as in [49], the Laplacian distribution provides the best description of the angle-of-arrival information. An intuitive explanation for the suitability of the Laplacian distribution in the indoor environment is that deviations in the propagation path from the line-of-sight (LOS) path will often result in a path with greater attenuation than the LOS path. Thus more signals are detected at arrival angles close to the LOS arrival angle, which gives rise to the distinct peak in the density function. In 6-52, all signals are weighted equally in the distribution, regardless of the recovered energy, while in 6-53, each signal contributes a weight to the distribution proportional to the recovered energy. The implication here again is that for these measurements, large signals tend to arrive at small deviations from the LOS path arrival angle. This result will explored in greater detail below. Figure 6-54 shows the best fit lognormal distribution to the recovered signal energies. In this case, a lognormal, a Nakagami and a

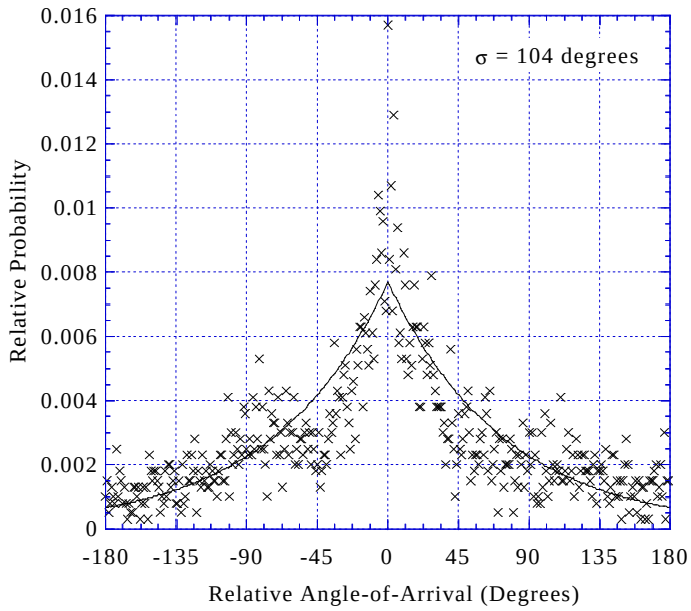

Figure 6-52: Best fit Laplacian distribution to the recovered angles from all measurement locations, with a resolution of 1°. All signals are weighted equally in the distribution.

Rayleigh distribution were fit to the data, and the lognormal distribution was retained as the one with the lowest mean-squared error. Intuition here follows the theory of lognormal fading in a shadowed environment [36]. Representing the lognormal distribution as

$$f_x(x) = \frac{1}{\sigma x \sqrt{2\pi}} e^{-(\ln x - \eta)^2 / 2\sigma^2} \tag{6.11}$$

the best-fit parameters of the lognormal distribution were found to be σ =1.93 and $\eta = 0$. In each case, the distributions are normalized to yield a total probability mass of 1. These distributions give a rough idea of the statistical properties of the channel, in the absence of any cluster information or correlation between the spatial and temporal distributions.

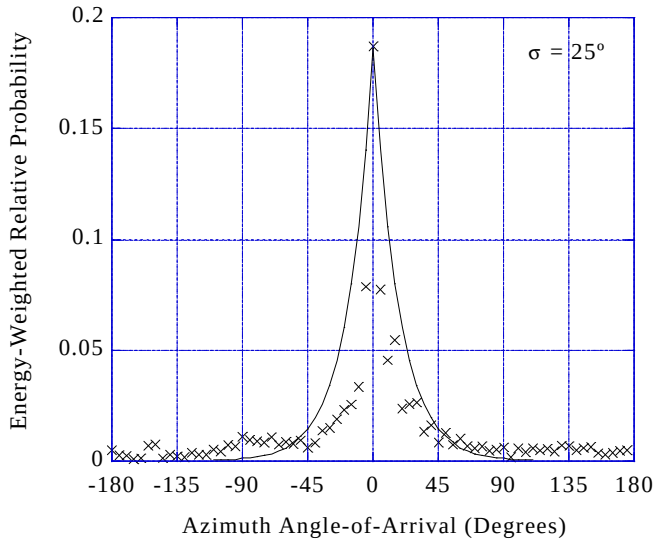

Figure 6-53: Best fit Laplacian distribution to the recovered angles from all measurement locations, with a resolution of 5°. All signals are weighted in the distribution according to the recovered energy.

6.3.2 Independent spatial and temporal channel descriptions - moments

Typical parameters by which the temporal and spatial distributions of signal energy are measured include the first moment and the root of the second moment of the power delay profile. These moments are defined here under the assumptions of discrete time signals and a specular multipath model. The temporal variations are described by the first and root of the second moment of the power delay profile as

$$\overline{T} = \frac{\sum_{k=0}^{K-1}\sum_{n=0}^{N-1}(nT_s)\,\beta_{n,k}^2}{\sum_{k=0}^{K-1}\sum_{n=0}^{N-1}\beta_{n,k}^2} \tag{6.12}$$

$$\sigma_T = \sqrt{\frac{\sum_{k=0}^{K-1}\sum_{n=0}^{N-1}\left(nT_s-\overline{T}\right)^2\beta_{n,k}^2}{\sum_{k=0}^{K-1}\sum_{n=0}^{N-1}\beta_{n,k}^2}} \tag{6.13}$$

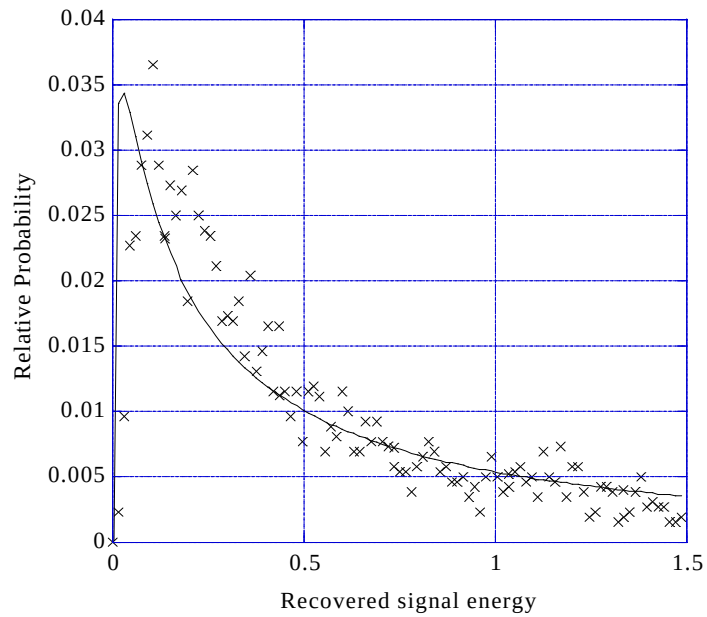

Figure 6-54: Best fit lognormal distribution to the recovered signal energy from all measurement locations except A and E, with $\sigma = 1.93$ and $\eta = 0$. Energy is calculated from the recovered waveforms.

where T_S is the sampling rate, N is the number of time samples considered in the calculation, and K represents the angular samples. $\overline{T}$ is called the power-weighted average time-of-arrival (TOA) and σ_T is known as the delay spread. Assuming that these moments are calculated without regard to the angle-of-incidence, the summation over K removes any dependence on angle from the results.

The spatial distribution of the signal energy can be measured by the first moment and root of the second moment of the received angular profile according to [30]

$$\overline{\phi} = \frac{\sum_{n=N_1}^{N_2-1} \sum_{k=0}^{K-1} \phi_k \beta_{n,k}^2}{\sum_{n=N_1}^{N_2-1} \sum_{k=0}^{K-1} \beta_{n,k}^2} \tag{6.14}$$

$$\sigma_\phi = \sqrt{\frac{\sum_{n=N_1}^{N_2-1} \sum_{k=0}^{K-1} \left(\phi_k - \overline{\phi}\right)^2 \beta_{n,k}^2}{\sum_{n=N_1}^{N_2-1} \sum_{k=0}^{K-1} \beta_{n,k}^2}} \tag{6.15}$$

where ϕ_k represents the kth angle considered in the calculation and n again is a time index. Equation 6.14 is referred to as the power-weighted average AOA, and equation 6.15 is called the rms angle-of-arrival (AOA) or angular spread.

In a narrowband context $\beta_{n,k}$ is the amplitude of the signal component incident at time n from angle k, and $\beta_{n,k}^2$ is then proportional to the incident signal power of this component. In the UWB case, if an assumption is made that all incident waveforms have the same shape, then $\beta_{n,k}$ is the amplitude of a signal incident from angle k at time sample n, and the energy in each pulse cancels between the numerator and the denominator. If the incident pulses are allowed to vary in shape in the calculations, then let $\beta_{n,k}^2$ represent the actual energy in the incident signal, calculated from the recovered waveform. The AOA and TOA statistics for both cases are summarized in Table 6.3 and Table 6.4. In these tables, $\overline{T}_a$ represents the absolute power-weighted average TOA, calculated without regard for the time-of-arrival of the LOS path signal. The symbol $\overline{T}_r$ represents a power- weighted average TOA which is calculated relative to the time-of-arrival of the LOS path signal. The resulting delay spread is the same in both cases.

Note that the angular spread is generally defined over some time window, given in the equation above as $[N_1, N_2 - 1]$. These results are reported for a single time interval which encompasses the entire measurement period in Figure 6-55, and for time intervals of 10 ns, in order to investigate variations in the channel statistics, in Figure 6-56 and Figure 6-57.

Figure 6-55 shows the power-weighted average AOA and the rms AOA, relative to the LOS path AOA, for the signals recovered at each measurement location, where the calculations are performed over the entire 300 ns window. In each plot, the results under an assumption of a static incident waveform and the results if the energy is derived from the individual recovered waveforms are shown. In general, the results corresponding to the two different calculations are close, which gives some validation to the assumption of a static

incident pulse shape. These results are summarized in Table 6.3 and Table 6.4, where the median values are also reported. Figure 6-56 shows the cumulative distribution function (CDF) of the calculated angular spreads. This compares with a figure in [29] for outdoor measurements, and the values calculated here are smaller than those in the reference, which is to be expected given that these measurements were made indoors.

The time delay spread is shown as a function of the measurement location in Figure 6-58. These results are catalogued in Table 6.3 and Table 6.4. Considering the results in Table 6.3, where the statistics are calculated without regard to the recovered waveform, the median power-weighted average TOA is given as $\overline{T}_{med} = 87.81$ ns in the absolute case and $\overline{T}_{med} = 51.98$ ns when calculated relative to the arrival time of the LOS path. For Table 6.4, the corresponding numbers are $\overline{T}_{med} = 89.51$ ns and $\overline{T}_{med} = 48.79$ ns. These averages are often not given in channel models, but the rms TOA is a commonly reported channel statistic. The result based on the recovered amplitudes only is $\sigma_T = 45.38$ ns, and $\sigma_T = 45.59$ ns is found when the energy in each recovered waveform is calculated. These numbers compare with median rms delay spreads of 25-50 ns reported in one set of indoor narrowband propagation measurements in an office building at 1.5 GHz [37], and 50-150 ns reported in another [35]. The worst case reported in Table 6.3 is $\sigma_T = 58.46$ ns and the standard deviation on the rms delay spread is 6.79 ns. In Table 6.4, the worst case is $\sigma_T = 54.88$ ns and the standard deviation of the rms delay spread is 6.68 ns. These results compare with worst case RMS delay spreads of 100-200 ns reported in another experiment [35]. The cumulative distribution function of the calculated angle spread numbers are shown in Figure 6-57.

From Table 6.3, Table 6.4 and the discussion above, it is seen that although there appears to be a rough correlation between the parameters and the SNR, as defined in equation 5.1, or propagation distance, the strongest dependence is on the geometry of the situation. This

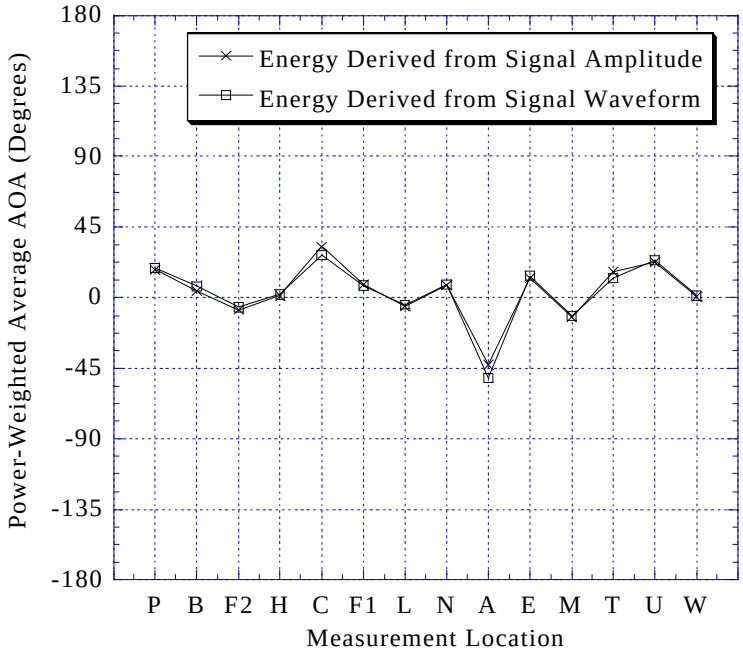

(a)

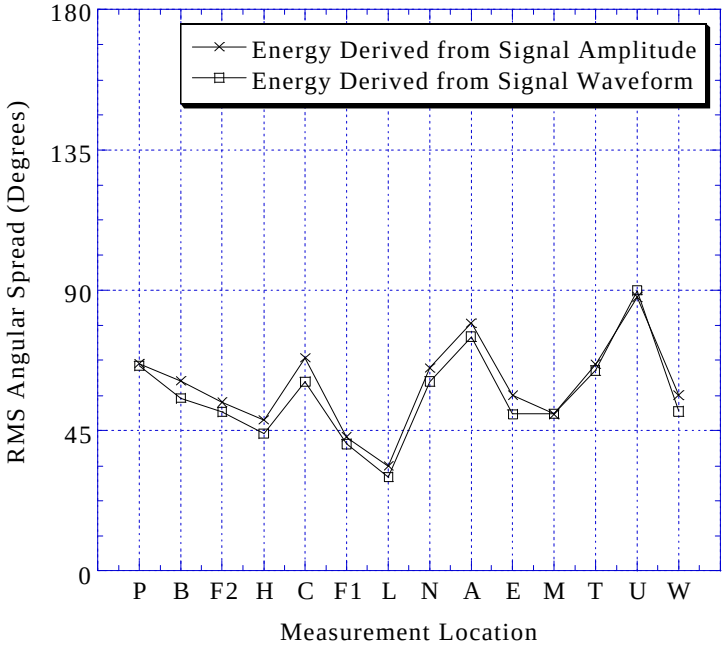

(b)

Figure 6-55: Power-weighted average AOA and rms angular spread for each measurement location. Calculations are reported relative to LOS path arrival angle.

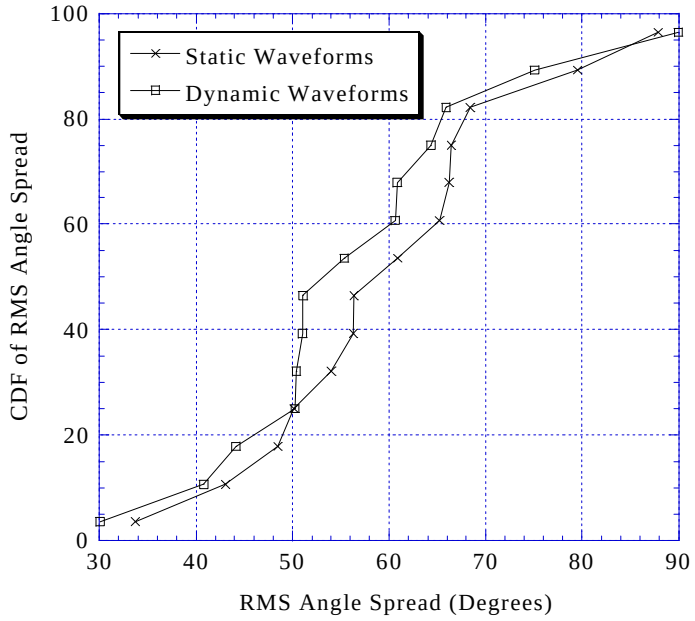

Figure 6-56: CDF of RMS angular spread, calculated over 300 ns window.

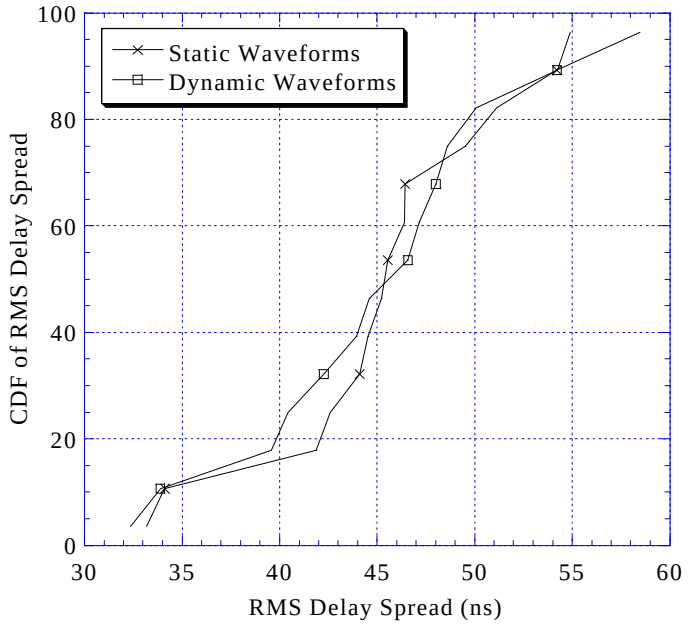

Figure 6-57: CDF of RMS delay spread, calculated over 300 ns window.

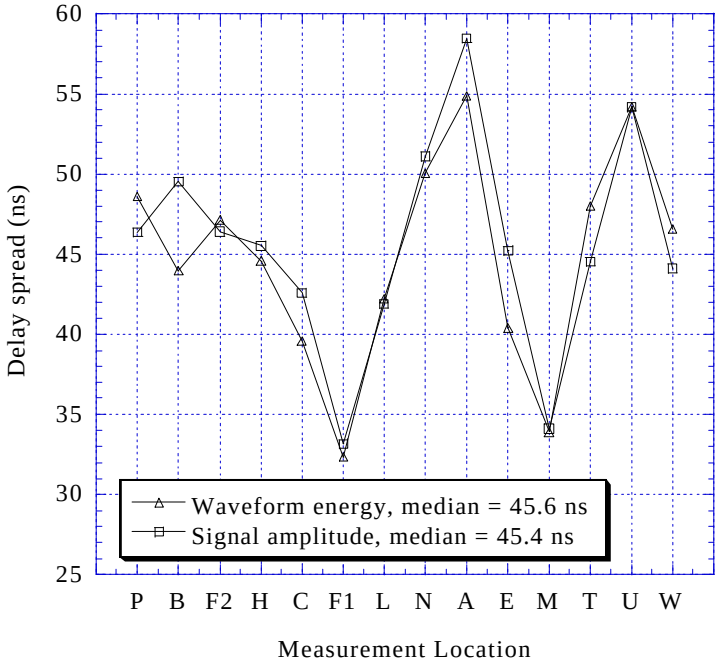

Figure 6-58: Delay spread as a function of measurement location. Results from the assumption that the signal energy is proportional to the recovered amplitude and from calculating the energy from the recovered waveform are shown.

Location	SNR (dB)	$\overline{T}_a$ (ns)	$\overline{T}_r$ (ns)	σ_T (ns)	$\overline{\phi}$ $(^o)$	σ_ϕ $(^o)$
P	31.93	72.96	52.11	46.38	17.95	66.41
B	11.56	112.89	53.86	49.53	4.01	60.92
F2	38.58	62.054	40.72	46.42	-7.80	54.00
H	18.88	91.59	54.97	45.52	1.30	48.45
C	13.76	110.32	50.26	42.58	32.49	68.39
F1	39.56	48.66	17.12	33.16	8.21	43.04
L	35.92	57.97	31.89	41.89	-5.43	33.68
N	25.98	67.16	46.90	51.12	7.78	65.24
A	-3.14	143.11	86.71	58.46	-42.94	79.52
E	-1.97	112.47	64.72	45.23	12.39	56.31
M	24.16	82.32	36.13	34.11	-12.22	50.14
T	21.08	93.05	55.50	44.53	16.69	66.24
U	15.69	104.69	66.85	54.20	22.52	87.87
W	23.09	84.03	51.85	44.09	0.52	56.35
Median	22.08	87.81	51.98	45.38	5.90	58.63

Table 6.3: Summary of propagation statistics when calculating energy from recovered signal amplitude

is similar to the narrowband case [30] and makes the properties difficult to predict without taking into account the floor plans.

6.3.3 Joint Spatio-Temporal Channel Models

The moments of the angular and temporal distribution of the received signal energy provide a description of the channel statistics which assumes that no correlation exists between the two measures. In [48], and [49] it is argued that this is a sufficient description of the channel; that, based upon a visual inspection of the received signal locations over time and angle, no apparent dependency exists. The goal of this section is to determine the extent to which this assumption holds for the UWB propagation experiment under consideration. It is important to note that the claim of time-invariant statistics given in [48] and [49] did not take into account the energy in the signal arrivals, but only the fact that an arrival had taken place. In the calculation of $\overline{\phi}$, $\overline{T}$, σ_ϕ and σ_T, on the other hand, the arrival statistics are weighted by the received signal energy. Contrary to the scatter diagram used to assess

Location	SNR (dB)	$\overline{T}_a$ (ns)	$\overline{T}_r$ (ns)	σ_T (ns)	$\overline{\phi}$ $(^o)$	σ_ϕ $(^o)$
P	42.14	76.07	55.22	48.61	18.64	65.88
B	20.69	100.79	41.76	43.95	7.39	55.33
F2	48.35	61.22	39.88	47.16	-6.11	51.06
H	27.12	93.36	56.74	44.61	2.09	44.14
C	24.11	98.57	38.51	39.56	27.02	60.61
F1	48.86	48.56	17.01	32.34	7.67	40.80
L	46.13	57.00	30.93	42.25	-4.58	30.06
N	35.99	64.38	44.11	50.06	8.35	60.84
A	-0.31	137.96	81.56	54.88	-51.38	75.06
E	2.02	106.79	59.03	40.42	14.06	50.27
M	33.05	81.03	34.84	33.90	-11.53	50.39
T	29.98	97.46	59.91	48.01	12.51	64.33
U	24.47	109.43	71.59	54.22	23.81	89.98
W	33.87	85.65	53.47	46.57	1.31	51.10
Median	31.56	89.51	48.79	45.59	7.53	53.21

Table 6.4: Summary of propagation statistics when calculating energy from recovered waveforms

these statistics in [48] and [49], a weak arrival does not carry the same weight in $\overline{\phi}$, $\overline{T}$, σ_ϕ and σ_T as does a higher energy arrival.

As a first measure of the time-variation of the UWB propagation channel, consider Figure 6-59 which shows the rms angular spread for the fourteen measurement locations as a function of time, using 10 ns wide bins to collect the received signal energy. The plot in (a) shows the results if no window is applied to the angular deviation from the mean, and in (b) a raised-cosine window is applied to the difference between the azimuth arrival angle of the received signal and the mean arrival angle. The purpose of this window is to limit the effect that a signal incident from a large angular deviation can have on the statistics. Overlaid onto each of these plots is the mean rms angular spread and $\pm 1\sigma$ bounds. From the plots it can be seen that the rms angular spread does vary as a function of time, taking on a broader range of values as time progresses. The cumulative distribution functions of the angular spread are shown in Figure 6-60, with and without a raised cosine filter on the angular deviation from the mean. This plot shows the ranges of values taken on by the

angular spread over the 300 ns window. It is clear from these plots that the angular spread is not static, but does take on different values as time progresses.

In the plots it is noted that the angular spread increases as a function of time, to a point, then decreases near the end of the 300 ns window. This decrease is an artifact that is due to the data from some measurement locations containing no signal arrivals in these late time bins. These measurement locations then contribute nothing to the mean calculation, which reduces the value.

6.3.4 Spatio-Temporal Distributions

In order to describe the spatio-temporal properties of the channel, the cumulative distribution function (CDF) for the incident UWB signals is calculated from the recovered signal information. First consider the distribution functions which results from a uniform weighting of all arrivals, assuming that all signals are incident with equal energy. This will allow for a further examination of the time variance of the UWB channel statistics against the claim of time-invariance made in [48] and [49]. This is shown for the measurement at location P in Figure 6-61 and location B in Figure 6-62. A noticeable difference between the plots is the arrival time of the first component, caused by the difference in the LOS path length between the two sets of measurements. Considering the time variation in the response of these channels, the marginal CDF for the two locations is shown in Figure 6-63 and Figure 6-64 along with a uniform CDF. The direction of increasing time is shown, and the degree to which the distributions change as a function of time is noted. The recovered signals from measurement location P are seen to be distributed more uniformly than those from location B. This was also noted in Figure 6-2 - Figure 6-10.

If all measurement locations are considered and the angle-of-arrival of each component is reported relative the angle-of-arrival of the LOS path for the particular measurement

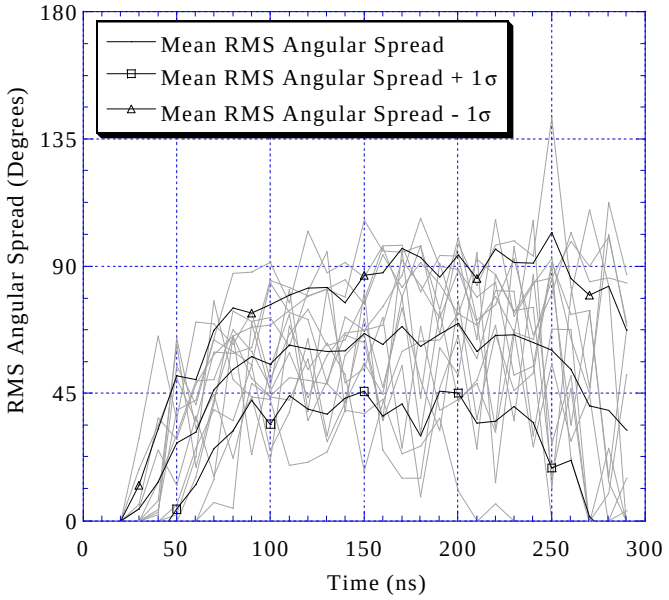

(a)

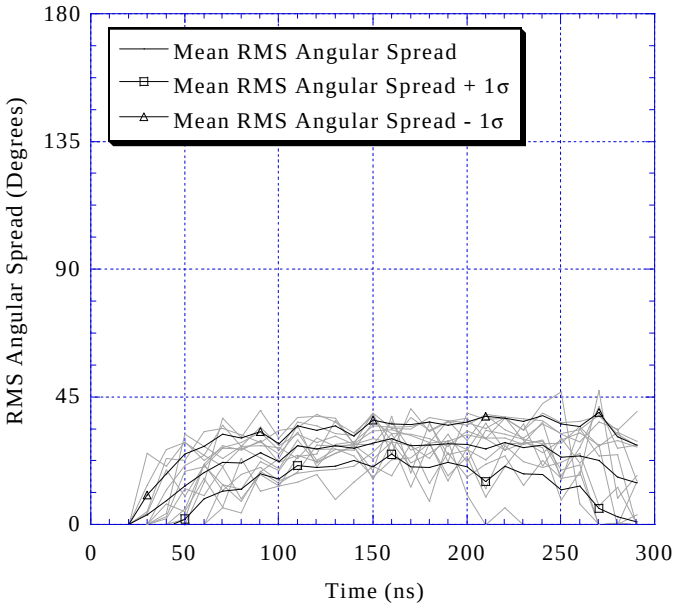

(b)

Figure 6-59: Power weighted rms angular spread (a) without and (b) with a raised cosine window for the 14 measurement locations. Mean angular spread and mean $\pm$ 1σ is overlayed.

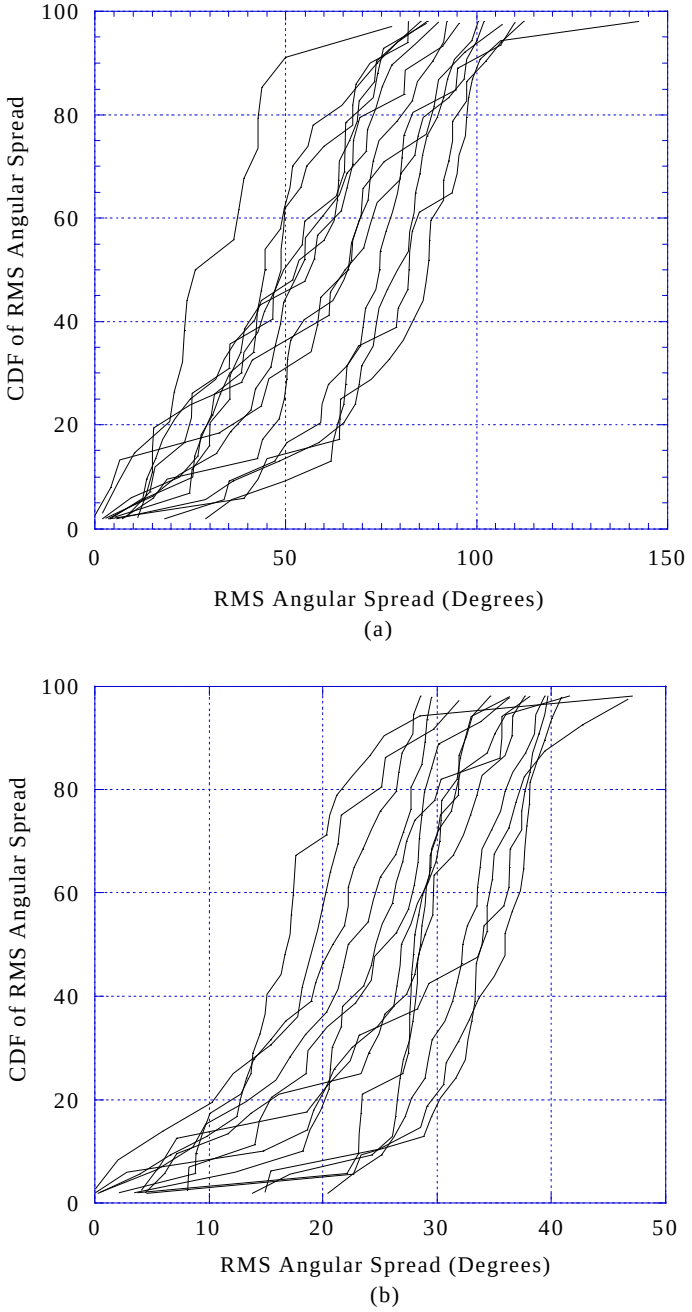

Figure 6-60: CDF of RMS angle spread calculated in 10 ns windows, for the 14 measurement locations. A raised cosine filter is applied to the results in (b).

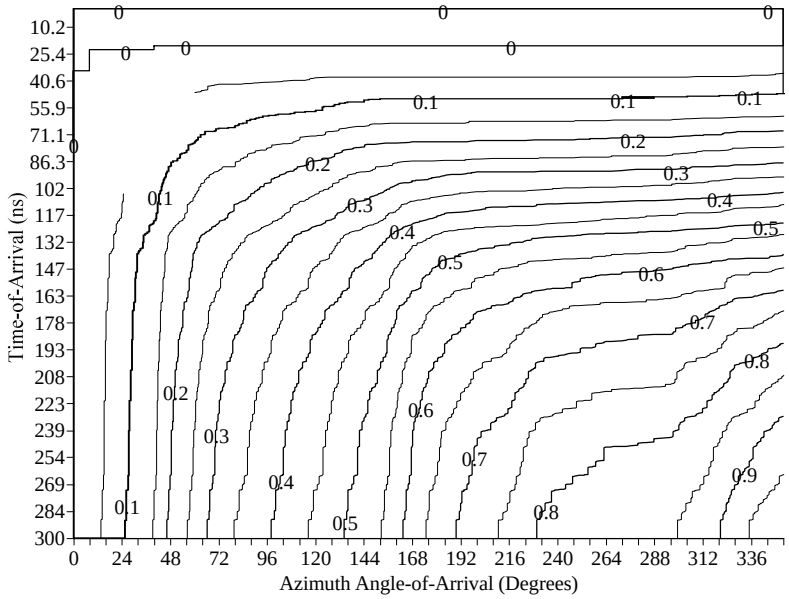

Figure 6-61: Distribution of incident signals at location P, with uniform weighting on each signal arrival.

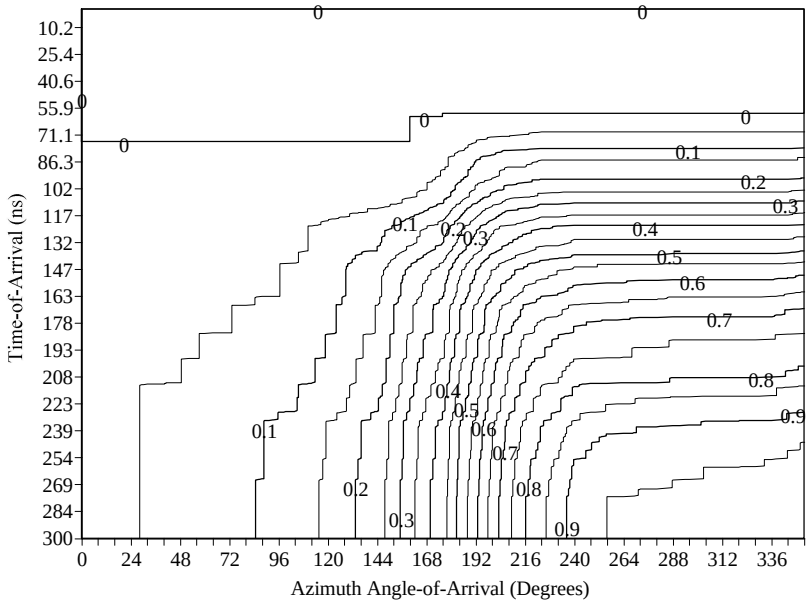

Figure 6-62: Distribution of incident signals at location B, with uniform weighting on each signal arrival.

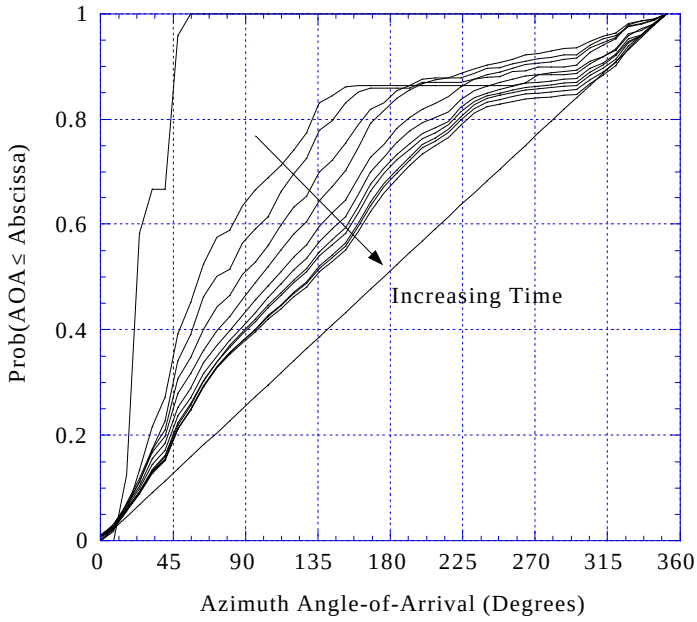

Figure 6-63: Marginal distributions as a function of time for the measurements at location P. A uniform distribution is also shown.

location, the resulting CDF of the signal arrivals is shown in Figure 6-65. The marginal distributions as a function of time are shown in Figure 6-66. It is clear from these plots that the statistics associated with a uniform weighting of the signals in the distribution do vary to some extent as a function of time for the UWB propagation channel under consideration.

In the interests of predicting communication system performance, it is not only the existence of a signal at a particular location in time and space that matters, but the energy carried by the signal as well, for a given noise level. For example, the bit error rate of a communication system is generally characterized by the bit energy to noise spectral density ratio, and is independent of other parameters related to the propagation channel. This motivates the study of the spatio-temporal distribution of the received signal energy. Define the distribution functions in this case by assigning a weight to each incident signal proportional to the recovered energy. For an angular increment of $\Delta\theta$ and a sampling frequency of $\frac{1}{\Delta t}$

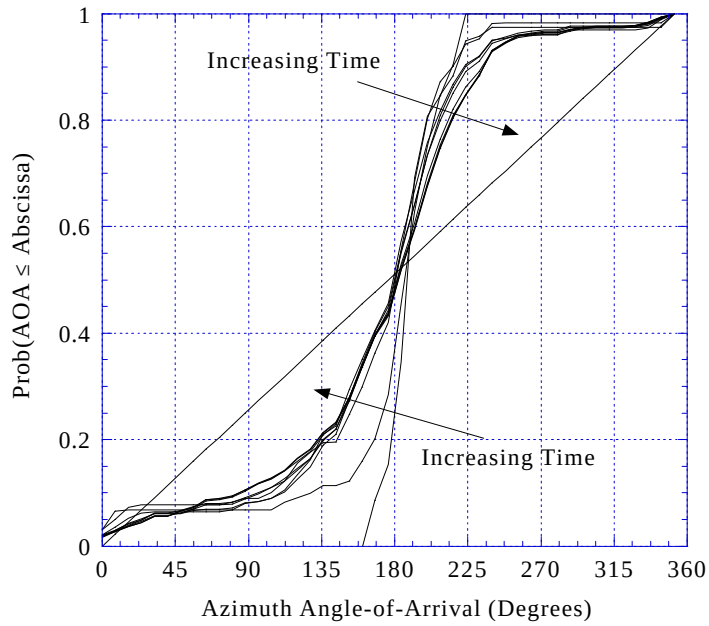

Figure 6-64: Marginal distributions as a function of time for the measurements at location B. A uniform distribution is also shown.

seconds, this weighted cumulative distribution function (CDF) is then calculated according to

$$\begin{aligned} F_{\theta,\tau}(k,n) &= \Pr\{\theta \square k\Delta\theta, t \square n\Delta t\} \\ &= \frac{1}{E}\sum_{j=0}^{k}\sum_{m=0}^{n}\beta_{m,j}^{2} \end{aligned} \tag{6.16}$$

where $k = 0, ..., K-1$, $n = 0, ..., N-1$, and $\beta_{m,j}^2$ has the same meaning as above, it is the energy in the received signal, either corresponding to the square of the amplitude of the component found at time m and angle j under an assumption of static incident waveforms, or as computed from the recovered waveform. The quantity E is the total recovered energy in all signal components, resulting from allowing the summations to run over the entire data

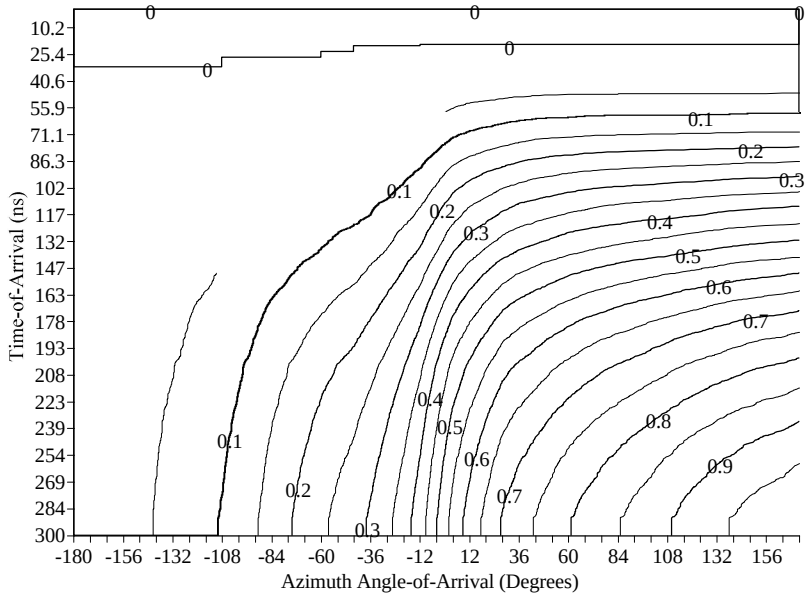

Figure 6-65: Distribution of incident signals from all locations, with uniform weighting on each signal arrival. All angles are relative to LOS angle-of-incidence for the measurement location.

collection window in time and in angle. Distributions calculated according to 6.16 will be referred to as (energy) weighted distributions or weighted cumulative distribution functions (CDFs), to distinguish them from distributions which account only for signal arrivals.

Examples of the weighted CDF for measurement locations P and B are shown in Figure 6-67 and Figure 6-68, respectively. In both of these figures, it is noted that the recovered signal for azimuth angles close to the LOS path contributes significantly to the total received signal energy, and the distribution is therefore less uniform than those in Figure 6-61 and Figure 6-62, where all signals were weighted equally.

As another case of interest, consider Figure 6-69, which shows the weighted CDF of energy arrival at location A, the measurement location with the lowest SNR. As demonstrated above, the algorithms had a great deal of difficulty estimating the waveform of the LOS path in this case. Even in this low SNR case, although the received signal energy is

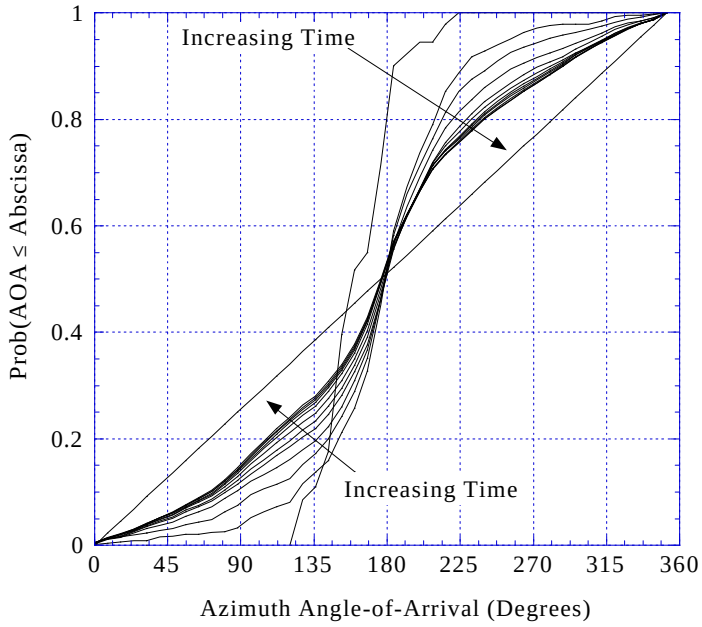

Figure 6-66: Marginal distributions as a function of time for the measurements at all locations. Each recovered signal contributes equally to the distribution functions. A uniform distribution is also shown.

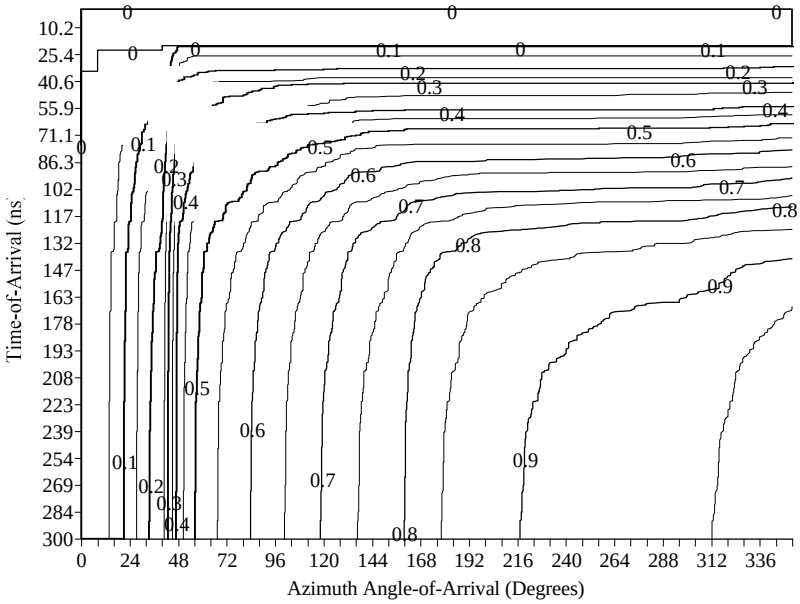

Figure 6-67: Weighted distribution of the received signal energy at location P when estimated from the recovered waveforms.

distributed more uniformly than the energy recovered either at location A or P, it is still biased around the LOS arrival angle.

As above, it is of interest to determine a measure of average performance or an average distribution which takes into account all measurement locations. There are two ways to consider this average. The first is to maintain the absolute relation in the total recovered energy between the measurement locations. The contribution from each location is then weighted in the distribution function by the recovered energy at the location divided by the energy recovered from all locations. The weighted CDF which results from maintaining this absolute relation between the recovered signal energies is shown in Figure 6-70, where all angles are reported relative to the LOS path arrival angle for the particular measurement location. The second approach is to generate a distribution function under the assumption that the channel or location within the building is selected randomly from all possible locations. This might be an appropriate assumption in a mobile scenario, where the receiver

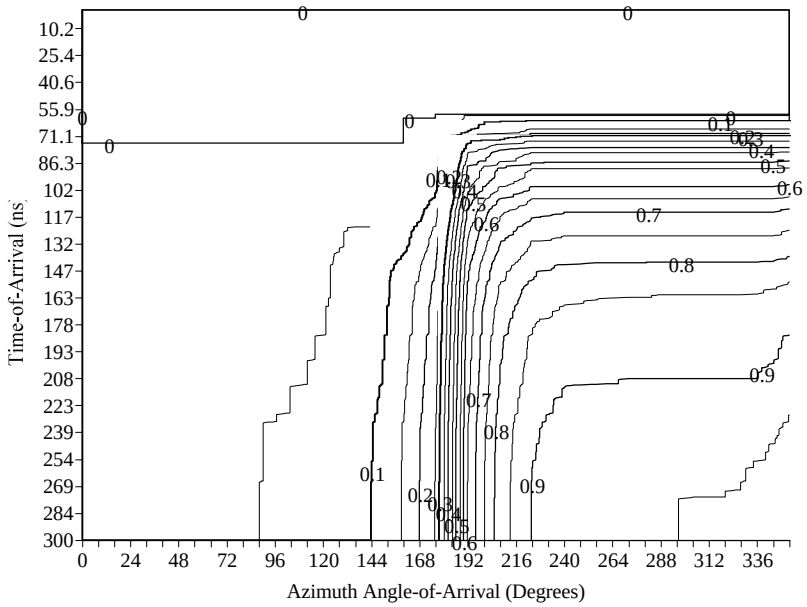

Figure 6-68: Weighted distribution of the received signal energy at location B when estimated from the recovered waveforms.

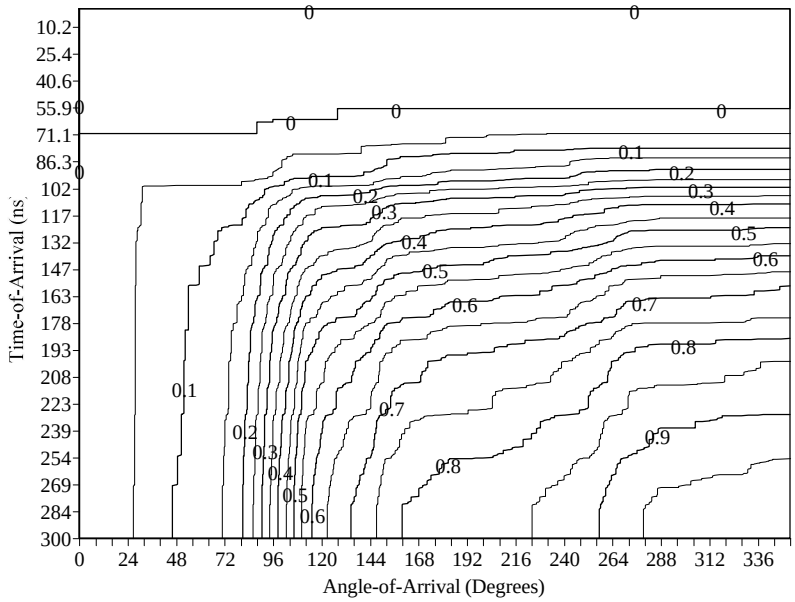

Figure 6-69: Weighted distribution of the received signal energy at location A when estimated from the recovered waveforms.

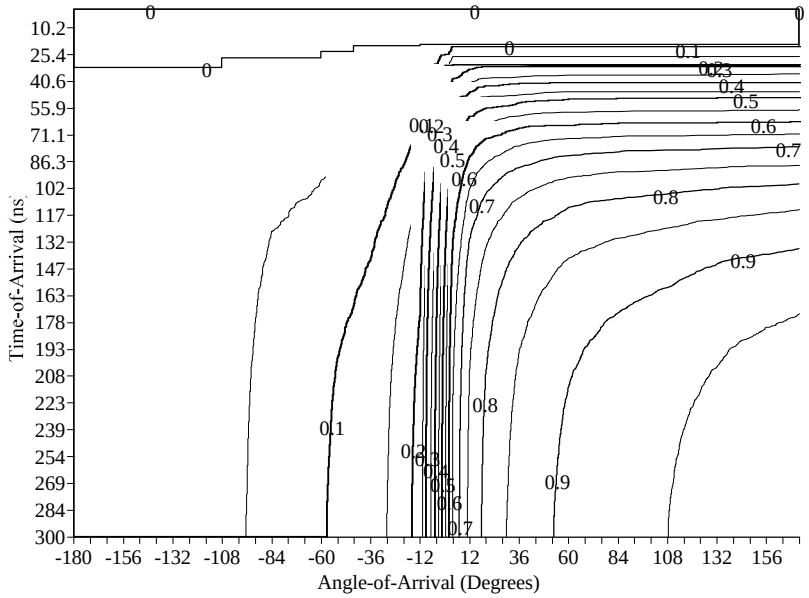

Figure 6-70: Weighted distribution of received signal energy over time and angle for all measurement locations. Energy is calculated from recovered waveforms.

is equally likely to be at any location in the building. In this case all channels contribute equally to the overall distribution, each getting a weight of 1/14 here, for the 14 different measurement locations. Within the distribution function for each channel, individual components are weighted according the signal energy. The distribution function associated with this scenario is shown in Figure 6-72, where again all angles are reported relative to the LOS path for the particular measurement location. Marginal distribution functions associated with these spatio-temporal distributions are shown in Figure 6-71 and Figure 6-73.

The results above are useful in terms of understanding the effect of the channel on propagating UWB signals. However, these results can exhibit a bias due to a large number of signals without enough energy to provide a reliable communication link, but with enough energy collectively to generate a noticeable effect on the distributions. In order to further the practical significance of the results, additional constraints were therefore placed on the contributing signals. In particular, two constraints were considered. The first involves the

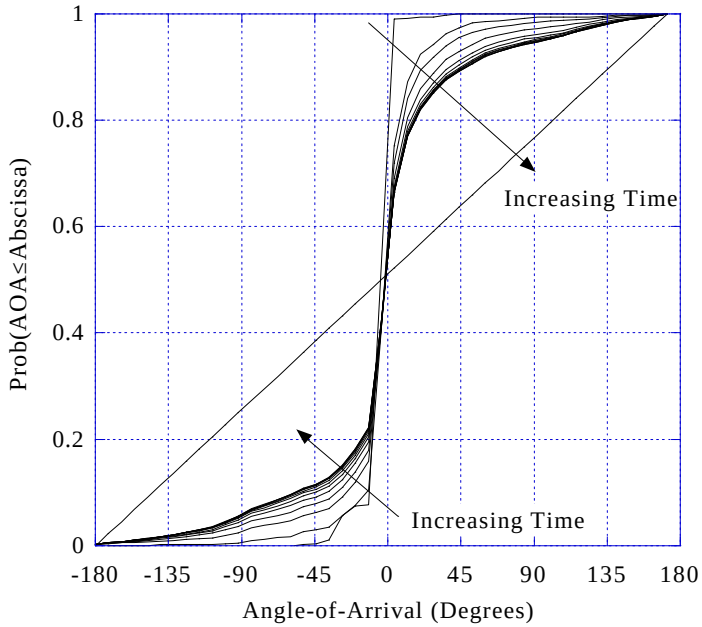

Figure 6-71: Marginal distribution functions vs. time. Each measurement location contributes an amount proportional to the received energy at that location divided by the total received energy.

realization that diversity reception is of interest in the indoor multipath channel. In a typical rake receiver, some finite number of correlators are available for the processing the received signals. Therefore the distribution of the received signal energy contained in some number of the strongest paths is of interest. For the purposes of this work, ten paths were selected. The weighted distribution of the signal energy in the ten strongest paths from all measurement locations is shown in Figure 6-74 and Figure 6-75 for the absolute and equiprobable channel cases, respectively.

Given that a rake receiver might not always select the strongest available paths or that these paths may be transient, particularly in an indoor or shadowed environment, the distribution functions were also characterized by only allowing signals within some number of decibels of the strongest arrival in each measurement location to contribute. For the

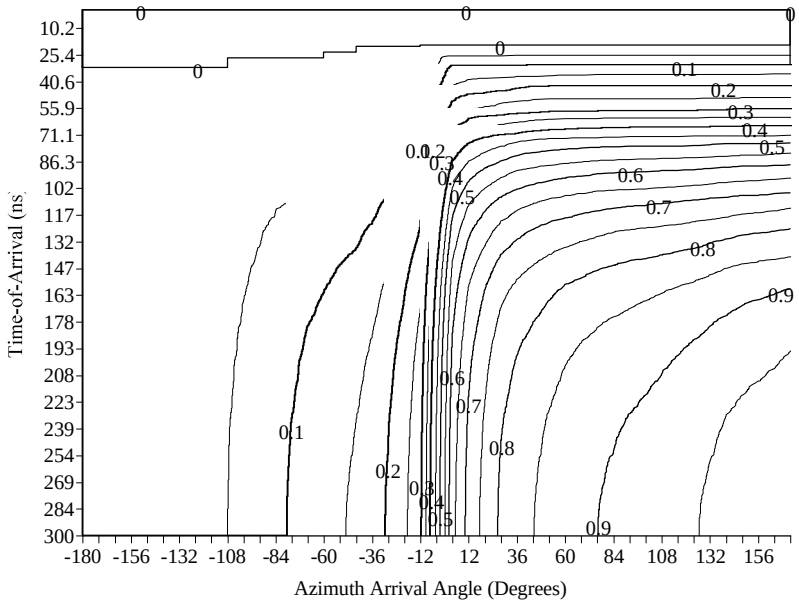

Figure 6-72: Weighted distribution of received signal energy over time and angle for all measurement locations, where each location contributes equally. Energy is calculated from recoverd waveforms.

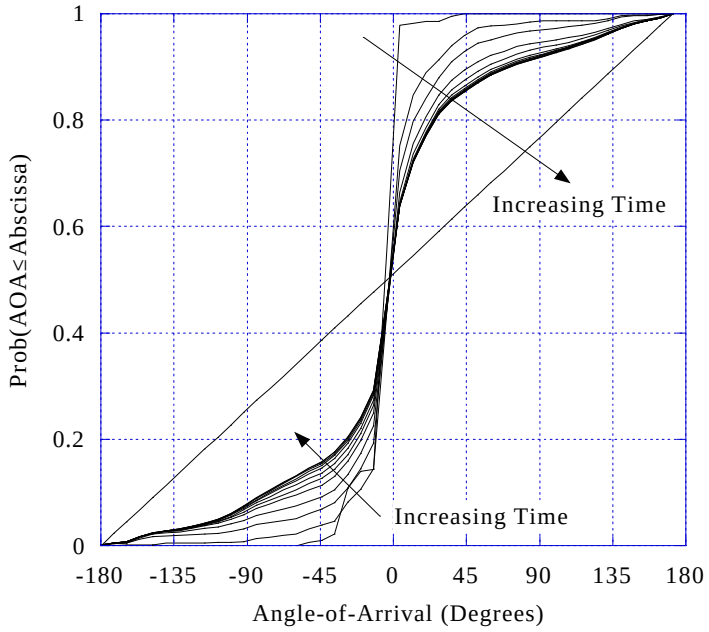

Figure 6-73: Marginal distribution functions vs. time for the case where each measuement location contributes an equal amount to the distributions.

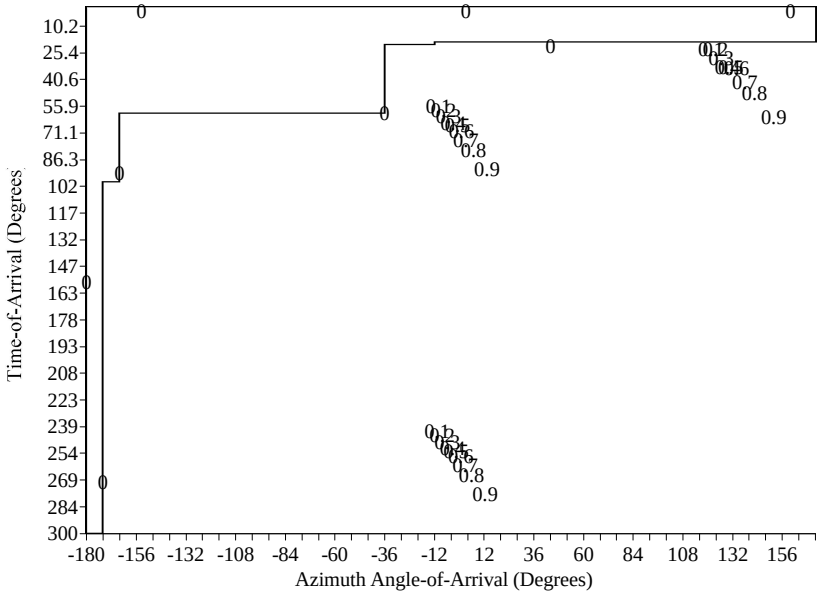

Figure 6-74: Weighted distribution of received signal energy over time and angle for all measurement locations, where only the largest ten signals at each location are considered.

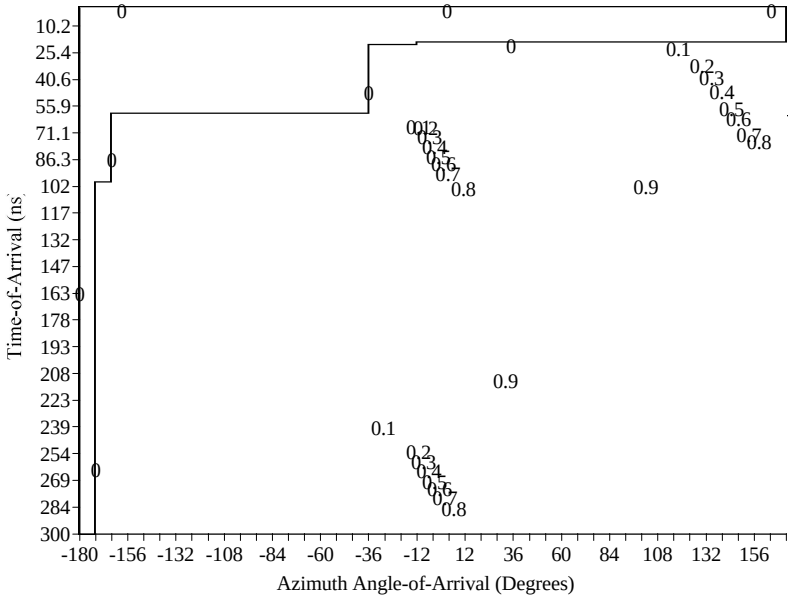

Figure 6-75: Weighted distribution of received signal energy over time and angle for all measurement locations, where only the largest ten signals at each location are considered. The contribution from each measurement location is weighted equally.

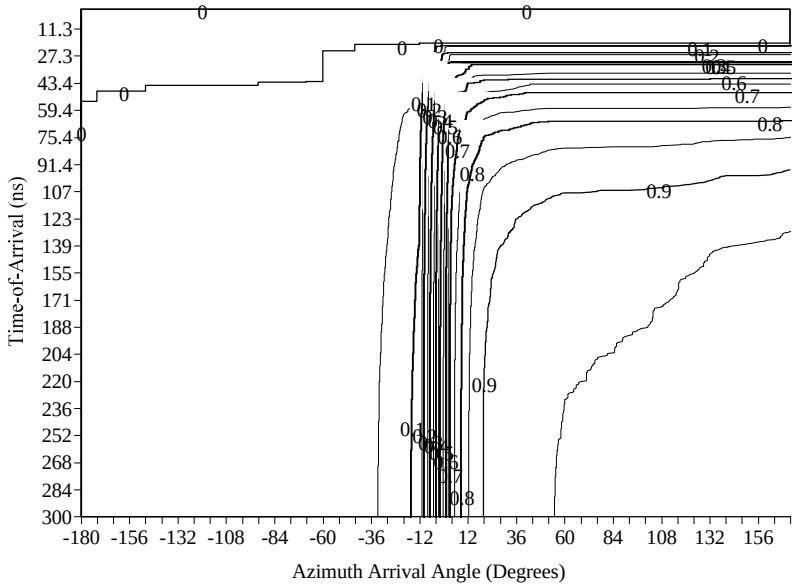

Figure 6-76: Weighted distribution of received signal energy over time and angle for all measurement locations, where only signals with received energy within 12dB of the largest signal at each measurement location are considered. The contribution from each measurement location is weighted equally.

results presented here, all signals within 12 dB of the strongest arrival in each measurement location were allowed to contribute to the weighted distribution functions. These results are shown in Figure 6-76 and Figure 6-77.

From a visual inspection, the threshold based on the signal energy rather than on the absolute number of contributing paths seems to have the effect of increasing the variance of the distribution slightly. This is due to the fact that the energy threshold permits more signals to contribute to the distribution. In general, however, both of these thresholds seem to lead to the same conclusion that the bulk of the recovered signal energy is contained in a relatively small range of arrival angles around the LOS path arrival angle.

Weighted distribution functions were also generated under the assumption of static incident waveforms, where the energy is calculated from the recovered signal amplitude information only. These are shown below in Figure 6-78 - Figure 6-83.

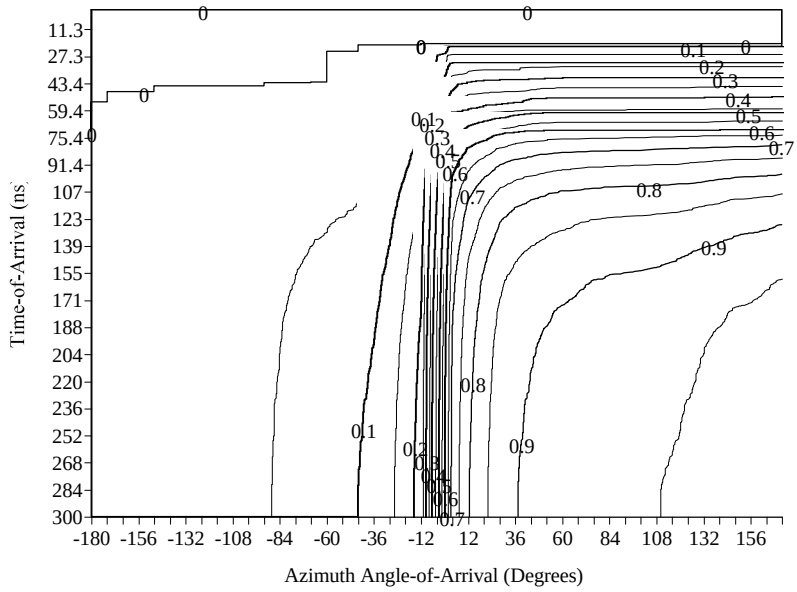

Figure 6-77: Weighted distribution of received signal energy over time and angle for all measurement locations, where only signals with received energy within 12dB of the largest signal at each measurement location are considered. The contribution from each measurement location is weighted equally.

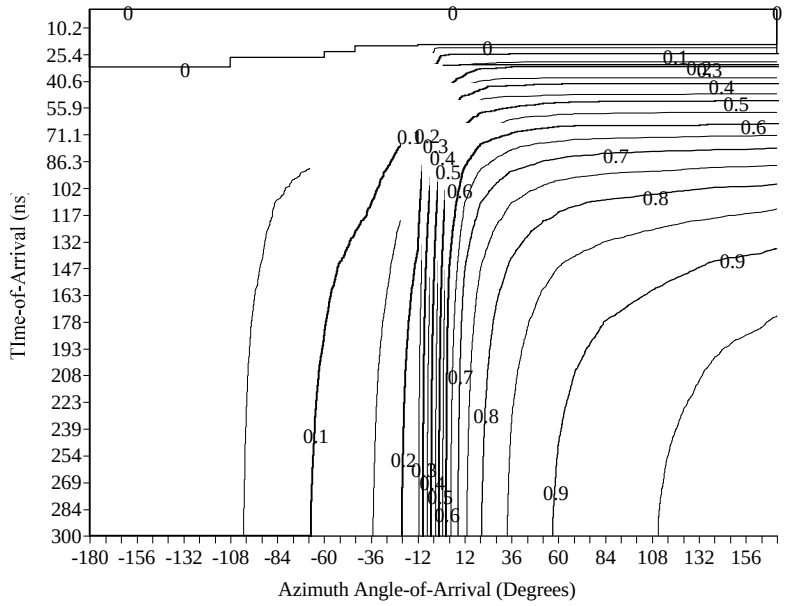

Figure 6-78: Weighted distribution of received signal energy over time and angle for all measurement locations. Energy is calculated from recovered signal amplitude.

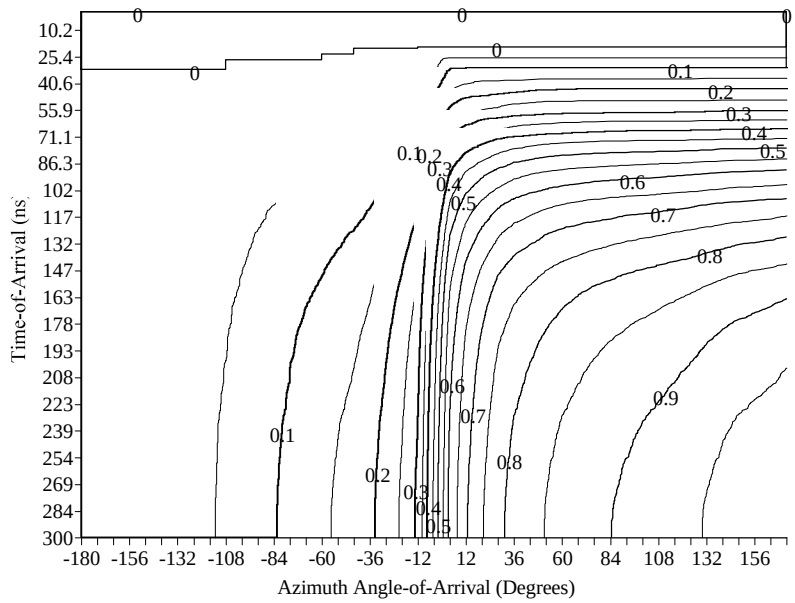

Figure 6-79: Weighted distribution of received signal energy over time and angle for all measurement locations. Each location contributes equally to the distribution. Energy is calculated from recovered signal amplitude.

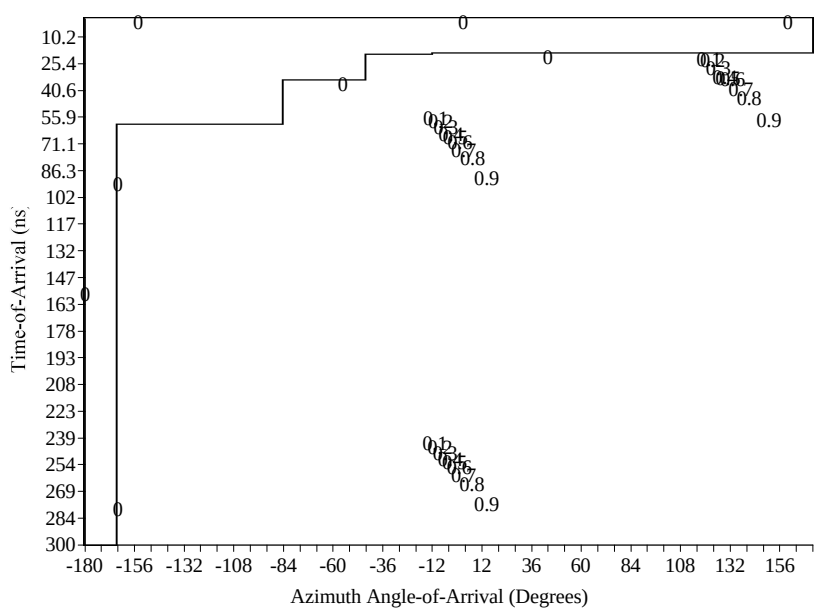

Figure 6-80: Weighted distribution of received signal energy over time and angle of the ten largest signals at each measurement location. Energy is calculated from recovered signal amplitude.

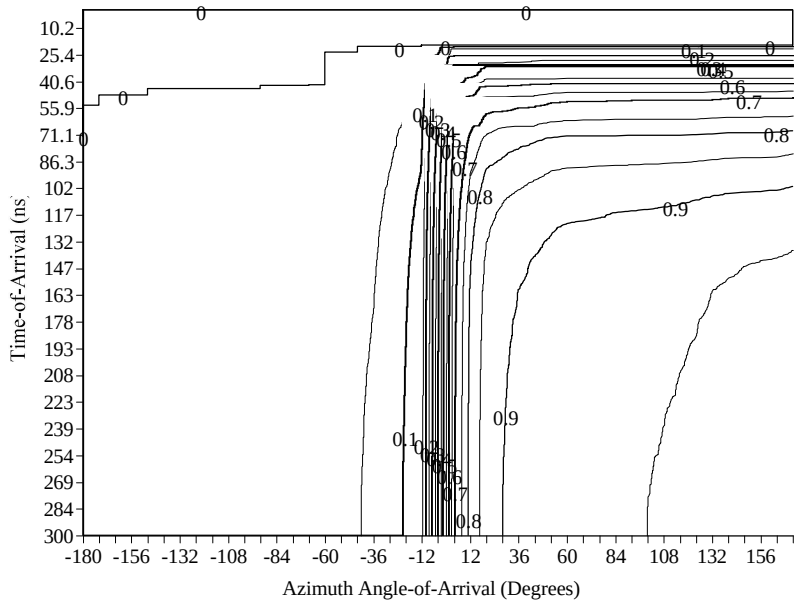

Figure 6-81: Weighted distribution of received signal energy over time and angle for all signals with energy within 12dB of the largest signal at each location. Energy is calculated from recovered signal amplitude.

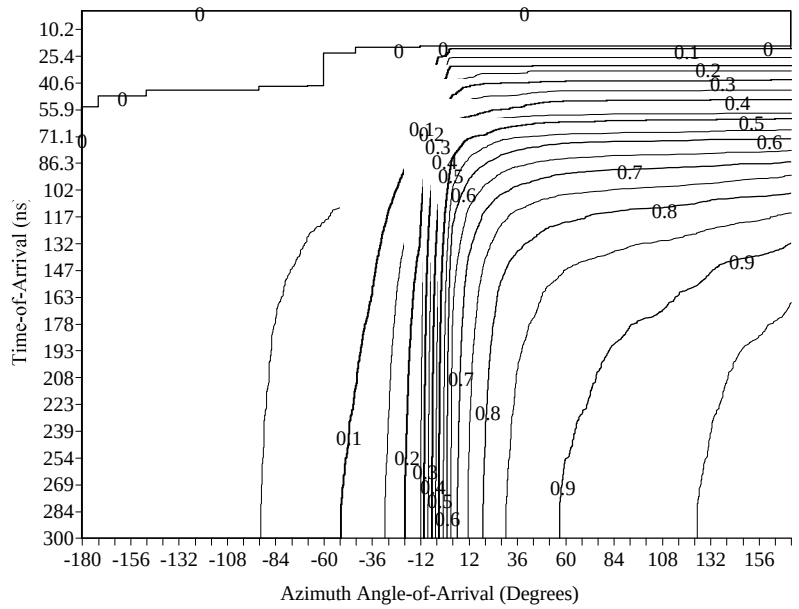

Figure 6-82: Weighted distribution of received signal energy over time and angle for the ten largest signals at each measurement location. Each location contributes equally to the distribution. Energy is calculated from recovered signal amplitude.

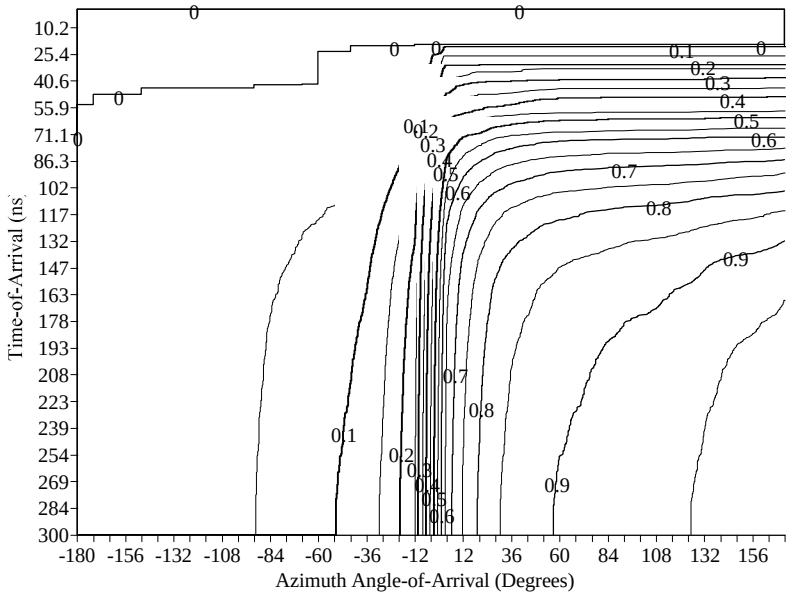

Figure 6-83: Weighted distribution of received signal energy over time and angle for all signals within 12dB of the largest signal at each measurement location. Each location contributes equally to the distribution. Energy is calculated from recovered signal amplitude.

6.4 Summary

In this chapter, the processing techniques developed in Chapter 4 and Chapter 5 were applied to the measured propagation data described in Chapter 1. The resulting signal information was used to develop models of the indoor UWB propagation channel. Several different models were developed to analyze different aspects of the UWB propagation problem. When comparable parameters existed, comparisons were drawn with more narrowband channel models from the literature.

The characterization provided in this chapter for the UWB propagation channel reflects measurement made at a number of locations in a single building. As has been reported in previous propagation experiments, the architecture of the building and the geometry of the particular situation can often have a strong impact on the received signals. As these results are based upon measurement taken in a single building, it is possible that additional

experiments will need to be conducted in different buildings in order to increase confidence in the parameters of a propagation model. It is possible, then, that although this work presents a propagation model for UWB signals in an indoor environment, the strongest contribution of this research will be in the development of a technique to facilitate the high-resolution analysis and processing of received UWB signals.

Chapter 7

Further Results on the Characterization of the UWB Propagation Channel

In the previous chapter, channel models were derived to describe the spatio-temporal distribution of the received UWB signal energy in an indoor environment. In this chapter, further studies are conducted on the signal information recovered from the processing algorithms. These include a ray-tracing study based on the angle-of-arrival of the received signal and the orientation of the transmitter and the receiver, under the assumption of a single-bounce elliptical model. This information may prove useful in the development of diversity reception schemes.

In addition to angle and time-of-arrival information, the Arrival Combiner also generates estimates of the received signals. These are examined here as well, in order to understand typical variations in the received pulse shape encountered in the indoor channel.

This chapter ends with an attempt to synthesize an UWB propagation channel based upon the cluster models from the previous chapter. The ability to accurately synthesize UWB propagation channels is significant in that it gives a realistic environment in which UWB radio algorithms can be tested and verified in software.

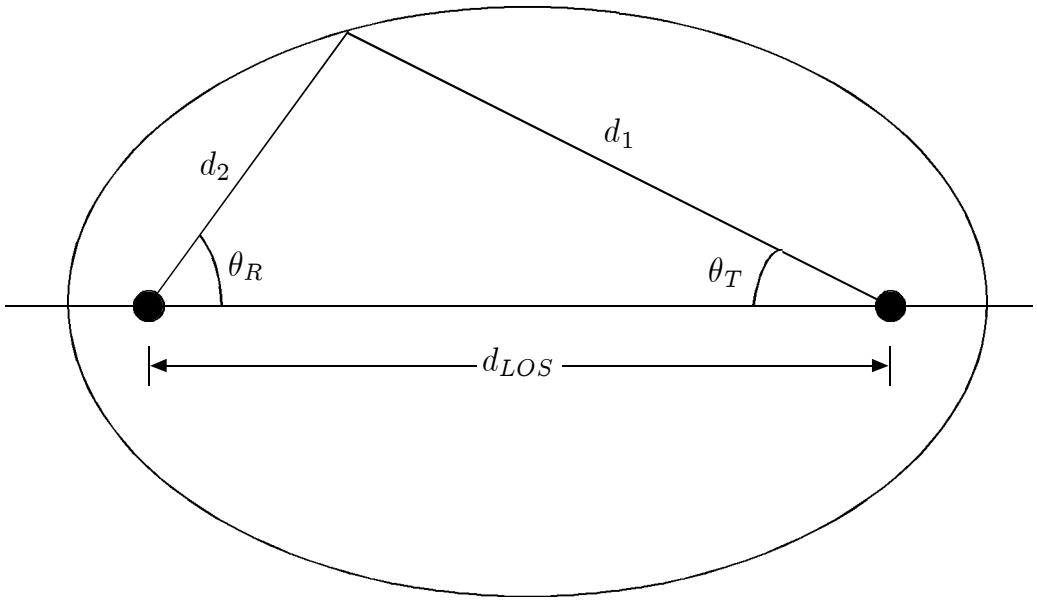

Figure 7-1: Ellipse which describes signal reflection

7.1 Ray tracing (Implications for Diversity)

Considering the applications for UWB radio discussed in Chapter 1, it is of interest to examine diversity algorithms for these systems. In particular, for the indoor environment, a useful performance measure is the ability of UWB communication systems to overcome transient blockages in the received signal paths, through the coherent addition of multipath signal components in a rake-type receiver. Given this measure, the resources required to maintain a communication link with a certain probability can be calculated.

Consider the transmitter and receiver pair shown in Figure 7-1, where the ellipse describes the locus of reflectors for all paths of identical propagation length corresponding to a single reflection. Let θ_T represent the angle at which a signal component emanates from the transmitter, and let θ_R represent the received angle. Given θ_R, the signal propagation distance and the LOS propagation distance, the angle θ_T at which the component is transmitted can be uniquely determined, based on the assumption of a single reflection.

Denote the LOS propagation distance by d_{LOS}, and the total propagation distance of the signal by $d = d_1 + d_2$. The eccentricity of the ellipse is then given by $e = d_{LOS}/d$. Defining

$$l = 0.5\left(d - \frac{d_{LOS}^2}{d}\right), \tag{7.1}$$

the distance d_2 can be calculated according to

$$d_2 = \frac{l}{1 - e\cos(\theta_R)}. \tag{7.2}$$

The angle θ_T is then given by

$$\theta_T = \cos^{-1}\left(\frac{d_{LOS} - d_2\cos\theta_R}{d - d_2}\right) \tag{7.3}$$

where this angle must be reflected about the major axis of the ellipse if θ_R is negative.

In practice, the utility of this approach is limited by the lack of an analytic technique for discriminating signal components which arrive at the receiver after a single reflection from those corresponding to multiple reflections. At present, this is accomplished either by correlating the calculated locations of the reflectors against the floor plan or by incorporating filters on the overall path length $d = d_1 + d_2$ or on the height at which the reflection occurs. The latter condition requires the received elevation angle to be incorporated into the calculations. From the received elevation angle,ϕ_2, the elevation angle at which the signal emanates from the transmitter can be calculated as,

$$\phi_1 = \cos^{-1}\left(\frac{d_2}{d_1}\cos\phi_2\right). \tag{7.4}$$

The vertical distance from the array to the point at which the reflection occurs, under the single-bounce elliptical model, is then $d_1 \cos \phi_1$. Assuming that the signal does not penetrate the ceiling or the floor, this parameter can be used to place a filter on the calculated location of the reflections, based upon the physical realities of the building.

The location of the reflections in the building calculated this way are shown for two different cases below. In both figures, the transmitter is located at the origin of the coordinate system, and the calculated location of the reflections are indicated throughout the building. Figure 7-2 shows the calculated reflection locations if the ten largest signals at each measurement location are considered. Figure 7-3 shows the results of the same calculations if all signals within 12 dB of the largest signal at each measurement location are considered. As can be seen from these plots, is difficult to draw meaningful conclusions regarding these results. One interesting note is that the corners of the rooms, particularly those closest to the transmitter do seem to be a likely place for a reflection to occur.

Potential advantages of UWB communication systems which employ baseband signals in the indoor environment include the ability to penetrate obstructions and the fine multipath resolution afforded by the narrow pulse width. These properties are useful since they increases the probability that a signal path will exist between the transmitter and the receiver. In general, the greater the angular spread of distinct paths between the transmitter and the receiver, the greater the probability of overcoming a transient blockage in the signal path, or equivalently, the lower the probability that all paths are not available.

In Figure 7-4 and Figure 7-5, the incident signal azimuth angle-of-arrival and the calculated transmit angle are shown for the ten largest paths at each measurement location and for all detected signals within 12 dB of the largest arrival, respectively. The effect of the single bounce elliptical model on the results is noted immediately in the results. For example, a transmit and receive angle pair must both be either in the range from 0° to

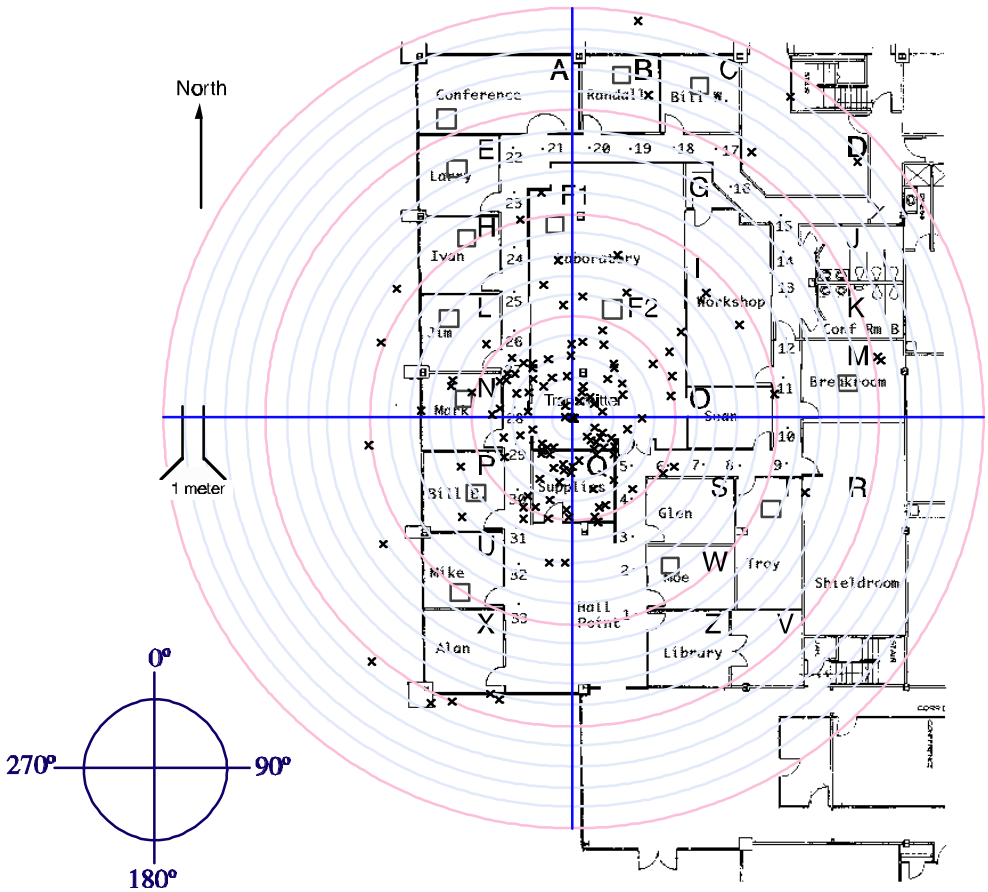

Figure 7-2: Calculated location of reflection for a single bounce elliptical model. The ten largest signals at each measurement location are considered.

180° or from 0° to -180°. The propensity of the reflections to occur close to the line-of-sight path, either at a transmit azimuth angle of 0° or 180°, and a corresponding receive azimuth angle of 0° or 180°, is also noted.

Considering the figures, for each azimuth angle at which a signal is received, the range of transmit angles which can give rise to this receive angle in the measured data is seen. The ability of an UWB communication system operating in this channel to overcome transient blockages or obstructions is a function of this angular spread.

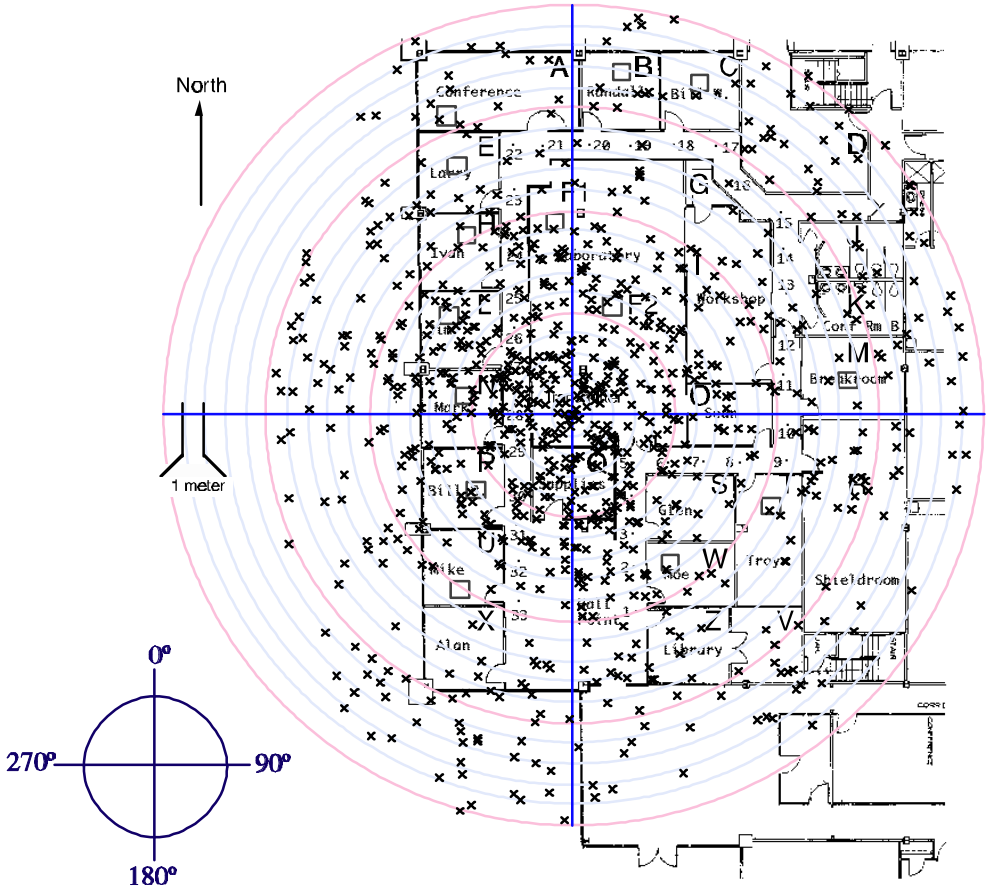

Figure 7-3: Calculated location of reflection for a single bounce elliptical model. All signals within 12dB of the largest signal at each measurement location are considered.

7.2 Received Waveforms (Eye-Diagrams)

When designing receivers for a communication system, it is important to understand the effect of the channel upon the transmitted signals, or, equivalently, to understand what the received signal is expected to look like. The receiver will generally include a filter or a correlator matched to the anticipated form of the received signal. A result with practical significance is therefore a characterization of the actual shape of the UWB signals received

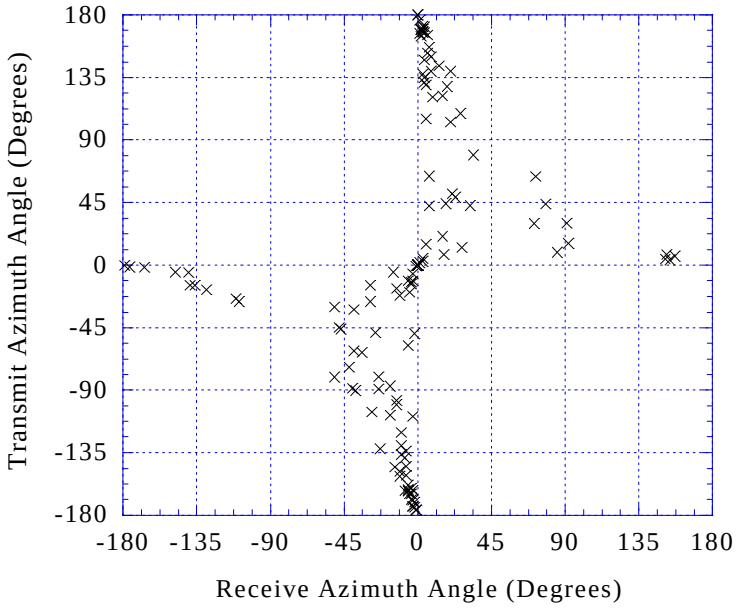

Figure 7-4: Recovered azimuth angle-of-arrival vs. calculated transmit angle for the single bounce elliptical model. The ten largest signals from each measurement location are considered.

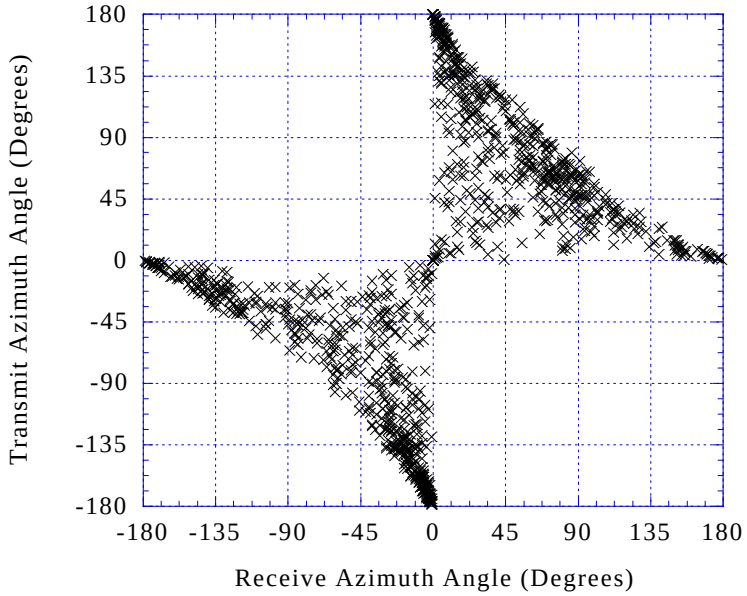

Figure 7-5: Recovered azimuth angle-of-arrival vs. calculated transmit angle for the single bounce elliptical model. All signals within 12dB of the largest signal at each measurement location are considered.

in the indoor environment. This information may find utility in the design of receivers for UWB communication systems.

Considering first the signal which arrives along the direct path or the LOS path, the recovered UWB signals are shown in Figure 7-6. In this diagram, the peak amplitude of each signal is normalized to one, and the waveforms are aligned so that this peak occurs at a common time sample. As can be seen from the figure, many of the normalized direct path waveforms have a similar shape, and in particular, a similar width from the peak to the first zero-crossing on either side. Recalling the recovered waveforms shown in Figure 6-12 through Figure 6-27, the waveforms which appear inverted may be from a propagation path which includes no walls, such as the measurements at location F2. These plots give an idea of what the characteristics of a filter matched to the direct path signal might need to be.

In a diversity or rake receiver, the goal is to consider more than one signal component. This implies that the characteristics of signals other than the direct path are also of interest. Defining the SNR as in equation 6.2, a detection threshold on the received signals is set at 12 dB below the SNR of the direct path signal at each measurement location. The lower envelope is defined as the smallest pulse width that might be encountered in a particular channel, and the upper envelope width is determined by the waveform with the largest extent in time that might be encountered in the channel. These numbers are determined by independently considering the upper and lower zero crossings on either side of the peak of the received signal waveform. In Figure 7-7, the ratio of the pulse with the largest support in time to the received waveform with the smallest support in time at each measurement location is plotted. There is a clear trend here in terms of the SNR of the LOS path at a particular measurement location. The larger the LOS SNR, the closer the ratio of the signal widths is to one, and the lower the SNR, the more this ratio tends to deviate from one. Two interpretations of this result can be put forth. First, the higher the SNR, the fewer the number of obstructions the pulse has experienced in propagating from the transmitter to the receiver. Thus fewer dispersion or distortion mechanism have perturbed the pulse, and the result is less variation in the shape of the received pulse. The second interpretation involves the detection threshold of 12 decibels below the SNR of the signal received on the direct path. In a high SNR case, a single signal with a large SNR might be received, followed by a rapid decay in the amplitude of the following signals. Thus the criterion is set relatively high, and a smaller percentage of the received signals exceed the detection threshold. In a smaller set of signals, less variation might be noted. Also shown in Figure 7-7 is a best fit line to the ratio of signal widths as a function of the SNR.

In Figure 7-8 through Figure 7-10, plots of the minimum and maximum time extent of the received signal waveforms at several different locations are shown.

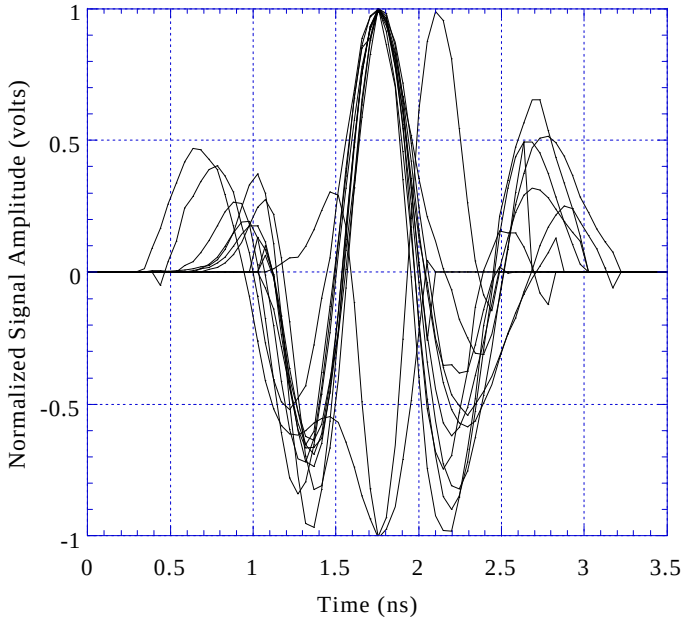

Figure 7-6: Received wavefroms from LOS path signals. Peak amplitude for each signal has been normalized to unity (recall recovered LOS signal at F2 for an example of the inverted pulse shape).

7.3 UWB Channel Synthesis

In order to realize the practical significance of the channel models developed in this work, it is important to be able to apply them to the test and verification of ultra-wideband radio algorithms. Along these lines, the clustering model and the associated statistics for the cluster and ray arrival rates and angles from Chapter 6 are used to synthesize an UWB propagation channel. For this study, ideal second derivative Gaussian pulses are assumed; only the time and angle-of-arrival are accounted for. No attempt is made to model the distortions and dispersive effects of the channel on a transmitted UWB pulse.

Some example scatter plots of the signal time-of-arrival and the angle-of-arrival information generated by the channel synthesis routine are shown below in Figure 7-11 - Figure 7-15. The signal arrival information shown in Figure 7-15 was also used to generate some

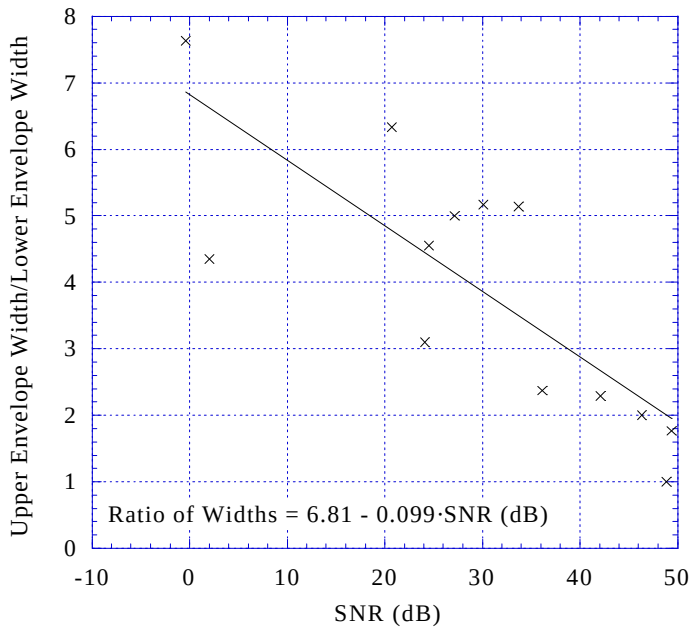

Figure 7-7: Ratio of the time extent of the upper envelope to the lower envelope vs. SNR. All signals within 12dB of the LOS path signal energy are considered.

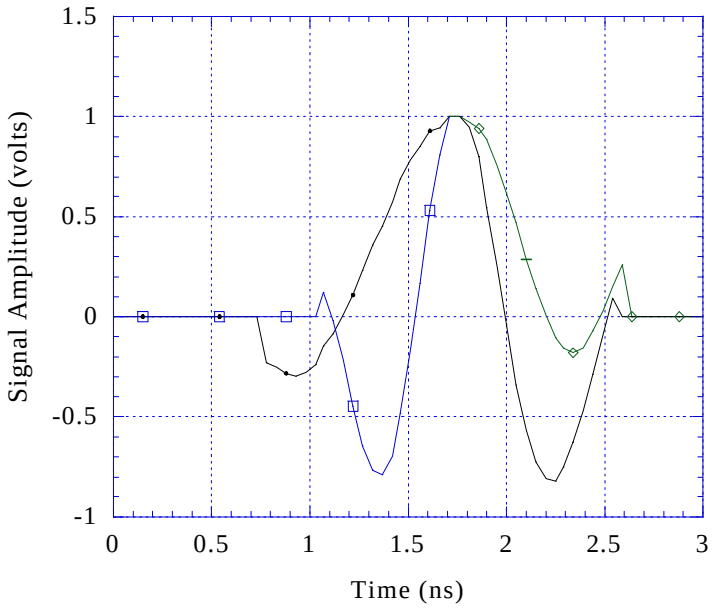

Figure 7-8: Upper and lower envelope of the received signal waveform at location P. All signals within 12dB of the strongest signal are considered.

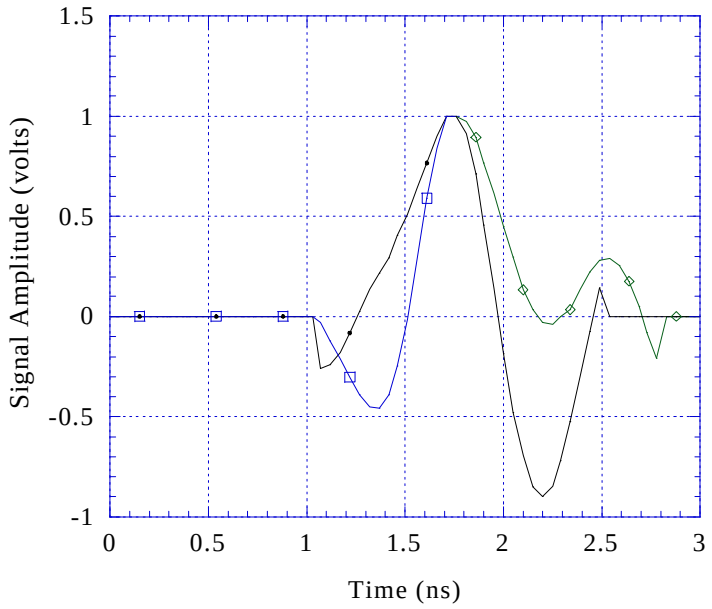

Figure 7-9: Upper and lower envelope of the received signal waveform at location L. All signals within 12dB of the strongest signal are considered.

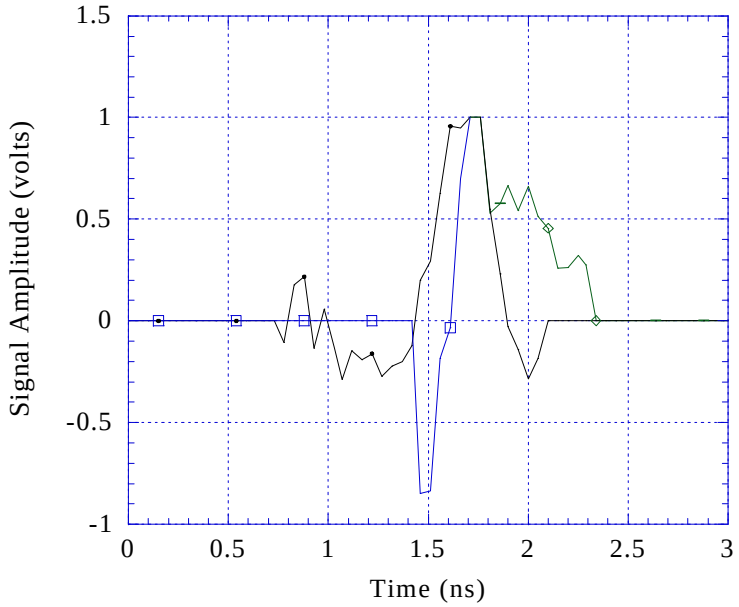

Figure 7-10: Upper and lower envelope of the received signal waveform at location C. All signals within 12dB of the strongest signal are considered.

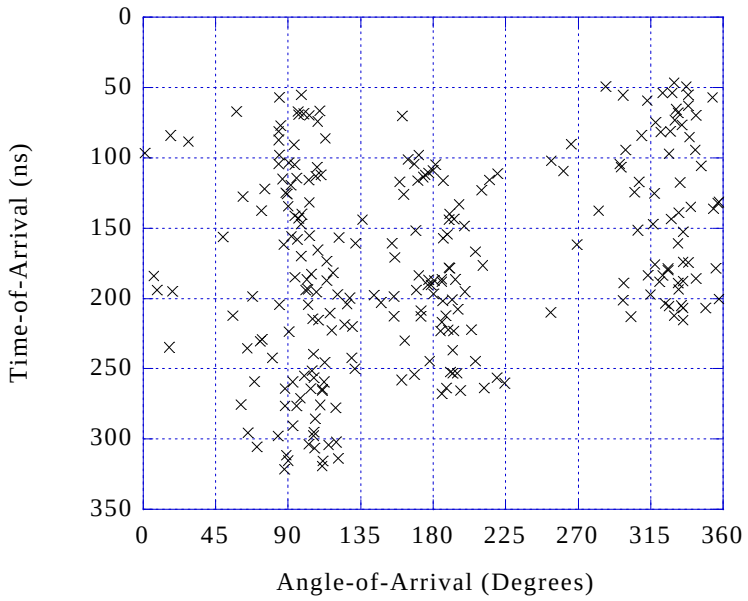

Figure 7-11: Example scatter plot of signal time-of-arrival vs. angle-of-arrival.

examples of the synthesized received signal measurements. Two examples are given for different location in the measurement array. The first example is shown for two different time windows in Figure 7-16, and Figure 7-19 and the second example is shown in Figure 7-18 and Figure 7-19. These plots demonstrate, at least upon visual inspection, some consistency between the measured results and the recovered signal information and the synthesized signal information.

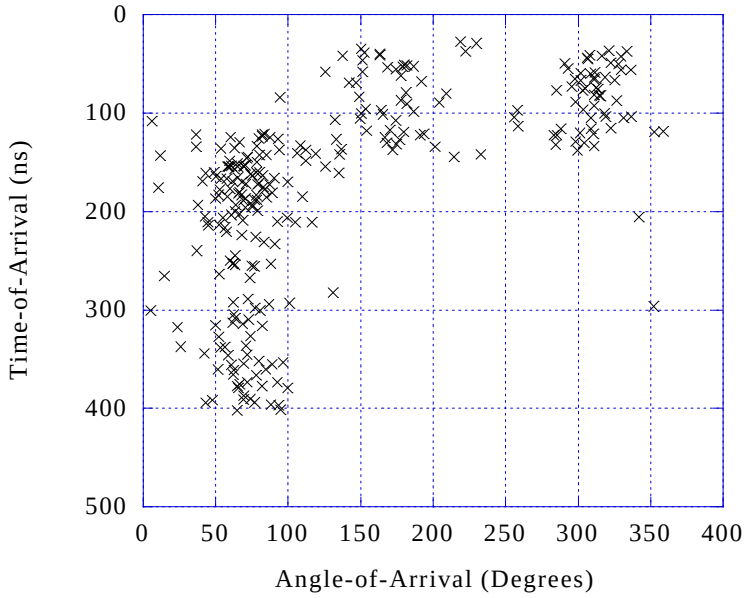

Figure 7-12: Example scatter plot of signal time-of-arrival vs. angle-of-arrival.

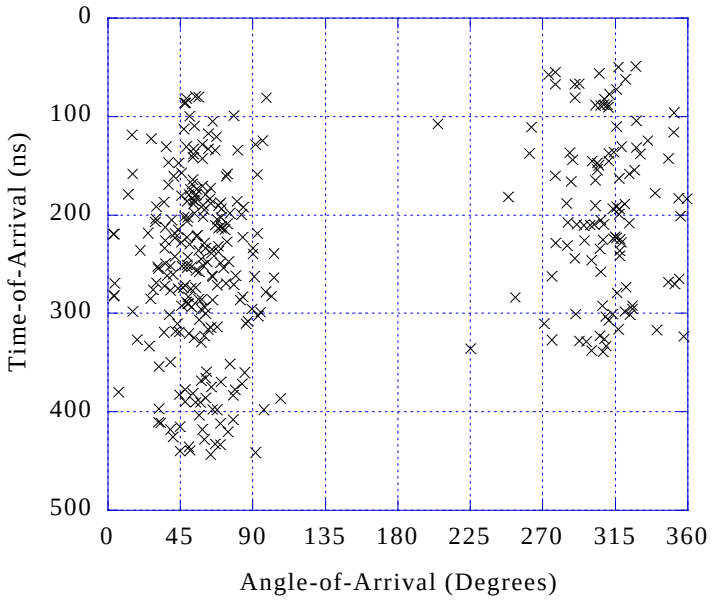

Figure 7-13: Example scatter plot of signal time-of-arrival vs. angle-of-arrival.

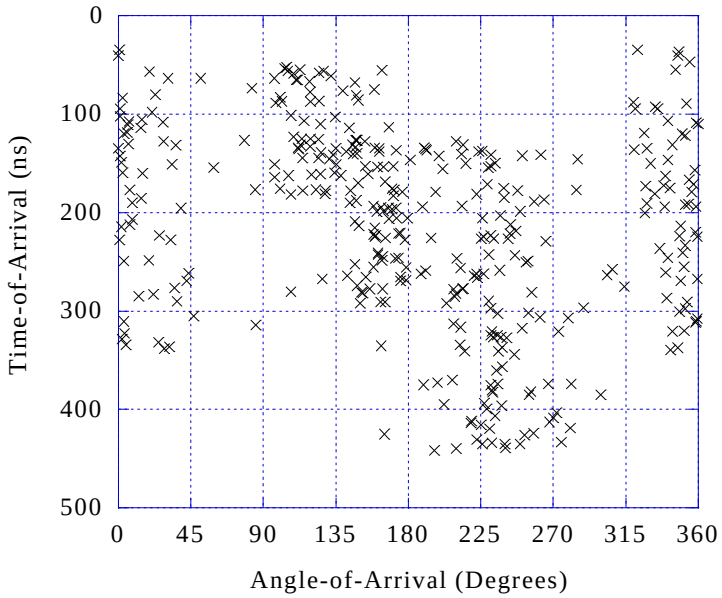

Figure 7-14: Example scatter plot of signal time-of-arrival vs. angle-of-arrival.

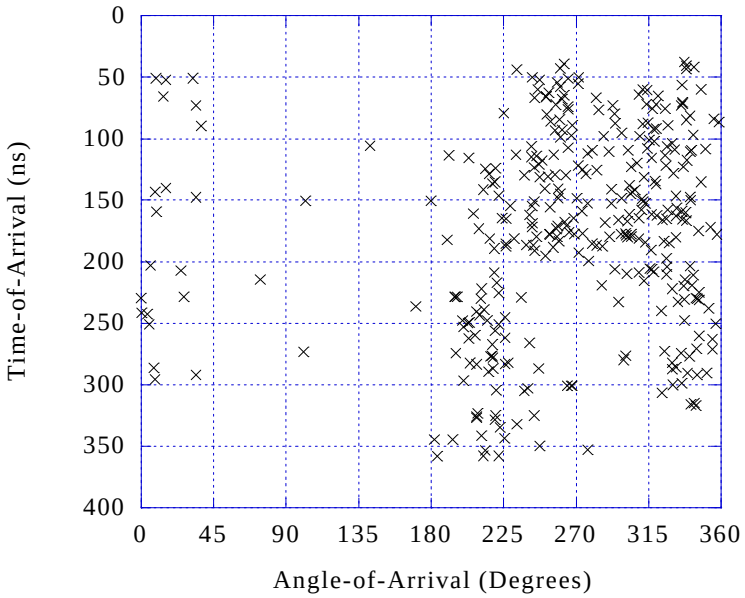

Figure 7-15: Example scatter plot of signal time-of-arrival vs. angle-of-arrival. This is the signal information used to generate the example profiles.

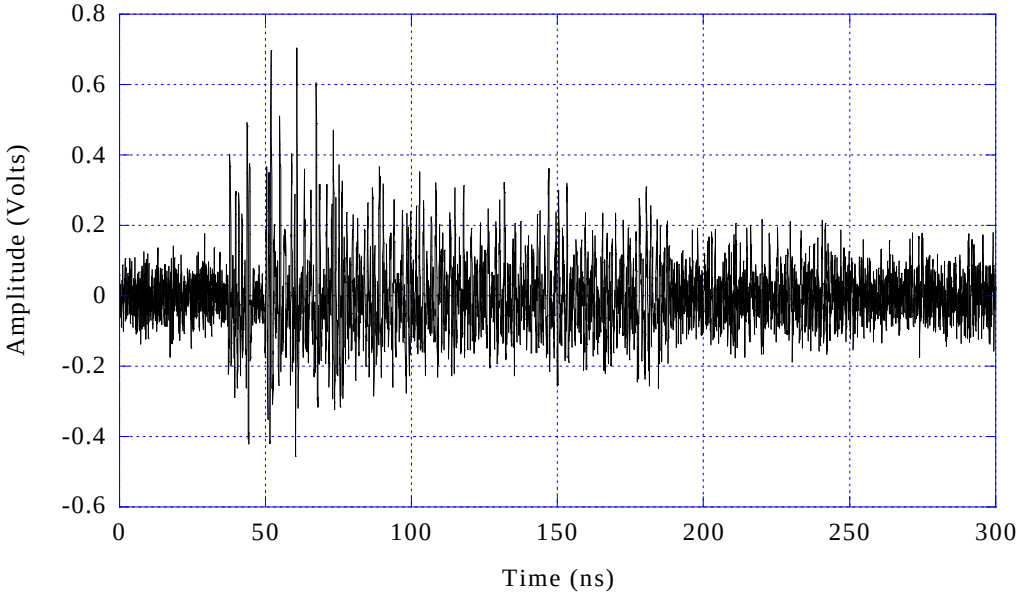

Figure 7-16: Example of the received signal profile generated by the channel synthesis routine.

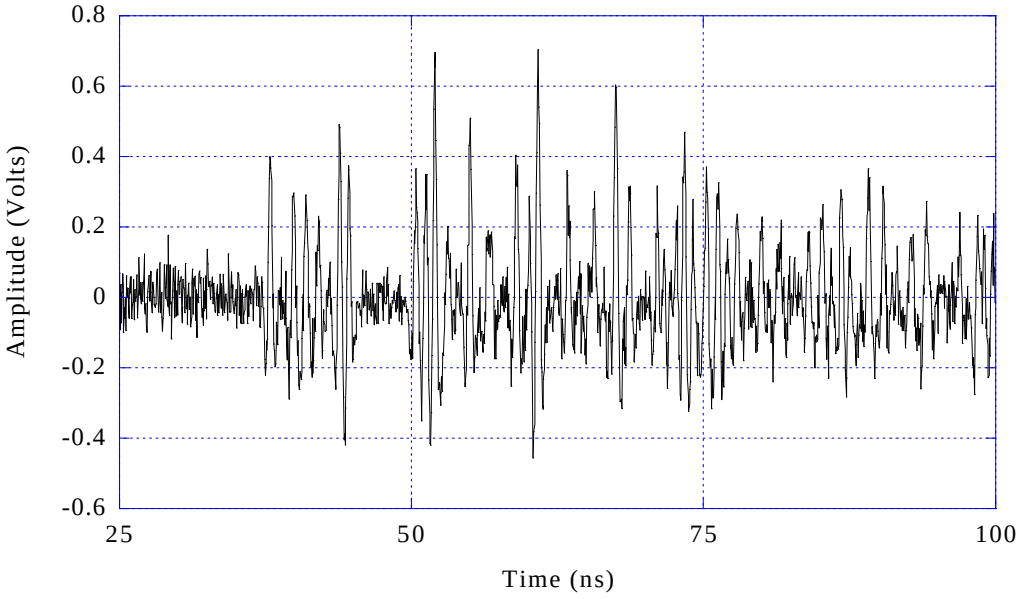

Figure 7-17: 75 ns window on the received signal profile.

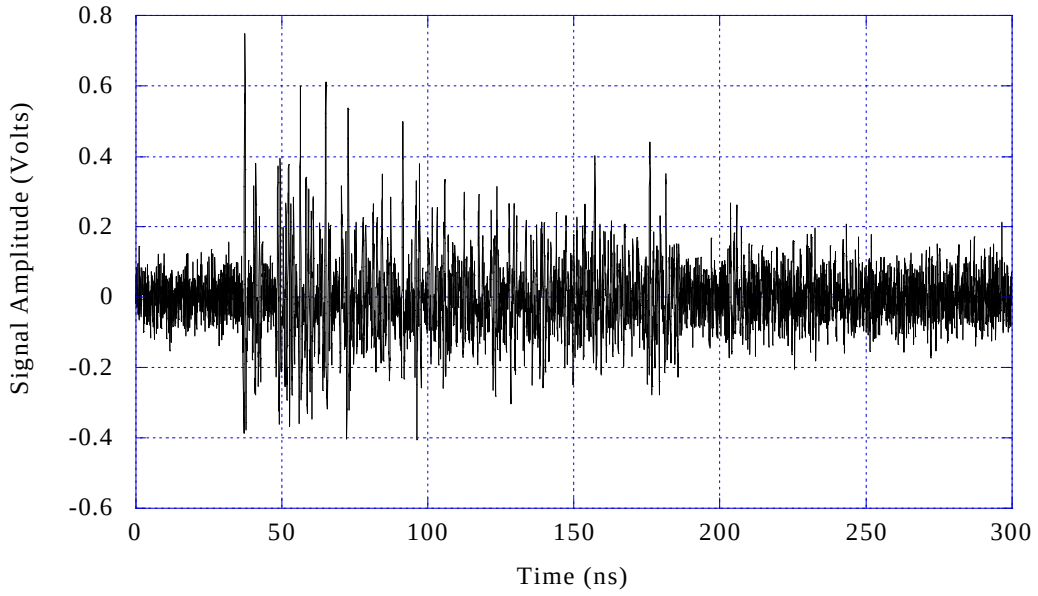

Figure 7-18: Example of the received signal profile generated by the channel synthesis routine.

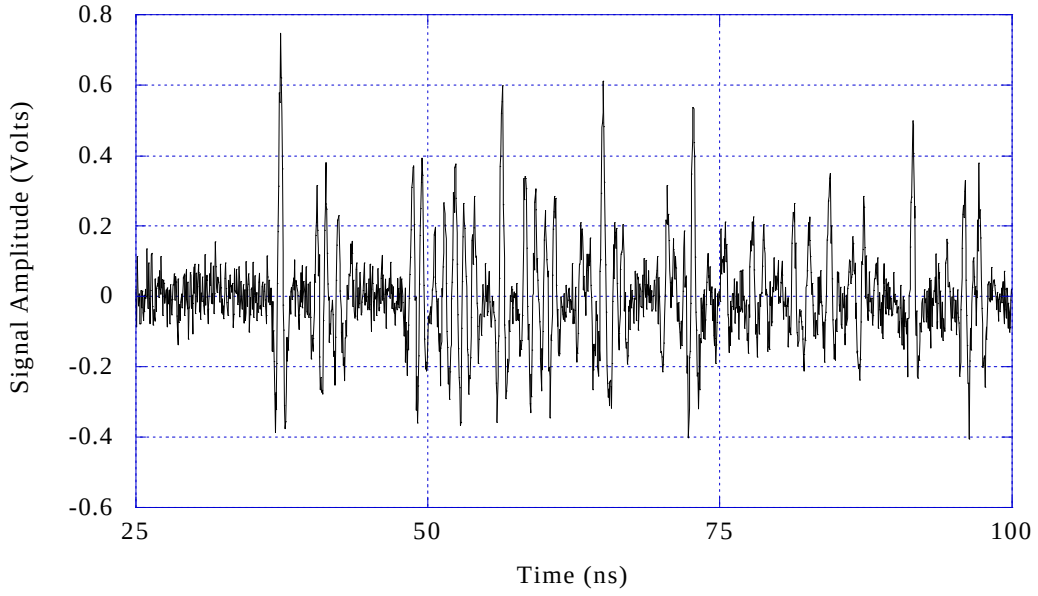

Figure 7-19: 75 ns. window on the received signal profile.

Chapter 8

Conclusion

The main goal of this dissertation was to develop an understanding of the indoor UWB propagation channel, including the time-of-arrival, angle-of-arrival and level distributions of a collection of received signals. To accomplish this, a set of algorithms suitable for processing UWB signals incident on an array of sensors was developed and then validated through application both to deterministic scenarios and to a set of measured data. Thus there were two main parts to this work, the development of the processing algorithms and the application of these techniques to measured data, resulting in the channel models.

Considering the first task, much of the existing array signal processing and source location literature is devoted to algorithms which operate on more narrowband signals than those of interest here. In general, these techniques are not applicable to signals with fractional bandwidths as large as those considered in this work. Many attempts were made to generalize these more narrowband algorithms for application to the UWB signals, before finally settling on the CLEAN algorithm as the core of the UWB signal processing routines.

A fundamental problem with the extension of the established processing algorithms to UWB signals is in one of the assumptions upon which this work was based. Due to the fractional bandwidth of the UWB signals, it was decided early in the project that the

processing algorithms should not exhibit a strong dependence on the precise form of the incident signals, as it is not known a-priori, nor is it static from one incident signal to another. Without an accurate model for the incident signals, it is difficult to conduct any sort of theoretical optimization or even to define maximum likelihood reception techniques. For example, as part of the study of narrowband extensions, methods were derived based on constrained optimization techniques. These performed well in the presence of idealized signals, but the performance degraded rapidly when applied to actual measured UWB signals. Other problems with the generalization of more narrowband algorithms, such as a penalty in the available time resolution, were discussed in Chapter 2.

It was the need for an algorithm general enough to handle this situation that motivated the use of the CLEAN algorithm. The CLEAN algorithm as described in [19] was modified in this work to operate with minimal assumptions on the form of the received signals. The only information assumed about the signals is that they have support in time of less than some number of samples. A trade is in the fact that it is very difficult to analyze the algorithm or even to derive criterion for the optimal selection of parameters. This is true in general for the CLEAN algorithm, not just for the application here. In fact, it was stated in [6] that although the algorithm has been widely accepted in radio-astronomy for the processing of images, it is the least understood of the main algorithms used for this purpose. Further, parameter selection is generally achieved through Monte-Carlo techniques. Nevertheless the CLEAN algorithm was adopted as the core of an UWB processing algorithm which was then applied to measured data to obtain a characterization of the UWB channel. Further post-processing routines were also developed here, in order to improve the quality of the signal estimates.

Following the development of the processing routines, the second part of this work involved the application of these techniques to the measured propagation described in Chapter

1. From this, models for the propagation of UWB signals in an indoor channel were generated and reported. Comparisons to more narrowband channel characterizations were made when possible.

The channel models presented in this work are based on a set of measurement made at a number of locations within an office building. It has been noted that the geometry of the situation and the building architecture can have a significant effect on the received signals [48], [49]. Therefore, further work remains in the collection and processing of propagation data from different buildings, in order to increase the significance of and augment the results presented in this work. It is possible therefore, that the strongest contribution of this work is in the development of the processing algorithms, and that as more measurements are taken in different environments, the parameters of the UWB channel model presented here will change to reflect this new information.

Bibliography

[1] D.N. de G. Allen, *Relaxation Methods in Engineering and Science*, McGraw-Hill Book Company, 1954.

[2] O. Axelsson, *Iterative Solution Methods*, Cambridge University Press, 1996.

[3] Constantine A. Balanis, *Antenna Theory*, Wiley, New York, Second Edition, 1997.

[4] Kevin M. Buckley and Lloyd J. Griffiths, "Broad-Band Signal-Subspace Spatial-Spectrum (BASS-ALE) Estimation", *IEEE Transactions on Acoustics, Speech, and Signal Processing*, vol. 36, no. 7, July, 1988.

[5] D. Colton and R. Kress, *Inverse Acoustics and Electromagnetic Scattering Theory*, Second Edition, Springer-Verlag, 1998.

[6] Tim Cornwell and Robert Braun, *Deconvolution, in Synthesis Imaging in Radio Astronomy*, Richard A. Perley, Frederic R. Schwab, Alan H. Bridle, ed., Astronomical Society of the Pacific, San Francisco, 1994.

[7] R. J.-M. Cramer, M.Z. Win and R.A. Scholtz, "Impulse Radio Multipath Characteristics and Diversity Reception", *Proc. of ICC '98*, vol. 3, p. 1650-1654.

[8] R. J.-M. Cramer, M.Z. Win, R.A. Scholtz, "Evaluation of the Multipath Characteristics of the Impulse Radio Channel", *Proc. of PIMRC '98*, vol. 2, p. 864-868.

[9] OSD/DARPA, *Ultra-Wideband Radar Review Panel, Assessment of Ultra-Wideband (UWB) Technology*, DARPA, Arlington, VA, 1990.

[10] G.E. Forsythe and W.R. Wasow, *Finite Difference Methods for Partial Differential Equations*, John Wiley & Sons, Inc., 1967.

[11] Avraham Freedman, Ranjan Bose and Bernard D. Steinberg, "Techniques to Improve the CLEAN Deconvolution Algorithm", *Journal of the Franklin Institute*, Vol 332B, no. 5, p535-553, Elsevier Science Ltd., Great Britain, 1995.

[12] Jean-Jacques Fuchs, "Multipath Time-Delay Detection and Estimation", *IEEE Trans. on Signal Proc.*, vol. 47, no. 1, January 1999.

[13] W. Hackbusch, *Iterative Solution of Large Sparse Systems of Equations*, Springer-Verlag, 1994.

[14] Henning F. Harmuth, *Transmission of Information by Orthogonal Functions*, Springer-Verlag, New York, 1969.

[15] Homayoun Hashemi, "The indoor radio propagation channel," *Proc. IEEE*, vol. 81, no. 7, pp. 943-968, July, 1993.

[16] Simon Haykin, ed., *Advances in Spectrum Analysis and Array Processing - Volume II*, Prentice-Hall, Englewood Cliffs, NJ, 1991.

[17] Simon Haykin, *Adaptive Filter Theory*, 2nd Edition, Prentice-Hall, Englewood Cliffs, NJ, 1991.

[18] T.C. Henderson, *Discrete Relaxation Techniques*, Oxford University Press, 1990.

[19] J.A. Högbom, "Aperture Synthesis with a Non-Regular Distribution of Interferometer Baselines", *Astron. and Astrophys. Suppl. Ser.*, vol. 15, p.417-426, 1974.

[20] J.E. Hudson, *Adaptive Array Principles*, Peter Peregrinus Ltd., 1981.

[21] Derek E. Iverson, "Measuring Moving Target Speed and Angle in Ultra-Wideband Radar", in *Ultra-Wideband Short-Pulse Electromagnetics 2*, Lawrence Carin and Leopold B. Felsen, editors, Plenum Press, New York, 1995, p.577-584.

[22] William C. Jakes, *Microwave Mobile Communications*, IEEE Press, 1974.

[23] Don H. Johnson, Dan E. Dudgeon, *Array Signal Processing*, Prentice-Hall, Englewood Cliffs, New Jersey, 1993.

[24] S.S. Kolenchery, J.K. Townsend, J.A. Freebersyser, "A Novel Impulse Radio Network for Tactical Military Wireless Communications", Proc. of Milcom '98.

[25] John D. Kraus, *Radio Astronomy*, 2nd Edition, Cygnus-Quasar Books, Powell, Ohio, 1986.

[26] D. Kundur and D. Hatzinakos, "A Novel Blind Deconvolution Scheme for Image Restoration Using Recursive Filtering", *IEEE Transactions on Signal Processing*, vol. 46, no. 2, February, 1998.

[27] R.L. Lagendijk and Jan Biemond, *Iterative Identification and Restoration of Images*, Kluwer Academic Publishers, 1991.

[28] N.N. Lebedev, *Special Functions*, Dover Publications, NewYork, 1972.

[29] J.C. Liberti and T.S. Rappaport, *Smart Antennas for Wireless Communications: IS-95 and Third Generation CDMA Applications*, Prentice-Hall, Englewood Cliffs, New Jersey, 1999.

[30] J. Litva and T. K-Y. Lo, *Digital Beamforming in Wireless Communications*, Artech House Publishers, 1996.

[31] D.G. Luenberger, *Optimization by Vector Space Methods*, John Wiley and Sons, 1969.

[32] R.A. Monzingo and T.A. Miller, *Introduction to Adaptive Arrays*, Wiley-Interscience, 1980.

[33] Richard O. Nielsen, *Sonar Signal Processing*, Artech House, Norwood, MA, 1991.

[34] O. Nørklit and J.B. Andersen,"Diffuse Channel Model and Experimental Results for Array Antennas in Mobile Environments", *IEEE Trans. on Antennas and Propagation*, vol. 46, no. 6, June 1998, pp. 834-840.

[35] D. Parsons, *The Mobile Radio Propagation Channel*, Halsted Press, 1992.

[36] R.L. Peterson, R.E. Ziemer, D.E. Borth, *Introduction to Spread Spectrum Communications*, 1995, Prentice Hall, Englewood Cliffs, NJ.

[37] A.A.M. Saleh and R.A. Valenzuela, "A statistical model for indoor multipath propagation", *IEEE JSAC*, vol. 5, no. 2, pp. 128-137, 1987.

[38] Robert A. Scholtz, "Multiple Access with Time-Hopping Impulse Modulation," in *Proc. Milcom*, Oct. 1993.

[39] R.A. Scholtz and M.Z. Win, "Impulse Radio", *Personal Indoor Mobile Radio Conference*, Helsinki, Finland, Sept. 1997, Printed in *Wireless Communications: TDMA vs. CDMA*, S.G. Glisic and P.A. Leppänen, eds., Kluwer Academic Publishers, 1997.

[40] R.A. Scholtz, R. J-M. Cramer, and M.Z. Win, "Evaluation of the Propagation Characteristics of Ultra-Wideband Communication Channels", Antennas and Propagation Society International Symposium, 1998, vol. 2, p. 626-630.

[41] Jodi Lisa Schwartz and Bernard D. Steinberg, "Properties of Ultrawideband Arrays", in *Ultra-Wideband, Short-Pulse Electromagnetics 3*, Edited by Carl E. Baum, Lawrence Carin and Alexander P. Stone, Plenum Press, New York, 1997, p. 139-145.

[42] U.J. Schwarz, "Mathematical-statistical Description of the Iterative Beam Removing Technique (Method CLEAN)", *Astronomy and Astrophysics,* vol. 65, 1978, pp. 345-356.

[43] U.J. Schwarz, "The Method CLEAN - Use, Misuse and Variations" in *Image Formation from Coherence Functions in Astronomy*, D. Reidel Publishing Company, 1979.

[44] Fred C. Schweppe, "Sensor-Array Data Processing for Multiple-Signal Sources", *IEEE Transactions on Info. Theory*, vol. IT-14, no. 2, March, 1968.

[45] F.S. Shaw, *Relaxation Methods - an introduction to approximational methods for differential equations,* Dover Publications, 1953.

[46] Merrill Skolnik, "The Radar Antenna - Circa 1995", *Journal of the Frankin Institute*, vol. 332B, no. 5, p503-519, Elsevier Science Ltd., Great Britain, 1995.

[47] R.V. Southwell, *Relaxation Methods in Engineering Science - A Treatise on Approximate Computation*, Oxford University Press, 1940.

[48] Q. Spencer, M. Rice, B. Jeffs, M. Jensen, "Indoor Wideband Time/Angle of Arrival Multipath Propagation Results", *IEEE Vehicular Technology Conference*, IEEE, 1997, p. 1410-1414.

[49] Q. Spencer, M. Rice, B. Jeffs, M. Jensen, "A Statistical Model for the Angle-of-Arrival in Indoor Multipath Propagation", *IEEE Vehicular Technology Conference*, IEEE, 1997, p. 1415-1419.

[50] Q. Spencer, B. Jeffs, M. Jensen, A. Swindlehurst, "Modeling the Statistical Time and Angle of Arrival Characteristics of an Indoor Multipath Channel", *IEEE Journal on Selected Areas in Communication*, vol. 18, no. 2, March 2000, p. 347-360.

[51] H. Stark and Y. Yang, *Vector Space Projections - A Numerical Approach to Signal and Image Processing, Neural Nets, and Optics*, Wiley Interscience, 1998.

[52] Jean-Luc Starck and Albert Bijaoui, "Multiresolution Deconvolution", *J. Opt. Soc. Am. A.*, vol. 11, No. 5, May, 1994.

[53] D.G. Steer, P.E. Dewdney, M.R. Ito, "Enhancements to the deconvolution algorithm "CLEAN"", *Astronomy and Astrophysics*, vol. 137, 1984, pp. 159-165.

[54] Bernard D. Steinberg, Donald Carson, Ranjan Bose, "High Resolution 2-D Imaging with Spectrally Thinned Wideband Waveforms", in *Ultra-Wideband Short-Pulse Electromagnetics 2*, Lawrence Carin and Leopold B. Felsen, editors, Plenum Press, New York, 1995, p.563-569.

[55] Bernard D. Steinberg and Harish M. Subbaram, *Microwave Imaging Techniques*, John Wiley and Sons, New York, 1991.

[56] James D. Taylor, *Introduction to Ultra-Wideband Radar Systems*, CRC Press, Boca Rator, FL, 1995.

[57] Jenho Tsao and Bernard D. Steinberg, "Reduction of Sidelobe and Speckle Artifacts in Microwave Imaging: The CLEAN Technique", *IEEE Trans. on Antennas and Prop.*, vol. 36, No. 4, April, 1988.

[58] S. Twomey, *Introduction to the Mathematics of Inversion in Remote Sensing and Indirect Measurements*, Dover Publications, New York, 1996.

[59] H. Urkowitz, C.A. Hauer, and J.F. Koval, "Generalized Resolution in Radar Systems", *Proceedings of the IRE*, 50, p. 2093-2105, 1962.

[60] Rodney G. Vaughan and Neil L. Scott, "Super-Resolution of Pulsed Multipath Channels for Delay Spread Characterization", *IEEE Trans. Commun.*, vol. 47, no. 3, March 1999.

[61] T.B. Vu and H. Chen, "A Real Time 'CLEAN' Method for Small Linear Arrays", *1996 IEEE MTT-S Digest*, pp1003 - 1006.

[62] Gilbert G. Walter, *Wavelets and Other Orthogonal Systems with Applications*, CRC Press, Boca Raton, 1994.

[63] Moe Z. Win and Robert A. Scholtz, "Ultra-wide bandwidth (UWB) time-hopping spread spectrum impulse radio for wireless multiple access communications," *IEEE Trans. Commun.*, Jan. 1997, submitted.

[64] M.Z. Win and R.A. Scholtz, "Impulse radio: How it works," *IEEE Commun. Lett.*, Feb. 1998.

[65] Moe Z. Win and Robert A. Scholtz, "Comparisons of Analog and Digital Impulse Radio for Multiple Access Communications", *Proc. IEEE Int. Conf. On Comm.,* June 1997.

[66] Moe Z. Win, Robert A. Scholtz, Mark A. Barnes, "Ultra-Wideband Signal Propagation for Indoor Wireless Communications", *Proc IEEE Int. Conf. on Comm.,* June, 1997.

[67] T.S. Rappaport, *Wireless Communications, Principles and Practice*, Prentice-Hall PTR, 1996.

Appendix A

UWB Signal Models

A.1 Properties of the Ultra-wideband Signals.

Given the signal models in Chapter 1, the UWB radio waveforms can be related to the Hermite polynomials, which are defined as [28],

$$H_n(x) = (-1)^n e^{x^2} \frac{d^n}{dx^n} e^{-x^2} \tag{A.1}$$

The first several Hermite polynomials are given by,

$$H_0(x) = 1 \tag{A.2}$$

$$H_1(x) = 2x \tag{A.3}$$

$$H_2(x) = 4x^2 - 2 \tag{A.4}$$

$$H_3(x) = 8x^3 - 12x \tag{A.5}$$

Utilizing these functions to lend mathematical structure to the waveforms and perhaps the subsequent processing is an attractive option, as the Hermite functions form a complete, orthonormal family, with weight $\rho(x) = e^{-x^2}$, on $L^2(-\infty, \infty)$. The orthonormality condition is stated formally as,

$$\int_{-\infty}^{\infty} H_n(x) H_m(x) e^{-x^2} = 0, \; n \neq m \tag{A.6}$$

Following the representation above, the impulse radio waveforms can be written to within a constant as,

$$p_n(t) = A \left(-\frac{\sqrt{2\pi}}{\tau_m} \right)^n H_n(x) e^{-x^2} \tag{A.7}$$

where,

$$x = \sqrt{2\pi} \left(\frac{t - t_d}{\tau_m} \right) \tag{A.8}$$

Note that this representation does not give orthogonality between pulses of different orders, as the resulting weight function in the integral of equation (A.6) is e^{-2x^2} instead of e^{-x^2}.Other representations are possible as well. In particular, if maintenance of orthonormality is a goal, and the precise form of the representation is not critical, then the following functions can be used to represent the first three waveforms,

$$p'_n(t) = A \left(-\frac{\sqrt{\pi}}{\tau_m} \right) H_n(x) e^{-x^2} \tag{A.9}$$

where,

$$x = 2\sqrt{\pi} \left(\frac{t - t_d}{\tau_m} \right) \tag{A.10}$$

The main problem with models based on these Hermite waveforms is in the fact that orthogonality between the different modes in the representation is lost when the impulse width parameters, τ_m, are not equal. In particular, if two multipath components arrive at the antenna having experienced different propagation and dispersion mechanisms in the channel, they may no longer belong to the same family, $H_n(t/\tau_m)$, of Hermite functions. This structure was explored, however, with the idea of developing a technique for deriving DOA information from the UWB signals received on an array of sensors, similar to what is available for more narrowband signals. In analogy with the narrowband techniques, a multiplicative delay operator is required, and the following equations were derived to serve that purpose. Denoting the nth derivative pulse as $p_n(t)$,

$$p_o\left(t-\tau\right) = p\left(t\right)\exp(-\alpha) \tag{A.11}$$

$$p_1\left(t-\tau\right) = p_1\left(t\right)\left.\frac{t-t_d-\tau}{t-t_d}\right]\exp\left(-\alpha\right) \tag{A.12}$$

$$p_2\left(t-\tau\right) = p_2\left(t\right)\left[\frac{\tau_m^2-4\pi\left(t-\left(t_d+\tau\right)\right)^2}{\tau_m^2-4\pi\left(t-t_d\right)^2}\right]\exp\left(-\alpha\right) \tag{A.13}$$

and,

$$\alpha = \frac{2\pi\tau\left(\tau-2\left(t-t_d\right)\right)}{\tau_m^2} \tag{A.14}$$

Considering again the idea of a data independent algorithm, it is of interest to examine the correlation functions of these Hermite functions against the same order Hermite function with a different width parameter. This provides a measure of the robustness of any algorithm based on these waveforms to the dispersive effects of the channel. Defining the orthonormal sequence $\{e_n\left(t\right)\}_{n=0}^{\infty}$ in the following manner,

$$e_n(t) = \frac{1}{\sqrt{2^n n! \sqrt{\pi}}} e^{-t^2} H_n(t) \tag{A.15}$$

The corresponding correlation functions are given below. In these equations, the superscript denotes the order of the Hermite function, γ is the fractional difference in the width parameter τ, and t_d is the delay at which the correlation is calculated.

$$R_\gamma^{(0)}\left(\frac{t_d}{\tau}\right) = \sqrt{\frac{2\gamma}{1+\gamma^2}} e^{-\frac{1}{2(1+\gamma^2)}\left(\frac{t_d}{\tau}\right)^2} \tag{A.16}$$

$$R_\gamma^{(1)}\left(\frac{t_d}{\tau}\right) = \sqrt{\frac{2\gamma}{1+\gamma^2}} e^{-\frac{1}{2(1+\gamma^2)}\left(\frac{t_d}{\tau}\right)^2} \left[\frac{2\gamma}{1+\gamma^2} - \frac{2\gamma}{(1+\gamma^2)^2}\left(\frac{t_d}{\tau}\right)^2\right] \tag{A.17}$$

$$\begin{aligned} R_\gamma^{(2)}\left(\frac{t_d}{\tau}\right) &= \sqrt{\frac{2\gamma}{\gamma^2+1}} e^{-\frac{1}{2(\gamma^2+1)}\left(\frac{t_d}{\tau}\right)^2} \\ &\times \left[\frac{2\gamma^2}{(\gamma^2+1)^4}\left(\frac{t_d}{\tau}\right)^4 + \frac{\beta}{(\gamma^2+1)^2}\left(\frac{t_d}{\tau}\right)^2 - \frac{\beta}{2(\gamma^2+1)}\right] \end{aligned} \tag{A.18}$$

where,

$$\beta = \frac{\gamma^4 - 10\gamma^2 + 1}{\gamma^2 + 1} \tag{A.19}$$

Also of interest is the correlation function of the impulse radio pulse $p_2(t)$, given by,

$$R_\gamma^{(p_2)}\left(\frac{t_d}{\tau}\right) = \frac{8}{3}\sqrt{\frac{\gamma^5}{2(1+\gamma^2)^5}} e^{-\frac{2\pi}{(1+\gamma^2)}\left(\frac{t_d}{\tau}\right)^2} \left[\frac{16\pi^2}{(1+\gamma^2)^2}\left(\frac{t_d}{\tau}\right)^4 - \frac{24\pi}{1+\gamma^2}\left(\frac{t_d}{\tau}\right)^2 + 3\right] \tag{A.20}$$

These equations are plotted in A-1, A-2, A-3 and A-4.

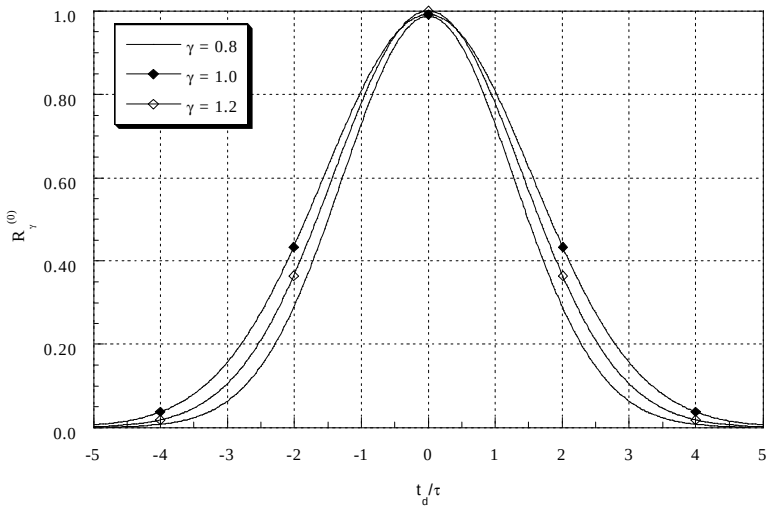

Figure A-1: Correlation of $e_0(t/\gamma\tau)$ with $e_0((t-t_d)/\tau$

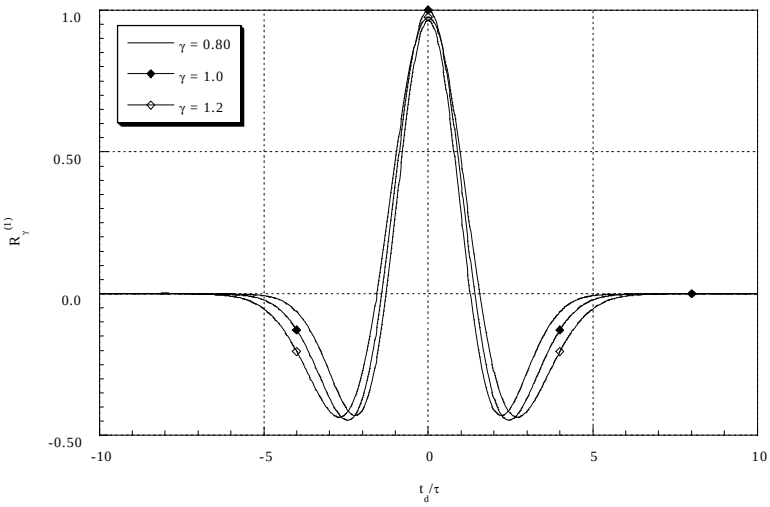

Figure A-2: Correlation of $e_1(t/\gamma\tau)$ with $e_1((t-t_d)/\tau$

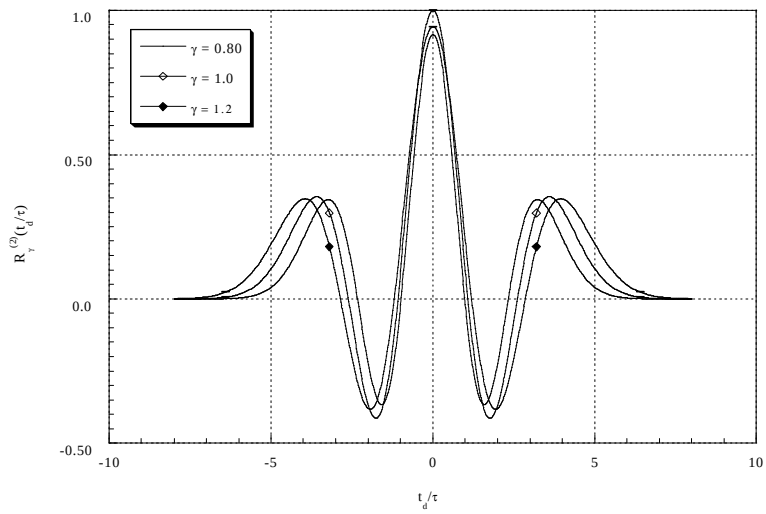

Figure A-3: Correlation of $e_2(t/\gamma\tau)$ and $e_2((t-t_d)/\tau$

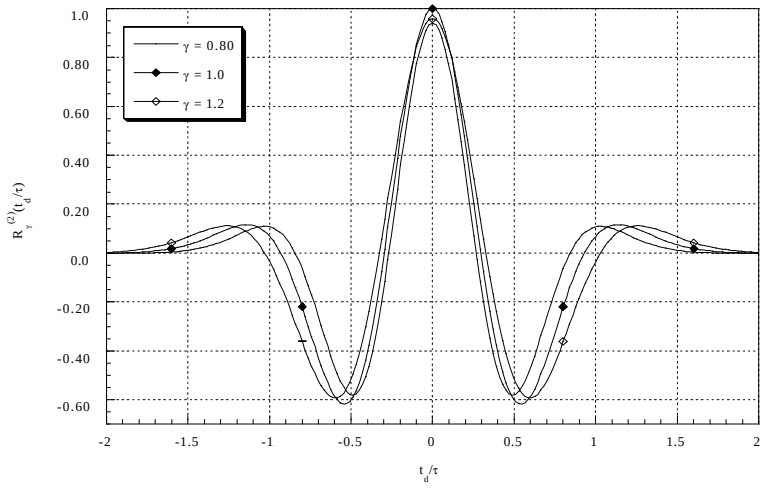

Figure A-4: Correlation of impulse radio waveform $p_2(t/\gamma\tau)$ and $p_2\left((t-t_d)/\tau\right)$

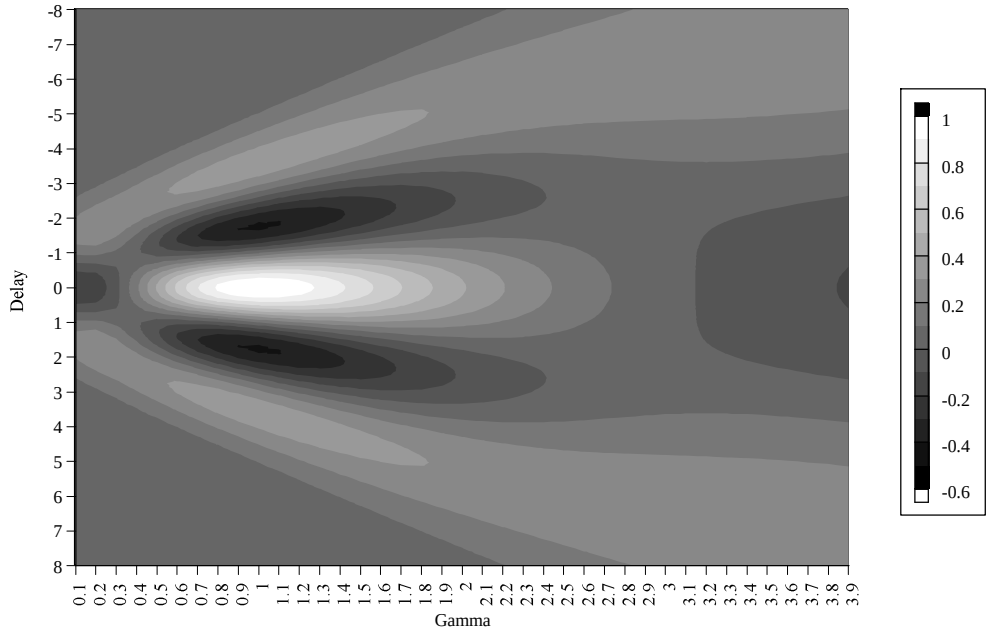

Figure A-5: Contour plot of $R_{\gamma}^{(2)}(t_d/\tau)$

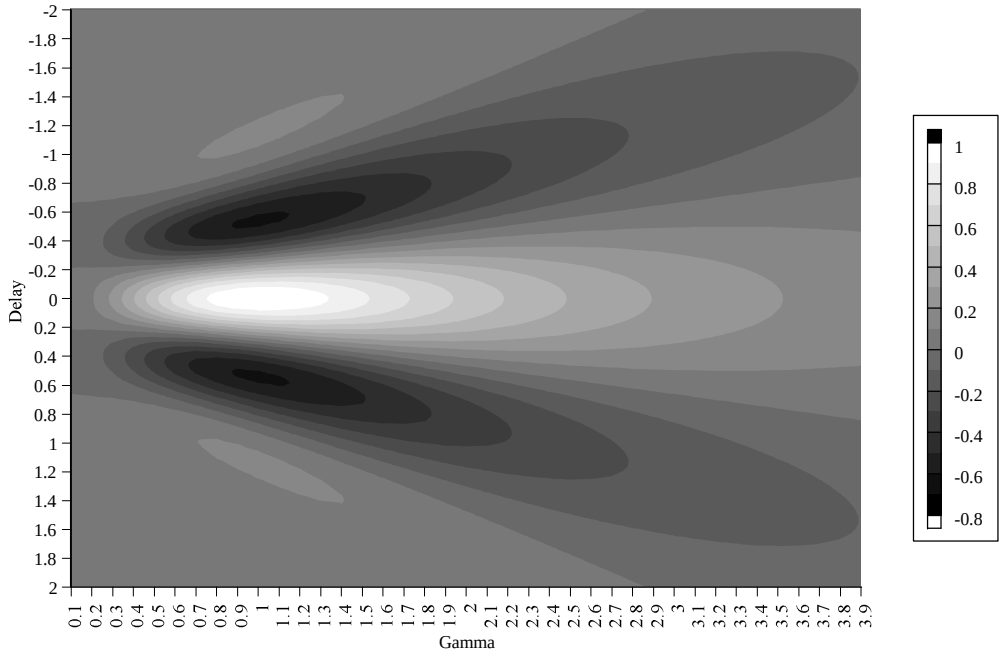

Figure A-6: Contour plot of $R_{\gamma}^{(p2)}(t_d/\tau)$

To complete the discussion on the correlation functions, it is necessary to demonstrate that orthogonality does not necessarily hold between $e_n(t/\tau_1)$ and $e_m(t/\tau_2)$ for $n \neq m$. This can be seen by considering the cross-correlation of $e_0(t/\gamma\tau)$ and $e_1(t/\tau)$, given as follows,

$$\begin{aligned} R_{\gamma}^{(1,2)}\left(\frac{t}{\tau}\right) &= \int_{-\infty}^{\infty} e_0\left(t/\gamma\tau\right) e_1\left(t/\tau\right) dt \\ &= \int_{-\infty}^{\infty} \exp\left(-\left(\frac{t}{\gamma\tau}\right)^2\right) \times 2\frac{t}{\tau} \exp\left(-\left(\frac{t}{\tau}\right)^2\right) dt \\ &\neq 0 \end{aligned} \tag{A.21}$$

A.2 Application of the model to measured data

Based on these signal models, the goal is to obtain channel models where, for a given transmitted pulse shape, the received UWB signals are members of this Hermite family of pulse shapes. A measure for the effectiveness of this technique is the percentage of the energy in the measured response of the channel which can be represented by time-shifted Hermite waveforms. Representations of the received signal by time-shifted Hermite functions are shown in Figure A-7 and Figure A-8. For the signal received at location P, a plot of the percent of the energy in the received waveform that can be represented by the time-shifted Hermite pulse shapes $p_0(t)$, $p_1(t)$, $p_2(t)$, $p_3(t)$, all of the same width parameter τ_m, is shown in Figure A-9. The curves reported here represent the mean value of the percent energy captured, when the received signal on all 49 sensors is taken into account.

m

These curves do not reflect any spatial information. If the Hermite model is extended beyond these energy capture curves, particularly to consider spatio-temporal issues, problems arise. In particular, the Hermite model does not have a shift orthogonality property.

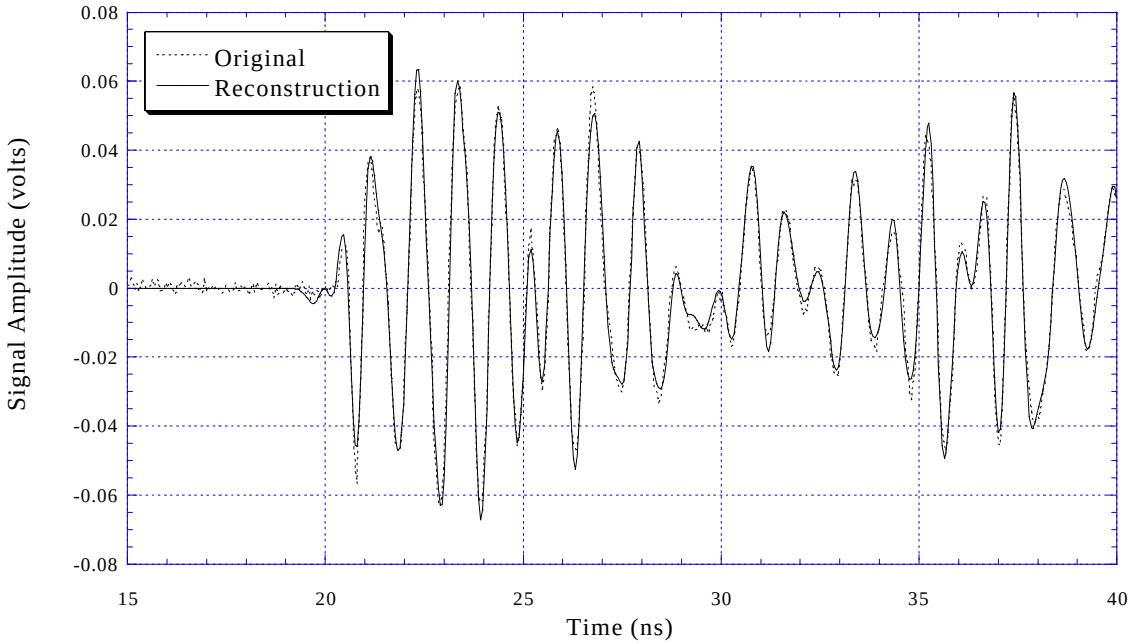

Figure A-7: Reconstruction of received waveform for sensor 0 at location P, using $p_0(t)$, $p_1(t)$, $p_2(t)$, $p_3(t)$.

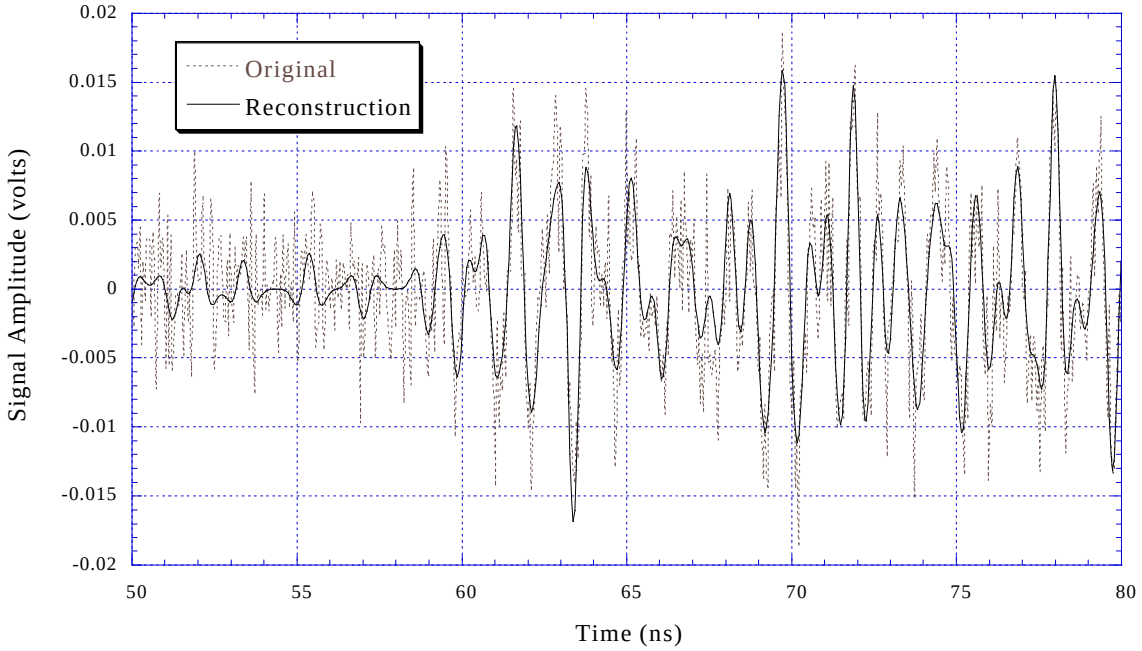

Figure A-8: Reconstruction of received waveform for sensor 0 at location B, using only $p_2(t)$.

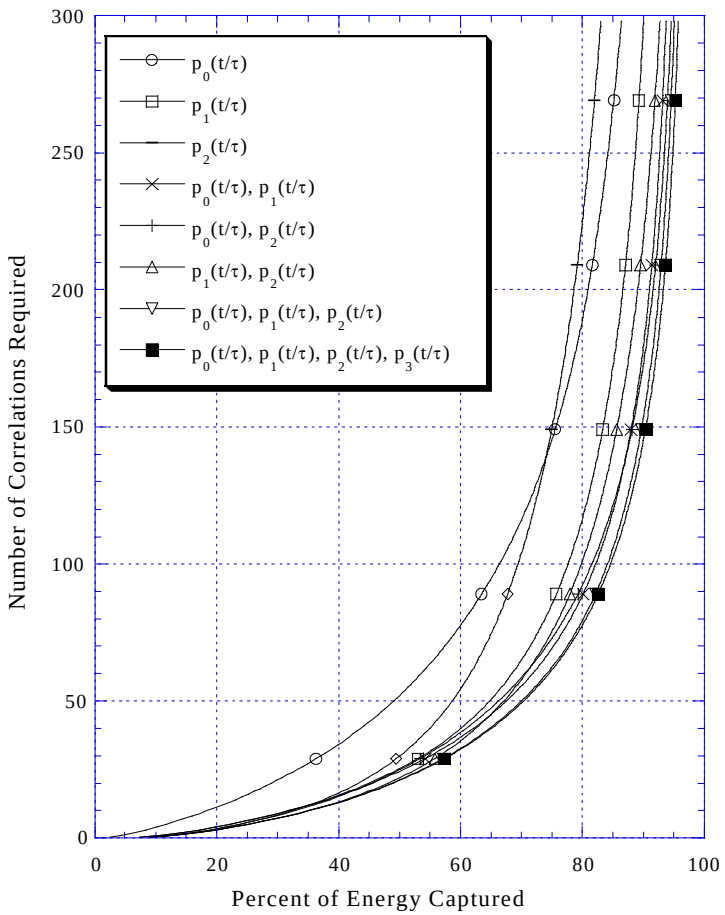

Figure A-9: Percentage energy capture vs. correlator resources for signal received at location P.

In other words, although two modes may be orthogonal and belong to different orthogonal subspaces at a particular instant in time, if one of them is shifted in time, this orthogonality is lost. Orthogonality between modes in the representation is also lost in the presence of changes in the pulse width parameter, τ_m. This is a problem, given the dynamics in the received signal, as seen from the measured data in Figure 1-3, Figure 1-4, and Figure 1-5. In other words, there is no guarantee that the received signals will all be best represented by a family of Hermite pulse shapes with the same width parameter, τ_m. Further, the main reason for employing such a set of basis functions is to enable decompositions of the observation space into orthogonal signal and noise subspaces, or to enable to the projection of the received UWB signals onto a low dimensional subspace. Given the arguments above, this is not possible with these basis functions. Thus the Hermite decomposition may have practical utility in the assessing correlation receiver performance, but it is of limited use from an analytic standpoint.

Other techniques which have been proposed for the analysis of transient signals, such as wavelet transforms, did not find great applicability in this work, as only a small number of scale values hold significant information. This can be seen in Figure A-10, which shows the result of a wavelet transform on measured data taken at location P in the building, where only scale values from $\tau_m = 0.2 \times 10^{-9}$ to $\tau_m = 0.5 \times 10^{-9}$ correlate with the received waveform to a strong degree. The kernel used to form this plot is a second derivative of Gaussian pulse, denoted by the Hermite polynomial function $e_2\left(t/\tau_m\right)$, with the scale factor of τ_m.

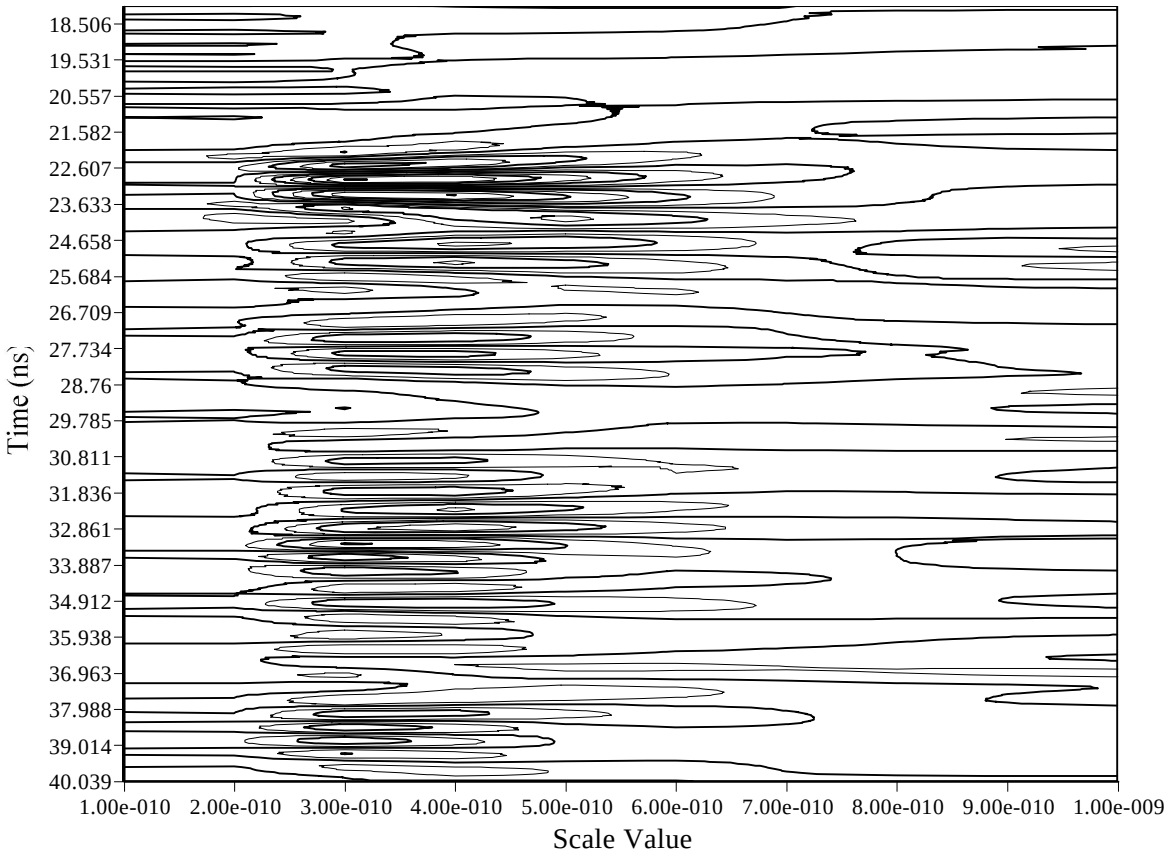

Figure A-10: Wavelet transform on measured UWB propagation data using the kernel $\mathrm{H}_2\left(t/\tau_m\right)$ for a scale value τ_m.